

Abstract

Title of Dissertation: A Spectral Survey of Black Hole Spin
 in Active Galactic Nuclei

Laura West Brenneman, Doctor of Philosophy, 2007

Dissertation directed by: Professor Christopher S. Reynolds
 Department of Astronomy

This dissertation explores the question of whether broad iron lines from the accretion disk can be used as viable diagnostic tools for constraining black hole spin. We begin by giving an overview of the importance of black hole angular momentum as a signature of General Relativity and as a means of testing this theory in the strong-field limit. We discuss the anatomy of the typical black hole/accretion disk system, focusing on the complex environments of active galactic nuclei, and in particular Seyfert-1 systems which we pursue in this work. After developing a robust technique for fitting the continuum and absorption parameters through a rigorous analysis of the *XMM-Newton* spectrum of the Sy-1 galaxy NGC 4593, we then discuss a new model we have developed that fits broad emission lines from the inner accretion disk. This model, *kerrdisk*, is fully relativistic and allows the black hole spin to be a free parameter in the fit. Using this model, we carefully analyze the 350 ks *XMM-Newton* spectrum of the Sy-1 source MCG-6-30-15, which has the broadest and best-studied iron line observed to date. Fitting for the black hole spin in this source, we conclude that $a > 0.987$ to 90% confidence. We then extend our source list to analyze the *XMM-Newton* spectra of nine other radio-quiet Sy-1 AGN that have previously been observed to harbor broad iron lines. We find that, given enough photons and a broad line indicative of an origin in the inner disk where relativistic effects are important, our new model enables us to place robust constraints on black hole spin. Four of our sampled AGN meet the criteria necessary to constrain spin. Those constraints

are given, along with the full spectral fit to each source. Interestingly, the spins of these sources range from moderate ($a \sim 0.5 - 0.7$) to very high ($a > 0.95$), and we do not find any AGN consistent with non-rotating black holes. For those objects that had marginal spin constraints or none at all, we discuss the spectral fits and the probable reasons for the lack of robustness of our results. This is the first ever survey of black hole spin in type-1 AGN.

**A Spectral Survey of Black Hole Spin
in Active Galactic Nuclei**

by

Laura West Brenneman

Dissertation submitted to the Faculty of the Graduate School of the
University of Maryland at College Park in partial fulfillment
of the requirements for the degree of
Doctor of Philosophy
2007

Advisory Committee:

Professor Christopher S. Reynolds, chair/advisor

Professor M. Coleman Miller

Professor Sylvain Veilleux

Professor Stacy S. McGaugh

Professor Theodore A. Jacobsen

Adjunct Professor Richard F. Mushotzky

© Laura West Brenneman 2007

Preface

The final results presented in this thesis are unpublished, but will be submitted to the *Astrophysical Journal* shortly after acceptance of this manuscript by the University of Maryland Department of Astronomy. Work published in refereed journals includes the material in Chapter 2 ([Reynolds et al. 2004a](#)), some of which is in press ([Brenneman et al. 2007](#)), and Chapters 3-4 ([Brenneman & Reynolds 2006](#)). Preliminary results that formed the basis of Chapter 5 were given at the AAS meetings in January 2006, January 2007 and May 2007, as well as the Triggering Relativistic Jets conference in Cozumel (March 2005), the Conference on Supermassive Black Holes in Santa Fe (July 2006), and the STScI Spring Symposium on Black Holes (April 2007).

For Mom, who read me books on astronomy, and for Dad, who took me
outside to say goodnight to the moon.

Acknowledgements

It really does take a village. This work would not have been possible without the guidance, patience and wisdom of my advisor, Chris Reynolds. He has helped me in countless ways: inspiring me with his talks and helping me prepare my own, helping me focus my work and my thinking, teaching me how to approach problems logically and creatively at the same time, grinding through fortran code with me, and providing helpful words on everything from XSPEC tricks to manuscript proofreading to career advice. I could not have asked for a better mentor.

Many thanks also to the members of my committee for putting up with all my emails and helping me to become a better scientist. Cole Miller, in particular, has taken the time to answer my questions whenever I've asked them since my first year, and has always done so with clarity, grace and thoughtfulness. Though not a member of my committee, Derek Richardson has nicely acted as a sounding board for my programming woes on several occasions, even though my work couldn't possibly have less to do with rubble piles.

The faculty and staff of the Astronomy Department have been wonderful teachers, colleagues and supporters for the duration of my time here. I am indebted to them for their knowledge, caring and consideration. Likewise, special thanks go out to my fellow graduate students, who have also doubled as housemates, teammates and fellow sufferers through late nights and long problem sets. Their scholarship has given me inspiration, and their humor has given me much-needed relief.

My parents have provided me with unconditional love, support and confidence, along with the occasional meal, wake-up call and spare bedroom to escape to. Even though neither is a scientist, they both smile and nod politely when I talk to them about my work. I would not be here without the lessons I learned from them, most importantly that intelligence alone is nothing without focus, discipline and determination.

I am grateful also to my family and friends, who have kept me sane and grounded during all my years of education and who have never wavered in their belief in me. And finally, thanks to Kathy, for more reasons than I can count.

Contents

List of Tables	viii
List of Figures	ix
1 Introduction	1
1.1 Overview	1
1.2 The History of Black Hole Studies in X-rays	2
1.3 Anatomy of a Black Hole-Accretion Disk System	7
1.3.1 Accretion Disk Properties	9
1.3.2 The Corona and Relativistic Jet Outflows	12
1.3.3 The Disk Reflection Spectrum	13
1.3.4 The Complication of Absorption	16
1.4 The History of Modeling Broad Iron Lines	21
1.5 Purpose and Structure of this Work	24
2 Modeling the X-ray Continuum in AGN: NGC 4593	26
2.1 Data Reduction	28
2.2 Spectral Analysis	29
2.2.1 Continuum and Absorption	29
2.2.2 On the Lack of Accretion Disk Signatures in NGC 4593	38
2.3 Variable Nature of the Source	44
2.3.1 Spectral Variability	44
2.3.2 Continuum Power Spectrum and Spectral Lags	49
2.4 Discussion and Conclusions	54
2.4.1 Summary of Results	54
2.4.2 Comparison with Previous Work	56
2.4.3 Implications for the X-ray Emission Region	57
2.4.4 Conclusions	58
3 A New Relativistic Line Emission Code	60
3.1 The kerrdisk Model	60
3.2 Comparison With Other Disk Line Models	66

3.2.1	The Convolution Model <code>kerrconv</code>	71
4	MCG–6-30-15: The Broadest Iron Line Found to Date	74
4.1	A Brief History of Broad Iron Line Studies in MCG–6-30-15	75
4.2	Determining the Spin of the Black Hole in MCG–6-30-15	80
4.2.1	Simple Power-Law Continuum and Iron Lines	82
4.2.2	Modeling the Warm Absorber	86
4.2.3	Model Including a Full Reflection Spectrum	93
4.2.4	Ruling out a Schwarzschild Black Hole	100
4.3	Discussion	103
4.3.1	Summary of Results	103
4.3.2	Conclusions	104
5	Spectral Fits to Other Broad Iron Line AGN	107
5.1	Data Reduction and Spectral Analysis Methodology	109
5.2	Results for Our Sample of Sy-1 AGN	114
5.2.1	MCG–5-23-16	115
5.2.2	NGC 3783	117
5.2.3	Mrk 766	124
5.2.4	3c273	127
5.2.5	3c120	133
5.2.6	NGC 2992	137
5.2.7	NGC 4051	141
5.2.8	Ark 120	146
5.2.9	Fairall 9	151
5.3	Comparison of Sample Results	156
6	Conclusions	165
6.1	Summary of Results	165
6.2	Discussion	169
6.3	Future Work	171
A	Computing <code>kerrdisk</code> Line Profiles	173
	Bibliography	183

List of Tables

2.1	Best fit parameters for the EPIC-pn spectrum of NGC 4593	37
2.2	The cold and ionized iron lines in the EPIC-pn spectrum of NGC 4593 . .	49
4.1	Best fit parameters for MCG–6-30-15	99
5.1	Best fit parameters for MCG–5-23-16	118
5.2	Best fit parameters for NGC 3783.	123
5.3	Best fit parameters for Mrk 766	128
5.4	Best fit parameters for 3c273	136
5.5	Best fit parameters for 3c120	138
5.6	Best fit parameters for NGC 2992	145
5.7	Best fit parameters for NGC 4051	147
5.8	Best fit parameters for Ark 120	152
5.9	Best fit parameters for Fairall 9	159
5.10	Comparison of <code>laor</code> and <code>kerrdisk</code> model fits for all sources.	162
5.11	Comparison of <code>reflion</code> and <code>kdblur(refl)</code> model fits for all sources. . .	163
5.12	Comparison of <code>kerrconv(refl)</code> model fits for all sources.	164

List of Figures

1.1	Important X-ray missions.	8
1.2	Anatomy of a BH system.	14
1.3	Diagram of coronal geometry.	15
1.4	Reflection spectrum of an accretion disk.	16
1.5	Formation of a broad emission line.	17
1.6	Relativistic blurring of emission lines.	18
1.7	AGN system with molecular torus.	18
1.8	Spectral model of a warm absorber.	20
1.9	Broad iron line in MCG–6-30-15.	21
1.10	Absorption near the Fe-K α line in MCG–6-30-15.	22
2.1	Photoabsorbed power-law fit to the 2 – 10 keV spectrum of NGC 4593.	31
2.2	Power-law and two Gaussians fit to the 0.5 – 10.0 keV spectrum of NGC 4593.	32
2.3	Model 1 global fit to NGC 4593.	35
2.4	Model 2 global fit to NGC 4593.	36
2.5	Variation from the time-averaged Model 2 spectrum in 10 ks segments.	46
2.6	Variation of the cold and ionized iron lines from the Model 2 spectrum in 10 ks segments.	47
2.7	Flux and equivalent width variation of the cold iron line over the 76 ks observation of NGC 4593.	48
2.8	Flux and equivalent width variation of the ionized iron line over the 76 ks observation of NGC 4593.	48
2.9	Light curve and power spectrum for NGC 4593.	51
2.10	Soft, intermediate and hard band light curves.	51
2.11	The cross-correlation function showing the hard-soft band time lag.	53
2.12	Hardness ratios vs. time and energy for NGC 4593.	54
3.1	Variation of kerrdisk lines profiles with various parameters.	67
3.2	Comparison of several accretion disk emission line models for a Schwarzschild BH.	68
3.3	Comparison of several accretion disk emission line models for a Kerr BH.	69
3.4	Comparison of the kerrdisk model profile to that of kerrconv(gauss).	72

4.1	Photoabsorbed power-law fit to the X-ray spectrum of MCG–6-30-15.	83
4.2	Modeling the emission features in MCG–6-30-15.	84
4.3	Modeling the WA in MCG–6-30-15.	88
4.4	Evidence for a multi-zone structure to the WA in MCG–6-30-15.	90
4.5	Relative contribution of the various components in Model 4.	92
4.6	Model for MCG–6-30-15 including a full ionized disk reflection spectrum.	94
4.7	Relative contributions of the components in Model 5.	96
5.1	Fe-K α line residual in MCG–5-23-16.	117
5.2	Best fit to the spectrum of MCG–5-23-16.	119
5.3	Relative contributions of the model components in MCG–5-23-16.	120
5.4	Fe-K α line residual in NGC 3783.	124
5.5	Best fit to the spectrum of NGC 3783.	125
5.6	Relative contributions of the model components in NGC 3783.	126
5.7	Fe-K α line residual in Mrk 766.	129
5.8	Best fit to the spectrum of Mrk 766.	130
5.9	Relative contributions of the model components in Mrk 766.	131
5.10	Fe-K α line residual in 3c273.	133
5.11	Best fit to the spectrum of 3c273.	134
5.12	Relative contributions of the model components in 3c273.	135
5.13	Fe-K α line residual in 3c120.	139
5.14	Best fit to the spectrum of 3c120.	140
5.15	Relative contributions of the model components in 3c120.	141
5.16	Fe-K α line residual in NGC 2992.	142
5.17	Best fit to the spectrum of NGC 2992.	143
5.18	Relative contributions of the model components in NGC 2992.	144
5.19	Fe-K α line residual in NGC 4051.	146
5.20	Best fit to the spectrum of NGC 4051.	148
5.21	Relative contributions of the model components in NGC 4051.	149
5.22	Fe-K α line residual in Ark 120.	153
5.23	Best fit to the spectrum of Ark 120.	154
5.24	Relative contributions of the model components in Ark 120.	155
5.25	Fe-K α line residual in Fairall 9.	156
5.26	Best fit to the spectrum of Fairall 9.	157
5.27	Relative contributions of the model components in Fairall 9.	158

Chapter 1

Introduction

1.1 Overview

Accreting black holes (BHs) are the driving force behind some of the most powerful processes in the universe. The central regions of active galactic nuclei (AGN) and Galactic black holes (GBHs), in particular, are two BH-driven systems that are prodigious sources of energy and radiation across the electromagnetic spectrum. Yet in spite of their extreme nature and power, much about these objects remains unknown. The mechanism of accretion onto the BH is a complex, magnetohydrodynamic (MHD) process whose detailed workings will remain the subject of ambitious simulations for many years until a computational marriage between General Relativity (GR) and MHD, including plasma effects and radiative transfer, can be mastered. Accretion disks in BH systems can be probed with observations, however, whereas (classically) BHs themselves emit no electromagnetic radiation. Fortunately BHs are mathematically simple objects that can be fully defined by only their mass and spin. Unfortunately, while mass is comparatively easy to calculate provided the BH has another object orbiting it, measuring spin requires detecting strong-field GR effects and is not so straightforward to ascertain.

In the current absence of any gravitational wave signatures detected from BH systems,

which would provide a clean and robust measure of BH spin, we are left to look for indirect electromagnetic evidence of this property in the spacetime immediately surrounding the event horizon. GR predicts that one should observe several characteristic signatures in the radiation from the material close to the event horizon (i.e., the central portions of the accretion disk): frame dragging and gravitational time dilation are prominent examples. Based on this theory, a powerful method for probing the properties of the BH is to observe the degree to which emission lines in the spectrum of the inner accretion disk are altered in their energy profiles by enhanced relativistic effects and extreme Doppler shifts. Proper modeling of these emission features and fitting these models to data provides us with one of the more robust and reliable diagnostic tools for constraining such relativistic effects as BH spin. That is the subject of this thesis.

1.2 The History of Black Hole Studies in X-rays

X-rays provide the cleanest probe of the central engine in AGN: lower-energy radiation is highly reprocessed before reaching the observer. The accretion disk itself typically radiates as a blackbody peaking in the ultraviolet, but inverse Comptonization processes involving the surrounding plasma boost these photons in energy until they become X-ray emission. In smaller GBH systems the disk is hotter to begin with and has a blackbody temperature in the X-ray range, compounding those X-rays produced by the Comptonization processes at work. Unfortunately, our atmosphere is opaque to X-rays, so the scientific study of these regions in BH systems simply was not possible until we were able to put detectors into orbit in the latter half of the twentieth century.

An excellent history of the early years of X-ray astronomy was written by Bradt in 1992 ([Bradt et al. 1992](#)). Though the first detection of cosmic X-rays came in 1949 ([Friedman et al. 1951](#)), when X-ray Geiger counters aboard a sounding rocket were briefly

carried above the atmosphere and detected X-rays coming from the Sun, it was over ten years later before improved technology enabled a detector to discover X-rays coming from sources outside our solar system. This group, led by Riccardo Giacconi at American Science and Engineering in 1962, discovered a bright X-ray source in the constellation of Scorpius, which they consequently named Sco X-1 ([Giacconi et al. 1962](#)). Even though the group had a scant few minutes of observing time, it was immediately apparent that the source was cosmic in origin and had an X-ray luminosity $\sim 10^8$ times stronger than the Sun. This source is now known to be a low-mass X-ray binary neutron star system within our own Milky Way.

Because successive sub-orbital rocket launches provided only brief glimpses of the X-ray universe, a sustained orbital observatory was needed in order to begin to truly study the sources found in detail. To this end, the first X-ray orbiting satellite, *Uhuru*, was launched in 1970. The main instrument was a series of proportional counting arrays sensitive to X-rays in the range of 2 – 20 keV. The final *Uhuru* catalog contained 339 objects, most of which were binary stellar systems, supernova remnants, Seyfert galaxies and galaxy clusters ([Forman et al. 1978](#)). *Uhuru* was followed by the *HEAO* missions beginning in 1977, which marked the start of the era in which big X-ray payloads were being put into orbit to make observations. *HEAO-1* was primarily a scanning mission dedicated to observing the entire X-ray sky and performing the first Large Area Sky Survey (LASS) from 1 – 20 keV. Important discoveries included a catalog of 842 X-ray sources and observations of aperiodic variability in the compact binary Cygnus X-1, which became the first confirmed GBH after optical radial velocity studies of its secondary star proved that the accreting object was too massive to be a neutron star. *HEAO-1* also collected numerous broad-band spectra of AGN of varying types ([Worrall et al. 1981](#)), greatly contributing to our knowledge of such objects. The mission was succeeded by *HEAO-2* in 1978, which was later renamed *Einstein*. This X-ray observatory was the first of its

kind to employ grazing incidence optics, providing a significant advancement in imaging and resolution capabilities. Its instruments combined to observe everything from coronal stellar emission to X-ray jets emitted from massive galaxies to the warm/hot intergalactic medium. But arguably some of the most important results were the spectral surveys of AGN such as quasars and Seyfert galaxies, which showed tantalizing correlations between radio flux and X-ray slope. These findings provided some of the best evidence that results from the two wavebands might reflect two sides of the same beast, and helped support the paradigm of the Unified Model of AGN (Bechtold et al. 1987; Kruper et al. 1990; Miller & Antonucci 1983; Wilkes & Elvis 1987).

After *Einstein* deorbited in 1981, American involvement in X-ray astronomy took an extended break. In the meantime, however, European and Japanese instruments made significant progress in the field. In 1983, *EXOSAT* was successfully launched and began an observing campaign from 1 – 50 keV. Notable among its many discoveries were the first detailed observations of quasi-periodic oscillations (QPOs) in several low-mass X-ray binary systems (Priedhorsky et al. 1986; van der Klis 1989), as well as a spectral survey of 48 Seyfert galaxies revealing the prevalence of a soft X-ray component in these sources (Turner & Pounds 1989). This soft component was thought to represent disk emission, thereby substantiating theories that postulated AGN as BH/disk-related phenomena.

The Japanese observatory *Ginga* launched in 1987. Among its notable accomplishments: detection of the systematic delay in variation of the hard X-ray to soft X-ray spectrum in Cyg X-1 (Miyamoto et al. 1988); detailed studies of iron emission and absorption features common to many Seyfert-1 (Sy-1) spectra (Matsuoka et al. 1990; Pounds et al. 1990, 1989); and highly absorbed Sy-2 spectra in contrast to Sy-1s, which again supported the Unified Model (Awaki et al. 1990). Interestingly, both *EXOSAT* and *Ginga* also discovered iron line emission and Compton reflection humps in BH spectra (Day et al. 1990; Pounds et al. 1990; White et al. 1985).

The next decade brought the advent of the German-led *ROSAT* mission in June of 1990, with which the U.K. and U.S. were also affiliated. Conducting a rigorous all-sky survey (the RASS), *ROSAT* expanded the X-ray source catalog to over 150,000 objects. With over 1000 times the sensitivity of *Uhuru*, this observatory enabled even deeper observations of AGN and other BH systems as well as a multitude of other X-ray sources (Boller et al. 1997; Wagner et al. 1994). *ROSAT* was followed by the joint Japanese-American satellite *ASCA* in 1993. This was the first X-ray telescope to combine imaging capability with a broad pass band, moderately high spectral resolution ($E/\Delta E \approx 100$) and large effective area, as well as the first to employ CCDs as an X-ray detector. *ASCA* revolutionized the study of iron emission lines around BHs, noting both the prevalence of the feature in Sy-1 sources and enabling astronomers to use this feature to attempt to constrain BH angular momentum (Mushotzky et al. 1995; Nandra et al. 1997).

The Rossi X-ray Timing Explorer (*RXTE*), launched in 1995, was designed specifically to monitor X-ray sources such as AGN and GBHCs with high timing resolution, since compact objects tend to display variability on short time scales in accordance with their small light crossing times. With its very large collecting area and dedication to all-sky monitoring, *RXTE* revolutionized the study of X-ray spectral and temporal variability in BH systems, enabling astronomers to probe the nature of the accretion disk with unprecedented detail (Lamer et al. 2001; Lee et al. 2000; Miller et al. 2004; Wilms et al. 1999). This mission is still active, as are two important, newer observatories in the X-ray regime: *XMM-Newton* of ESA and *Chandra* of NASA, both launched in 1999. Although both instruments offer superior resolution and throughput, *Chandra* excels more in the area of precision X-ray imaging, whereas *XMM-Newton* enjoys a larger collecting area and is more ideally suited for spectroscopy. The two observatories act as excellent complements for each other and have enabled astronomers to examine the nature of accretion and radiation within BH systems with unprecedented detail. Just as their predecessors did

before them, *Chandra* and *XMM-Newton* have focused on many different types of X-ray phenomena during their lifetimes: everything from resonating galaxy clusters (Reynolds et al. 2005) to millisecond pulsars (Juett et al. 2003) to the nature of the cosmic X-ray background (Gilli et al. 2007). But some of the most important progress has been made in the study of AGN and GBH systems. With the spectral resolution and throughput of these two telescopes, scientists are coming closer than ever before to being able to describe the complex interaction between a BH and its accretion disk (Fabian et al. 2002; Miller et al. 2006a; Wilms et al. 2001). Efforts to measure BH spin via detailed characterization of the emission features from the disk are finally able to produce reliable constraints due to the precision of the data (Brenneman & Reynolds 2006). These studies are a central component of this thesis.

The next generation of X-ray telescopes promises to improve upon this legacy. Even as *RXTE*, *Chandra* and *XMM-Newton* remain operable and active, new instruments such as *Swift* (2004), *Suzaku* (2005) and the upcoming *GLAST* mission (2008) are already making giant steps forward and adding more pieces to the puzzle of high energy phenomena in the universe. While *Swift* is ostensibly a Gamma-ray burst mission, its X-ray telescope (covering 0.2 – 10 keV) is ideally suited for examining the continua and iron line regions of AGN and GBHs. *Suzaku* is already contributing greatly to iron line studies itself: with its spectral coverage of 0.3 – 600 keV and enhanced spectral resolution, it is already making important distinctions between different models of emission and absorption from the inner accretion disk (Miniutti et al. 2007; Reeves et al. 2007). These distinctions enable astronomers to place vital constraints on the reflected emission from the accretion disk as well as any intrinsic absorption within the system, thereby allowing BH spin to be more robustly constrained.

The planned observatory *Constellation-X*, if it comes to fruition, will be another invaluable tool for probing BH spin and the BH-disk interaction. The microcalorimeters

generating the spectra for this mission will provide an order of magnitude enhancement in resolution and will greatly lower the necessary integration time for any given object, enabling deeper and more precise measurements to be made from spectral studies than are possible with the instruments currently in orbit. And *GLAST*, the Gamma-ray Large Area Space Telescope planned for launch later this year, will allow for an in-depth study of jets and other relativistic outflows powered by BH systems, providing a unique view of the transfer of angular momentum within these systems as well as the disk-jet interaction and jet triggering mechanisms. Graphs charting the advent of X-ray missions with time and with energy are shown in Fig. 1.1.

The aforementioned missions are giving us images and spectra of the X-ray universe in unprecedented detail. Given enough photons and enough spectral resolution, we have the necessary information to robustly constrain relativistic effects such as BH spin for the first time, and to quantitatively probe the strong-gravity regime to test the accuracy of GR's predictions. But in order to separate out the evidence of spin from other manifestations of the accretion disk or BH-disk interaction, we need to have an accurate model for disk emission that correctly describes the intricate physics of the BH-disk system. In creating such a model, it is imperative to begin with a physically consistent picture of the accretion disk itself as well as the spacetime in which it resides.

1.3 Anatomy of a Black Hole-Accretion Disk System

The general picture of an accreting BH system, whether a GBH, AGN, or even an intermediate mass black hole (IMBH; thought to be on the order of $10^2 - 10^4 M_{\odot}$ (Miller & Colbert 2004)), consists of a BH and surrounding accretion disk that can extend out to tens of thousands of gravitational radii ($r_g = GM/c^2$ where M is the mass of the BH). The disk forms by virtue of conservation of angular momentum in the material gravita-

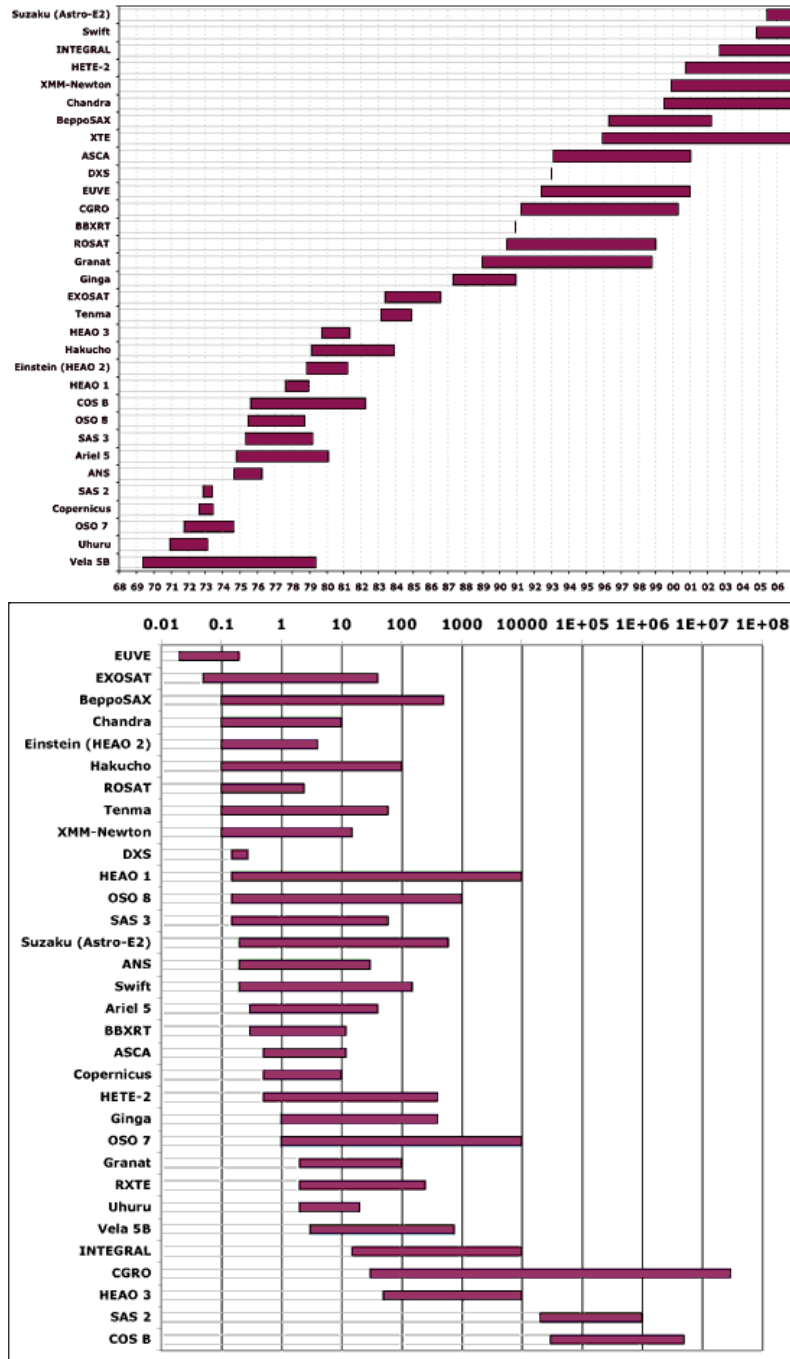


Figure 1.1: X-ray missions plotted versus time (top) and energy range in keV (bottom). Credits: <http://heasarc.gsfc.nasa.gov/docs/heasarc/missions/time.html>, <http://heasarc.gsfc.nasa.gov/docs/heasarc/missions/energy.html>

tionally captured by the hole. In the case of a non-spinning BH pulling in material with no preferred direction of net angular momentum, the material will be accreted via the Bondi-Hoyle mechanism, i.e., in spherically symmetric fashion (Bondi & Hoyle 1944). It is thought, however, that BHs totally lacking in angular momentum are quite rare if they do indeed exist at all: statistically, there will almost always be enough angular momentum in the accreted material to form a significant accretion disk, enabling the BH to accrete material and its angular momentum, thus leaving the BH with a non-zero net spin.

1.3.1 Accretion Disk Properties

The classic picture of the accretion disk involves gaseous matter gaining in speed as it falls toward the event horizon, and also being acted upon by the intense gravitational field of the BH (Page & Thorne 1974; Shakura & Sunyaev 1973). The infalling material forms an optically thick, geometrically thin disk around the BH, not unlike water spiraling down a drain. Matter cannot be transported inwards unless it loses angular momentum, however. This can be readily shown using the simplifying assumptions of Newtonian gravity and Keplerian orbits within the disk: the velocity of a particle within the disk at radius r is $v_K = (GM/r)^{1/2}$, where M is the mass of the accretion disk. The specific angular momentum of the particle at this radius is then $l_K = (GMr)^{1/2}$, so in order for the particle to be accreted (i.e., gain speed in its infall toward the BH) it *must* lose angular momentum.

The exact mechanism by which mass is transported involves weak magnetic fields threading the accretion disk (Balbus & Hawley 1991). In this scenario, a differentially rotating disk possessing a weak magnetic field undergoes a local instability, which then gets twisted within the disk as the magnetic field lines get progressively twisted and torqued by the disk rotation. The instability propagates throughout the disk, growing according to its rotational velocity. Motion of the disk material associated with the instability pro-

duces both poloidal and toroidal magnetic field components and propagates the instability, which has the effect of transporting angular momentum outwards in the disk as it transports mass inwards. By virtue of this magneto-rotational instability (MRI), turbulence within the disk is created, which then drives the angular momentum transport within the disk, enabling matter to spiral inwards towards the BH until it reaches the innermost stable circular orbit (ISCO) in the disk. This radius, also known as the radius of marginal stability (or r_{ms}), defines the last point at which a particle can orbit the BH before it enters the plunging region and falls precipitously inward past the event horizon. The ISCO is a direct function of the BH spin:

$$Z_1 \equiv 1 + (1 - a^2)^{1/3} [(1 + a)^{1/3} + (1 - a)^{1/3}] \quad (1.1)$$

$$Z_2 \equiv (3a^2 + Z_1^2)^{1/2} \quad (1.2)$$

$$r_{\text{ms}} = 3 + Z_2 - \text{sgn}(a)[(3 - Z_1)(3 + Z_1 + 2Z_2)]^{1/2} \quad (1.3)$$

The variable a is the dimensionless spin parameter of the BH and is a unitless quantity defined as $a = cJ/GM^2$, where M is the mass of the BH and J is its angular momentum. The radius r_{ms} is given in units of r_g . As the spin of the hole increases, the radial coordinate for the ISCO is pulled in closer to the event horizon, and this coordinate in turn is also pulled closer in towards the singularity:

$$r_{\text{eh}} = 1 + (1 - a^2)^{1/2} \quad (1.4)$$

For a non-spinning BH $r_{\text{ms}} = 6r_g$ (event horizon at $r_{\text{eh}} = 2r_g$), whereas for a BH spinning in the prograde direction as fast as possible $r_{\text{ms}} = 1r_g$ (event horizon at $r_{\text{eh}} = 1r_g$). The disk itself generates an ultraviolet blackbody component of radiation for AGN and an X-ray blackbody for GBHs, based on the relative size difference between these

two classes of objects:

$$T_{disk} \propto M_{BH}^{-1/4} (L/L_{Edd})^{1/4} \quad (1.5)$$

So assuming the disk of an AGN and GBH each accrete and radiate at the same fraction of the Eddington luminosity, the disk temperature will be greater for the GBH because of its smaller mass and associated smaller radiating area. The Eddington luminosity is achieved by setting the inward force of gravity equal to the outward force of radiation for a given body:

$$L_{Edd} = 4\pi GMm_p c / \sigma_T \approx 1.3 \times 10^{38} (M/M_\odot) \text{ erg s}^{-1} \quad (1.6)$$

where M is the mass of the body in question, m_p is the mass of a hydrogen atom (or proton), and σ_T is the Thomson scattering cross-section. The Eddington luminosity is believed to set an upper limit to the luminosity of a steadily accreting source such as a BH.

In certain cases when the BH is not actively accreting material at such a prodigious rate (i.e., well below the Eddington rate), it is thought that the optically thick accretion disk may not extend all the way in to the ISCO. Rather, it would truncate at some radius outside r_{ms} and the flow of material from this point to the event horizon would become optically thin and geometrically thick, in contrast to the rest of the disk (Narayan & Yi 1994). In this advection dominated accretion flow (ADAF) scenario, most of the energy stored in the accreted material is kept as entropy rather than being radiated. As a result, ADAF models of accretion disks predict very low luminosities for their central engines and are thought to be a leading candidate to explain the phenomenon of low-luminosity AGN (LLAGN), in particular. Due to this net storing of energy and the “puffing up” of the accretion disk to accommodate the quasi-spherical flow that develops, net outflows in the form of a wind from the disk are possible (Blandford & Begelman 1999). As a

consequence, only a small fraction of the material may actually fall into the BH, and the binding energy it releases could blow off the remainder via a torque-induced wind.

1.3.2 The Corona and Relativistic Jet Outflows

In addition to the accretion disk, BH systems often have a plasma layer associated with them, known as the “corona.” It is unclear at present what geometrical form this sea of charged particles might take, though possible options are a sandwich-type layer above and below the disk, a “pill-box” or clumpy distribution, or perhaps a more-or-less spherical appearance (Paczynski 1978). The presence of the plasma itself in this picture likely originates in magnetized outflows from the surface layer of an ionized disk as discussed in the preceding paragraph. Alternatively, because BH systems are often associated with bipolar outflows in the form of collimated jets (Blandford & Payne 1982; Blandford & Znajek 1977), the plasma we think of as coronal material may indeed be charged particles in the base of such a jet (Merloni & Fabian 2002; Miller et al. 2006b). Fig. 1.2 provides an illustration of jets in relation to the disk and BH, and Fig. 1.3 diagrams four different possible geometries for the corona that are often considered (Reynolds & Nowak 2003).

Whatever the origin of the plasma in question, the observed X-ray continuum (which is accurately approximated by a power-law from ~ 2 keV up to ~ 100 keV in AGN and GBHs) is thought to be produced by inverse Comptonization processes in the corona (or base of a jet) surrounding the inner part of the accretion disk. As photons emitted from the disk interact with energetic electrons in the surrounding plasma (moving at high speeds due to the high temperature of the plasma), the photons receive a boost in energy from each encounter. A given photon may undergo many such collisions depending on the geometry and covering fraction of the plasma around the disk. If the electrons move relativistically, each collision increases the energy of the photon by a factor of γ^2 , where $\gamma = (1 - v_e^2/c^2)^{-1/2}$, and v_e is the velocity of the electrons or other charged particles in

the plasma. If the electrons are thermal in nature (with $kT \sim 100$ keV), and therefore sub-relativistic, each collision will change the fractional energy of the photon by a factor of $4kT/m_e c^2$, where kT is the energy of an average electron and m_e is its mass (Rybicki & Lightman 1979). Taking into account a thermal distribution of seed photons and a relatively uniform distribution of electrons, the inverse Comptonization produces the characteristic power-law form of the continuum seen in the X-ray spectrum of AGN and GBHs. A portion of the X-ray photons produced in the corona are scattered outwards and seen as continuum to the observer, while another fraction of the photons are backscattered down onto the disk, irradiating it and producing the so-called “X-ray reflection” signatures in the observed spectrum (Guilbert & Rees 1988; Lightman & White 1988). These X-ray reflection signatures consist of fluorescent and recombination emission lines sitting on the continuum and the summed radiative recombination continua of the excited ions in the photoionized disk surface (George & Fabian 1991; Ross & Fabian 2005). See Fig. 1.4 for an example of spectra from a disk with varying levels of ionization.

1.3.3 The Disk Reflection Spectrum

The Fe-K α line is the most prominent of these features due to its energy (at 6.4 keV it is visible above the direct power-law continuum), and the high astrophysical abundance and fluorescent yield of iron. As high-energy reflected photons are absorbed by iron in the accretion disk, they can kick electrons out of the K-shell of the atom, provided that the iron is not so highly ionized that there are no K-shell electrons present. When the K-shell electron is taken away, an L-shell electron preferentially drops down an energy level to take its place (also assuming an L-shell electron is present), liberating a photon of characteristic rest energy 6.4 keV (although if the iron in question is highly ionized this energy can be as high as 6.97 keV for Fe-K α). This line is often significantly broadened and skewed by both the standard Doppler effect, special relativistic time dilation and gen-

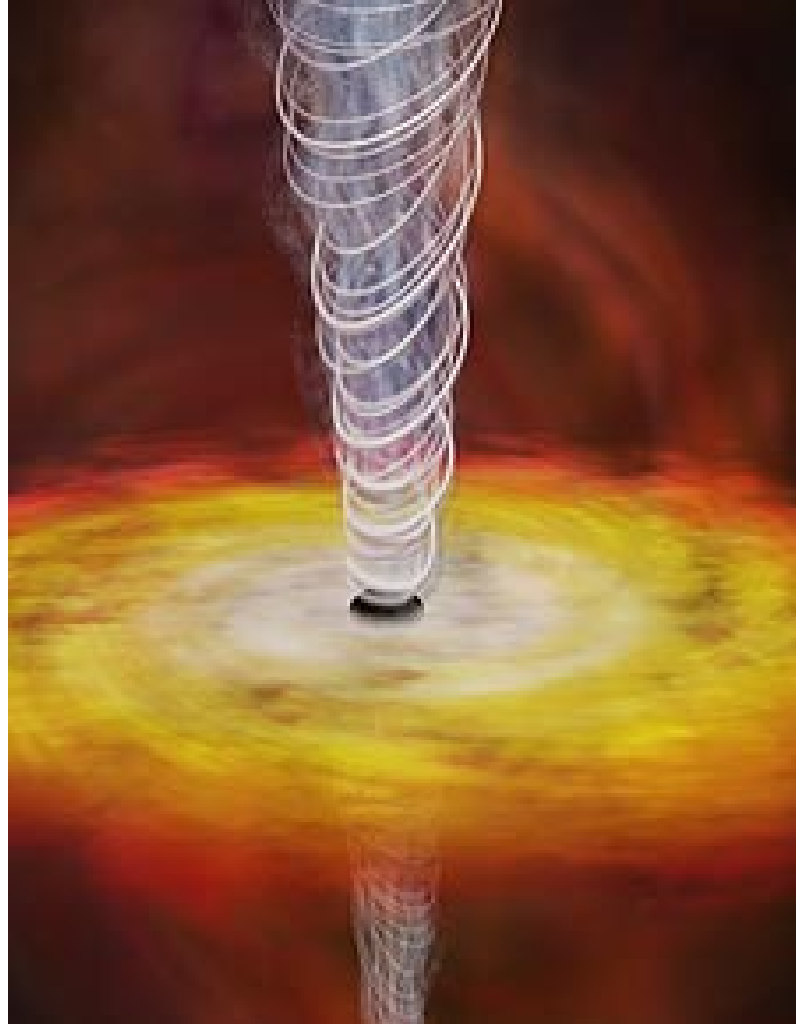


Figure 1.2: A BH is shown surrounded by an accretion disk, with bipolar magnetized jets visible. The so-called “corona” surrounding many BH systems may actually be plasma in the base of such a jet, or the jet itself may grow out of coronal plasma collected in some geometry around the inner disk. Credit: <http://www.nasa.gov>.

eral relativistic processes in the disk, the effects of which increase the closer the line is emitted to the event horizon (Fabian et al. 1989; Laor 1991). These general relativistic processes include light bending, beaming and gravitational redshifting, all of which result in a greatly elongated and skewed line profile; in particular, the line profile can display an extended low-energy tail primarily resulting from gravitational redshift. Because accretion disks generally radiate more copiously the closer one gets to the event horizon, the principal line emission region is sufficiently close to the BH that frame-dragging ef-

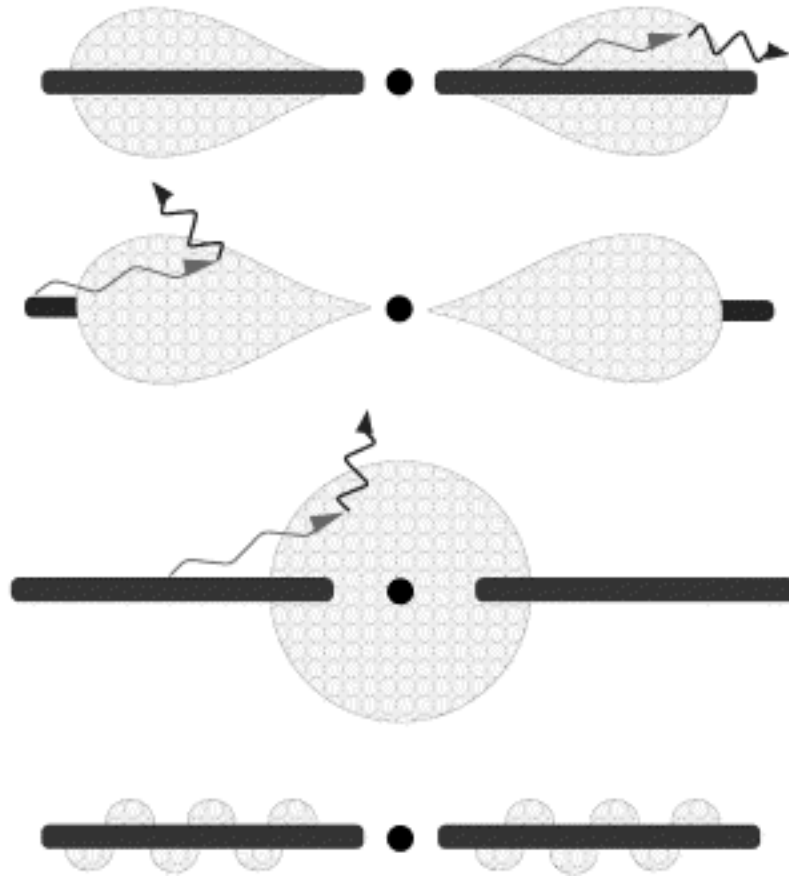


Figure 1.3: Possible geometries for a simple AGN corona are presented. From top to bottom, the corona is seen sandwiching the inner disk, truncating the inner disk isotropically, and existing in a patchy form around the disk as a “pill-box.” The top configuration is often called a slab geometry, but tends to predict spectra that are softer than observed. The bottom three schematics represent “photon-starved” geometries wherein the corona is less effectively cooled by inverse Compton scattering of disk photons. Credit: Michael Nowak (2003).

fects associated with the BH spin can be important in determining the line profiles. As stated above, increasing spin results in the inner edge of the disk being pulled in closer to the event horizon such that its radiation is subject to greater relativistic effects and more powerful Doppler shifts as it escapes this region. The broad iron line is therefore a powerful probe of the relativistic effects on the spacetime immediately surrounding the BH. As such, we are motivated to construct a new model to fit the Fe- $K\alpha$ line profiles seen in BH systems; one which can extract best-fit values for parameters such as the BH spin, disk inclination angle and inner radius of emission from the disk. An illustration

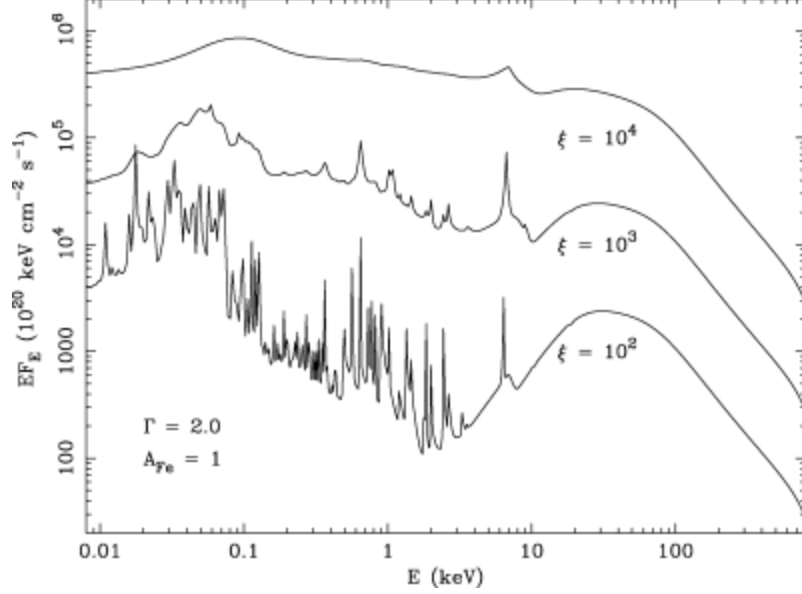


Figure 1.4: The spectrum resulting from irradiation of an ionized slab (e.g., an accretion disk) with an incident power-law X-ray spectrum of spectral index $\Gamma = 2$. The disk has an iron abundance frozen at the solar value. As one increases the ionization of the disk, note the decrease in observable emission features. Credit: Ross & Fabian (2005).

of how various effects combine to alter spectral line morphology is seen in Fig. 1.5, and the effect of this type of smearing on an entire reflection spectrum from the disk is shown in Fig. 1.6. The building of this iron line model is an important part of this thesis and is presented in detail in Chapter 3.

1.3.4 The Complication of Absorption

Unfortunately, our view of the inner disk spectrum is often complicated by intervening absorption lines and edges. These features can come from several sources: partly ionized “warm” absorption (Halpern 1984) within the BH system (most frequently seen in AGN, though not totally ruled out in GBHs), a cooler dusty torus thought to surround many BHs at large radii ($\sim 10^4 - 10^5 r_g$; also more often seen in AGN), and cold absorption from neutral hydrogen in our own Galaxy. See Fig. 1.7 for schematic and artistic representations of the anatomy of an AGN system, including the putative locations of these absorbers. The lines and edges produced by photons traveling through these types

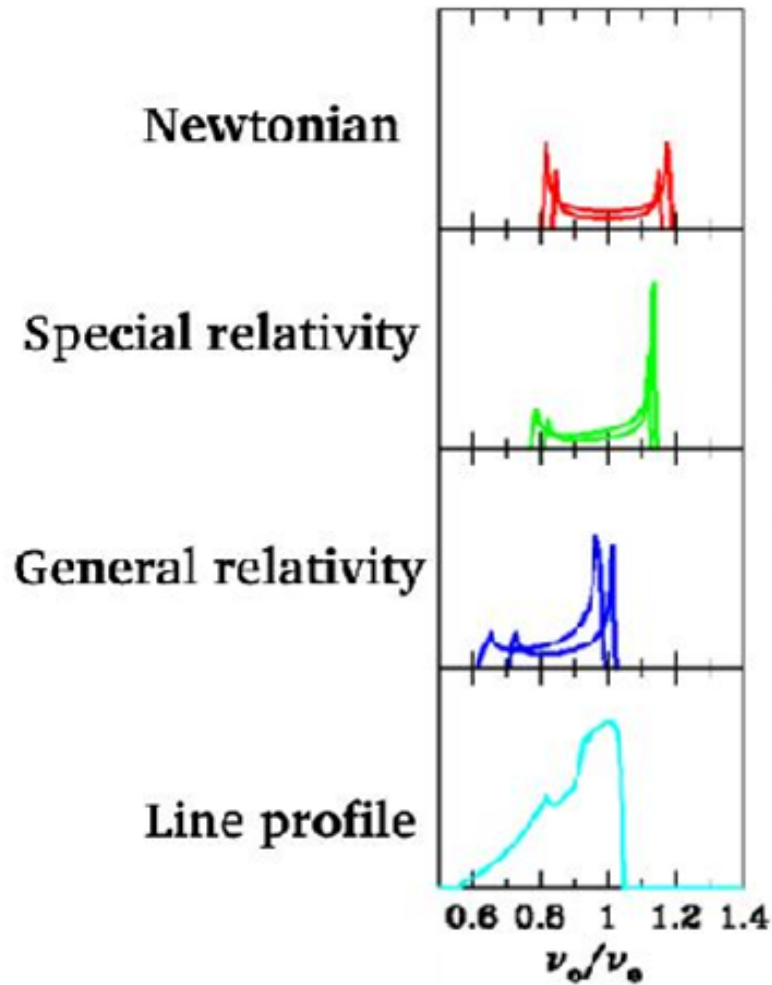


Figure 1.5: Schematic representation of the effects of Doppler shifting, special and general relativity on the morphology of a spectral line emitted from an accretion disk around a BH. Credit: A. Young (2001).

of intervening gases are superposed onto the intrinsic X-ray spectrum from the accretion disk and corona and can often overlap with important diagnostic emission features such as the Fe-K α line or soft excess emission from the seed disk photons. Absorption, if not taken properly into account and modeled accordingly, can greatly complicate our ability to constrain BH-disk properties such as BH spin (Reynolds 1997; Reynolds & Nowak 2003).

The absorption in question comes most often from neutral hydrogen atoms in the

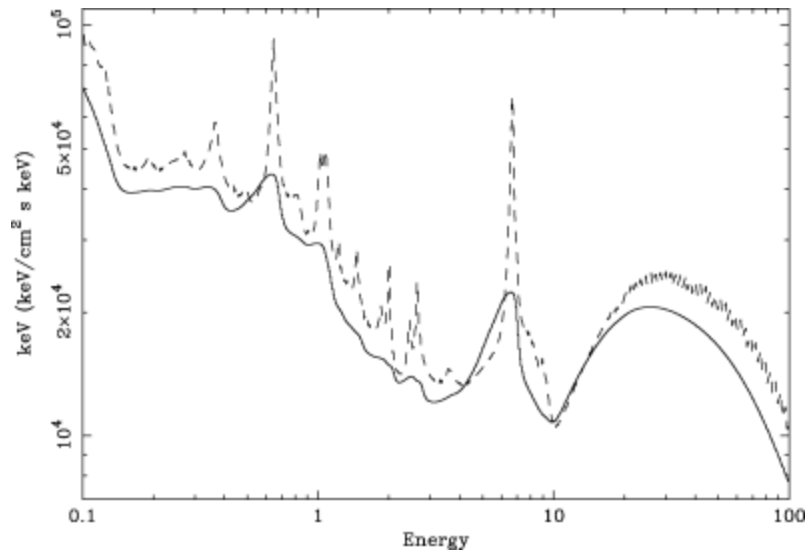


Figure 1.6: The ionized disk spectral model of Ross & Fabian (2005; dotted line) convolved with a relativistic smearing kernel assuming a near-maximally-spinning Kerr BH (solid line). Note the dulled, broadened appearance of the emission features when relativistic blurring is acting on the system.

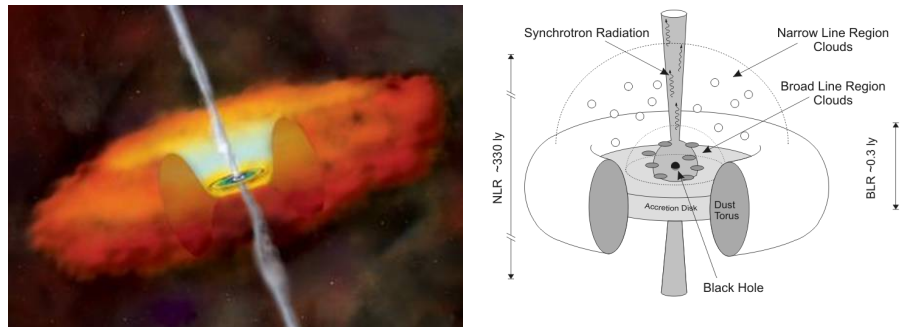


Figure 1.7: A canonical AGN is thought to be surrounded by a cold, dusty torus of neutral molecules and atoms at a distance on the order of $\sim 10^4 r_g$. In the unified model, depending on the observer's viewing angle, this torus may obscure the central parts of the accretion disk and prevent broad lines from being seen in the X-ray spectrum of the source. Absorption from ionized gas may also take place in the central region from an ionized outflow or perhaps clouds of material in the broad line region. Image credits: <http://chandra.harvard.edu>, Cork Institute of Technology Astronomy and Instrumentation Group.

Milky Way and/or neutral atoms and molecules in the torus surrounding an AGN that fall along our line of sight. However, very often the AGN will also exhibit absorption features from warm, partly ionized material thought to reside in clouds or patches surrounding the accretion disk; it has been proposed that these clouds become ionized by radiation emitted from the AGN (Halpern 1984). More recent X-ray observations have indicated that perhaps these warm absorbers are actually a multi-temperature wind created by photoionized evaporation of material from the inner edge of the torus (Krolik & Kriss 2001), or by accretion disk outflows and/or winds (Blustin et al. 2005).

Warm absorbers (WAs) are often characterized by prominent edges of OVII and OVIII, as well as by lines and edges from many other elements including neon, argon, calcium, silicon, sulfur and nitrogen. The material in question has been found on many occasions to possess a multi-layer structure with physically and kinematically distinct zones of differing temperature, column density and ionization level (Otani et al. 1996). This type of structure is evident in many Sy-1 AGN (George et al. 1998b; Reynolds 1997; Reynolds & Fabian 1995), e.g., MCG-6-30-15 (Brenneman & Reynolds 2006; Lee et al. 2001; Turner et al. 2004) and NGC 3783 (Kaspi et al. 2001), and likely correlates with the distance of the absorbing material from the central engine, which is the source of the ionizing radiation. An example of a WA spectrum can be seen in Fig. 1.8.

Because these absorption features can exist simultaneously with emission features in the AGN system, and because we see the spectrum filtered through several layers of source and local absorption, it is imperative to model these features correctly in order to separate out the true reflection spectrum of the accretion disk and isolate the Fe-K α line for study. Absorption lines and edges from the WA can alter the shape of the overall spectrum to such a degree that they can mimic the redshifted wing of a very broad Fe-K α line in some cases, rendering proper modeling of this line nearly impossible unless absorption has been adequately taken into account. In the case of the canonical broad iron

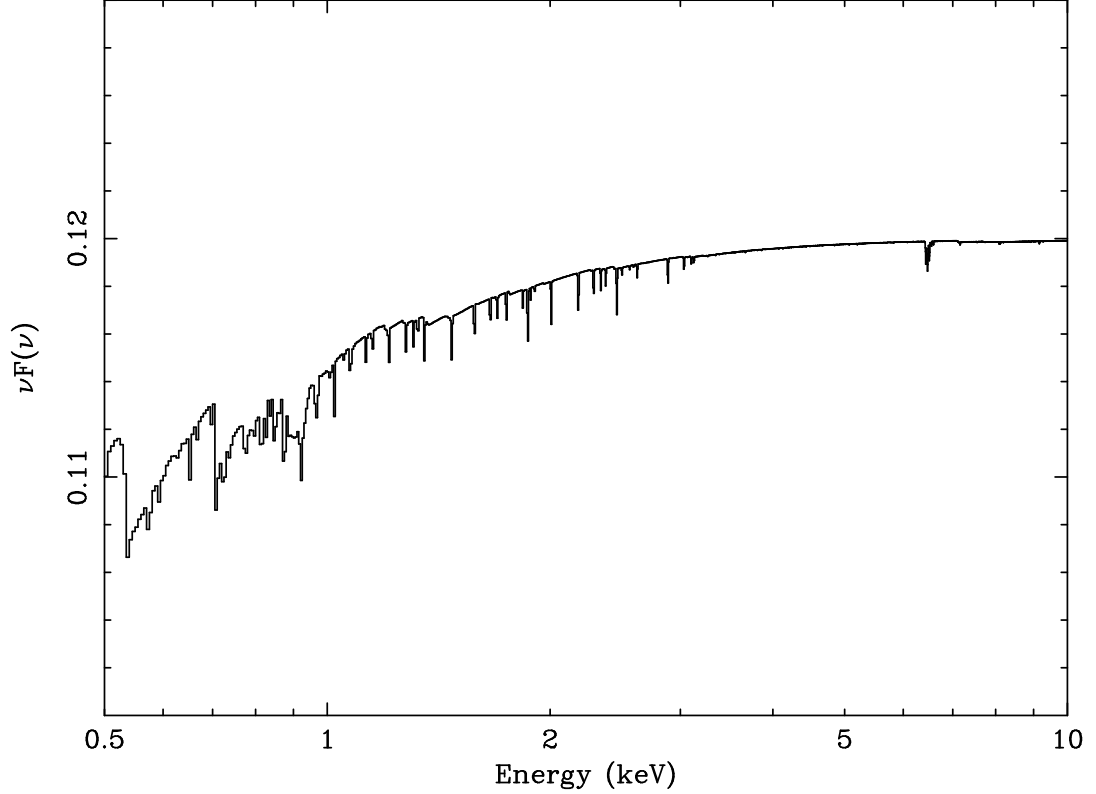


Figure 1.8: A template spectral model of a typical WA showing various lines and edges. Galactic photoabsorption and absorption from neutral iron in the Fe-L₃ edge are also included, as is a power-law continuum from 0.5 – 10 keV. In this case, the Galactic $N_{\text{H}} = 10^{20} \text{ cm}^{-2}$, $N_{\text{WA}} = 10^{22} \text{ cm}^{-2}$, $\xi_{\text{WA}} = 100 \text{ erg cm}^{-1} \text{ s}^{-1}$, $N_{\text{Fe}} = 10^{16} \text{ cm}^{-2}$, $\Gamma = 2$, and the power-law flux is $10^{-2} \text{ ph cm}^{-2} \text{ s}^{-1}$. Solar abundances are used for all elements in the WA. WA model created by Brenneman & Reynolds (2006).

line Sy-1 galaxy MCG–6-30-15, for example, an iron feature is seen that extends down to $\sim 3 \text{ keV}$ on the red wing, making it the broadest iron line observed to date. Because of the extreme breadth of this line, however, some within the astrophysical community doubted that it could be a disk reflection feature, insisting that it could just as easily be a faux emission line created by the juxtaposition of two adjacent absorption edges of iron (Fe-K and Fe-L). This absorption hypothesis was finally laid to rest after a $\sim 522 \text{ ks}$ *Chandra*/HETGS observation of the source (Young et al. 2005). In order for Fe-L absorption edges to have the optical depth necessary to mimic a broad red wing of Fe-K α , the overall amount of iron in the source would dictate the presence of a deep absorption

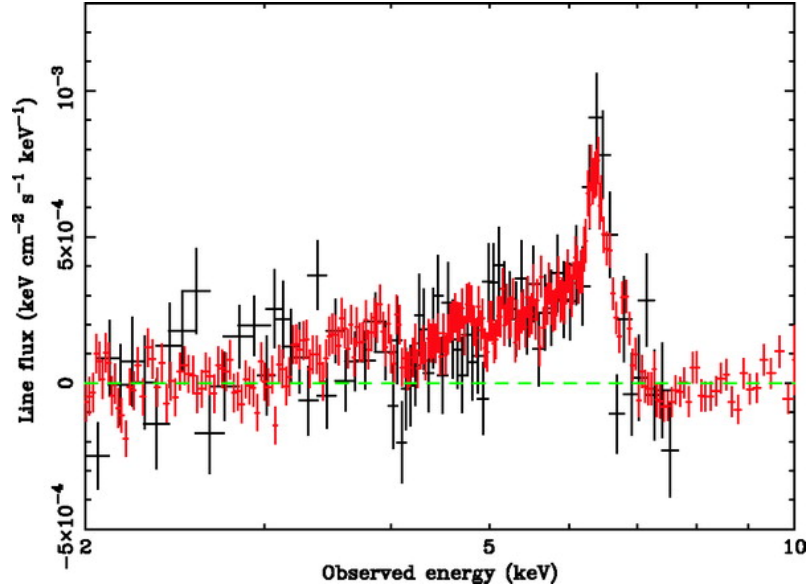


Figure 1.9: The continuum-subtracted spectrum from the *Chandra*/HETGS observation of Sy-1 galaxy MCG–6-30-15 (Young et al. 2005) in black, *XMM-Newton*/EPIC-pn data of the same object (Fabian et al. 2002) in red. Note the extent of the broad Fe-K α line.

line of iron at a rest energy between 6.4 – 6.6 keV. This line was not seen in the *Chandra* data at a confidence level substantially above 99%, implying that the broad iron line seen is in fact an emission feature from the accretion disk. This case is an excellent example of the importance of modeling the WA properly in order to rule out the effects of absorption on observed emission line profiles. The broad iron line and absorption model used in fitting the X-ray spectrum of MCG–6-30-15 are shown in Figs. 1.9-1.10.

1.4 The History of Modeling Broad Iron Lines

Clearly, iron line fitting is a complicated process requiring due diligence in modeling the rest of the X-ray spectrum in order to obtain reliable results and accurately measure the accretion disk properties that affect line morphology. Better spectrographs and more precise relativistic line modeling techniques are now allowing us to begin to place statistical constraints on disk parameters such as BH spin for the first time, but the history of broad iron line studies upon which our modern science was built dates back nearly two

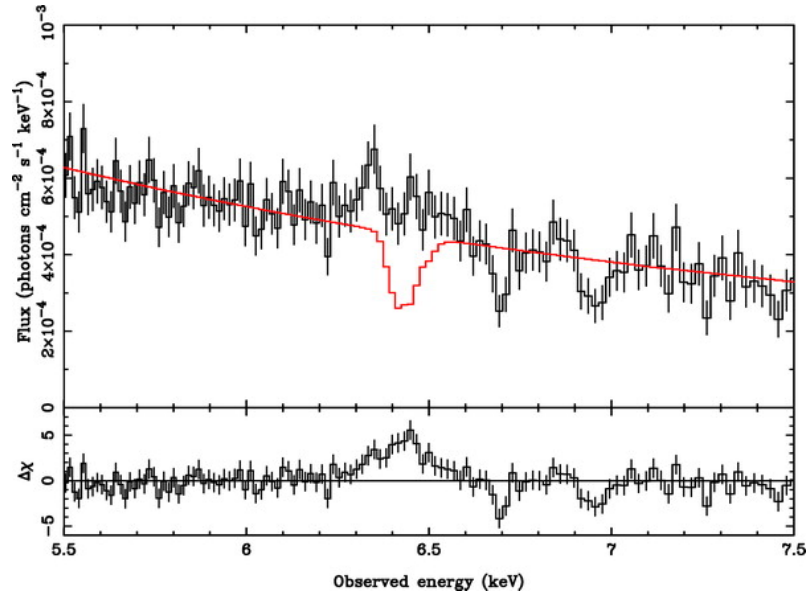


Figure 1.10: The *Chandra*/HETGS data (Young et al. 2005) fit with a broad-iron-line-mimicking ionized WA model. Note that lack of an absorption line between 6.4 – 6.6 keV, as would be expected if the apparent breadth of the Fe-K α emission line is an artifact of nearby iron absorption edges.

decades. The first broad iron line robustly detected and resolved in an AGN was found by *ASCA* in MCG-6-30-15 (Iwasawa et al. 1996; Tanaka et al. 1995), and since then has been extensively studied with *BeppoSAX* (Guainazzi et al. 1999), *RXTE* (Lee et al. 1999, 2000), *Chandra* (Lee et al. 2002; Young et al. 2005) and *XMM-Newton* (Fabian et al. 2002; Wilms et al. 2001). All of these results show that the broad iron line feature is consistent with a highly redshifted line from the inner parts of an accretion disk, and as mentioned previously, no alternative hypothesis has yet explained the spectrum of MCG-6-30-15 satisfactorily (Fabian et al. 1995; Reynolds & Wilms 2000; Vaughan & Fabian 2004; Young et al. 2005). Subsequent *ASCA*, *Chandra* and *XMM-Newton* studies have discovered broad iron line profiles in several other Seyferts, such as MCG-5-23-16 (Dewan et al. 2003), NGC 3516 (Turner et al. 2002), Mrk 335 (Gondoin et al. 2002), and Mrk 766 (Pounds et al. 2003b). The advent of *Suzaku*, in particular, promises to expand this source list even further.

In addition to having a sample of objects that have been observed with robust broad

iron lines, it is equally important to have a precise model to use in fitting the data if one wants to measure BH spin. The two line profiles currently included as standard in the X-ray spectral fitting package XSPEC (Arnaud 1996) are useful as a starting point, but ultimately quite limited in terms of their ability to accurately parameterize the line. The `diskline` model (Fabian et al. 1989) describes the line profile from a disk around a non-rotating Schwarzschild BH, and, due to the approximations employed, does not include relativistic light bending. Similarly, the `laor` model (Laor 1991) has important limitations as well: this is a fully-relativistic model, but the dimensionless spin parameter (a) of the BH is hard-wired at $a = 0.998$, the equilibrium spin of a BH accreting from a standard accretion disk (Thorne 1974). Furthermore, due to the computational realities of the early 1990s, the relativistic transfer functions underlying the `laor` model are pre-calculated and tabulated rather sparsely, yielding noise (or even gross inaccuracies) in the line profiles produced, especially at very high disk inclination angles. Given these limitations, as well as the high quality of AGN spectra currently being obtained with *Chandra*, *XMM-Newton* and *Suzaku*, it is imperative that X-ray astronomers have access to effective models that are fully relativistic, accurate, and that allow BH spin to be fit as a free parameter.

Three new relativistic line models have recently been developed for this purpose and implemented in a form that can be readily used by X-ray astronomers: the `ky` suite (Dovčiak et al. 2004) and two similar codes (Beckwith & Done 2004; Čadež & Calvani 2005). These models achieve comparable results for the morphologies of the line profiles, and all offer significant improvements over the `diskline` and `laor` results in terms of accuracy and precision over a wider range of physical parameters. Most importantly, these models leave the spin of the BH as a free parameter and compute fully relativistic photon transfer functions. These models, as well as my own, will be discussed more fully in Chapter 3.

1.5 Purpose and Structure of this Work

Given the X-ray observatories currently in orbit and the vast improvement in computing resources over the past decade, the time is ripe for exploring the details of BH-disk spectra in greater detail than has previously been able to be attempted. In this dissertation, under the guidance of my advisor, Chris Reynolds, I consider the question of BH spin in AGN. As stated above, we have created a new relativistic emission line model taking into account all major factors influencing the shapes of lines fluoresced by reflected X-rays incident on the accretion disk. We have fit this model to several AGN from the *XMM-Newton* archive that have been seen to harbor broad iron lines (Miller 2007; Nandra et al. 2006). We have extracted best-fit parameters for the properties of the accretion disk in all these sources, including the spin parameter of the BHs in question. In so doing, we have begun the first true survey of BH spin in AGN.

Herein, we assess the constraints on the iron line profiles and BH spins of each source in question, taking into account the complications introduced by other spectral components displayed by these systems, especially the substantial columns of absorbing photoionized gas seen along the line of sight to the central disks in many of the sources in my sample. We begin in Chapter 2 by describing the “control” case of the Sy-1 galaxy NGC 4593, which does not possess a broad iron line, in order to detail the algorithms used to fit the continuum and absorption parameters in an AGN and to explore the interesting spectral and temporal variability often found in Sy-1 AGN. In Chapter 3 we present the new variable-spin accretion disk emission line profile model, *kerrdisk*, that we have developed for public use in the *XSPEC* package. Chapter 4 describes the fit of the new model to the much-studied broad iron line in MCG–6-30-15, which has the largest number of counts of any of the observations presented here, enabling the most accurate physical constraints to be placed on the spin parameter in this source. Chapter 5 expands

the source list to several other broad iron line AGN and presents the results of spectral fitting and the BH spin constraints for each. Conclusions are presented in Chapter 6.

Chapter 2

Modeling the X-ray Continuum in AGN: NGC 4593

As stated in Chapter 1, we present an X-ray spectral analysis of the central regions of the canonical Seyfert-1 galaxy NGC 4593 as a “control” case to illustrate the complexities involved in modeling such systems. Sy-1 galaxies are of particular interest for the study of accretion onto supermassive BHs since they are typically oriented such that we can view the accreting BH free of substantial obscuration or absorption from surrounding circumnuclear material. Furthermore, we believe that significant amounts of the continuum radiation seen in radio-quiet Sy-1 galaxies originate in the disk rather than, for example, a relativistically beamed jet (as is the case for BL-Lac objects). As such, we are better positioned to study the inner parts of the accretion disk in Sy-1 galaxies than in other systems. The following is an expansion of our published work on NGC 4593 in Brenneman et al. (2007; in press).

NGC 4593 is a spiral galaxy with a central bar classified as Hubble type SBb. At a redshift of $z = 0.009$, it lies at a proper distance of ~ 38 Mpc toward the constellation Virgo. This is consistent with the same angular size distance and a luminosity distance of

using $H_0 = 71 \text{ km s}^{-1} \text{ Mpc}^{-1}$, $\Omega_m = 0.27$, and $\Omega_\Lambda = 0.73$.¹ The galaxy has an apparent visual magnitude of 11.67 and an approximate angular diameter of 3.9×2.9 arcmin. As already noted, it hosts an AGN of a Sy-1 type (Lewis et al. 1978). Previous studies of the source with *EXOSAT* demonstrated a soft excess (Pounds & Turner 1988), and *BeppoSAX* data confirm a broad absorption dip of 15% below 1 keV which may be attributable to the presence of a warm absorber along the line of sight (Kaastra & Steenbrugge 2001). *ASCA* spectra display a slightly broadened cold iron line at 6.4 keV, in addition to evidence for a warm absorber within the system (Nandra et al. 1997; Reynolds 1997). The source also displays significant variability in flux. Between two *ASCA* observations 3.5 years apart, the 2 – 10 keV flux of this source increased by $\sim 25\%$, though no significant variability of the iron line was detected between the two pointings (Weaver et al. 2001). Within the *ASCA* observation, a count rate decrease of $\sim 60\%$ in 10 ks was witnessed, with smaller flares and dips throughout the data set (Reynolds 1997). In terms of the overall properties of the system, this author calculated a luminosity of $L_X = 8.53 \times 10^{42} \text{ erg s}^{-1}$ (2 – 10 keV) with *ASCA*, and more recently, McKernan et al. (McKernan et al. 2003) used *Chandra* to derive a luminosity $L_X = 5.37 \times 10^{42} \text{ erg s}^{-1}$ (2 – 10 keV). It should be noted that this change in L_X is larger than the flux calibration uncertainty of the observation, so this does appear to be a robust finding.

We examine results from a 76 ks exposure of NGC 4593 with the *XMM-Newton*/EPIC-pn instrument from 2002 June 23/24. The spectral and temporal variability of NGC 4593 are discussed, as well as the soft X-ray features and their comparison with the “typical” parameters defining a warm absorber. We also weigh the consistency of our findings with other observations of this source and compare it with similar Sy-1 galaxies, especially with respect to the possible existence of a broad iron line originating in the accretion disk.

¹These values have been obtained from Ned Wright’s Cosmology Calculator web page: <http://www.astro.ucla.edu/wright/CosmoCalc.html>.

2.1 Data Reduction

We use data taken with the European Photon Imaging Camera pn (EPIC-pn) camera on board *XMM-Newton*. The data were obtained during revolution 465 of *XMM-Newton*, during which the pn was operated in its small-window mode to prevent photon pile-up, using the medium filter to avoid optical light contamination. The EPIC MOS-1 camera took data in the fast uncompressed timing mode, and the MOS-2 camera operated in prime partial W2 imaging mode. Although the MOS results will not be discussed further here, they mirrored the EPIC-pn data within the expected errors of calibration effects. The average EPIC-pn count rate for this source was 29.78 cts s^{-1} . Due to calibration difficulties between the pn and RGS instruments, the RGS data are also not discussed further in this work. These data were analyzed, but the discrepancies between the pn and RGS results, the relatively small number of counts for NGC 4593 and the calibration issues at play between the pn and RGS forced us to exclude RGS spectra in our model fits to the data. Kirsch et al. provide a detailed discussion of these calibration uncertainties (Kirsch et al. 2005).²

The pipeline data for the pn instrument were reprocessed using the Science Analysis Software and the corresponding calibration files, version 6.5.0. From these, we rebuilt the calibration index file using `cifbuild`. For the EPIC-pn data the event files were mildly edited in spectral coverage to observe the region from 0.2 – 15 keV, and bad pixels and cosmic ray spikes were removed via narrow time filtering using the `evselect` task within the SAS. No background flares were detected during the observation. Extraction of spectra followed the procedure used by Wilms et al. , in which source and background spectra were generated using the `xmmselect` task (Wilms et al. 2001). Response matrices and

²See also http://xmm.vilspa.esa.es/external/xmm_sw_cal/calib/index.shtml for a thorough discussion of these cross-calibration issues.

ancillary response files were created using `rmfgen` and `arfgn`, and the data were then grouped using the `grppha` task with a binning factor of 25 cts bin^{-1} . Binning is required in order to get sufficient counts per bin to make χ^2 spectral fitting a valid statistical process. An indicator of the global goodness-of-fit of the model to the data, the χ^2 statistic for a given set of measurements is defined as the difference between the data and model divided by the square of the uncertainty in the data, summed over all the measurements, or

$$\chi^2 = \sum_{i=1}^k \frac{(X_i - \mu_i)^2}{\sigma_i^2}. \quad (2.1)$$

Spectral modeling and analysis from $0.5 - 10 \text{ keV}$ was performed using the `XSPEC` package version 11.3.2 (Arnaud 1996). Timing studies were performed using various routines in the `XRONOS` package (Stella & Angelini 1992).

We have used the `SAS` `epatplot` task to compute the fraction of single, double, triple and quadruple events as a function of energy and compared these fractions to their nominal values as measured from weak source observations. For sources that are affected by pile-up, these fractions deviate from the nominal values due to the higher probability of wrong pattern classification. No significant deviation from the nominal single and double distributions was found, indicating that our EPIC-pn observation of NGC 4593 is not affected by pile-up.

2.2 Spectral Analysis

2.2.1 Continuum and Absorption

We began our analysis by fitting the $2 - 10 \text{ keV}$ EPIC-pn data with a simple photoabsorbed (`phabs`; (Balucinska-Church & McCammon 1992)) power-law model with abundances (Anders & Grevesse 1989), as shown in Fig. 2.1. Here we assume a Galactic hydrogen

column density of $N_{\text{H}} = 1.97 \times 10^{20} \text{ cm}^{-2}$ (Elvis et al. 1989). This initially yields a best-fit power-law photon index of $\Gamma = 1.74 \pm 0.01$ and a flux of $7.06 \times 10^{-11} \text{ erg cm}^{-2} \text{ s}^{-1}$ from 2 – 10 keV. The spectrum above 2 keV is well described by this model ($\chi^2/\text{dof} = 1879/1450$ (1.30)), with the exception of two residual emission features with rest frame energies of 6.4 keV (identified as the fluorescent $\text{K}\alpha$ emission line of cold iron) and 6.97 keV (likely to be the $\text{Ly}\alpha$ recombination line of hydrogen-like iron). The cold iron line likely arises from fluorescence on the surface layers of the outer accretion disk, optically thick optical broad emission line clouds, or the putative “molecular torus” in response to hard X-ray irradiation from a hot corona in the inner accretion disk (Basko 1978; George & Fabian 1991; Guilbert & Rees 1988; Lightman & White 1988; Matt et al. 1991). The ionized line, by contrast, could be formed either by ionized disk irradiation or by radiative recombination in highly ionized outflowing material above the plane of the disk. Because these two iron lines are relatively narrow, fitting them with relativistic disk emission models such as `diskline`, `laor` or `kerrdisk` (Brenneman & Reynolds 2006) has no statistical advantage over fitting them with Gaussians, and the parameters governing the disk emission are not well constrained. Therefore, using Gaussians to describe the iron lines, the 6.4 keV line in this model has a flux of $5.71 \pm 0.53 \times 10^{-13} \text{ erg cm}^{-2} \text{ s}^{-1}$ and an equivalent width of $131 \pm 12 \text{ eV}$, while the 6.97 keV line has a flux of $1.80 \pm 0.45 \times 10^{-13} \text{ erg cm}^{-2} \text{ s}^{-1}$ and an equivalent width of $45 \pm 13 \text{ eV}$. Inclusion of these components significantly improves the goodness-of-fit to $\chi^2/\text{dof} = 1424/1446$ (0.98). The flux and luminosity for the 2 – 10 keV spectrum are $4.11 \times 10^{-11} \text{ erg cm}^{-2} \text{ s}^{-1}$ and $7.38 \times 10^{42} \text{ erg s}^{-1}$, respectively. These values for the continuum and iron line parameters are in keeping with those determined previously for this data set by Reynolds et al., within error bars, and these conclusions are therefore robust to the calibration changes in the EPIC-pn that have occurred since publication of our previous work (Reynolds et al. 2004a). The results from this study and the discussion

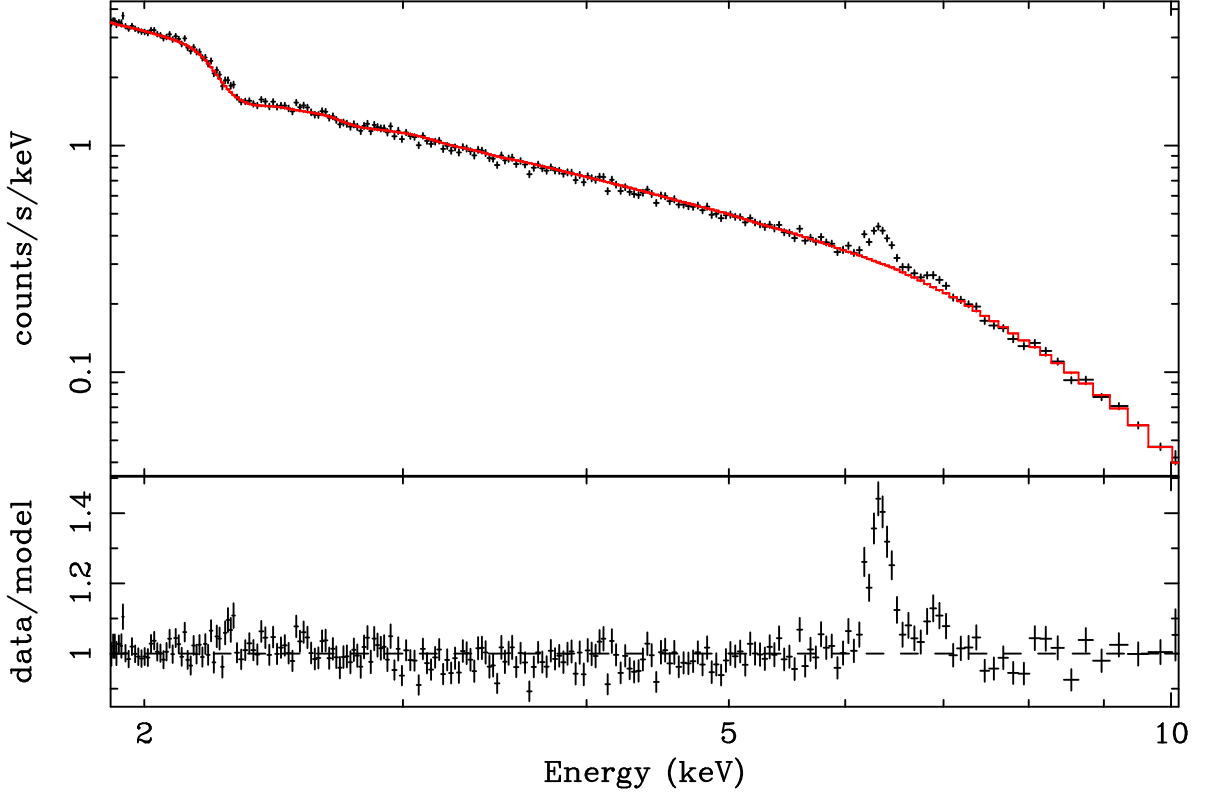


Figure 2.1: The 2 – 10 keV spectrum of NGC 4593 fit with a simple photoabsorbed power-law (phabs po). Note the residual iron features at 6.4 keV and 6.97 keV. For this fit, $\chi^2/\text{dof} = 1879/1450 (1.30)$.

of fitting a broad iron line to this source can be found in the following Section.

Below ~ 2 keV there is significant spectral complexity beyond a simple power-law form (Fig. 2.2) which is most likely due to a combination of a soft excess and the presence of absorbing material along our line of sight within the X-ray continuum source. As a first, purely phenomenological attempt to describe the soft excess component, we have employed a thermal bremsstrahlung emission model (zbrems). The best-fit value for the energy of this component is $kT \approx 0.21^{+0.00}_{-0.00}$ keV, with a flux of $2.01^{+0.33}_{-0.11} \times 10^{-14}$ erg cm $^{-2}$ s $^{-1}$. Addition of this component again improves the goodness-of-fit to $\chi^2/\text{dof} = 2398/1738$ (1.38) from 0.5 – 10.0 keV, down from 11423/1736 (6.58) before the bremsstrahlung emission was included (and after the energies from 0.5 – 2.0 keV had been noticed in the spectrum).

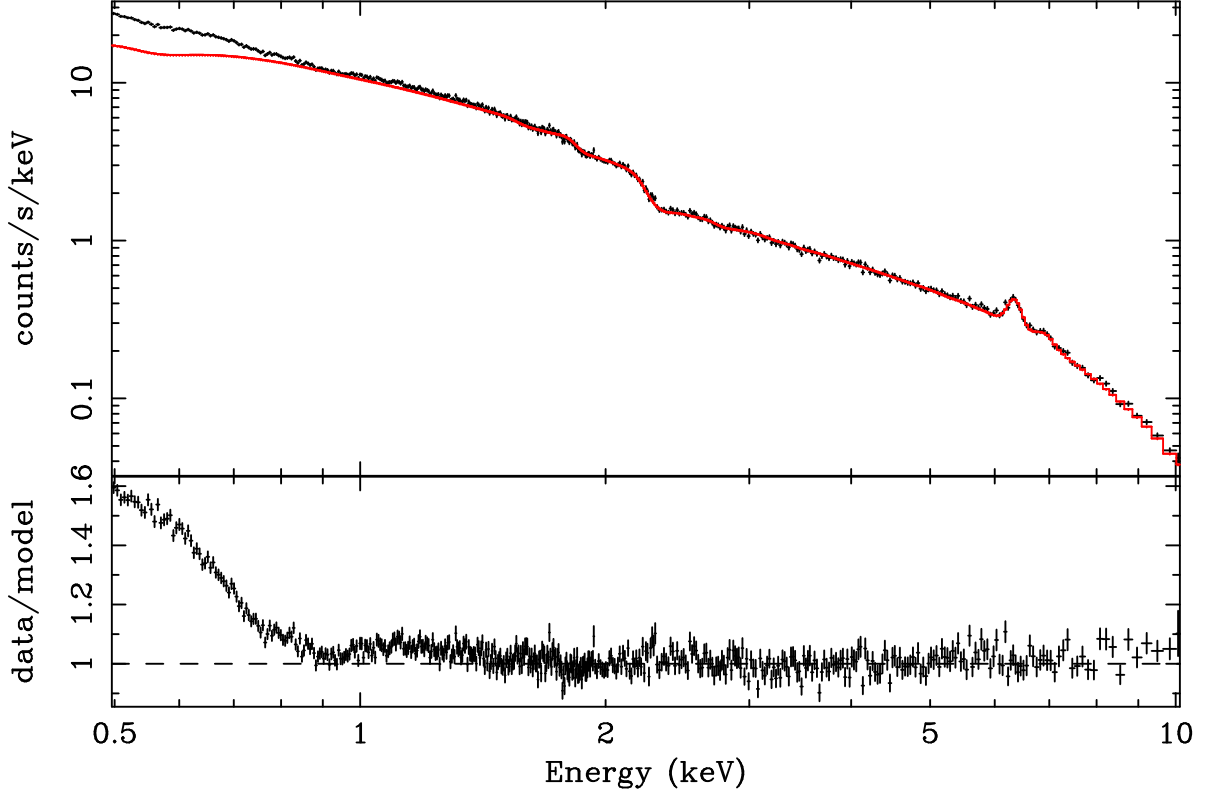


Figure 2.2: The 0.5 – 10.0 keV spectrum of NGC 4593 fit with a photoabsorbed power-law and two Gaussians to model the iron lines. Note the clear evidence for a soft excess, possibly complicated by absorption features from a “warm absorber” within NGC 4593. For this fit, $\chi^2/\text{dof} = 11423/1736$ (6.58).

Evidence for a warm absorber in this source was initially found through approximating it simply with the O VII and O VIII K-shell photoelectric edges first observed with *ASCA* (Reynolds 1997). This author quotes an O VII edge depth of $\tau = 0.26 \pm 0.04$, and an O VIII edge with $\tau = 0.09^{+0.04}_{-0.03}$. Interestingly, we do not find similar edge depths in the *XMM-Newton* data set here: employing this simple model gives for O VII at 0.74 keV, $\tau = 0.15^{+0.01}_{-0.02}$. For O VIII at 0.87 keV, $\tau = 0.00^{+0.01}_{-0.00}$ (error bars are at the 90% confidence level). As with other components in our global fit, we elected to freeze the redshifts at the cosmological value for the source: $z = 0.009$. Allowing the redshifts to fit as free parameters does not significantly improve the goodness-of-fit, and results in best-fit redshifts with large error bars that allow outflow velocities on the order of many thousand km s^{-1} . Adding the O VII edge to the model improves the goodness-of-fit to $\chi^2/\text{dof} = 2018/1740$

(1.16).

It is thought that a more physical representation of a typical warm absorber would incorporate not just oxygen edges, but a host of edges and absorption lines from several other elements as well (nitrogen, neon and silicon, to name a few). With this in mind, ionized plasma codes such as XSTAR (version 2.1kn3; originally developed in Kallman & Krolik (1995)³) can in principle model these warm absorbers much more accurately than the O VII and O VIII edges alone. Using XSTAR, we have constructed a warm absorber table as a function of the absorbed column density (N_{H}) and ionization parameter (ξ) local to a given area surrounding the source. The ionization parameter is given by the usual definition,

$$\xi = \frac{L_{\text{i}}}{n_{\text{e}} r^2}, \quad (2.2)$$

where L_{i} is the luminosity above the hydrogen Lyman limit, n_{e} is the electron number density of the plasma and r is the distance from the (point) source. We have constructed 20×20 grids of models uniformly sampling the $(\log N_{\text{H}}, \log \xi)$ plane in the range $N_{\text{H}} = 10^{20} \rightarrow 10^{24} \text{ cm}^{-2}$ and $\xi = 1 \rightarrow 10^4 \text{ erg cm}^{-1} \text{ s}^{-1}$. While these were made to be multiplicative models and hence can be applied to any emission spectrum, the ionization balance was solved assuming a power-law ionizing spectrum with a photon index of $\Gamma = 2$, cut off at an energy $E_{\text{c}} = 20 \text{ keV}$. This is a good approximation of the typical AGN continuum.

Replacing the oxygen edges with our warm absorber model described above, we find that the WA has a column density of $N_{\text{H}} = 3.54 \times 10^{22} \text{ cm}^{-2}$ and an ionization parameter of $\log \xi = 2.09 \text{ erg cm}^{-1} \text{ s}^{-1}$. However, replacing both oxygen edges with one WA table actually worsens the fit to $\chi^2/\text{dof} = 2123/1740$ (1.22), and significant residuals remain. To address this issue, we added in a second WA component and re-fit. Including the second WA we find that $\chi^2/\text{dof} = 1864/1742$ (1.07), a substantial improve-

³XSTAR Manual, available at <http://legacy.gsfc.nasa.gov>.

ment over the one-WA model and the two-edge model. Furthermore, adding the second WA produced a notable two-zone structure within the absorbing system, in terms of the column densities and ionization states of the two components: $N_{\text{H1}} = 1.64_{-0.09}^{+0.07} \times 10^{23} \text{ cm}^{-2}$ and $\log \xi_1 = 0.57_{-0.17}^{+0.13} \text{ erg cm}^{-1} \text{ s}^{-1}$ vs. $N_{\text{H2}} = 2.97_{-0.73}^{+0.31} \times 10^{21} \text{ cm}^{-2}$ and $\log \xi_2 = 2.54_{-0.04}^{+0.03} \text{ erg cm}^{-1} \text{ s}^{-1}$. A natural interpretation is that the WA has distinct components at physically different distances from the central engine. We note that attempting to add a third zone, or table, into the model results in no statistical improvement in fit. Abundances for the WAs were kept frozen at the solar values for each element in question throughout. Freeing these components added in too many additional degrees of freedom and prevented us from obtaining a statistically meaningful fit.

Even utilizing two WAs to try and model the soft spectrum more accurately, we note that residuals still remain between the data and model, especially around $\sim 0.7 - 0.8 \text{ keV}$. If there is significant dust in the WA, it is likely that iron absorption plays a role, given its elemental abundance in most AGN systems. To gauge the importance of iron absorption here, we added in another multiplicative table model to the fit, representing the Fe-L₃ edge at 0.707 keV (kindly provided to us by Julia Lee). Indeed, including this component greatly improved the fit: $\chi^2/\text{dof} = 1830/1743$ (1.05). The iron column density necessary for this fit is $\log N_{\text{Fe}} = 16.81_{-0.05}^{+0.02} \text{ cm}^{-2}$. Hereafter, we shall refer to this spectral model simply as Model 1.

Model 1 describes the data quite well with a goodness-of-fit parameter of $\chi^2/\text{dof} = 1813/1745$ (1.04). However, we note that it is purely phenomenological in nature, especially with respect to the arbitrary thermal bremsstrahlung model that has been included to model the soft excess. Ideally, we would like to describe the soft excess with a model that has a direct physical interpretation. Initially, we attempt to describe the soft excess as soft X-ray reflection from a mildly-ionized accretion disk (for a successful application of this model to the Seyfert galaxy MCG-6-30-15 see Chapter 4 of this work, also published in

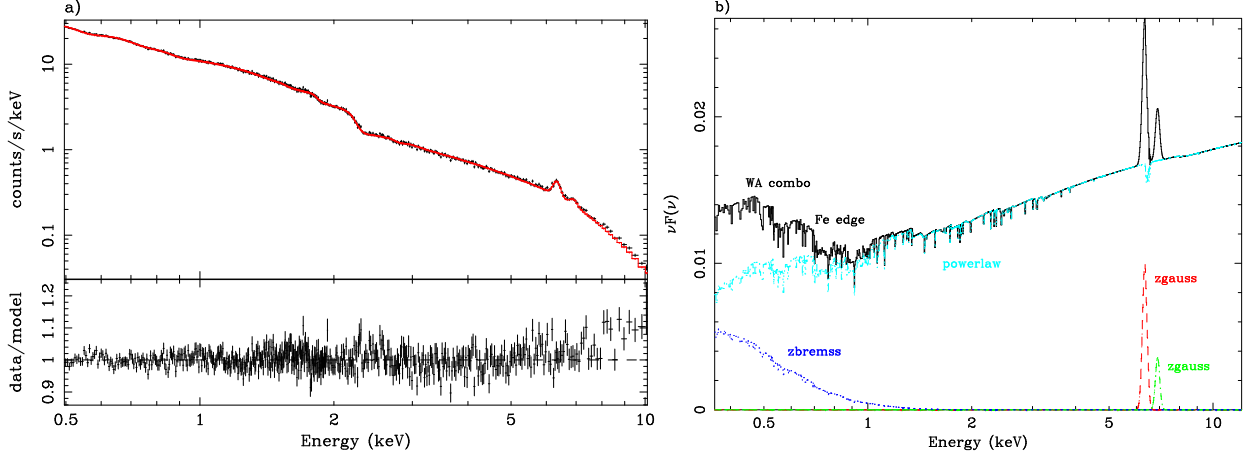


Figure 2.3: (a) The best fit for Model 1, including a zbremss component to represent the soft emission: $\chi^2/\text{dof} = 1813/1745$ (1.04). (b) The relative strength of the model components for Model 1. The 6.4 and 6.97 keV Gaussians are shown in red and green, respectively. The zbremss soft emission is in dark blue, and the photoabsorbed power-law is in light blue. Other absorption components are indicated in black.

Brenneman & Reynolds (2006)). Operationally, we replace the thermal bremsstrahlung component in Model 1 with the ionized disk model `reflion` (Ross & Fabian 2005). Because the irradiated matter is also responsible for producing the Fe-K α line in many sources, this model has the potential for self-consistently describing the soft excess as well as the 6.4 keV emission line feature. Interestingly, we find that we cannot successfully describe both the soft emission and the Fe-K α line with the disk reflection model. The resulting best fit is $\chi^2/\text{dof} = 2652/1745$ (1.52), and we found that either significant residuals remained on the soft or hard end, or that the 6.4 keV iron line was simply not fit adequately. Even adding the Gaussian component back to explicitly model the 6.4 keV iron line, the disk reflection model was unable to adequately fit the form of the soft excess. We thus conclude that ionized disk reflection is not an important process in shaping the soft X-ray spectrum of NGC 4593. Given the relative narrowness of the Fe-K α line in this source (discussed further in the following Section, (Reynolds et al. 2004a)), we believe it is not originating in the inner disk, and hence the above is not a surprising conclusion.

Another possibility is that the soft excess is due to thermal Comptonization by plasma

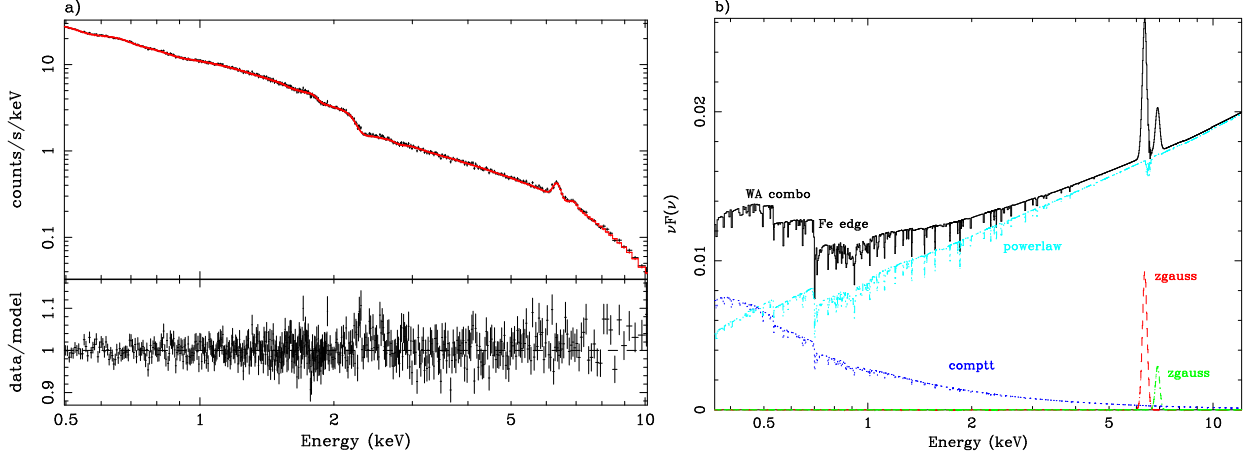


Figure 2.4: (a) The best fit for Model 2, including a `comptt` component to represent the soft emission in place of the `zbremss` component of Model 1. $\chi^2/\text{dof} = 1808/1744$ (1.04). (b) The relative strength of the model components for Model 2. The color scheme is the same as in Fig. 2.3.

at a temperature between that of the disk and the hard X-ray corona (possibly in a transition zone). To reflect this, we use the `comptt` model (Titarchuk 1994) to parameterize the soft excess. Hereafter, we shall refer to this spectral model as Model 2. This preserves the physical realism of the soft emission arising from the accretion disk, but allows the iron line to be produced elsewhere, perhaps farther away in the molecular torus where it would not be as intrinsically broad. Model 2 reaches a best fit of $\chi^2/\text{dof} = 1759/1744$ (1.01), a slight improvement over the statistical best fit of Model 1. The best fit and model for Model 2 are shown in Fig. 2.4. Here we have frozen the seed photon temperature at $T_0 = 50$ eV and have kept a slab geometry for the corona. The best-fit Comptonizing plasma temperature is $kT_c = 42$ keV with an optical depth of $\tau = 0.12$, though both parameters were not very well constrained by the fit. This is not surprising, given that both are equally involved in shaping the spectrum via the Compton- y parameter: $y \propto \tau T_c$. We note that for Model 2 the equivalent widths of the 6.4 and 6.97 keV Gaussians remain approximately unchanged from their values in the Model 1 fit.

Table 2.1 reports the parameter values and goodness-of-fit for both the final best-fitting phenomenological model (Model 1, with `zbremss` and including all other com-

Model Component	Parameter	Model 1 Value	Model 2 Value
phabs	$N_{\text{H}} (\text{cm}^{-2})$	1.97×10^{20}	1.97×10^{20}
WA 1	$N_{\text{H1}} (\text{cm}^{-2})$	$1.64^{+0.07}_{-0.09} \times 10^{23}$	$9.29^{+1.46}_{-9.15} \times 10^{22}$
	$\log \xi_1 (\text{erg cm s}^{-1})$	$2.54^{+0.03}_{-0.04}$	$2.75^{+0.12}_{-0.32}$
WA 2	$N_{\text{H2}} (\text{cm}^{-2})$	$2.47^{+0.31}_{-0.73} \times 10^{21}$	$1.13^{+1.21}_{-0.94} \times 10^{22}$
	$\log \xi_2 (\text{erg cm}^{-1} \text{s}^{-1})$	$0.57^{+0.13}_{-0.17}$	$1.70^{+0.30}_{-0.59}$
Fe-L ₃ edge	$\log N_{\text{Fe}} (\text{cm}^{-2})$	$16.81^{+0.02}_{-0.05}$	$16.92^{+0.04}_{-0.08}$
po	Γ	1.87 ± 0.00	$1.75^{+0.02}_{-0.03}$
	flux ($\text{erg cm}^{-2} \text{s}^{-1}$)	$5.11^{+0.04}_{-0.02} \times 10^{-13}$	$4.44^{+0.41}_{-0.54} \times 10^{-13}$
zgauss	$E (\text{keV})$	6.4	6.4
	$\sigma (\text{keV})$	0.10 ± 0.08	0.10 ± 0.01
	flux ($\text{erg cm}^{-2} \text{s}^{-1}$)	$4.46 \pm 0.32 \times 10^{-15}$	$4.15^{+0.33}_{-0.34} \times 10^{-15}$
	$E (\text{keV})$	6.97	6.97
	$\sigma (\text{keV})$	0.10 ± 0.02	0.10 ± 0.06
zbremss	flux ($\text{erg cm}^{-2} \text{s}^{-1}$)	$9.47^{+2.00}_{-2.07} \times 10^{-16}$	$7.77^{+2.07}_{-2.37} \times 10^{-16}$
	$kT (\text{keV})$	$0.21^{+0.00}_{-0.01}$	
comptt	flux ($\text{erg cm}^{-2} \text{s}^{-1}$)	$2.01^{+0.33}_{-0.11} \times 10^{-14}$	
	$T_0 (\text{keV})$		0.05
	$kT (\text{keV})$		$42.19^{+140.67}_{-40.19}$
	τ		$0.12^{+0.06}_{-0.11}$
χ^2/dof	flux ($\text{erg cm}^{-2} \text{s}^{-1}$)		$6.46^{+0.90}_{-0.92} \times 10^{-14}$
		1813/1745(1.04)	1759/1744(1.01)

Table 2.1: The energy range from 0.5 – 10.0 keV is considered for the EPIC-pn. Best fit Model 1 contains a zbremss component to parameterize the soft excess below ~ 2 keV, while best fit Model 2 represents this component with a comptt model. All quoted error bars are at the 90% confidence level. All redshifts used were frozen at the cosmological value for NGC 4593: $z = 0.009$.

ponents added in), and the more physical model (Model 2, including comptt and all other components). Using the Model 2 fit from Table 2.1, the total 0.5 – 10 keV flux is $F_{\text{X}} = 6.74 \times 10^{-11} \text{ erg cm}^{-2} \text{ s}^{-1}$. Assuming a flat universe WMAP cosmology, this corresponds to a luminosity of $L_{\text{X}} = 1.21 \times 10^{43} \text{ erg s}^{-1}$. Considering only the energy range from 2 – 10 keV, $L_{2-10} = 7.40 \times 10^{42} \text{ erg s}^{-1}$. This is roughly 21% greater than the 2 – 10 keV luminosity observed by McKernan et al. (2003), but only about 86% of the value from the ASCA observation reported by Reynolds (1997).

2.2.2 On the Lack of Accretion Disk Signatures in NGC 4593

As noted in the previous Section, the 2 – 10 keV spectrum of NGC 4593 is well-fit by a photoabsorbed power-law form to within 3 – 5%. The only two significant deviations from this model occur from 6 – 7 keV, and modeling these features with Gaussian emission lines provides a much better fit and significantly reduces the value of χ^2 . Though we have frozen the rest-frame energies of these two components in our global fit, we performed a more rigorous statistical analysis on the hard spectrum of NGC 4593 (Reynolds et al. 2004a). Revisiting and expanding upon that work (forthcoming in Brenneman et al. 2007), we find that the first line corresponds to cold Fe-K α at $E_1 = 6.39 \pm 0.01$ keV with a flux of $F_1 = 5.71 \pm 0.53 \times 10^{-13}$ erg cm $^{-2}$ s $^{-1}$ and an equivalent width of $EW_1 = 131 \pm 12$ eV. The second line, corresponding to hydrogen-like Fe-K α , has $E_2 = 6.95 \pm 0.05$ keV and a flux of $F_2 = 1.80 \pm 0.45 \times 10^{-13}$ erg cm $^{-2}$ s $^{-1}$ with an equivalent width of $EW_2 = 45 \pm 13$ eV. We do not detect a helium-like Fe line at 6.67 keV: the upper limit on the equivalent width of such a feature would have to be less than 13 eV.

These relatively narrow emission lines most likely originate from material that is comparatively distant from the central BH. The cold iron line is centered on the systemic velocity of NGC 4593 and is well resolved ($\text{FWHM} = 10900 \pm 2200$ km s $^{-1}$). For comparison, the broad optical H β line in this source has a $\text{FWHM} = 4910 \pm 300$ km s $^{-1}$ (Grupe et al. 2004), roughly half of the velocity width of cold Fe-K α here. Thus, it seems clear that the cold iron line is originating from a region that lies significantly inside the optical broad emission line region (OBLR), and hence cannot be identified with X-ray reflection from the putative “molecular gas torus” theorized by Seyfert unification schemes. We note that the *XMM-Newton* data sets no useful constraints on the presence of a Compton back-scattered continuum expected from X-ray reflection by cold matter. Thus the

possibility remains that this line might be formed by the fluorescence of optically *thin* accretion disk material (as opposed to the optically *thick* material normally envisaged in the scenario of X-ray reflection).

The hydrogen-like Fe-K α line, on the other hand, is only marginally resolved (FWHM = 12200_{-9400}^{+11200} km s $^{-1}$). It is therefore not possible to conclude where this ionized emission originates relative to the OBLR. It is, however, possible to say something about the physical process underlying this emission. If we suppose that this line is emitted by a collisionally ionized thermal plasma (described by the `mekal` model in XSPEC; (Liedahl et al. 1995; Mewe et al. 1985, 1986)), the EPIC-pn data dictate that the plasma must possess a temperature of at least $kT \sim 50$ keV in order to reproduce the constraint on the hydrogen-like/helium-like equivalent width while simultaneously not curving the overall continuum excessively. The required emission measure would then be $EM \equiv \int n_e^2 dV = 1.6 \times 10^{67}$ cm $^{-3}$, where n_e is the electron number density and V is the volume of the thermal plasma. If we also suppose that this plasma surrounds the central engine in a spherical geometry which is optically thin to Compton scattering (or else we would not observe rapid X-ray variability from the AGN), we can use the column density and emission measure constraints to conclude that the thermal plasma must have an extent of at least 4×10^{16} cm. It is hard to rationalize the existence of such hot plasma many thousands of gravitational radii from the central BH. We therefore largely rule out this origin for the ionized Fe-K α line. It is more likely that this feature originates via radiative recombination and resonant scattering in strongly photoionized gas within the central engine of the AGN. While a detailed exploration of this postulate is beyond the scope of this paper, it is tempting to identify this feature with the same plasma that produces the highly ionized absorption features seen in several other AGN (Pounds et al. 2003a; Reeves et al. 2003).

We do not find evidence for additional broad emission features once these narrow ones have been modeled. In addressing this issue, we added a relativistic iron line to

the spectral fit using two different models: the Schwarzschild model (Fabian et al. 1989), known as `diskline` in the XSPEC package, and the near-extreme Kerr model (Laor 1991), known as `laor`. The energy of the emission line (E_{broad}) was allowed to vary across the range of possible Fe-K α transition energies (from 6.40 – 6.97 keV in the rest-frame). The inner radius of the emitting region (r_{in}), the emissivity index of the disk (β), the viewing inclination (i) and the line normalization were also free parameters in the fit. The outer radius of the line-emitting region was fixed at $r_{\text{out}} = 1000 r_{\text{g}}$. The improvement in the goodness-of-fit was $\Delta\chi^2/\Delta\text{dof} = -11/-5$ and $\Delta\chi^2/\Delta\text{dof} = -10/-5$ for the `diskline` and `laor` models, respectively. Such a change is not significant at the 90% confidence level, indication that we have not robustly detected any broad Fe-K α lines in the fit.

In order to obtain a meaningful upper limit to the equivalent width of any broad iron line, we must specify its shape (since the data cannot statistically make such a distinction themselves). Empirically, we can proceed assuming that any such line has the “typical” profile found in co-added ASCA data (Nandra et al. 1997), i.e., the `diskline` model with $E_{\text{broad}} = 6.4$ keV, $r_{\text{in}} = 6 r_{\text{g}}$, $\beta = 2.5$ and $i = 29^\circ$. Using these assumptions, we can set an upper limit (with a 90% confidence level for one interesting parameter) to the broad line equivalent width of $EW_{\text{broad}} = 87$ eV. Taking a theoretical approach, we assume the simplest model (Novikov & Thorne 1974; Page & Thorne 1974; Shakura & Sunyaev 1973) is one in which the accretion disk is geometrically thin and radiatively efficient, extends from the radius of marginal stability to large radii, and possesses an iron line emissivity that tracks the underlying dissipation (Reynolds & Nowak 2003). Applying such a line profile to the NGC 4593 data in the case of a near-extreme Kerr BH (with dimensionless spin parameter $a = 0.998$) results in an upper limit to the equivalent width of $EW_{\text{broad}} = 99$ eV. These are significantly less than the values expected from theoretical reflection models (~ 200 eV for solar abundances (Matt et al. 1997) or than those observed in the Seyfert galaxy MCG–6-30-15 (~ 400 eV; (Fabian et al. 2002)). Thus, there appears

to be a significant absence of spectral features from a relativistic accretion disk.

Given that the BH accretion paradigm of AGN is very well established and supported by a significant body of evidence, the results of our spectral analysis of NGC 4593 demand that we consider why we are not seeing the X-ray reflection signatures of a relativistic accretion disk, given that we believe it exists and is responsible for the AGN emission features that we observe. A straightforward solution to this problem would be to postulate subsolar abundances of iron in the BH accretion disk (Reynolds et al. 2004a). However, it would be surprising if the solution to the lack of a broad iron line was simply an underabundance of iron, given the highly evolved nature of stellar populations in the nuclei of galaxies such as NGC 4593. With this motivation, we explore modifications of the canonical line models discussed above and show that it is, in fact, rather easy to bury relativistic spectral features in the noise even if they are present at the level associated with cosmic abundance material.

One possibility is that the disk reflection signatures are present in the spectrum, but are so broad that they are lost in the continuum. Such broad features can be produced when the emission is very centrally concentrated (i.e., coming from deep within the potential well of the BH and therefore subject to intense gravitational redshift). Alternatively, if the disk is viewed at high inclination, the spectral lines will be especially broadened. An example of the former can be found in the Sy-1 AGN MCG–6-30-15 (Brenneman & Reynolds 2006; Reynolds et al. 2004b; Wilms et al. 2001). Using the models of Agol & Krolik (Agol & Krolik 2000), Reynolds et al. suggest that the highly centrally concentrated emission profile of the disk seen when this source is in its “Deep Minimum” state (also found in (Brenneman & Reynolds 2006): for the inner disk, $\alpha_1 > 6$) may be due to a magnetic torque exerted on the inner disk by field lines threading the disk and BH. Such a torque would explain the observed enhanced energy loss from this region of the disk. Because the disk inclination of MCG–6-30-15 has been constrained at $i \sim 30^\circ$ (Brenne-

man & Reynolds 2006; Fabian et al. 2002), however, the extremely broad iron line is still discernible above the continuum. With lower signal-to-noise and a higher inclination angle this would not be the case. Perhaps this is the scenario at work in NGC 4593. To test this possibility, we added to the spectral fit a cold iron line with a profile corresponding to an infinite-efficiency (torqued) accretion disk around a near-extreme Kerr BH ($a = 0.998$). The inclination and normalization of the line were left as free parameters. This led to only a slight improvement in the goodness-of-fit over the simple power-law plus narrow-line model ($\Delta\chi^2/\Delta\text{dof} = -3/-2$). The upper limit on the equivalent width is $EW_{\text{broad}} < 250$ eV. Thus, a broad line with the strength expected from a cosmic abundance accretion disk is consistent with these data if the emissivity profile is very centrally concentrated.

An increase in the ionization level of the disk surface could also repress fluorescent emission features. We address this question (Reynolds et al. 2004a) using the ionized reflection models of Ballantyne et al. (2001) convolved with the relativistic smearing model corresponding to a “standard” Novikov-Page-Thorne accretion disk around a near-extremal Kerr BH. We found that in the ionization range $\log \xi = 1.5 - 2.5$, the fluorescent iron line is strongly suppressed by resonant scattering followed by Auger destruction (Matt et al. 1993). A standard Novikov-Page-Thorne accretion disk is permissible in this object as long as it is either highly ionized (in which case the iron atoms are fully stripped) or moderately ionized (when the fluorescent line is strongly suppressed by resonant scattering and Auger destruction).

Limb-darkening and coronal attenuation could also be at fault. It is believed that any broad iron line is produced via fluorescence in the outer few Thomson depths of the optically thick part of the accretion disk. If viewed at high inclination (i.e., almost edge-on), there are two distinct limb-darkening effects that can suppress the observed line flux (Reynolds & Wilms 2000). First, iron line photons can be photoelectrically absorbed on

their passage through the outer layers of the disk, either by the K-shell edges of elements lighter than iron or the L-shell edges of iron. The resulting excited ion will then de-excite either via the Auger effect or through the emission of new fluorescent line photons, each resulting in a net loss of iron line photons from the observed spectrum. Secondly, iron line photons can be Compton scattered by energetic electrons in the corona, as discussed in Chapter 1. The fractional energy gained by a photon in each interaction with a coronal electron is of order unity for a thermal plasma with $kT \sim 100$ keV. Thus, Compton scattering effectively removes photons from the iron line, spreading them out in energy space until they become indistinguishable from the power-law continuum. Both photoelectric absorption in the disk and Compton scattering in the corona are strongly accentuated for high-inclination observers since the photons then have to follow trajectories that graze the disk atmosphere and corona. The primary continuum photons, on the other hand, are not subject to limb-darkening since the corona is optically thin. Hence, the equivalent width of a broad iron line would be expected to drop as the disk is viewed increasingly edge-on. While there is little evidence that the inner disk of NGC 4593 is viewed at high inclination, the possibility that limb-darkening is responsible for the absence of a broad line in this object cannot be ruled out with current data.

If the broad iron line is genuinely absent from the data, perhaps the accretion disk is in a radiatively inefficient state, e.g., possessing an advection-dominated accretion flow, or ADAF (Blandford & Begelman 1999; Ichimaru 1977; Narayan & Yi 1994; Rees 1982). In such a state, the disk does not radiate the dissipated energy locally due to a low accretion rate, leading to narrower emission line profiles since the lines would not originate in the inner part of the disk. Indeed, it is possible that we are seeing just such a component in the form of the narrow 6.4 keV line modeled in this Section. If we model this feature with a diskline profile possessing an inner truncation radius, instead of a narrow Gaussian profile, we determine that the inner truncation radius to the line emit-

ting region is $r_{\text{in}} > 200r_{\text{g}}$. In deriving this number, we have fitted the diskline model assuming an emissivity index of $\beta = 3$ (appropriate for illumination of a flat disk by a central raised corona or advection-dominated region), and a rest-frame line energy of 6.4 keV. The equivalent width of this feature is $EW = 113 \pm 13$ eV with a goodness-of-fit of $\chi^2/\text{dof} = 1529/1470$; i.e., the truncated diskline profile produces very comparable results to the narrow Gaussian profile.

It is possible that the observed X-ray continuum does not originate from or irradiate the accretion disk. The most likely alternative is that the continuum has its origins in a relativistic jet flowing from the central engine; the primary X-rays are then beamed away from the accretion disk, strongly suppressing any X-ray reflection features. Given the high-amplitude variability seen on hour-long timescales within this object, the X-rays would have to originate from the inner parts of any jet.

2.3 Variable Nature of the Source

NGC 4593 displays significant variability (over a factor of two in 0.5 – 10 keV flux) during the course of this observation. In this Section, we examine the detailed variability properties of this source.

2.3.1 Spectral Variability

We have analyzed the spectral variability of the source as seen in the EPIC-pn data. As an initial assessment of spectral variability, Fig. 2.5 plots the data-to-model ratios of consecutive 10 ks segments of the EPIC-pn data using the `comptt` best-fit spectrum model discussed in §2.2.1. Experimentation suggested that intervals smaller than 10 ks contain insufficient counts to maintain the integrity of the spectrum. As well as the obvious variations in the normalization of the spectrum, there are clear changes in slope between seg-

ments (with the source becoming softer as it brightens). There is also a feature of variable equivalent width seen at ~ 6.4 keV, corresponding to the cold Fe-K α line. Interestingly, though, we see no variable discrete features in the soft X-ray spectrum suggesting that there is no significant warm absorber variability during our observations.

To examine variability of the iron lines in more detail, Fig. 2.6 plots the renormalized interval data over the time-averaged data from 2 – 10 keV. Direct spectral fitting of the cold and ionized Fe-K lines in each interval with Gaussian profiles illuminates the nature of their variability (or lack thereof). As can be seen in Table 2.2, the data show that the cold line exhibits only slight variations in flux. In other words, the cold iron line flux does not appear to respond to changes in the X-ray continuum. Its equivalent width, however, shows significant variability, as we illustrate in Fig. 2.7. Constraints on the ionized line are not strong enough to rule out a constant flux and equivalent width, as is shown in Fig. 2.8 and Table 2.2.

The simplest way to interpret the lack of continuum response of the cold iron line is to suppose that it exists on spatial scales with light travel times greater than the duration of our observation. For an observation time of 76 ks, as is the case here, the light would travel approximately 150 AU, or roughly $1.9 \times 10^3 r_g$ if NGC 4593 harbors a $8.1 \times 10^6 M_\odot$ BH at its core (see discussion at the end of §2.4.3). The lack of response for the iron line flux would suggest that this size is a lower limit for the size of the line emitting source. This would place the line emission in the outer regions of the accretion disk or the putative molecular torus of the Seyfert unification scheme.

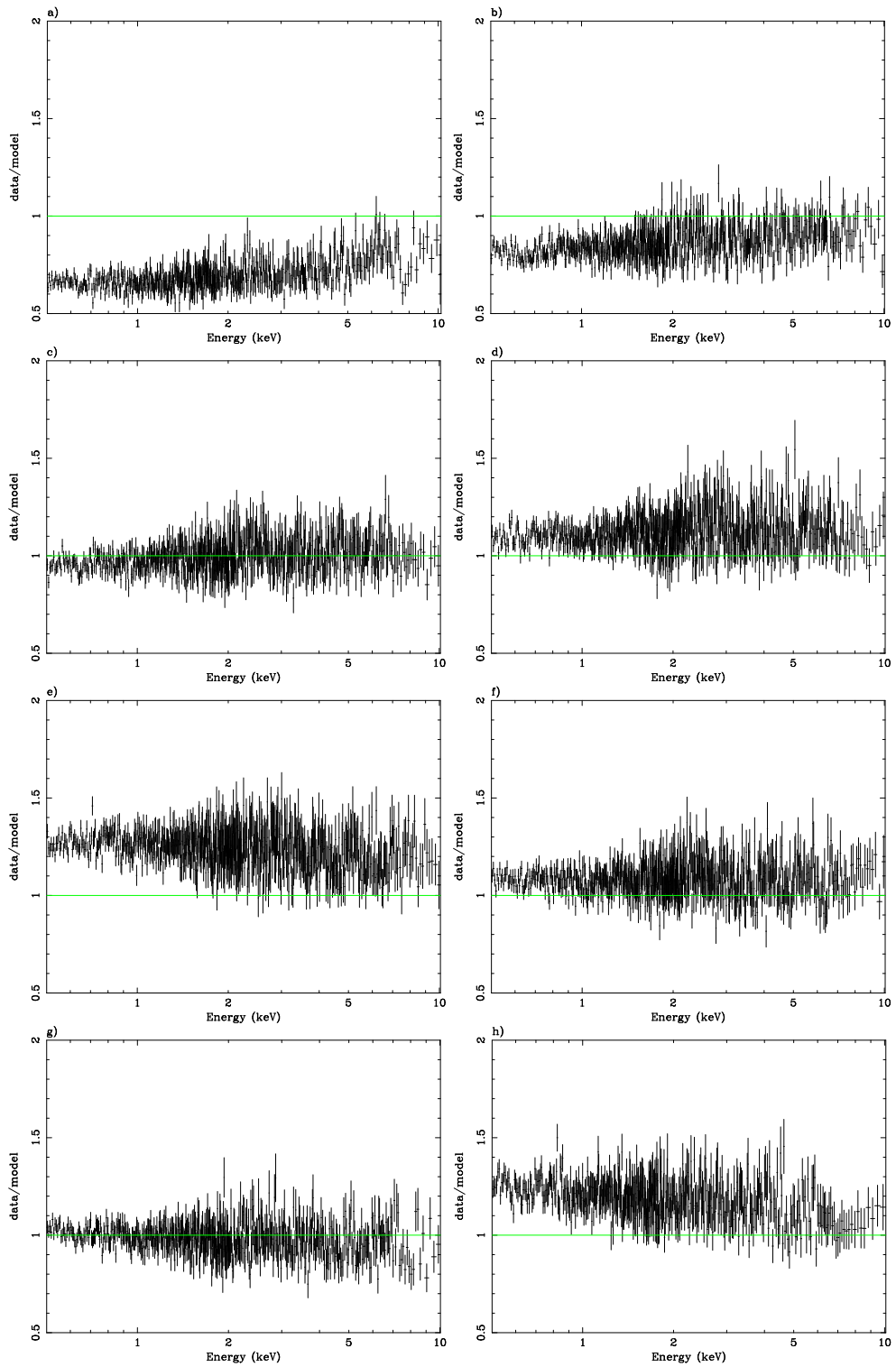


Figure 2.5: Variation of the EPIC-pn time-averaged spectrum from the `comptt` best-fit model discussed in §2.2.1. Time intervals are 10 ks in length except for the last, which is ~ 6.1 ks. Segments a) - h) are shown in chronological order of the observation.

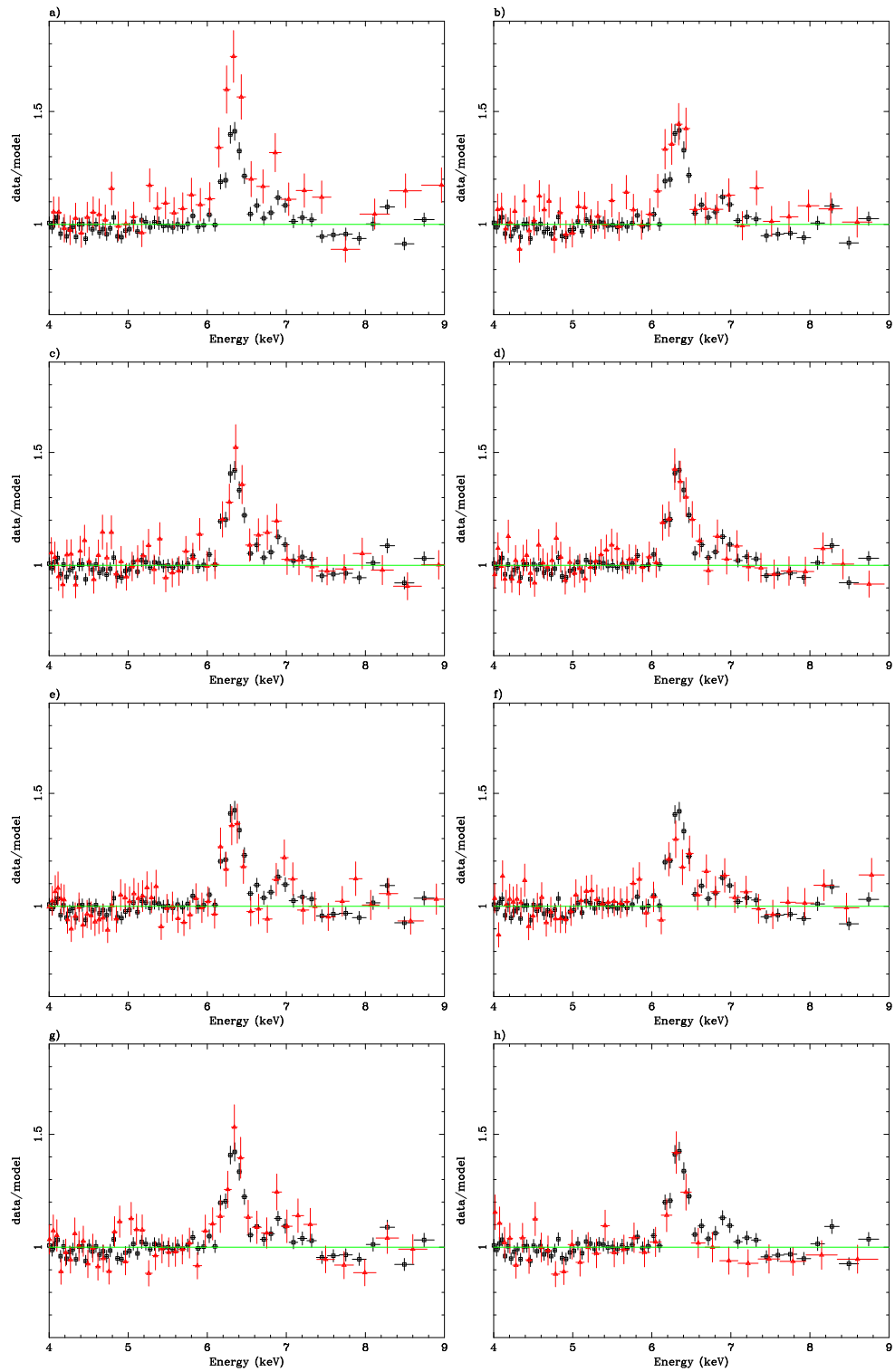


Figure 2.6: The cold and ionized Fe- $K\alpha$ lines from the time-separated EPIC-pn spectrum. Time intervals are as above in Fig. 2.5. Lines are above a phabs po continuum. The time-averaged data appear in black squares, interval data in red triangles.

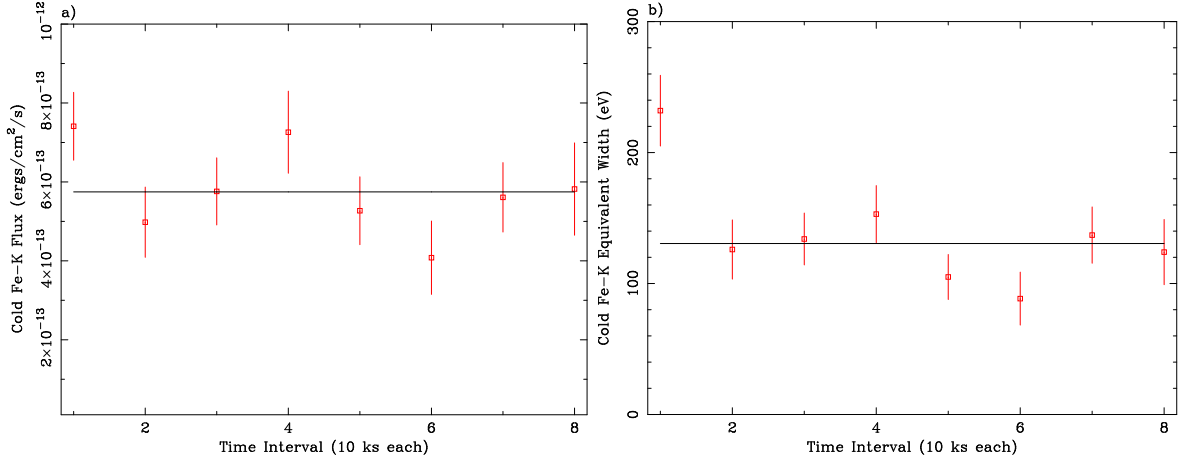


Figure 2.7: Variation of the flux (a) and equivalent width (b) of the cold Fe-K α line (6.4 keV) over the course of the 76 ks observation. Note that a fit to the data with a constant model is marginally robust for the flux: $\chi^2/\text{dof} = 10/7$ (1.43). This translates to a $\sim 20\%$ chance of the data agreeing with a constant model. Also note that the data point with the greatest offset corresponds to the point of lowest flux on the source light curve, unsurprisingly, but is still statistically valid. The constant fit is not statistically robust for the equivalent width plot: $\chi^2/\text{dof} = 22/7$ (3.14). This indicates a $< 1\%$ chance of agreement between the data and model.

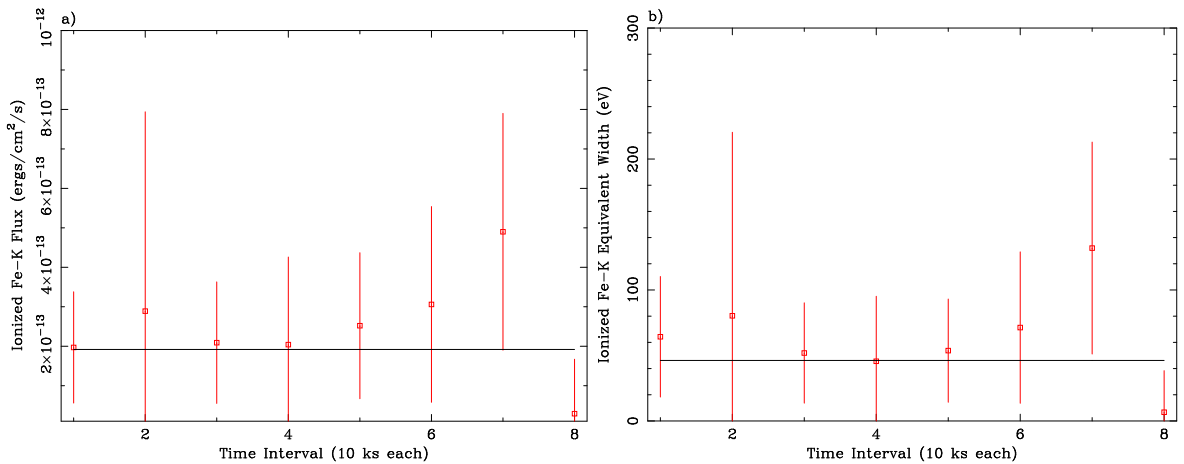


Figure 2.8: Variation of the flux (a) and equivalent width (b) of the ionized Fe-K α line (6.97 keV) over the course of the observation. Here the uncertainty in the data is so great that a constant flux cannot be ruled out: $\chi^2/\text{dof} = 3/7$ (0.43). A constant equivalent width is similarly likely: $\chi^2/\text{dof} = 3/7$ (0.43).

Line	FWHM (km s^{-1})	Flux ($\text{erg cm}^{-2} \text{s}^{-1}$)	EW (eV)
Cold Fe-K α (6.40 keV)	13245 ± 2208	$7.41 \pm 0.86 \times 10^{-13}$	232 ± 27
	8831 ± 2208	$4.98 \pm 0.89 \times 10^{-13}$	126 ± 22
	9934 ± 2208	$5.76 \pm 0.85 \times 10^{-13}$	134 ± 20
	13246 ± 3311	$7.26 \pm 1.04 \times 10^{-13}$	153 ± 22
	8831 ± 2208	$5.27 \pm 0.86 \times 10^{-13}$	105 ± 17
	11038 ± 4415	$4.08 \pm 0.93 \times 10^{-13}$	88 ± 20
	8831 ± 2208	$5.61 \pm 0.88 \times 10^{-13}$	137 ± 22
	11038 ± 3311	$5.82 \pm 1.17 \times 10^{-13}$	124 ± 25
Ionized Fe-K α (6.97 keV)	7095 ± 6081	$1.97 \pm 1.41 \times 10^{-13}$	64 ± 46
	50678 ± 83111	$2.89 \pm 5.05 \times 10^{-13}$	80 ± 140
	6081 ± 6081	$2.09 \pm 1.54 \times 10^{-13}$	52 ± 38
	14190 ± 11149	$2.04 \pm 2.22 \times 10^{-13}$	46 ± 50
	9122 ± 6081	$2.52 \pm 1.85 \times 10^{-13}$	54 ± 39
	18244 ± 9122	$3.06 \pm 3.48 \times 10^{-13}$	71 ± 58
	24325 ± 9122	$4.90 \pm 3.00 \times 10^{-13}$	132 ± 81
	_____	_____	_____

Table 2.2: Each row represents a time interval of 10 ks in the observation. Fits were done in XSPEC using a phabs po model for the continuum and two Gaussian lines with parameters fit to the data in each time interval. Error bars are at 1σ . The blank lines in the ionized Fe-K α table represent time intervals for which a robust fit to the data could not be achieved.

2.3.2 Continuum Power Spectrum and Spectral Lags

The light curve for the full-band (0.5 – 10.0 keV) data set is shown in Fig. 2.9a. The light curve is characterized by an initial rapid drop up to ~ 5 ks, followed by a relatively steady increase peaking at ~ 45 ks, a drop until ~ 65 ks, and then a final increase that shows possible signs of tapering off around the end of the observation at 76 ks. There are indications of smaller scale variability on time scales of < 1000 s, with slight flares and drops occurring throughout the data set.

Fig. 2.9b shows the Leahy normalized power spectrum of the 0.5 – 10.0 keV EPIC-pn light curve. The power spectrum demonstrates that the variability of the source becomes dominated by Poisson statistics on timescales of about 200 s once it drops to a power of ~ 2 , as expected. Before this point, the slope of the power spectrum for low frequen-

cies is $-2.63_{-0.25}^{+0.66}$. This value for the PSD slope is consistent with results from several other Sy-1 AGN such as NGC 3783 (Markowitz 2005), MCG-6-30-15 (Papadakis et al. 2005; Vaughan et al. 2003), NGC 4051 (at high frequencies; (McHardy et al. 2004)), and Mrk 766 (also at high frequencies; (Vaughan et al. 2003)).

Given the range of X-ray energies available in this data set, it is also useful to study the continuum variability in different energy bands. Hardness ratios and time lags between different energy bands in the continuum, in particular, can help constrain the emission mechanisms of the source as well as the physical scale of the emitting region(s). We divided the X-ray spectrum into three energy bands, each with an approximately equal number of counts ($\sim 5 \times 10^5$). The soft band ranges from 0.50 – 0.84 keV, the mid band extends from 0.84 – 1.50 keV, and the hard band covers 1.50 – 10.00 keV. The light curves for all three bands are represented in Fig. 2.10. In order to test whether a time lag exists between these energy bands, we computed the cross-correlation function between the three energy bands using the XRONOS package as well as the discrete correlation function (DCF; (Edelson & Krolik 1988)). We measured the hard-to-soft band lag to be 226 ± 53 s (i.e., the hard band lags the soft band by this amount of time; Fig. 2.11).

The most straightforward interpretation of this time delay envisions it as representing the finite scattering time within the Comptonizing disk-corona system that is thought to be responsible for the primary X-ray production. One should be cautioned, however, that this interpretation invokes numerous underlying simplifications with regard to the physical mechanism that produces such a time lag. See Pottschmidt et al. and Nowak et al. for more detailed accounts of other factors that can be responsible for or affect the observed time lag between the hard and soft energy bands (Nowak et al. 2002, 1999; Pottschmidt et al. 2003). We assume here that both the hard and soft X-ray photons originate from seed UV photons from the disk, which are then Comptonized by a corona of relativistic electrons surrounding the accretion disk. The energy of a given photon in our simplified

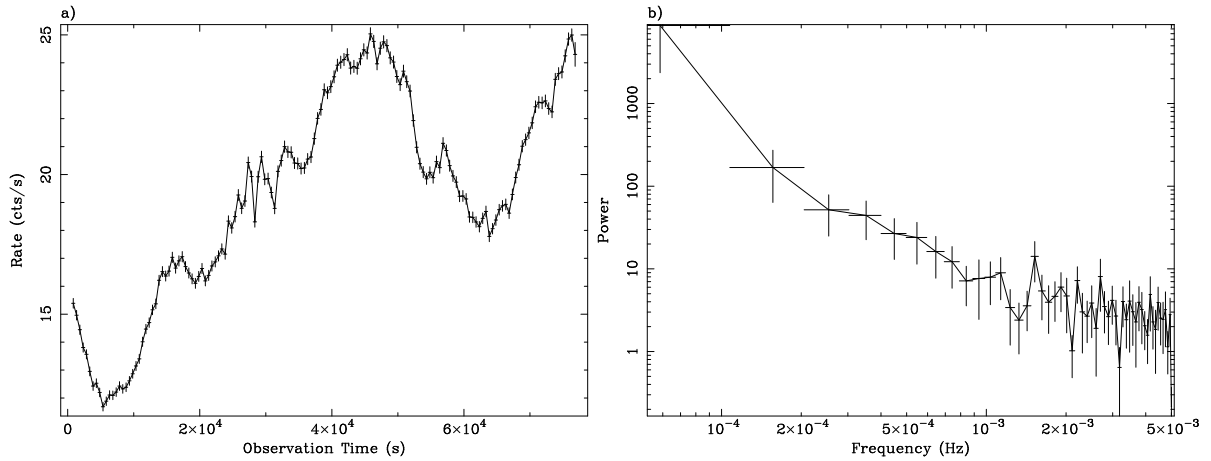


Figure 2.9: The light curve (a) and power spectrum (b) for the time-averaged pn data from NGC 4593. Variations on timescales as small as hundreds of seconds appear visible in the source. Note that the frequency at which the power spectrum flattens into Poisson noise is about 5×10^{-3} Hz. Inverting this means that the smallest timescale of variability we can reliably observe from this source is ~ 200 s. At low frequencies, the slope of the power spectral density curve is $-2.63^{+0.66}_{-0.25}$.

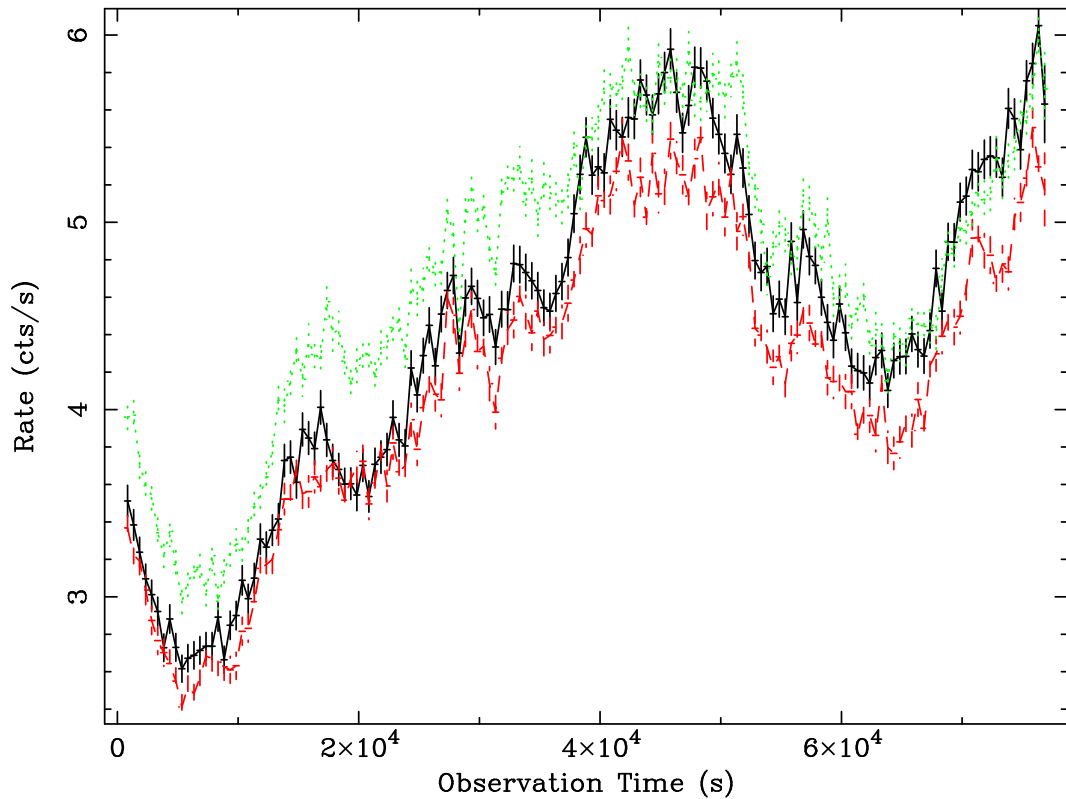


Figure 2.10: Light curves for the different energy bands: the soft band runs from 0.50 – 0.84 keV (solid black), the mid band runs from 0.84 – 1.50 keV (dashed red), and the hard band runs from 1.50 – 10.00 keV (dotted green).

scheme will thus depend on the number of scatterings it undergoes with the electrons, and one may therefore infer that the more energetic photons have experienced more interactions. It is thus possible to estimate the size of the coronal region by measuring the time lag between the peaks of the hard and soft photon light curves of the source, as we have done, and making the simplified assumption that the corona possesses a slab or spherical geometry. With each scattering, a seed photon gains on average a fractional energy $\Delta E/E \approx 4k_B T/m_e c^2$, where T is the temperature of the electrons in the corona. So the energy of a Comptonized photon after a given number of scatterings will be:

$$E \approx E_0 \left(1 + \frac{4k_B T}{m_e c^2} \right)^n \quad (2.3)$$

where E_0 is the initial seed photon energy and n is the number of scatterings (Chiang et al. 2000; Rybicki & Lightman 1979). The time delay of this photon relative to the seed photon source will be roughly proportional to the number of scatterings, $t \approx nt_0$. Here $t_0 \sim l_T/c$ where l_T is the mean free path for Thomson scattering in an optically thick corona or, if the corona is optically thin, simply the size of the corona. We take the effective photon energy in the soft range (0.50 – 0.84 keV) to be 0.67 keV. For the hard range (1.5 – 10.0 keV) we calculate the effective photon energy to be 2.17 keV. Both estimates are based on taking weighted averages (based on flux) of the energies in the soft and hard ranges, and accounting for the energy-dependent effective area of the EPIC-pn. Assuming that the energy of the coronal electrons ranges anywhere from 50 – 100 keV, our measured soft-hard time lag of ~ 226 s suggests that the corona occupies a region around the disk $1.91 - 3.34 \times 10^{12}$ cm in size. This is derived assuming the size of the corona is given by

$$r \approx tc \frac{\log \left(1 + \frac{4k_B T}{m_e c^2} \right)}{\log \frac{E}{E_0}} \quad (2.4)$$

We will assume that the central BH in NGC 4593 has a mass of $8.1 \times 10^6 M_\odot$ based on

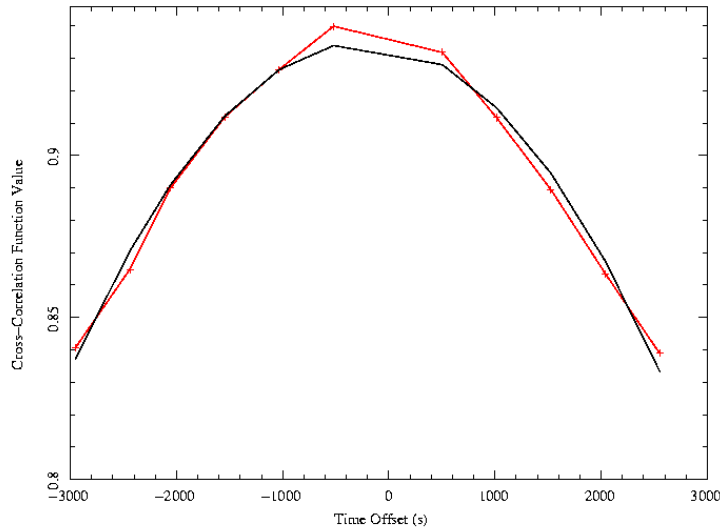


Figure 2.11: The cross-correlation function for the soft-to-hard energy bands in NGC 4593 in red (with data points), plotted with the best fit curve in solid black. The vertical line represents a zero time delay between the two bands; the off-centeredness of the curve peak indicates that the hard band lags the soft band by 226 ± 53 s at 90% confidence.

reverberation mapping (Gebhardt et al. 2000; Nelson & Whittle 1995). Using this mass for the NGC 4593 BH, the characteristic length scale of the corona would be in the range of $1.6 - 2.8 r_g$.

The hardness ratio for the source also varied with respect to both time and energy flux (soft band flux was used since it had the highest photon count): see Fig. 2.12 for details. Note the downward trend of the hardness ratio in both the time and energy graphs. It looks as if the ratio fluctuates almost periodically in time, tracking the variations in the light curve. Over the course of the observation the hardness ratios decrease by a factor of ~ 1.28 .

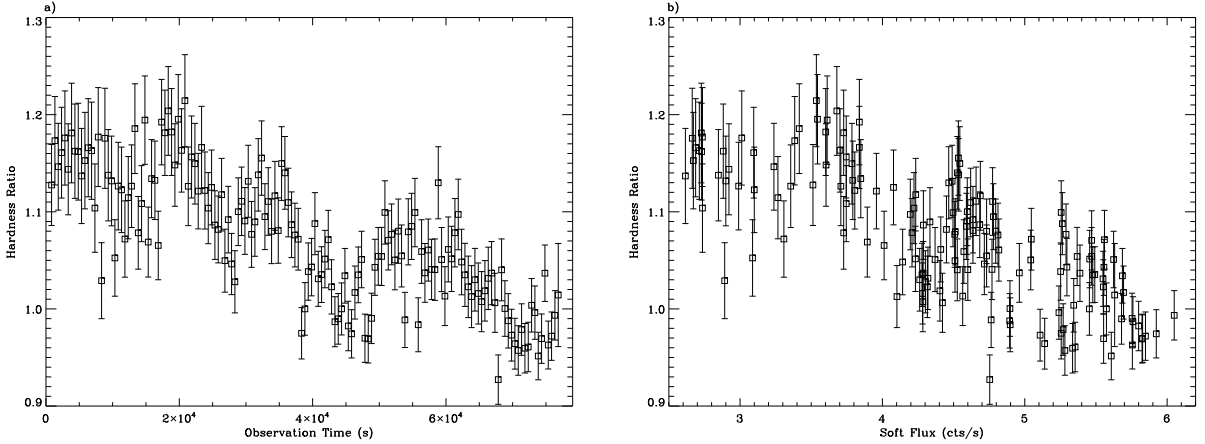


Figure 2.12: a) The hardness ratio of the source vs. observation time. The ratio is determined by taking the ratio of the counts in the hard band to the counts in the soft band. b) The hardness ratio of the source vs. energy flux. Ratios were computed in the same way as above.

2.4 Discussion and Conclusions

2.4.1 Summary of Results

We have obtained a 76 ks *XMM-Newton* observation of the Sy-1 galaxy NGC 4593. An examination of the best-fitting EPIC-pn spectrum shows that the continuum is well modeled by a photoabsorbed power-law with $N_{\text{H}} = 1.97 \times 10^{20} \text{ cm}^{-2}$, $\Gamma = 1.75$, and a flux of $4.44 \times 10^{-13} \text{ erg cm}^{-2} \text{ s}^{-1}$. The best fit to the hard spectrum can be achieved by including two Gaussian emission lines representing cold and ionized fluorescent iron at 6.4 and 6.97 keV, respectively.

We see clear evidence for a complex warm absorber in the EPIC-pn spectrum. Fitting a grid of photoionization models computed using the XSTAR code, we infer a warm absorber with two physically and kinematically distinct zones: one with a column density of $N_{\text{H}} = 9.29 \times 10^{22} \text{ cm}^{-2}$ and an ionization parameter of $\log \xi = 2.75$, the other with $N_{\text{H}} = 1.13 \times 10^{22} \text{ cm}^{-2}$ and $\log \xi = 1.70$, which is likely more distant from the central engine. We robustly detect the L_3 edge of neutral iron presumed to exist in the

form of dust grains along the line-of-sight to the central engine, as cited by McKernan et al. (McKernan et al. 2003). The iron associated with this edge has a column density of $N_{\text{Fe}} = 8.32 \times 10^{16} \text{ cm}^{-2}$.

A soft excess below $\sim 2 \text{ keV}$ is also seen in the data, and can be accounted for either phenomenologically by a redshifted bremsstrahlung component (Model 1) or, more effectively and physically, a component of Comptonized emission from an accretion disk of seed photons upscattered by a plasma of relativistic electrons existing in either a corona or the base of a jet near the disk in some geometry (Model 2). The latter scenario yields the best statistical fit to the data, with a seed photon temperature of $T_0 = 50 \text{ eV}$, an electron temperature of $kT = 42 \text{ keV}$, a plasma optical depth of $\tau_p = 0.12$ and a flux of $6.46 \times 10^{-14} \text{ erg cm}^{-2} \text{ s}^{-1}$.

We do not detect any X-ray reflection features from a relativistic accretion disk (Reynolds et al. 2004a). However, we show that, even if a radiatively efficient geometrically thin disk exists, its X-ray reflection signatures would be buried in the noise if the disk has either a very centrally concentrated irradiation profile or an appropriately ionized surface. Either of these models can be tested by longer EPIC observations which would be sensitive to the subtle features displayed by a highly blurred or ionized reflection spectrum. If longer observations still fail to detect any accretion disk signatures, we are forced to consider other possibilities. The inner disk may be very hot and optically thin, thereby being incapable of producing any X-ray reflection features. Alternatively, the observed X-ray continuum might be highly anisotropic and beamed away from the disk, thereby rendering any reflection features undetectable.

In terms of variability, the cold line Gaussian had a time-averaged equivalent width of $EW = 131 \text{ eV}$, while the ionized component had an $EW = 45 \text{ eV}$. Although the continuum varied with time over the course of our observation, the flux of the cold Fe-K α showed marginal evidence for variability between successive 10 ks intervals. The equiva-

lent width of this line, on the other hand, is shown to vary significantly. The simplest interpretation of this result is to suppose that the cold line originates from a region with a light-crossing time larger than the length of our observation. For a BH mass of $8.1 \times 10^6 M_\odot$ this places the cold line emitting region beyond about $2000 r_g$ from the BH, i.e., in the outer accretion disk or the putative molecular torus of Seyfert unification schemes. Our statistics on the ionized Fe-K line are insufficient to constrain its variability properties — these data are consistent with both constant flux and constant equivalent width.

We have detected a 226 s time-lag between the hard and soft EPIC-pn bands, with the hard band lagging the soft. In a simple model in which this corresponds to scattering times within a Comptonizing corona, we conclude that the corona can only possess a size of $\sim 1.6 - 2.8 r_g$.

2.4.2 Comparison with Previous Work

Previous studies of NGC 4593 with *EXOSAT* demonstrated a soft excess below 2 keV, and *ASCA* spectra display a slightly broadened cold iron line at ~ 6.4 keV. *BeppoSAX* data confirm a broad absorption dip of 15% below 1 keV which may be attributable to the presence of a warm absorber, characterized by an optical depth of $\tau = 0.32$ for the O VII edge, and $\tau < 0.22$ for the O VIII edge (Kaastra & Steenbrugge 2001). Reynolds quotes *ASCA* values for these edges of $\tau = 0.26$ and 0.09, respectively (Reynolds 1997).

McKernan et al. calculated a 2 – 10 keV *Chandra* luminosity of $L_X = 6.10 \times 10^{42} \text{ erg s}^{-1}$ for $H_0 = 70 \text{ km s}^{-1} \text{ Mpc}^{-1}$ and $q_0 = 0$, versus $L_X = 8.53 \times 10^{42} \text{ erg s}^{-1}$ as determined by Reynolds with *ASCA*. The latest *Chandra* data from McKernan et al. states that the 0.5 – 5 keV spectrum is well modeled by a single-zone warm absorber with broken power-law of hard index $\Gamma = 1.79$, soft index $\Gamma = 2.27$ and a break energy of $E = 1.07$ keV. The soft spectrum is complicated by the presence of absorption edges of O VII, O VIII and Fe-L₃ below ~ 2 keV, as well as some weaker emission features.

Our observed 2 – 10 keV luminosity is $L_X = 7.40 \times 10^{42} \text{ erg s}^{-1}$ ($H_0 = 70$, $q_0 = 0$, $\Lambda = 0.7$), which is roughly 21% above that observed with *Chandra* by McKernan et al. , or 13% below that recorded with *ASCA* by Reynolds.

The optical depth of our O VII edge is $\tau = 0.15$, 57% of the value obtained by Reynolds and 46% of that calculated by Kaastra & Steenbrugge, but matching that found by McKernan et al. within errors. The O VIII edge is not wanted statistically by the fit, in contrast to the McKernan et al. observation ($\tau = 0.14$) and the Reynolds data, and the 2001 Kaastra observation. Our best-fit value for the galactic absorption is $N_H = 1.97 \times 10^{20} \text{ cm}^{-2}$, closely resembling that used by McKernan in the hard band *Chandra* data. McKernan’s value for the column density of the soft emission from the warm absorber was significantly lower than our own two-zone model: $N_H = 5.37 \times 10^{21} \text{ cm}^{-2}$ versus our $9.29 \times 10^{22} \text{ cm}^{-2}$ and $1.13 \times 10^{22} \text{ cm}^{-2}$. It should be noted, however, that the authors based this value on the RGS data rather than the EPIC-pn.

2.4.3 Implications for the X-ray Emission Region

The narrowness of the fluorescent iron line together with the lack of response of this line to changes in the hard X-ray continuum suggest an absence of a cold, optically thick matter within the central $\sim 10^3 r_g$ of the accretion disk. The standard framework for accommodating such a result is to postulate that the inner regions ($r \leq 10^3 r_g$) of the accretion flow have entered into a radiatively inefficient mode which is extremely hot (electron temperatures of $T \sim 10^{10} \text{ K}$), optically thin, and geometrically thick (Narayan & Yi 1994; Rees 1982). Within this framework, the hard X-ray source is identified as thermal bremsstrahlung or Comptonization in origin. However, the variability of the X-ray continuum is inconsistent with X-ray emission from a structure which is $\sim 1000 r_g$ in extent. The rapid continuum variability and the short time lag between the hard and soft X-ray photons dictate that, at any given time, the X-ray emission region is only $\sim 1 - 3 r_g$

in extent.

We are therefore led to consider alternative geometries and/or origins for the X-ray source. We consider three possibilities. Firstly, the inner accretion flow may indeed be in the form of a radiatively inefficient flow, but the observed X-ray emission may come from the compact base of a relativistic jet powered by BH spin. Secondly, the X-ray emission may indeed originate from the body of the radiatively inefficient flow but, at any given instant in time, be dominated by very compact emission regions within the flow. Such emission regions may arise naturally from the turbulent flow or, instead, may be related to a magnetic interaction between the inner parts of the flow and the central spinning BH (Wilms et al. 2001; Ye et al. 2007). In this case the iron line could still plausibly originate at a distance of thousands of r_g and thus be quite narrow. Finally, it is possible that the accretion disk is radiatively *efficient* (and hence optically thick and geometrically thin) close to the BH and supports a compact accretion disk corona. Of course, an immediate objection to this scenario is the lack of a broadened iron line. However, as demonstrated in Reynolds et al. (2004b) and discussed in §2.2.2, it is possible the iron line is so broad that it is buried in the noise of the continuum. Alternatively, the accretion disk surface may have an ionization state such that iron line photons are effectively trapped by resonant scattering and destroyed by the Auger effect. Longer observations with better spectral and timing resolution will be necessary in order to confirm our results and differentiate between these different possible scenarios.

2.4.4 Conclusions

We have shown that the Sy-1 galaxy NGC 4593 has a continuum spectrum that is fit remarkably well by a simple photoabsorbed power-law above ~ 2 keV. Below this energy, we see evidence for spectral complexity that can be attributed to the presence of a possible multi-zone layer of absorbing material intrinsic to the source, as well as a soft excess that

cannot be explained by a reflection model from an ionized disk. Also arguing against a disk-reflection-dominated source is that unlike other sources of its kind (e.g., MCG–6-30-15), NGC 4593 has relatively narrow cold and ionized Fe-K α line features at 6.4 and 6.97 keV, respectively. We can say that the cold line is most likely formed quite far out in the accretion disk based on its narrowness and lack of significant variability over the 76 ks duration of our observation. We find no evidence for reflection features from the inner accretion disk (e.g., a “broad iron line”) in the spectrum.

Based on the time lag between the soft and hard spectral bands, we estimate that the corona occupies a region around the central source on the order of $\sim 1.6 - 2.8 r_g$, assuming that NGC 4593 harbors a $8.1 \times 10^6 M_\odot$ BH at its core and that the energies of the electrons in the corona range from $\sim 50 - 100$ keV. This estimate for the coronal size is reinforced by our measurements of continuum variability on timescales as small as ~ 200 s, equivalent to a light travel time of $\sim 4 r_g$ for the BH mass in question.

Taken together, the implications of a narrow iron line emitted far out in the disk or torus and the small coronal size in NGC 4593 present an atypical picture of an AGN. We postulate that the primary X-ray source is associated with the compact base of a jet or compact emission regions within a much larger optically thin accretion flow. Alternatively, the accretion disk may be radiatively-efficient with a compact corona but not display a broad iron line due to the effects of extreme broadening or disk ionization.

Chapter 3

A New Relativistic Line Emission Code

As discussed in Chapter 1, we now have access to X-ray spectral data of sufficient quality that we are motivated to construct an iron line model that allows the spin of a BH to be a free parameter in the fit. Emission lines from an accretion disk around a BH vary greatly from their standard Voigt profiles seen in an Earth-bound laboratory: they are strongly influenced by the effects of extreme Doppler shifting as well as those of Special and General Relativity. As such, a fully relativistic computational treatment of these effects is necessary in order to accurately parameterize the line shapes and extract meaningful constraints on those parameters in question, such as BH spin.

3.1 The `kerrdisk` Model

As mentioned in §1.4, other groups have recently been developing similar models for the purpose of fitting for BH spin as well. These models ([Beckwith & Done 2004](#); [Čadež & Calvani 2005](#); [Dovčiak et al. 2004](#)) all produce consistent results with each other and with our new model, `kerrdisk`, in terms of the line profiles produced for a given set of input parameters. However, `kerrdisk` has the added advantage of portability. In practice, the XSPEC modules that implement both the `ky` and Beckwith & Done models use relativistic

transfer functions stored in very large (multi-gigabyte) pre-calculated tables. By contrast, `kerrdisk` uses much smaller pre-calculated tables of transfer function values and linearly interpolates between them. This technique enables accurate line profile calculations while also saving the user disk space and computing power. A more detailed comparison between `kerrdisk` and these other available models will be made in §3.2.

Using their respective models, both the Dovčiak and Beckwith groups conclude that fitting broad iron lines cannot truly constrain the spin of the BH. We argue that this is not the case. Since their models allow emission from *any* radius of the accretion disk outside of the event horizon, the aforementioned groups can produce iron line profiles with arbitrarily redshifted wings even if the underlying BH spacetime has no spin. One must consider the physicality of this assumption, however: it is not possible to get line emission from radii deep within the plunging region for several reasons. Firstly, the closer one gets to the event horizon, the smaller the geometrical area of the disk available for emission becomes, while the gravitational redshift affecting any emission from such regions increases correspondingly. Both of these effects would tend to minimize the contribution to the line profile from most of the emission inside the radius of marginal stability. Further, the ionization of the disk material within $\sim 4r_g$ of a Schwarzschild BH is inevitably too high to produce significant line emission in the first place, and the optical depth of this material also decreases rapidly within the radius of marginal stability (Reynolds & Begelman 1997; Young et al. 1998). For all of these reasons, one simply cannot produce significant line emission from any arbitrary radius outside the event horizon. This must be taken into account when modeling such line emission.

Our new relativistic emission line code, `kerrdisk`, is written in FORTRAN77 so that it can be easily meshed with XSPEC, and has now been compiled successfully on Solaris, Linux and Apple-MAC platforms. The dimensionless spin parameter of the BH (a) can take on any value in the range $-1 \leq a \leq 1$, where negative values of a correspond to a BH

that is rotating in a retrograde sense relative to the accretion disk. Although, according to the equations of GR, a could have any arbitrary value, the cosmic censorship hypothesis states that naked singularities cannot exist in the universe, so a BH must be shrouded by an event horizon. This limits the acceptable range of spin parameters to $-1 \leq a \leq 1$. For simplicity we consider only prograde spins up to the theoretical spin-equilibrium limit, i.e., $0 \leq a \leq 0.998$.

The limiting value of $a = 0.998$ for BH spins was first discussed by Kip Thorne (Thorne 1974). Therein, the author contends that if BHs were simply accreting matter, their spins would ascend to $a \approx 1$ rather quickly, but because material in the accretion disk radiates, and some of that emitted radiation is swallowed by the hole, a counteracting torque is produced. The origin of this counteracting torque lies in the photon capture cross-section of the hole: BHs have a higher capture cross-section for photons of negative angular momentum (opposite to that of the hole itself) than for photons of positive angular momentum. Thus, the accretion of emitted radiation from the disk results in an overall reduction in the angular momentum of the hole until it reaches a theoretical equilibrium value of $a = 0.998$. Recent work on magnetohydrodynamic (MHD) accretion disks suggest that the continued transport of angular momentum from matter within the radius of marginal stability, as well as angular momentum lost from the rotating BH itself via Blandford-Zjanek-like mechanisms (Blandford & Znajek 1977), may lead to a rather lower equilibrium spin (e.g., see recent GR MHD simulations (Krolik et al. 2005)). Equilibrium spins as low as $a \sim 0.90$ are within the realm of possibility.

Following the method of Cunningham, we compute the line profile by employing a relativistic transfer function (Cunningham 1975). For a given BH spin a and disk inclination i , the observed accretion disk spectrum can be written as

$$F_{\text{obs}}(E_o) \propto \int \frac{g^2}{\sqrt{g^*(1-g^*)}} I(E_o/g, \theta_e, r_e) \psi(r_e, g^*; a, i) dg^* r_e dr_e. \quad (3.1)$$

Here, $I(E, \theta_e, r_e)$ is the rest-frame specific intensity of the disk at radius r_e and energy E emitted at an angle θ_e to the disk normal, ψ is the Cunningham transfer function which accounts for the effects of light-bending on the observed solid angle from each part of the disk, g is the ratio of the observed to the emitted photon energy ($g = E_o/E_{em}$), and g^* is the relative value of g with respect to the redshift extremes obtained from the disk annulus in question,

$$g^* = \frac{g - g_{\min}(r_e)}{g_{\max}(r_e) - g_{\min}(r_e)}. \quad (3.2)$$

This formulation is attractive from the computational point of view; light bending effects are isolated from relativistic beaming effects and encoded in the transfer function $\psi(r_e, g^*; a, i)$ which is a slowly varying function of its variables. This allows us to perform full computations of the transfer function at a relatively sparse set of points in parameter space, and then use linear interpolation to accurately determine the transfer function at a general point.

Specializing to the case of a δ -function emission line allows us to eliminate the g^* integration from Eqn. (3.1). Assuming that the surface emissivity of the emission line is a function of emission radius r_e and angle θ_e is $f(r_e, \theta_e)$, this gives

$$F_{obs}(E_o) \propto \int_{r_{\min}}^{r_{\max}} \frac{g^3}{\sqrt{g^*(1-g^*)}} \frac{1}{g_{\max} - g_{\min}} \psi(r_e, g^*; a, i) f(r_e, \theta_e) r_e dr_e. \quad (3.3)$$

We use the algorithms of Speith to compute the transfer function $\psi(r_e, g^*; a, i)$ as well as $g_{\min}(r_e)$ and $g_{\max}(r_e)$, thereby allowing us to perform this integration (Speith et al. 1995). Following laor, we assume a limb-darkening law of $I \propto 1 + 2.06(\cos \theta_e)$ (Laor 1991), though this is trivial to change in the driver code. For a given spin a and inclination i , high quality line profiles (including all those presented herein) are produced using a transfer function computed at 50 radial bins, equally spaced in the variable $1/\sqrt{r_e}$, and 20 linearly spaced relative redshift bins (g^*) across the line profile at any given radius.

These values were determined via extensive trial and error to make the best, smoothest possible line profile while keeping computation time to a reasonable length. Increasing either the number of radial or relative redshift bins did not significantly improve the integrity of the line profiles produced. Also, because the transfer function varies quite slowly with radius, relative redshift, a and i , greater frequency of sampling was not warranted.

Our choice for the radial spacing corresponds to equal spacing of non-relativistic Keplerian velocities. We then evaluate the line profile integral (Eqn. (3.3)) with a densely spaced logarithmic grid in r_e , using linear interpolation in r_e of the (rather sparsely sampled but slowly varying) transfer function. In practice, we use $5n_e$ -zones per decade of r_e where n_e is the number of frequency elements in the output line profile (specified by the response matrix of the data being fit). Experimentation shows that this produces high quality line profiles even at very high resolution (i.e., large n_e).

The Cunningham transfer function $\psi(r_e, g^*; a, i)$ is computed for a 20×20 grid in (a, i) -space and is stored in a 40 MB table that is accessed by the driver script for `kerrdisk`. The grid of spins is spaced in a weighted fashion by the square root of the gridpoint such that more sampling takes place as the spin parameter increases. The grid of inclination angles is spaced linearly in terms of $\cos i$. Again, due to the slowly varying nature of the transfer function, simple linear interpolation to arbitrary spins and inclination angles produces accurate and high quality line profiles.

To parameterize the emissivity function of the accretion disk, we follow Fabian et al. (Fabian et al. 2002) and assume a line emissivity characterized by a broken power-law

between some inner radius r_{\min} and outer radius r_{\max} , i.e.,

$$f(r_e) = \begin{cases} 0 & r_e < r_{\min} \\ (r_e/r_{\text{br}})^{-\alpha_1} & r_{\min} \leq r_e < r_{\text{br}} \\ (r_e/r_{\text{br}})^{-\alpha_2} & r_{\text{br}} \leq r_e < r_{\max} \\ 0 & r_e \geq r_{\max} \end{cases} \quad (3.4)$$

That is, the accretion disk is expected to behave qualitatively as a Page-Thorne (Page & Thorne 1974) disk and radiate more copiously at smaller radii (i.e., deeper within the gravitational well where more potential energy is being liberated). In reality, we would expect the disk to exhibit a continuous range of emissivity indices (α 's), but for computational simplicity we arbitrarily split the disk into an outer and inner portion, each with their corresponding emissivity index that can be fit to the data.

We note that, at present, the publicly available Speith algorithms on which this work is based do not support the proper computation of emission from within the radius of marginal stability, i.e., we are restricted to $r_{\min} \geq r_{\text{ms}}$. Hence, all `kerrdisk` line profiles currently assume that the emission profile is truncated within $r = r_{\text{ms}}$. As discussed in §1.4, truncating the emission in this way will not significantly affect the resulting line profile due to the high ionization and low optical depth of material within the plunge region.

The code takes ~ 4 s to produce a single line profile on a 2 GHz processor linux machine. When the model is used to fit data within XSPEC, several hundreds or thousands of iterations of the code are often needed to get a good fit, resulting in run times that can be on the order of an hour or more. In principle, this run time can be significantly reduced by employing a parallelization scheme when fitting. Such a parallelization scheme is possible to implement in the ISIS spectral analysis package (Houck 2002) using the PVM module (Michael Nowak and Andrew Young, private communication).

The best way to examine the results of the code’s line profile simulations is to look at how the morphology of the line changes with alterations made in certain important parameters. For illustrative purposes, Fig. 3.1 shows model line profiles with a rest-frame energy of $E = 1$ keV. The line profiles shown in this figure have the same parameter settings as those shown in the review by Reynolds & Nowak (Reynolds & Nowak 2003) to enable easy comparison. The Reynolds & Nowak profiles are also based on the Speith algorithms but sample the transfer function more sparsely and employ a cruder integration technique to evaluate the line profile. The fact that our line profiles agree with, but are much less noisy than the Reynolds & Nowak profiles validates our newer integration/interpolation technique.

3.2 Comparison With Other Disk Line Models

Verification of our new line profile code can be demonstrated through detailed comparisons with existing public models, such as `laor` and `diskline` — where $a = 0.998$ and 0.0 , respectively — as well as those of the newer models we have mentioned (Beckwith & Done 2004; Čadež & Calvani 2005; Dovčiak et al. 2004). Since the `kyrline` model of Dovčiak has already been compared with the `kdline` model of Beckwith & Done and that of Čadež & Calvani, we need only to compare `kerrdisk` with `kyrline`. These comparisons are shown in Figs. 3.2-3.3 and discussed in this Section.

Given the lack of relativistic light bending in the `diskline` model, we expect our fully relativistic `kerrdisk` line profiles with $a = 0$ to differ slightly from those computed with `diskline`, especially at large inclination angles. We indeed see slight differences (Fig. 3.2). We should stress, however, that the differences are minor and that `diskline` should still be considered a perfectly acceptable model for disks around Schwarzschild BHs for all but the highest signal-to-noise data. Examining the comparison of the `laor`

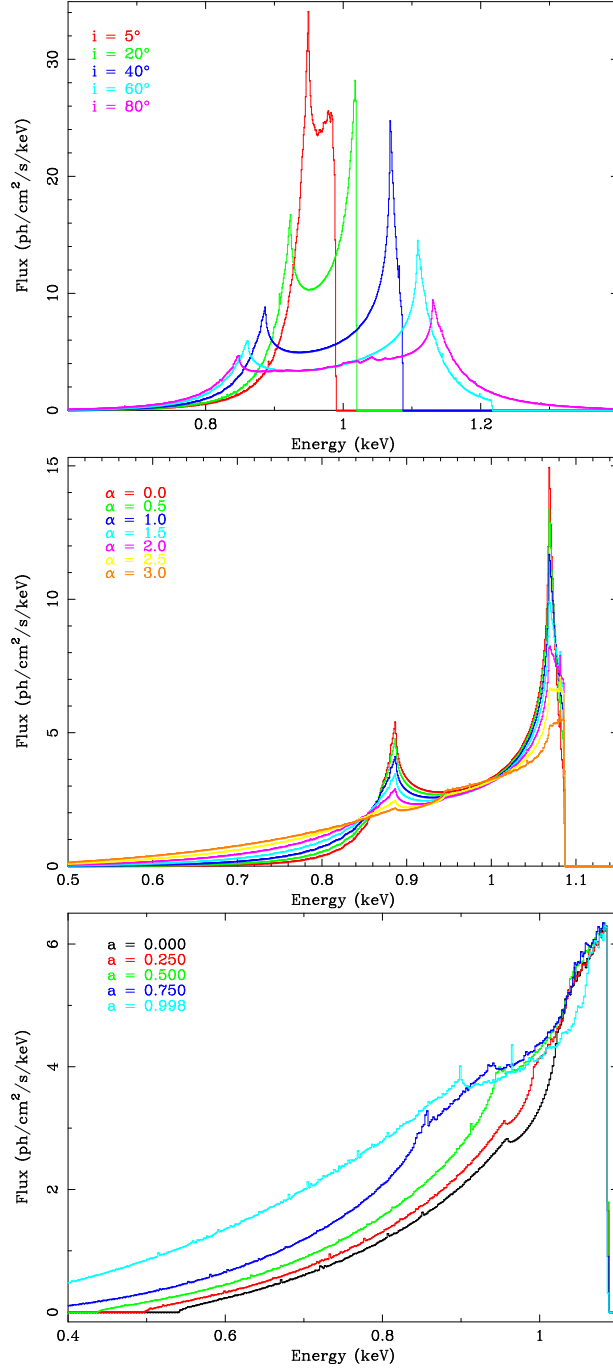


Figure 3.1: Variation of the kerrdisk line profile with (a) disk inclination angle, (b) disk emissivity index, and (c) BH spin parameter. In each case the range of emission in the disk is from $r = r_{\text{ms}} - 50 r_g$. In (a), $a = 0.998$, $\alpha = 0.5$. In (b), $a = 0.5$, $i = 40$. In (c), $i = 40$, $\alpha = 3$, and the lines are normalized the the same flux the illustrate the effects of gravitational redshift on the line profile with an increase in spin.

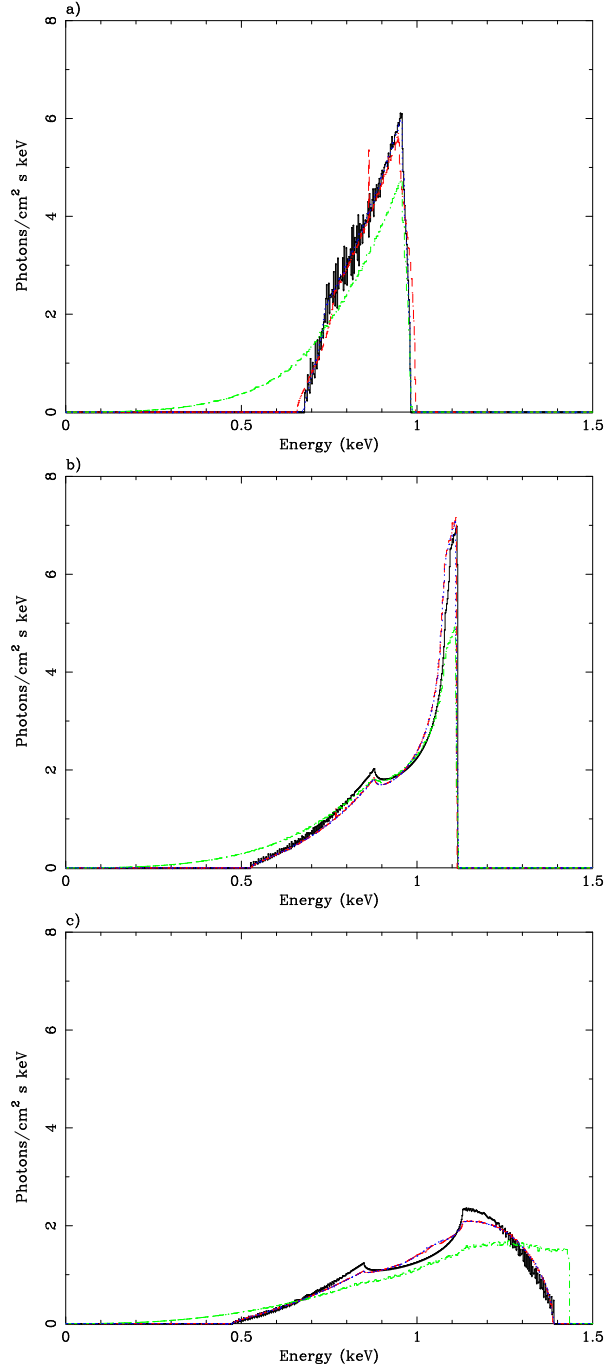


Figure 3.2: Various iron line models for a Schwarzschild BH. The inclination angles represented are 5° for (a), 45° for (b), and 80° for (c). Here $\alpha_1 = \alpha_2 = 3.0$, and r_{\min} and r_{\max} are held constant at $6r_g$ and $50r_g$, respectively. The diskline profile is in solid black, the kerrdisk profile is in dashed red, the kyrline profile including emission from within the ISCO is in dash-dotted green and the kyrline profile not including ISCO radiation is in dotted blue.

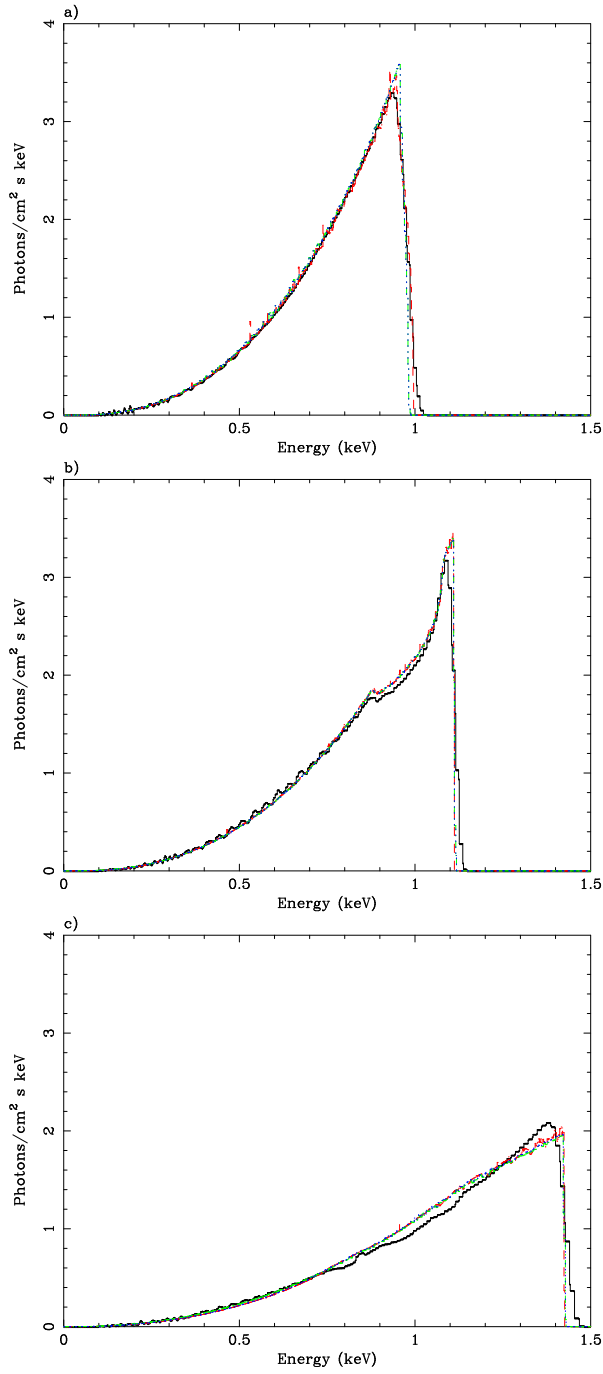


Figure 3.3: Various iron line models for a maximally spinning Kerr black hole. The inclination angles vary as above for the Schwarzschild case in (a)-(c). Other parameters are the same as those used in the Schwarzschild case, but now $r_{\min} = 1.235 r_g$, corresponding to the radius of marginal stability for a maximal Kerr BH, rather than the $6 r_g$ Schwarzschild r_{ms} . The 1aor profile is in solid black and the rest of the color scheme is the same as that used in Fig. 3.2 above.

models with the $a = 0.998$ `kerrdisk` model, we note good agreement (Fig. 3.3). The slight differences that do exist are caused by an artificial smoothing of the `laor` line due to interpolation of a sparsely sampled transfer function. Again, however, we note that the `laor` model is perfectly acceptable model for disks around $a = 0.998$ BHs for all but the highest signal-to-noise data.

The real power of this new generation of line profile models is the freedom in the spin parameter of the BH. Therefore, the real verification of our code lies in a detailed comparison of `kerrdisk` and `kyrline`. Indeed, as shown in Figs. 3.2-3.3, the line profiles for `kerrdisk` and `kyrline` are virtually indistinguishable when one does not include radiation from within the radius of marginal stability in `kyrline`. Also shown in these figures are the effects of including emission from within the radius of marginal stability (down to the horizon, for the sake of illustration), as computed by Dovčiak et al. This has the greatest effect on the line profiles from the slowly spinning holes since it is only in these systems that an appreciable fraction of the plunging region is subject to modest gravitational redshift (as opposed to the extremely large redshift experienced by the material in the plunging region of a Kerr BH; in this case the BH spin has pulled r_{ms} down quite close to the event horizon and much deeper within the gravitational potential well). We intend to extend our model to include the region within the radius of marginal stability in future work, carefully considering the effects of both the level of ionization and the optical depth of the material within the plunging region, in particular, as discussed in Chapter 1. Both of these effects can have a substantial impact on the contribution of emission from this region to the overall line profile.

3.2.1 The Convolution Model `kerrconv`

As mentioned in §1.3.2, the irradiation of the accretion disk by the primary X-ray source results in a whole X-ray reflection spectrum consisting of Compton and radiative recombination continua plus numerous fluorescent and radiative recombination lines. The Fe- $K\alpha$ line is the most prominent due to its high rest-frame energy and its intrinsic strength, but many other species are also excited (e.g., oxygen, nitrogen, silicon and sulfur). The whole X-ray reflection spectrum from the disk will be subject to the same extreme Doppler and relativistic processes that combine to alter the morphology of the iron line. The most physically realistic simulation of the reflected spectrum from a photoionized disk surface has been presented by Ross & Fabian. These high-quality models capture the “traditional” X-ray reflection processes (Compton scattering, photoelectric absorption and fluorescent line emission) as well as the powerful soft X-ray radiative-recombination line emission expected from an X-ray irradiated photoionized surface of an optically thick accretion disk (Ross & Fabian 2005). These authors have provided their results in the form of tabulated spectra that can be used in XSPEC. We then wish to apply the Doppler and relativistic effects discussed to the reflected spectrum by convolving it in velocity space with a relativistic smearing kernel such as the one used to generate the `kerrdisk` line profile. To facilitate this, we have also produced a convolution form of our line profile model, `kerrconv`, whose results mirror those of the `kyconv` model designed by Dovčiak et al. and the `kdconv` model of Beckwith & Done, provided that no radiation from within the ISCO is included in the latter two models, as was the case for the comparison of `kerrdisk` with `kyline` and `kdline` in §3.2 above. As with `kerrdisk`, the `kerrconv` parameters include emissivity indices for the inner and outer disk separated by a break radius, inner and outer radii for the disk emission, the spin parameter of the BH, and the inclination angle of the disk with respect to our line of sight. The `kerrconv` model is

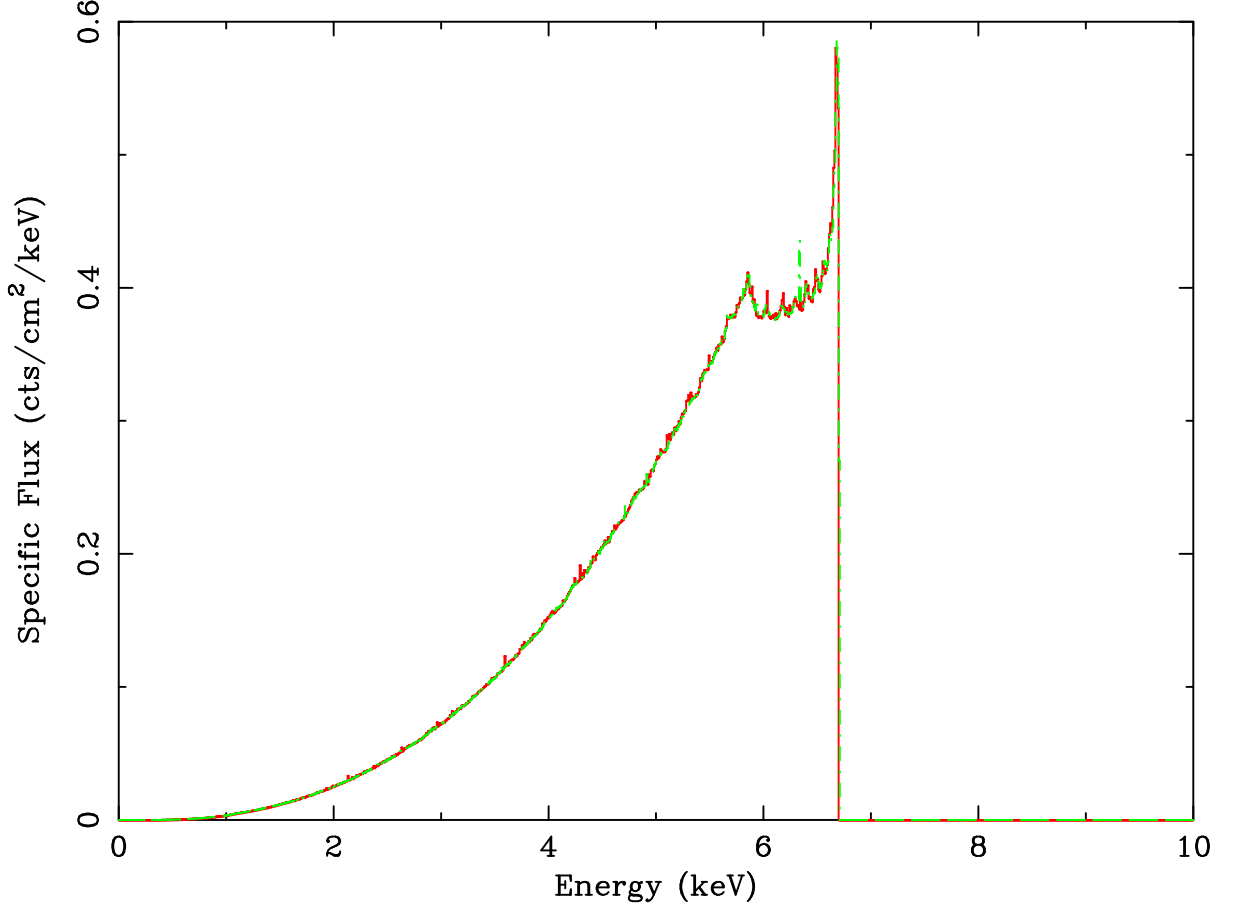


Figure 3.4: A simulated Fe-K α line at 6.4 keV. The `kerrdisk` results are shown in solid red, the `kerrconv(gauss)` results in dashed green. Both lines are given the same set of input parameters: $\alpha_1 = \alpha_2 = 3$, $a = 0.998$, $i = 30^\circ$, $r_{\min} = r_{\text{ms}}$, $r_{\max} = 50 r_{\text{ms}}$. The fact that `kerrconv` reproduces the `kerrdisk` results verifies its accuracy.

readily validated by applying it to a narrow Gaussian emission line and comparing the resulting spectrum with the regular `kerrdisk` model, as in Fig. 3.4.

The `kerrconv` model applies relativistic smearing to the entire reflected accretion disk spectrum, and as such is quite computationally expensive when used in a fit to real data of high quality (i.e., high count number). It is therefore advisable to use this model as a final step in a rigorous spectral analysis such as that performed on MCG–6-30-15 (Chapter 4) or any of the other Sy-1 AGN discussed in Chapter 5. For sources with broad iron lines such as the ones analyzed herein, a reliable technique that can speed the fitting process is to first attempt to fit the spectrum with one of the unsmeared ionized disk reflection

models. Initially freezing the iron abundance at the solar value ($\text{Fe}/\text{solar} = 1$) and the ionization level at neutral ($\xi = 30$) can also help constrain the relevant parameter space. These variables can be freed at a later time. If it is clear that a broader iron feature is present — one that is not accounted for by the model — then applying a `kdblur` smearing kernel is a logical next step. This convolution model is similar to `kerrconv`, but employs a `laor` kernel ($a = 0.998$) rather than a `kerrdisk` kernel (arbitrary spin). Because `laor` is a pretabulated model, this fit to the data will be quite a bit faster than `kerrconv` and will allow some further preliminary constraints to be placed on the disk emissivity profile, disk inclination, and reflection parameters. Finally, once a good fit has been achieved with `kdblur`, one can substitute in `kerrconv` using the `kdblur` best-fit parameters as a starting point. This will cut down fitting time considerably and also produce a more reliable fit by gradually narrowing down the relevant regions of parameter space in the model. This step-wise modeling technique is detailed in Chapter 5.

Chapter 4

MCG–6-30-15: The Broadest Iron Line Found to Date

As mentioned in Chapter 3, the Seyfert-1 galaxy MCG–6-30-15 is considered the benchmark in broad iron line AGN studies, possessing the broadest Fe-K α feature yet observed. The extreme width of the line is almost certainly an indication of relativistic origin in the inner accretion disk of this source, making it an ideal candidate on which to test our new `kerrdisk` model. Because MCG–6-30-15 has also been so extensively studied, in large part because of its extreme Fe-K feature, we are fortunate to have more photons to work with than in any other broad iron line AGN (350 ks with *XMM-Newton*; ([Fabian et al. 2002](#))). This allows us to place viable statistical constraints on the angular momentum of the BH in this source.

4.1 A Brief History of Broad Iron Line Studies in MCG–6-30-15

MCG–6-30-15 is an S0-type galaxy in the constellation of Centaurus that hosts a Sy-1.2 nucleus. It has a measured redshift of $z = 0.008$, placing it at a distance of $d \approx 37$ Mpc using WMAP cosmological parameters. X-ray studies of this AGN have revealed a powerful central source along with a significantly broadened Fe-K α feature. As mentioned above, this broad line has led MCG–6-30-15 to become one of the most studied AGN in the X-ray band due to its potential as a probe of BH and accretion disk physics. Although the mass of the hole is not yet well constrained, estimates based on X-ray studies have placed it in the range of $10^6 - 2 \times 10^7 M_{\odot}$ (Nowak & Chiang 2000; Reynolds 2000). McHardy et al. have further narrowed this mass range to $3 - 6 \times 10^6 M_{\odot}$ using a variety of methods such as the M- σ relation, line widths from optical spectra, BLR photoionization arguments and X-ray variability (McHardy et al. 2005).

Reflection signatures from neutral material had been observed with *EXOSAT* (Nandra et al. 1989) and *Ginga* (Matsuoka et al. 1990; Nandra et al. 1990), but it was not until deep observations of MCG–6-30-15 by *ASCA* that the broadened and skewed iron line was robustly detected (Tanaka et al. 1995). It was determined that the line profile matched that expected due to X-ray reflection from the surface of a relativistic accretion disk; the robustness of this interpretation was demonstrated by Fabian et al. (Fabian et al. 1995). Broad-band *BeppoSAX* data (Guainazzi et al. 1999) confirmed the Tanaka et al. detection of a broadened and redshifted iron line with an equivalent width of $EW \approx 200$ eV.

A detailed re-analysis of this observation (Iwasawa et al. 1996) identified a period of time when the source entered the so-called “deep minimum” state, marked by low continuum emission. While in this state, the iron line width (and especially the extent of the red wing of the line) markedly increased to the point that emission from a disk around

a Schwarzschild BH truncated at the radius of marginal stability ($r_{\text{ms}} = 6r_{\text{g}}$) could no longer reproduce the observed line profile. Noting that the radius of marginal stability moves inwards (to a location characterized by higher gravitational redshift) as the BH spin is increased, it was subsequently argued that the BH in MCG–6-30-15 must be rapidly rotating. Fitting sequences of Novikov-Thorne (Novikov & Thorne 1974; Thorne 1974) models to the deep minimum *ASCA* data (and assuming that the X-ray irradiation tracks the local dissipation in the underlying disk), Dabrowski et al. derived a lower limit of $a > 0.94$ on the rotation of the BH (Dabrowski et al. 1997). At this point, however, Reynolds & Begelman noted that physically plausible scenarios could result in sufficient X-ray reprocessing (including ionized iron line emission) from within the radius of marginal stability to fit the *ASCA* deep minimum state with even a Schwarzschild BH (Reynolds & Begelman 1997). In order to illuminate the region of the disk within r_{ms} , the authors hypothesized an X-ray source on the symmetry axis some height above the disk, and suggested that iron line profile changes (and some part of the X-ray continuum flux changes) could be attributed simply to changes in the height of this X-ray source.

After the discovery of its broad iron line feature, MCG–6-30-15 became the subject of many more observations. With the first observations of *XMM-Newton* in 2000, astronomers had a new tool with unparalleled throughput with which to examine this source in finer detail. The first *XMM-Newton* observation of MCG–6-30-15 was fortunate enough to catch the source in its “deep minimum” state characterized by low continuum flux and a broader than normal Fe-K α profile. The resulting high signal-to-noise spectrum revealed an extremely extended red wing to the line profile extending down to 3 – 4 keV (Wilms et al. 2001). Because so much emission seemed to be coming from radii deep within the gravitational potential well, and because the emissivity index was correspondingly quite high, the authors hypothesized an interaction between the spinning BH and its accretion disk. Magnetic torquing effects between the two could result in the

extraction of rotational energy from the BH which would, in turn, power the high coronal emission seen from the inner radii of the disk (Agol & Krolik 2000; Garofalo & Reynolds 2005). An alternative mechanism consists of the strong gravitational focusing of a high-latitude source above a rapidly rotating BH (Martocchia & Matt 1996; Miniutti & Fabian 2004). In contrast with data from the *ASCA* era, a Schwarzschild model appeared not to work for these data — a line extending down to ~ 3 keV would require line emission from extremely deep within the plunge region: $r \approx 3 r_g = 0.5 r_{\text{ms}}$, a situation which appears unphysical due to the high ionization expected in this part of the flow (Reynolds & Begelman 1997).

Reynolds et al. performed a follow-up and more detailed analysis of the *XMM-Newton* observation of MCG–6-30-15 taken by Wilms et al. (Wilms et al. 2001). They explicitly demonstrated that the iron line profile was inconsistent with an X-ray irradiation profile that follows a Novikov-Thorne (Novikov & Thorne 1974) dissipation law, even for an extremal Kerr BH (Reynolds et al. 2004b). Employing a generalized thin disk model (Agol & Krolik 2000) that includes a torque applied at $r = r_{\text{ms}}$, Reynolds et al. suggested that this torque has a great impact on the disk emission seen in this observation. In the “deep minimum” state, the torqued-disk scenario requires that the disk is largely emitting via the extraction of rotational energy from the BH rather than via accretion. These authors also examined spectral variability during the deep minimum state. By studying difference spectra and direct spectral fits to 10 ks segments of data from this observation, Reynolds et al. concluded that the intensity of the broad line seems to be proportional to the hard 2 – 10 keV flux of the source: the equivalent width of the line remains approximately constant while the source fluctuates substantially in amplitude. Such behavior is consistent with simple X-ray reflection models.

The longest *XMM-Newton* observation of the source to date was recorded by Fabian et al. in 2001. This group found MCG–6-30-15 in its normal state, and recorded data for over

87 hours (Fabian et al. 2002). In this state, the bulk of the iron line emission was in a narrower line compared with the “deep minimum” state, although a very extended red wing was still evident. The time-averaged EPIC-pn spectrum again showed that the Fe-K α feature was very strong, and the long data set was of sufficient resolution and quality that the spectrum demanded a fit incorporating a full reflection model. Relativistic smearing needed to be applied not just to the cold iron line, but to the entire reflection continuum. Taking this into account, the iron line was once again found to produce emission within the radius of marginal stability for a Schwarzschild BH. Fitting the line with the maximally spinning ($a = 0.998$) BH `laor` model suggested that the line emissivity followed a $\varepsilon \propto r^{-\alpha}$ dependence with $\alpha = 4.5 - 6$ between an inner radius $r_{\min} < 2r_g$ and a break radius $r_{\text{br}} \approx 6r_g$. Beyond the break radius, the emissivity profile flattened to $\alpha \sim 2.5$. This broken power-law form was strongly preferred by the data over the usual simple power-law emissivity functions usually fitted to such data — again, this reflects the high quality of the data. Fabian et al. also note that, in its normal state, difference spectra of MCG–6-30-15 show spectral variability from 2 – 10 keV in the form of a power-law: the iron line flux changed little between successive 10 ks frames of the observation, whereas the continuum flux varied by as much as a factor of ~ 2 . This result is in contrast to that found by Reynolds et al., who observed an iron line flux proportional to the 2 – 10 keV continuum flux when MCG–6-30-15 was in its “deep minimum” state (Reynolds et al. 2004b). Comparing these two studies, it appears that the iron line flux is proportional to the observed X-ray power-law continuum at low fluxes and then “saturates” to an approximately constant level once the observed X-ray continuum exceeds a certain level. This complexity could be due to light-bending effects if the power-law X-ray continuum source is situated close to the spin axis of the BH (Miniutti & Fabian 2004). Alternatively, patchy ionization of the disk surface might produce such a saturation (Reynolds 2000).

The `ky` suite of iron line profile models (Dovčiak et al. 2004) was used to fit the

time-averaged spectrum of MCG–6-30-15 as well, also using data from the long *XMM-Newton* observation (Fabian et al. 2002). They fit the 3 – 10 keV spectrum with four combinations of *ky* models, all involving a broad Fe-K α *ky*line, a narrow Gaussian emission line at 6.9 keV (likely an ionized line of iron, as cited in Fabian et al.), and a Compton-reflection continuum from a relativistic disk (smeared using a *kyconv* kernel). The authors also found that models describing the disk emissivity as a broken power-law rather than a single power-law in radius achieved significantly better statistical fits, though among these broken power-law models, comparable fits can be obtained for a wide variety of BH spin values. These authors therefore concluded that iron line profiles are not a good way to constrain BH spin. At some level, this objection amounts to the obvious point that arbitrarily large redshifts can be obtained around *any* BH (rotating or not) if one is at liberty to produce emission from any radius arbitrarily close to the event horizon. As stated in Chapter 3, however, one must consider the physical realism of this assumption in general, and the best-fit spectral parameters determined by these authors in particular. For their low-spin ($a = 0.25$) best-fitting model, Dovčiak et al. concluded that a substantial amount of iron line emission had to originate from deep within the radius of marginal stability; translating the fit parameters of Dovčiak et al. into standard quantities, they require an inner emissivity profile of $\varepsilon \propto r^{-9}$ starting at an inner radius of $r_{\text{in}} = 3.2 r_{\text{g}}$, to be compared with the radius of marginal stability for a $a = 0.25$ BH which is at $r_{\text{ms}} \approx 5.2 r_{\text{g}}$. As has already been noted and will be explored further in §4.2, it is hard to understand how this region of the accretion flow could contribute to any part of the observed iron emission given that the fact it will be very tenuous and extremely highly photoionized (Reynolds & Begelman 1997; Young et al. 1998).

The medium resolution (CCD) data discussed so far leave ambiguous the possible role of complex ionized absorption in distorting the observed X-ray continuum shape and hence the inferred iron line profile. To assess the role of this absorption, Young et

al. performed and analyzed a deep, 522 ks grating observation of MCG–6-30-15 in May 2004 with the HETGS instrument on *Chandra* (Young et al. 2005). This observation produced two important results: first, the authors found that the difference in the hard continuum spectrum between the high and low flux states was well described by a power-law of photon index $\Gamma = 2.0^{+0.2}_{-0.1}$. This finding agreed with previous studies that indicated that the spectral variability of MCG–6-30-15 in its normal state is dominated by a power-law component (Fabian et al. 2002). Second, and most importantly, ionized absorption models whose continuum curvature mimics the red wing of a broad iron line from 3 – 6 keV were ruled out. Such models generically predict strong $K\alpha$ absorption lines of intermediately ionized iron. Young et al. showed that these lines are conclusively absent, falsifying the ionized absorption model and further strengthening the relativistic smearing hypothesis.

4.2 Determining the Spin of the Black Hole in MCG–6-30-15

In this Section, we use our new models (`kerrdisk` and `kerrconv`) along with the `ky` models of Dovčiak et al. to confront the issue of determining the spin of the BH in MCG–6-30-15. Because of the extremely robust, broad, well-studied iron line in this system, MCG–6-30-15 is an excellent candidate for such a study. Given the complexity of the spectrum displayed by the source, it is important to perform this exercise in a step-by-step manner, clearly enumerating all of the assumptions at each stage, and employing physical models to represent the spectral complexity whenever possible.

This guides the study presented in this Section. Due to the unprecedented signal-to-noise, we use the EPIC-pn data from the aforementioned long *XMM-Newton* observation of MCG–6-30-15 (Fabian et al. 2002). Data preparation and reduction followed Vaughan

& Fabian exactly (Vaughan & Fabian 2004). We present a step-by-step analysis of these data using models of increasing complexity and physical realism. Initially, to illustrate the potential power of broad iron lines for spin determination, we modeled the 2 – 10 keV EPIC-pn as a simple power-law continuum modified by a broad iron line (and absorption by the Galactic column of $4.1 \times 10^{20} \text{ cm}^{-2}$ toward this source); this is comparable to the study performed by Dovčiak et al. It does, however, neglect the significant effects that continuum curvature due to ionized absorption could have on the inferred iron line parameters (and hence inferred BH spin). To assess these effects, we next model the effects of multiple warm absorbers and dust on first the 2 – 10 keV spectrum and then the full 0.6 – 10.0 keV spectrum. In our most sophisticated spectral model, we describe the 0.6 – 10.0 keV band including multiple absorption components and augmenting the simple broadened iron line with a relativistically smeared ionized X-ray reflection spectrum (Ross & Fabian 2005).

The best-fit parameters and error bars for each progressive model fit are shown in Table 4.1. Each fit and the corresponding change in the global goodness-of-fit ($\Delta\chi^2$) with respect to changes in a in each case are shown in Figs. 4.1-4.6. The unfolded spectrum and the best-fit model components for both the single `kerrdisk` case and the full ionized reflection spectrum convolved with `kyconv` are shown in Figs. 4.5-4.7. For the warm absorber tables described in Table 4.1 and §4.2.2, all abundances are frozen at the solar value. For all model components, the redshift is set to $z = 0.008$, the optically determined value for MCG–6-30-15 (Reynolds et al. 1997). In all of the fitting below, the inner disk radius contributing to the iron line emission (or X-ray reflection spectrum in the case of Model 5) was not allowed to be smaller than the radius of marginal stability.

4.2.1 Simple Power-Law Continuum and Iron Lines

Initially, we perform an analysis of the 2 – 10 keV spectrum assuming that the underlying continuum is a simple power-law (absorbed by the Galactic hydrogen column along our line of sight) and that the disk spectrum is just a single iron line (rather than a whole reflection spectrum). Fig. 4.1 shows the hard spectrum as fit by this photoabsorbed power-law (Model 1). To accurately model the continuum we have initially ignored the 4 – 7 keV range when fitting this component. This prevents any contamination of the fit by the presence of an iron line reflection signature. Once the fit was complete, energies from 4 – 7 keV were included again. As suspected, the data/model ratio shown in the lower panel demonstrates a significant residual feature above the continuum, which appears to have the form of a highly broadened iron line peaking at 6.4 keV. The presence of this large residual feature results in a poor fit, $\chi^2/\text{dof} = 4577/1106$ (4.14).

Fig. 4.2a plots the data/model ratio again, this time for a model including a single, broad kerrdisk line with a rest-frame energy of 6.4 keV (Model 2). Two narrow redshifted Gaussians representing a cold Fe-K α line and an ionized line of iron are also included at 6.4 and 6.9 keV, respectively (Fabian et al. 2002). The 6.4 and 6.9 keV lines both have equivalent widths of ~ 14 eV.

It should be noted here that Fabian et al. acknowledged that a 6.74 keV absorption line of $EW = -138 \pm 35$ eV fit the data as well as an emission line at 6.9 keV and $EW = 18 \pm 6$ eV. This absorption feature was also preferentially used in the MCG–6-30-15 work of Vaughan & Fabian, and was consistent with the prediction of Sako et al. based on an RGS observation of this source in 2001 (Sako et al. 2003). However, the 6.7 keV absorption line detected in the deep high-resolution *Chandra*/HETGS spectrum (Young et al. 2005) is significantly weaker than that fitted by Fabian et al. , with equivalent widths of $EW = -18_{-5}^{+7}$, $EW = -13 \pm 9$, and $EW = -25 \pm 9$ eV during the average, low and

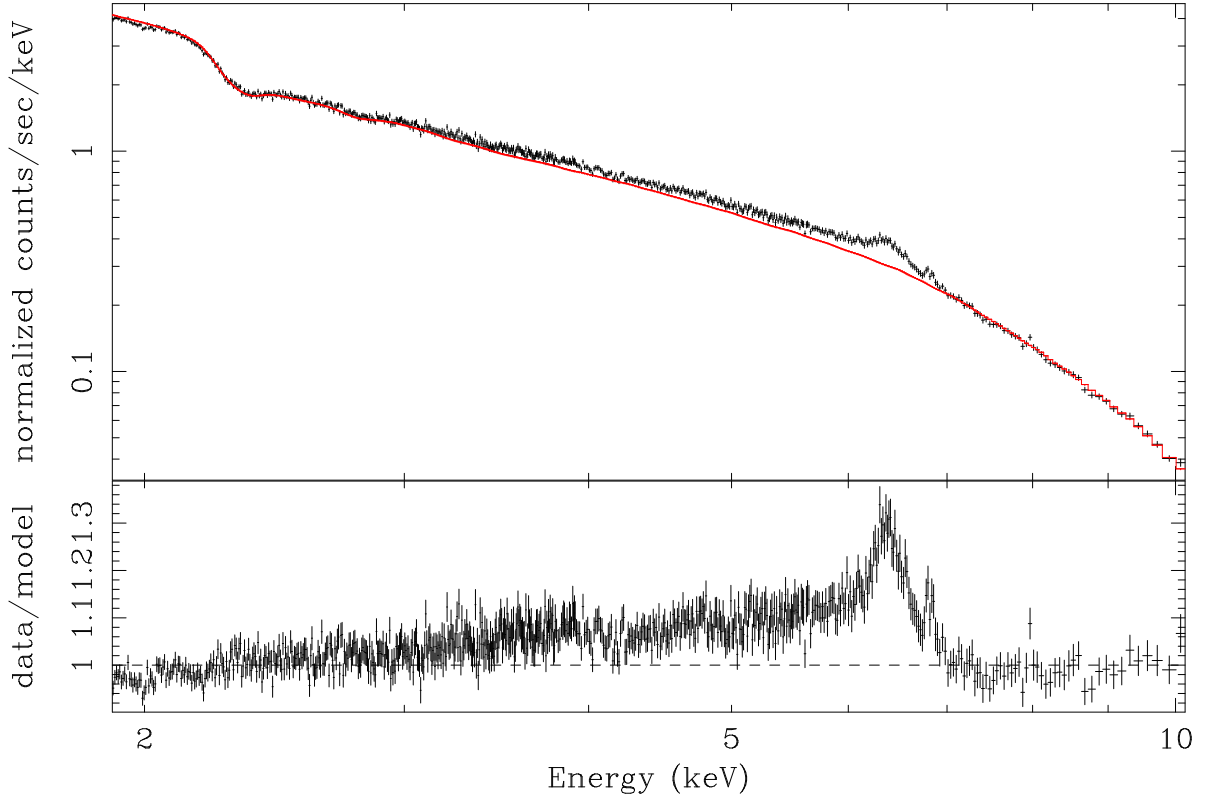


Figure 4.1: The `phabs(po)` fit to MCG-6-30-15. Notice the significant deviations of the data from this model, especially around 6.4 keV. Formal $\chi^2/\text{dof} = 4577/1106$ (4.14).

high flux states of the source, respectively. Thus, the high-resolution *Chandra* spectrum does not support a spectral model for the EPIC spectrum in which the complexity in the 6.6–7.0 keV range includes a very strong absorption line. Two possible loopholes in this argument are: (1) an order of magnitude temporal change in the helium-like iron column density between the *XMM-Newton* and *Chandra* grating observations, and (2) extreme $\sim 10^4 \text{ km s}^{-1}$ velocity broadening of the absorption feature which would diminish its detectability in the high-resolution spectrum. More plausible is the notion of a weak ($EW \sim 40 \text{ eV}$) and slightly broad emission line from hydrogen like iron (Fe XXVI). Given that *Chandra* shows there to be a weak ($EW \sim -20 \text{ eV}$) narrow Fe XXVI absorption line at 6.97 keV, the EPIC-pn spectrum would be expected to show a net emission feature with $EW \sim 20 \text{ eV}$.

Most importantly, however, the details of whether this spectrum complexity is de-

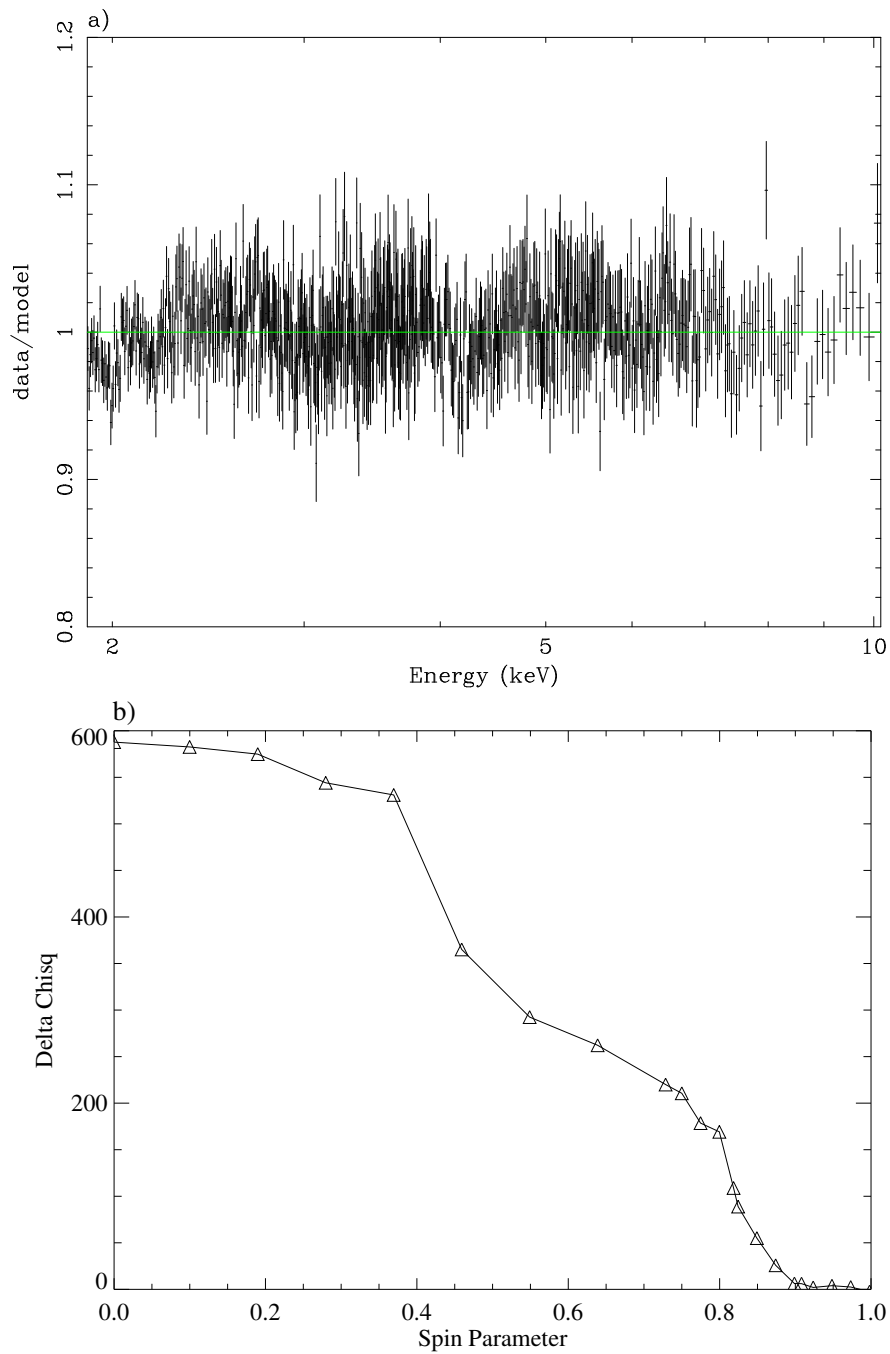


Figure 4.2: (a) A kerrdisk line near 6.4 keV has been added to the phabs(po) fit, as have two zgauss lines modeling out the narrow, cold iron line at 6.4 keV as well as the narrow, ionized iron line at 6.9 keV. Formal $\chi^2/\text{dof} = 960/1096$ (0.88). Note the flatness of the ratio plot shown here as compared with that shown above for the phabs(po) case. (b) The corresponding plot of the change in χ^2 vs. a for this model. Formally at 90% confidence, $a = 0.970^{+0.003}_{-0.015}$.

scribed by an ionized iron emission or absorption line has almost negligible effect on the broad iron line. In terms of the effect on the overall fit, Fabian et al. note that the relativistic line parameters differ insignificantly when one employs an absorption line rather than an emission line in the model. Getting ahead of ourselves slightly, we have checked this result in our own analysis by replacing the 6.9 keV Gaussian in Model 4 with a 6.74 keV Gaussian in absorption (i.e., negative flux). The result was a $\Delta\chi^2/\Delta\text{dof} = +26/0$, indicating a marginal decrease in the overall goodness-of-fit. Visually, this fit was indistinguishable from the best fit from Model 4, and as per Fabian et al. , we also found minimal change in the relativistic line parameters. The inner emissivity index of the disk became marginally steeper and its inclination angle increased very slightly, but the changes were well within the statistical error bars. The most interesting point, however, is that the best-fit equivalent width of this absorption line was only $EW = -21.3 \text{ eV}$; much less than the $EW = -138 \text{ eV}$ found by Fabian et al. Such a modest equivalent width in comparison to what should be necessary suggests that this line is not robustly wanted in our fit to the data.

Returning to Model 2, the three iron lines (two narrow and one broad) that we do choose to include significantly improve the fit ($\chi^2/\text{dof} = 960/1096 (0.88)$), and succeed in modeling out the residual feature shown in Fig. 4.1. Formally at 90% confidence for one interesting parameter, our best fit for Model 2 indicates a very rapidly rotating BH ($a = 0.970^{+0.003}_{-0.015}$). To gauge the sensitivity of this fit to the spin of the BH, Fig. 4.2b plots the change in the goodness-of-fit parameter $\Delta\chi^2$ as a function of BH spin parameter a . This clearly demonstrates that χ^2 improves dramatically as one approaches very rapid spins. The equivalent width of the broad iron line in our best-fitting model is $\sim 729 \text{ eV}$, quite a bit higher than the $\sim 550 \text{ eV}$ cited by Fabian et al. , the 450 eV found by Ballantyne et al. (Ballantyne et al. 2003), or the $\sim 250 \text{ eV}$ found by Dovčiak et al. (Dovčiak et al. 2004). This unphysically high equivalent width is due to the simplicity of this model —

the effects of absorption and the X-ray reflection continuum, in particular, will introduce additional curvature into the continuum, thereby alleviating the need for such a strong line.

4.2.2 Modeling the Warm Absorber

As discussed in Chapter 2, in order to accurately assess the width and morphology of the iron line in an AGN, it is imperative that the soft portion of the spectrum be modeled correctly. One must be concerned about confusing a broad red wing of a relativistic iron line with continuum curvature resulting from a putative “warm absorber” present within the AGN system. In fact, it has been argued that broad iron lines may be entirely unnecessary once one correctly accounts for the effects of a WA (see Sako et al. for a discussion of MCG–6-30-15 (Sako et al. 2003); see Turner et al. for a discussion of NGC 3516 (Turner et al. 2005)). As mentioned in §4.1, a deep *Chandra*/HETGS observation of MCG–6-30-15 fails to find the K-shell absorption lines of the intermediate charge states of iron predicted from a model in which a WA is mimicking the whole relativistic red wing of the iron line. However, the question remains as to the effects that warm absorption has on fitting of the extreme red wing of the iron line which drives BH spin constraints. Very long data sets are needed in order to obtain spectra with enough signal to put both broad line and WA models to the test and pursue the question of their overlap with statistical validity. The ~ 350 ks observation of MCG–6-30-15 (Fabian et al. 2002), which we use here, is ideal for such a study because of its large number of counts and its resolution of the broad iron feature this galaxy is thought to possess.

We have used the XSTAR spectral synthesis package for photoionized gases to construct a grid of WA models as a function of the absorbed column density N_{H} and ionization parameter ξ . This is the same grid we use and reference in Chapter 2 for the spectral analysis of the warm absorber in NGC 4593.

Initially, we side-step the complexities of the soft (< 2 keV) spectrum and apply this WA model to the $2 - 10$ keV only. In many ways, neglecting any constraints from the spectrum below 2 keV maximizes the impact that it may have on the broad iron line; the sole “job” of the absorption component in this setting is to attempt to fit the curvature of the spectrum otherwise attributed to the broad iron line. We do notice a modest reduction in the goodness-of-fit parameter compared with Model 2 (the simple power-law and `kerrdisk` model) $\Delta\chi^2/\Delta\text{dof} = -26/-2$. The warm absorber in Model 3 is of modest optical depth and rather weakly ionized: $N_{\text{H}} = 4.22 \times 10^{22} \text{ cm}^{-2}$ and $\log \xi = 0.84$. Although the change in the goodness-of-fit is not dramatic, the additional continuum curvature introduced by the warm absorber leads to a reduction in the equivalent width of the iron line from $EW = 729$ eV down to the more physically reasonable value $EW = 521$ eV. As can be seen from Table 4.1, the parameters that determine the best-fitting shape of the iron line (the emissivity indices, inner radius, break radius, outer radius, inclination of the disk and BH spin) are essentially unaffected by the inclusion of this warm absorbing component. As shown in Fig. 4.3, a rapidly rotating BH is still preferred in this case (formal 90% confidence constraints being $a = 0.997^{+0.001}_{-0.035}$). However, in contrast to the case with Model 2, the inclusion of a WA to the $2 - 10$ keV spectrum allows models with low BH spin to fit the data adequately (with low-spin cases producing a goodness-of-fit parameter which is only $\Delta\chi^2 \sim 40$ worse than high-spin cases) — in these cases, the $3 - 4$ keV curvature is being modeled as the effects of warm absorption rather than the extreme red wing of the iron line.

Of course, the soft X-ray band (< 2 keV) is extremely important for constraining the properties of WAs; the opacity of most well-studied WAs is dominated by oxygen and iron edge/line absorption in this band. Hence, to be complete, we must extend our study of the effects of warm absorption on X-ray reflection features to the full $0.6 - 10.0$ keV band.

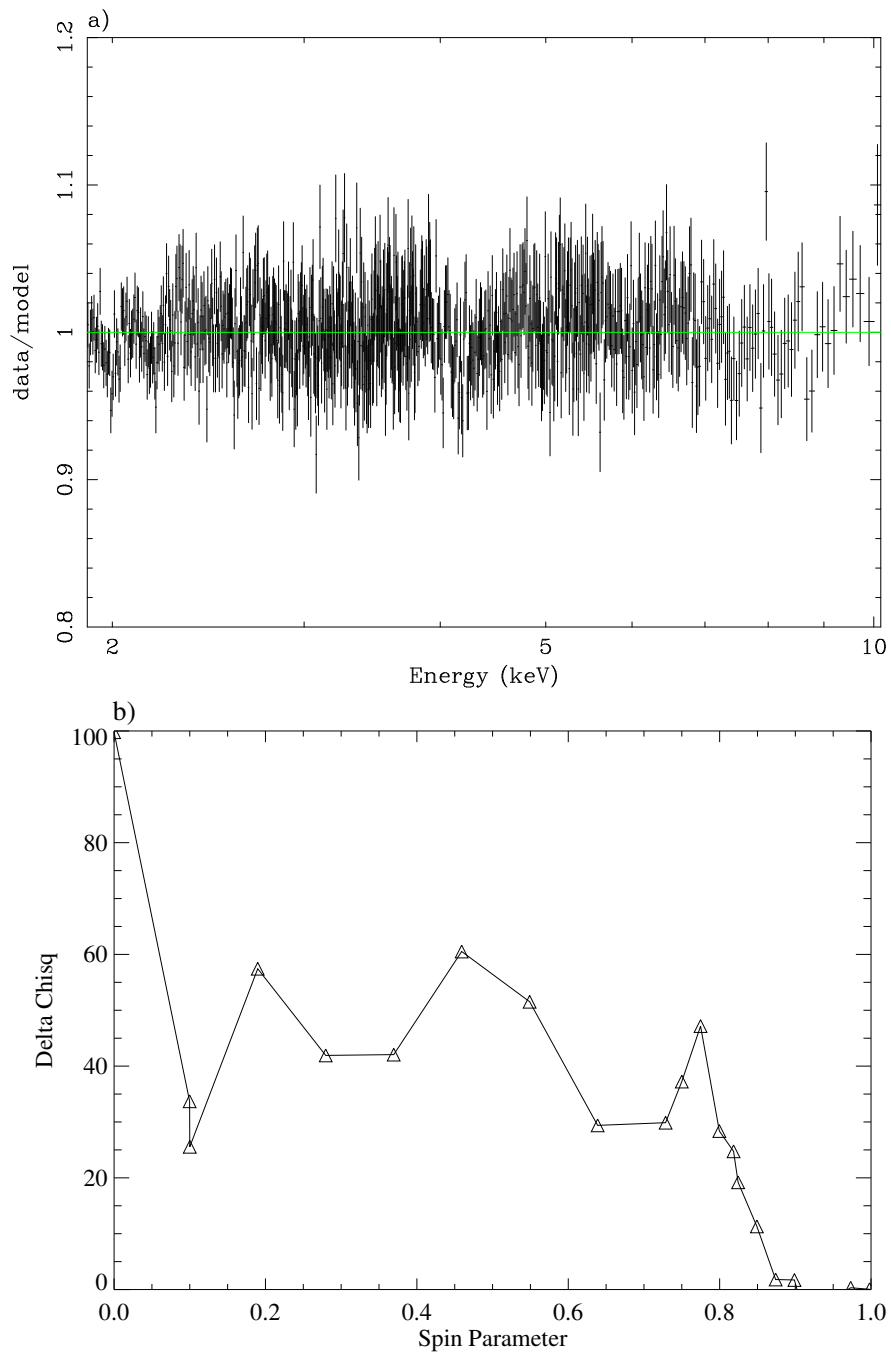


Figure 4.3: (a) A WA table has been added to the fit to try and model the soft end of the spectrum more accurately. Formal $\chi^2/\text{dof} = 934/1094$ (0.85). (b) $\Delta\chi^2$ vs. a plot. Formally at 90% confidence, $a = 0.997^{+0.001}_{-0.035}$.

When fitting the 0.6 – 10.0 keV band, we find that we *cannot* produce an acceptable fit with a model consisting of a simple power-law and `kerrdisk` line subjected to the effects of Galactic absorption and a one-zone WA. This is not surprising: it is generally thought that WAs must be physically more complex than a one-zone model can account for, i.e., they cannot be well described by a single value of the column density and ionization parameter. Physically, the WA likely represents a wind emanating from the accretion disk and/or cold torus surrounding the central engine and may well contain dust. A continuum of ionization parameters likely exists along the line of sight. For computational purposes, however, it is convenient to approximate this as a discrete number of zones, each of which is characterized by a single column density and ionization parameter. Adding in a second WA dramatically improves the fit and, indeed, the two absorbers do seem to represent distinct “zones” of material based on their physical properties (see Table 4.1 for details).

Even taking both WA models into account, however, there still appears to be significant remaining absorption in the spectrum below 2 keV, as well as a strong soft excess below ~ 0.7 keV. A strong edge due to the L₃-edge of neutral iron (presumably in dust grains embedded within the WA) has already been noted in high-resolution *Chandra* and *XMM-Newton* grating spectra of MCG–6-30-15 (Lee et al. 2002; Turner et al. 2003). Incorporating this edge into our fit (employing spectral tables provided to us by Julia Lee) makes a significant visual and statistical improvement, largely explaining the unmodeled absorption mentioned above. It is worth noting that the edge demands quite a high column density of iron: $\log N_{\text{Fe}} = 17.54$, which is approximately a factor of two higher than that found by Turner et al. (Turner et al. 2003). To address the soft excess seen below 0.7 keV, we employ a simple blackbody model. Since the data are only sensitive to the tail of this component, the other parameters describing the spectrum are completely insensitive to the precise model used for this soft excess. Table 4.1 details the fit, which includes two warm absorption zones, the Fe-L₃ edge and the additional soft excess.

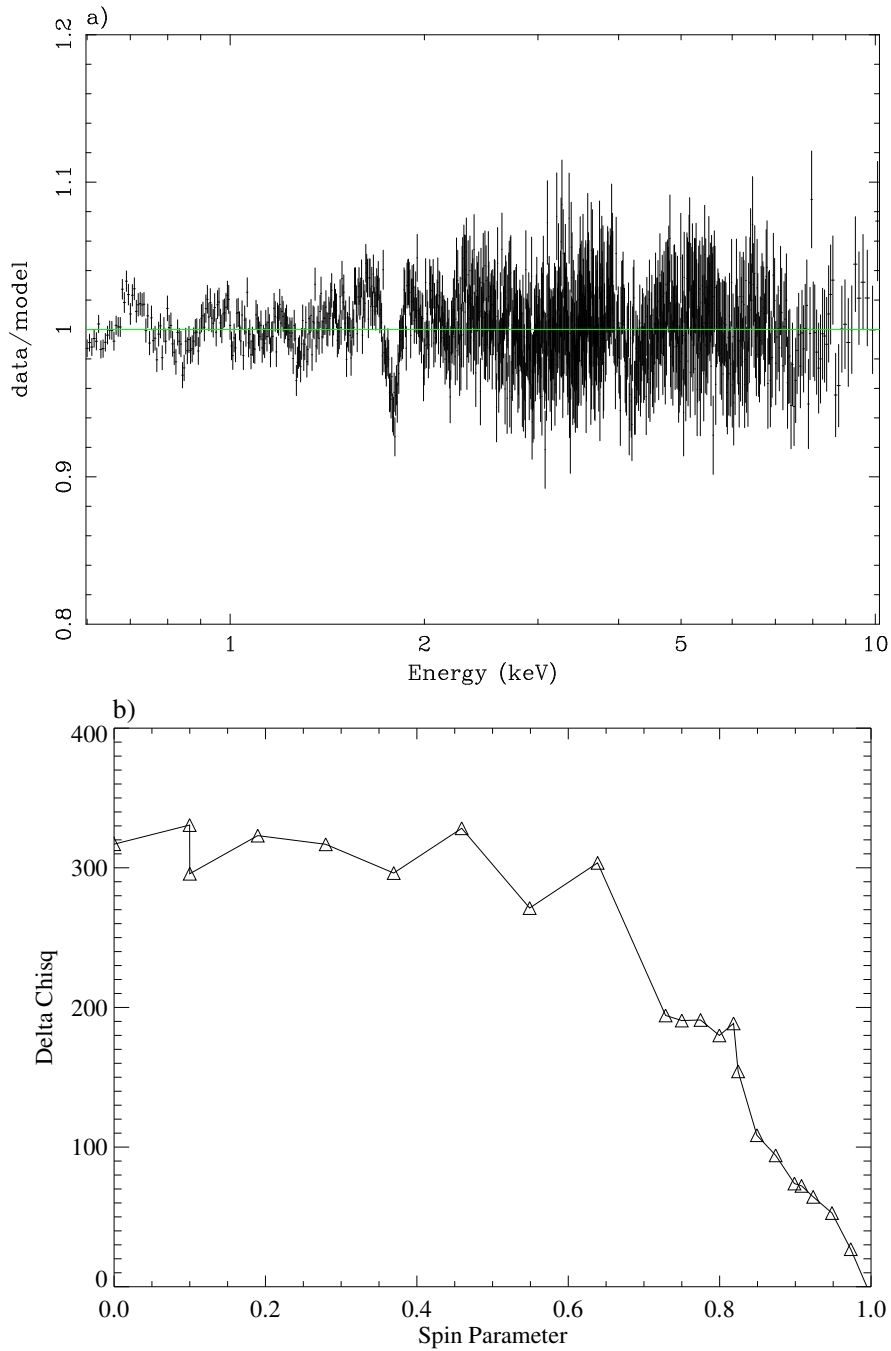


Figure 4.4: (a) A second WA has been added, as well as an iron edge at 0.707 keV and a blackbody component to model direct disk emission below ~ 1 keV. The data now include energies from 0.6 – 2.0 keV. The residual feature at ~ 1.8 keV is a calibration artifact (the Si-K edge). Formal $\chi^2/\text{dof} = 1742/1375$ (1.27). (b) $\Delta\chi^2$ vs. a plot. Formally at 90% confidence, $a = 0.997 \pm 0.001$.

Although we cannot statistically compare the Model 3 and Model 4 fits (since we have expanded the energy range of study between these models), Model 4 does appear to describe the full 0.6 – 10 keV spectrum very well (see Fig. 4.4). As before, the data strongly prefer a rapidly rotating BH. The inclusion of the 0.6 – 2.0 keV data apply extra constraints on the WAs; the partial degeneracy found in Model 3 between the red wing of the iron line and the curvature introduced by warm absorption is now removed. At 90% confidence, Model 4 gives formal constraints on the BH spin of $a = 0.997 \pm 0.001$, and the broad iron line has an equivalent width of ~ 926 eV. This is significantly higher than we find for Models 2-3, or in any of the other analyses of this data set, and reflects the breadth of the red wing of the iron line feature in this fit. The values for the best-fit parameters for Model 4 are shown in Table 4.1.

Fig. 4.5 shows the unfolded spectrum for MCG–6-30-15 fit with Model 4 using a simple `kerrdisk` line. Each model component is colored and labeled separately to highlight its relative contribution to the fit. Note the relatively strong blackbody component that must be included at ~ 0.1 keV in order to accurately model the spectrum below ~ 2 keV, as well as the redshifted Gaussian emission lines at 6.4 and 6.9 keV that must be added to the broad neutral iron line to fully capture the shape of the hard spectrum.

Turner et al. have approached the question of absorption in MCG–6-30-15 by analyzing the RGS spectrum from the same *XMM-Newton* observation used here (Turner et al. 2003). In fitting the 0.32 – 1.7 keV range, these authors have identified six components of absorption: absorption by the cold Galactic column, four “zones” of warm absorbing plasma, and an absorbing L_3 edge of neutral iron (from dust embedded in one or more of the warm absorbing zones). Considering this detail in structure identified by Turner et al., it might appear that our spectral model (which only requires two WA zones plus the neutral Fe- L_3 edge to describe the spectrum) is inconsistent with the picture painted by the RGS. Upon closer inspection, however, we see that this is not the case. Firstly,

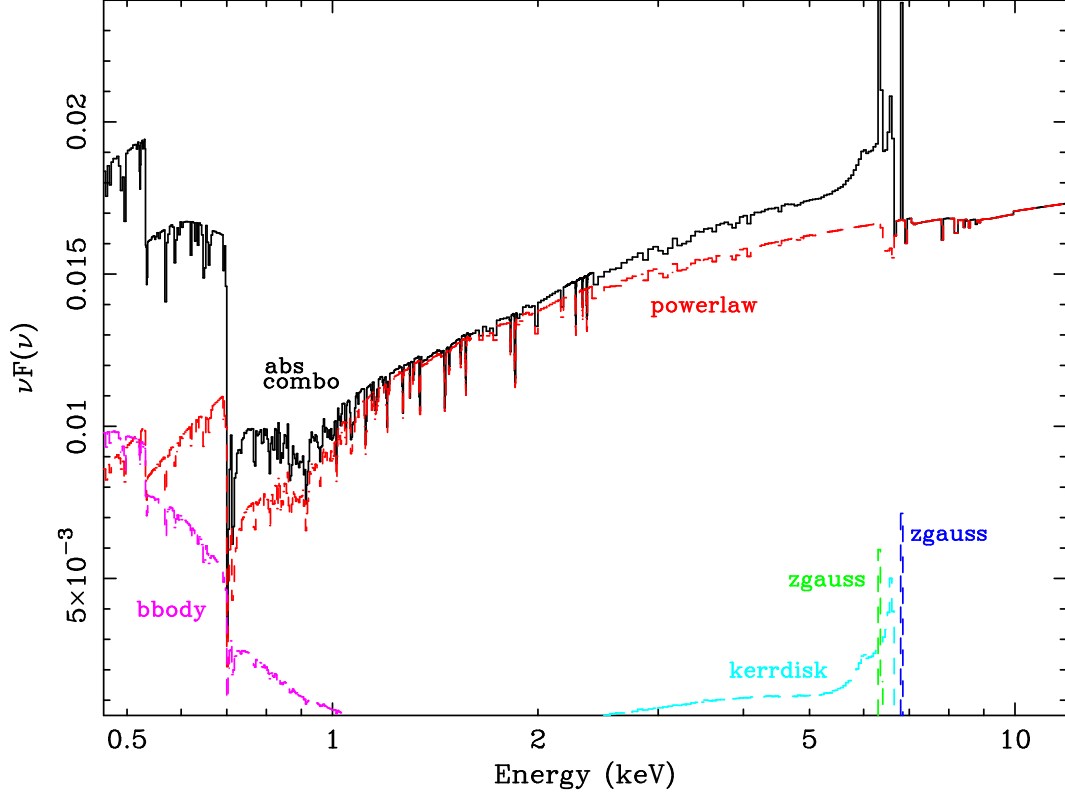


Figure 4.5: A νF_ν plot of the relative contributions of the model components for Model 4. The two redshifted Gaussian components (zgauss) are shown in green and dark blue, the kerrdisk line is in light blue, the blackbody component (bbody) representing soft emission from the disk is in purple, and the power-law continuum (powerlaw) is in red. The soft components labeled “abs combo” in black represent the combination of absorption features present in the spectrum: Galactic photoabsorption, two WA models and an iron absorption edge. The solid black line represents the combined model including all the dashed components.

the lowest ionization WA seen in the RGS ($\log \xi \sim -4.42$) cannot be distinguished from neutral absorption by our 0.6 – 10.0 keV EPIC-pn spectrum and hence is accounted for through the neutral absorption column present in our model. Secondly, the two highest ionization WAs identified by the RGS actually have rather similar ionization states ($\log \xi \approx 1.6 - 1.7$ for Model 2 of Turner et al.) and are only separated into two zones through their kinematics; they are separated by $\sim 2000 \text{ km s}^{-1}$ in velocity space by the RGS. The EPIC-pn instrument, however, would not be able to resolve the velocity difference of these two zones. Accounting for these two facts, we would expect the Turner et

al. four-zone RGS model to reduce to a two-zone model when applied to EPIC-pn data.

The column densities and ionization parameters are lower in the Turner et al. fit than in ours but, unfortunately, it is difficult to compare these values in a meaningful way due to calibration issues in the continuum response that presently exist with RGS data. This renders it nearly impossible to perform simultaneous RGS/EPIC-pn fits in XSPEC, which is why we have chosen not to address such a joint fit within the scope of this work. Cross-calibration issues similarly affect our ability to compare EPIC-pn data with *Chandra*/HETGS results, making it difficult to obtain a more precise, independent check on the model fit to energies below ~ 2 keV.

4.2.3 Model Including a Full Reflection Spectrum

The broadened iron emission line of Models 1-4 is, of course, just the tip of the iceberg; the disk produces a whole spectrum of fluorescent and recombination lines, radiation-recombination continua and Compton backscattered continuum. To obtain truly reliable constraints, we must consider the full X-ray reflection spectrum.

In Model 5, we take the basic continuum/absorption components of Model 4 and augment the simple iron line with the full X-ray reflection spectrum from an ionized disk surface (Ross & Fabian 2005). The Ross & Fabian models describe the reflected spectrum emitted by an optically thick atmosphere (here, the surface of an accretion disk) of constant density that is illuminated by radiation with a power-law spectrum (here, photons that have been inverse Compton-scattered by relativistic electrons in the corona or base of a jet). We then convolve this reflection spectrum with the effects of relativistic smearing via `kerrconv`. Interestingly, as will be noted below, the soft X-ray emission associated with the photoionized disk surface naturally explains the soft excess without the need for an additional ad hoc blackbody component. Hence, Model 5 does not include the blackbody component of Model 4.

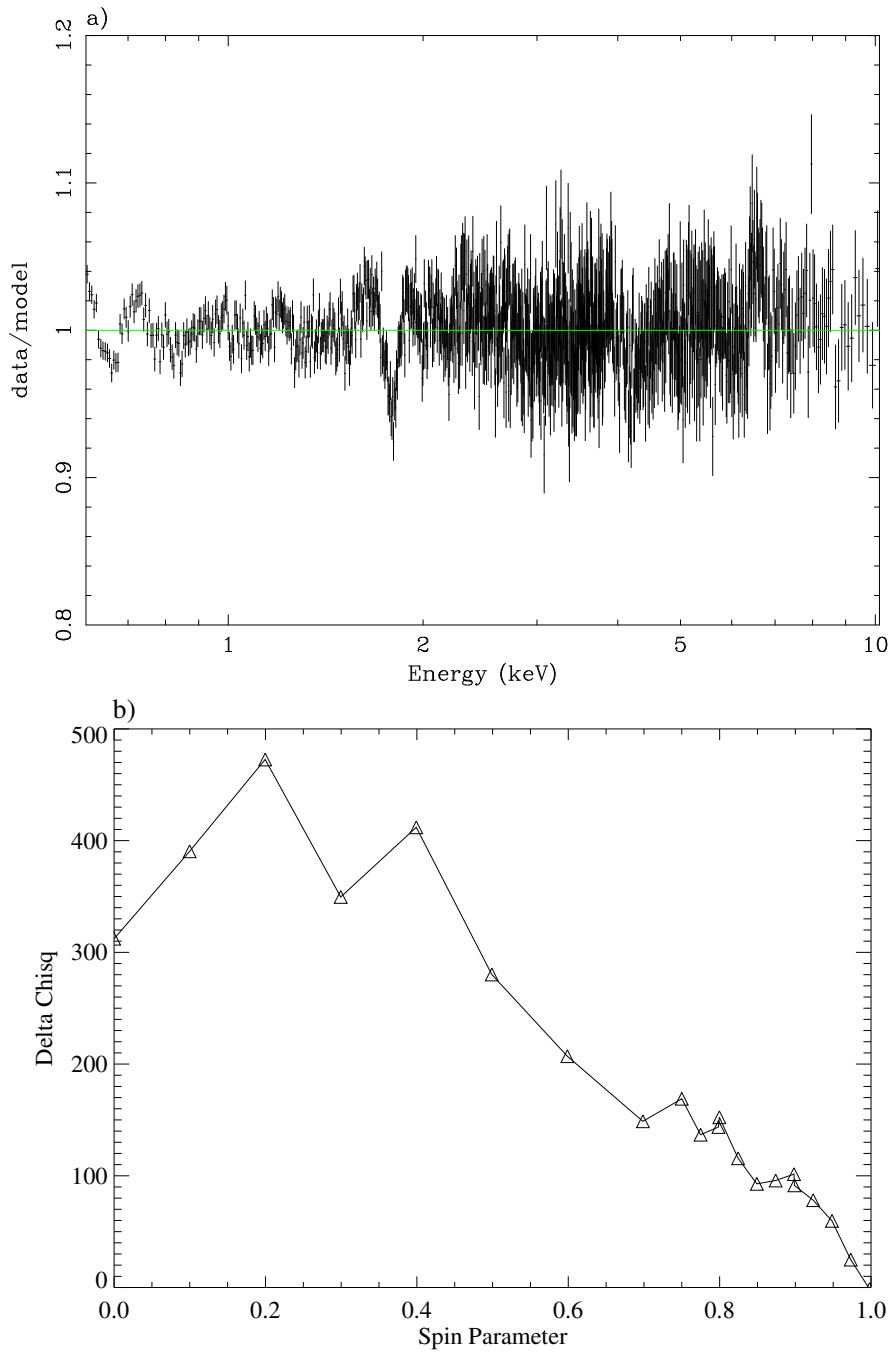


Figure 4.6: (a) The bbody component has been replaced by a smeared ionized disk reflection spectrum. Formal $\chi^2/\text{dof} = 1793/1374$ (1.30). Again, the residual feature at ~ 1.8 keV is a calibration artifact (the Si-K edge). While this fit statistically seems less robust than that achieved with Model 4, the ionized reflection model is thought to be more physically accurate in its ability to account for both the soft excess as well as the broad iron feature at 6.4 keV. (b) $\Delta\chi^2$ vs. a plot. Formally at 90% confidence, $a = 0.989^{+0.009}_{-0.002}$.

The best-fit parameters for this model are shown in Table 1, and in comparison with Models 1-4 it appears that Model 5 provides a statistical fit to the data that is not as good: ($\chi^2/\text{dof} = 1793/1374$; $\Delta\chi^2 = +51$ for one more degree of freedom compared with Model 4). Model 5 is, however, our most physical model in the sense that the whole reflection spectrum is treated as opposed to just the iron line, resulting in a natural explanation for the soft excess. That is to say that both the somewhat arbitrary blackbody component and the broad kerrdisk line of Model 4 are not required in this fit; the soft excess and broad iron feature are instead both fully described by the smeared radiative recombination line/continuum emission from the irradiated accretion disk. This change in the modeling of the soft excess increases the photon index of the continuum power-law component to $\Gamma = 2.09$, and also results in an increase in the inferred depth of the neutral Fe-L₃ edge to an iron column density of $\log N_{\text{Fe}} = 17.68$ (over 17.54 in Model 4). The column densities and ionization parameters of the two included WAs also vary somewhat from Model 4, but the clear delineation between them remains evident. See Table 4.1 for details.

The inclusion of an ionized X-ray reflection spectrum also has important implications for the derived spin parameter, as can be seen in Fig. 4.7. The fact that a significant component of the line broadening in this model is now due to Compton scattering reduces the inferred BH spin to $a = 0.989_{-0.002}^{+0.009}$, slightly lower than the value determined in Model 4, but still consistent with a very rapidly spinning BH. We do find, again, that a narrow Fe-K α line at 6.4 keV is necessary in order to properly model the shape of the spectrum, as well as a 6.9 keV line of ionized iron as in Model 4. The equivalent widths of these narrow lines are 24.7 eV and 27.3 eV, respectively. Including all of these components, we find that the total 0.6 – 10 keV luminosity of MCG–6-30-15 is $L_{\text{X}} = 9.34 \times 10^{42} \text{ erg s}^{-1}$ using WMAP cosmological parameters.

Fig. 4.7 shows the plot of the relative contributions of the best-fit model components

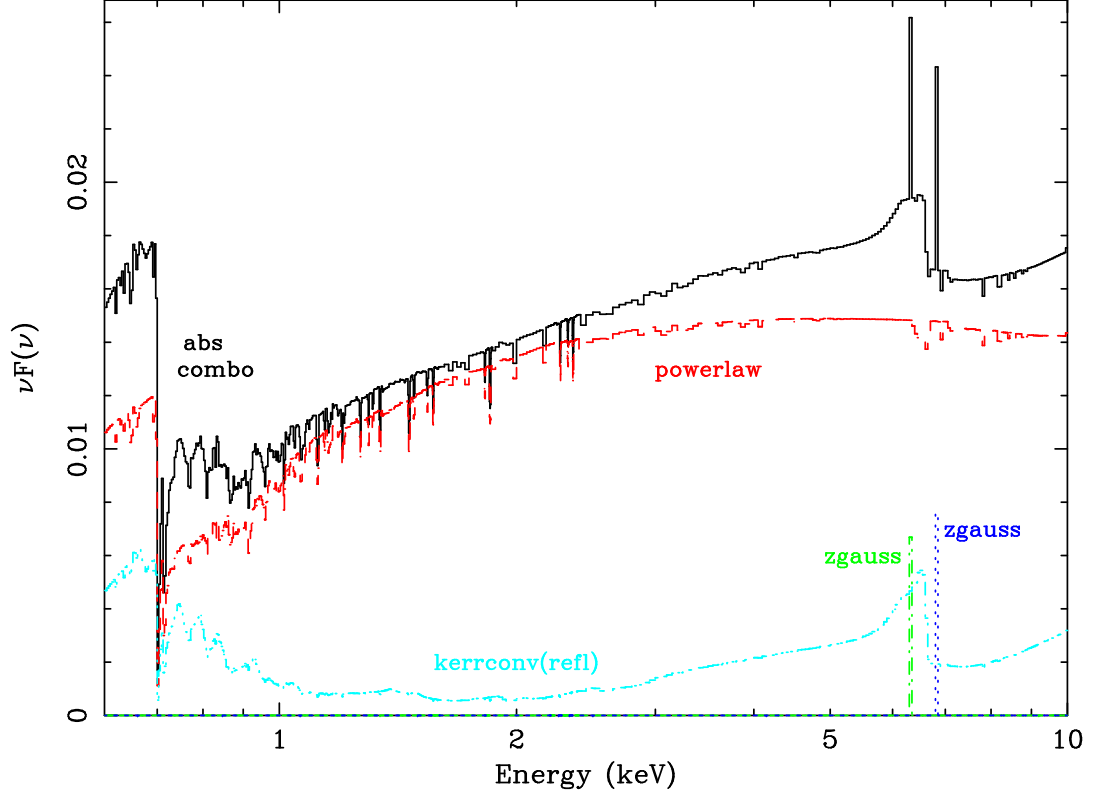


Figure 4.7: A νF_ν plot of the relative contributions of the model components for MCG-6-30-15, as above in Fig. 4.5. Now the fit is from Model 5, as shown in Fig. 4.6a. The color scheme is the same as for Fig. 4.5, but in this case the blackbody component has been replaced by an ionized reflection spectrum to model the soft emission as well as the broad neutral iron line. This component appears in light blue.

for Model 5. The main features are an ionized disk reflection spectrum relativistically blurred with a `kerrconv` convolution model to represent the soft emission and ionized iron features, as well as two `zgauss` components to model the cold, neutral iron line at 6.4 keV and the 6.9 keV line included in previous fits (Fabian et al. 2002). The absorption components in the soft spectrum are the same as those used for Model 4. Note that the presence of the ionized disk reflection negates the need for the blackbody component of Model 4 shown in Fig. 4.5.

While not essential for the principal issue of this thesis (i.e., determining BH spin), it is instructive to estimate the “reflection fraction” of the ionized reflection spectrum, f_{refl} . This parameter is defined to be proportional to the ratio of the normalization of the

reflection spectrum to that of the intrinsic spectrum, and normalized such that $f_{\text{refl}} = 1$ corresponds to a reflector that subtends half of the sky as seen from the X-ray source. Operationally, the ionized reflection model of Ross & Fabian is characterized by an absolute normalization and hence one cannot fit trivially for f_{refl} . We estimate this parameter by extending Model 5 out to 100 keV and setting f_{refl} to be the ratio of the normalization of the reflected and intrinsic spectra at the peak of the Compton reflection hump at 35 keV. This technique yields $f_{\text{refl}} \approx 1.25$. Previous studies have also found the reflection parameter to be in this range for MCG–6-30-15, but it should be noted that in these cases $f_{\text{refl}} = \Omega/2\pi$ has been a fitted parameter in the reflection model used, and as such has been considered an indication of the covering fraction of the reflecting material. For example, Fabian et al. began their spectral fitting by assuming $f_{\text{refl}} = 1$, but discovered that when this parameter was left free they achieved better statistical fits to the data (Fabian et al. 2002). The best-fit value determined by these authors was $f_{\text{refl}} = 2.2^{+1.1}_{-0.7}$, which is roughly consistent with our own, within error bars. By contrast, Lee et al. used a ~ 400 ks simultaneous *ASCA/RXTE* observation of MCG–6-30-15 to identify four distinct spectral states for the source (Lee et al. 2000). These authors noted that as the flux increased, Γ_{3-10} steepened while Γ_{10-20} gradually flattened at approximately the same rate. Lee et al. modeled the reflection with a *pexrav* component in XSPEC, using a reflection inclination angle matching that of the accretion disk at $i = 30^\circ$ and possessing an exponential cutoff for the Comptonizing source power-law at 100 keV. The iron abundance was maintained at twice the solar value. These authors found that as the source flux increased, f_{refl} did as well, beginning at $0.35^{+0.15}_{-0.16}$ and topping off at $1.37^{+0.23}_{-0.14}$. The last two flux states are consistent with our result within error bars.

A very high iron abundance in this disk is required by our Model 5 fit ($Z_{\text{Fe}} > 9.8Z_{\odot}$ at 90% confidence). Previous studies have also detected an overabundance of iron in the disk of MCG–6-30-15 (Ballantyne et al. 2003), though none have proposed this high an

abundance. If we freeze the iron abundance to be $3Z_{\odot}$ and re-fit, as in Ballantyne et al. , the goodness of fit parameter is increased by $\Delta\chi^2 = +463$ for one more degree of freedom, and there are obvious residual features created in the model fit by employing this tactic. Most of the absorption parameters remain relatively unchanged, but the disk parameters are altered considerably: $r_{\min} = 1.88r_g$ and $r_{\max} = 12.26r_g$, so the disk only radiates over a fairly thin ring near the radius of marginal stability. The emission profile consists of $\alpha_1 = 5.60$, $\alpha_2 = 1.00$, and $r_{\text{br}} = 3.22r_g$, reinforcing this conclusion. The inclination angle of the disk is reduced to $\sim 20^\circ$ from $\sim 30^\circ$ in the best-fitting Model 5, and the spin of the BH is considerably lowered to $a = 0.31$. Even though this is the best fit with $Z_{\text{Fe}} = 3Z_{\odot}$, it is clear from the form of the residuals around 6.4 keV that the reflection spectrum is being insufficiently broadened. Based on this fact and the substantial worsening of χ^2 , it appears that our fit indeed prefers a higher abundance of iron than that found by Ballantyne et al.

Our confidence in the goodness-of-fit provided by Model 5 is strengthened by the consistency with which the continuum model we have employed extends to fit the *BeppoSAX*/PDS spectrum of MCG–6-30-15 at high energies. The *BeppoSAX* observation was taken simultaneously with the *XMM-Newton* in 2001 (Fabian et al. 2002), acting as a valued “sanity check” to the derived EPIC-pn fit by providing spectral data from $\sim 15 - 100$ keV. We have performed a joint fit to the PDS and pn data within XSPEC, applying our Model 5 to both sets of data. Even with the paucity of counts at high energies, the results of this fit clearly show that Model 5 provides an excellent description of both the pn and the PDS continuum. The ability to place such additional constraints on our continuum and absorption parameters gives us greater confidence in the constraints we have correspondingly derived for the broad iron line parameters, including BH spin.

Model Component	Parameter	Model 1	Model 2	Model 3	Model 4	Model 5
phabs	$N_{\text{H}} (\text{cm}^{-2})$	4.10×10^{-2}				
	WA 1			4.22×10^{22}	2.00×10^{22}	4.17×10^{22}
WA 2	$\log \xi_1$			0.84 ± 0.49	1.76 ± 0.09	1.6 ± 0.03
	$N_{\text{H}2} (\text{cm}^{-2})$				3.49×10^{23}	2.19×10^{23}
Fe edge	$\log \xi_2$				3.90 ± 0.17	3.45 ± 0.09
	$\log N_{\text{Fe}} (\text{cm}^{-2})$				17.54 ± 0.03	17.68 ± 0.01
bbody	kT (keV)				$9.36 \pm 0.28 \times 10^{-2}$	
	flux ($\text{ph cm}^{-2} \text{ s}^{-1}$)				$3.38 \pm 0.68 \times 10^{-6}$	
po	Γ_{po}	1.91 ± 0.01	1.90 ± 0.01	1.97 ± 0.01	1.95 ± 0.07	2.09 ± 0.01
	flux ($\text{ph cm}^{-2} \text{ s}^{-1}$)	$1.39 \pm 0.01 \times 10^{-2}$	$1.36 \pm 0.01 \times 10^{-2}$	$1.30 \pm 0.06 \times 10^{-3}$	$1.07 \pm 0.03 \times 10^{-4}$	$1.18 \pm 0.03 \times 10^{-4}$
kerrdisk kerrconv	E (keV)		6.58 ± 0.04	6.50 ± 0.04	6.40 ± 0.06	
	α_1		5.65 ± 0.63	5.46 ± 1.13	6.56 ± 0.43	6.06 ± 0.26
	α_2		2.86 ± 0.11	2.66 ± 0.26	2.44 ± 0.27	2.78 ± 0.18
	$r_{\text{br}} (r_{\text{g}})$		5.75 ± 0.82	5.68 ± 1.6228	5.14 ± 0.87	5.56 ± 0.66
	a		$0.970^{+0.003}_{-0.015}$	$0.997^{+0.001}_{-0.035}$	0.997 ± 0.001	$0.989^{+0.009}_{-0.002}$
	i ($^\circ$)		20 ± 2	23 ± 2	29 ± 2	30 ± 1
	$r_{\text{min}} (r_{\text{g}})$		1.74 ± 0.24	1.28 ± 0.18	1.28 ± 0.16	1.62 ± 0.08
	$r_{\text{max}} (r_{\text{g}})$		113 ± 2	102 ± 1	134 ± 1	397 ± 495
	flux ($\text{ph cm}^{-2} \text{ s}^{-1}$)		$2.98 \pm 0.36 \times 10^{-4}$	$1.78 \pm 0.33 \times 10^{-5}$	$2.68 \pm 0.52 \times 10^{-6}$	
	Fe/solar					10.00 ± 0.72
refl	$\log \xi_{\text{refl}}$					2.03 ± 0.00
	Γ_{refl}					2.09 ± 0.01
χ^2/dof	flux ($\text{ph cm}^{-2} \text{ s}^{-1}$)					$1.51 \pm 0.32 \times 10^{-7}$
		4577/1106 (4.14)	960/1096 (0.88)	934/1094 (0.85)	1742/1375 (1.27)	1793/1374 (1.31)

Table 4.1: Models 1 – 3 are from 2 – 10 keV, Models 4 – 5 also include energies from 0.6 – 2.0 keV. Error bars quoted are all at the 1σ level except for those on the spin parameter, which are all at formal 90% confidence. 1σ errors for the column densities of the WAs were not well constrained. For Model 5, the kerrconv component has no line energy or flux parameters, and the large error bars on the maximum disk radius indicates that this parameter is not robustly constrained.

4.2.4 Ruling out a Schwarzschild Black Hole

As mentioned above, Dovčiak et al. and Beckwith & Done argue that broad lines cannot be used as BH spin diagnostics due to the degeneracy that exists between the physical parameters that go into composing the line profile (Beckwith & Done 2004; Dovčiak et al. 2004). We contend that this is not necessarily the case; broad lines *can* be used to constrain BH spin if one takes into account the physical realism of the best-fit parameters. The degeneracy between parameters makes it difficult to calculate the precise angular momentum for a given BH, but we can nonetheless statistically rule out certain regions of parameter space provided that the data used has the spectral resolution to enable accurate model fitting.

In the case of MCG–6-30-15, the Fabian et al. data set is noteworthy for its length and unprecedented resolution of the broad iron feature. This makes it an ideal candidate for examining the parameter space of the new models in question. The width of the iron line implies that this feature is produced in the accretion disk immediately surrounding a rapidly spinning BH, and indeed the best-fit `kerrdisk` parameters for the simplest model including an iron line (Model 2, from 2 – 10 keV) suggest that $a = 0.970^{+0.003}_{-0.015}$ with 90% confidence (see Fig. 4.2a). The `kerrdisk` parameters are consistent with those of the `kyrline` best fit as well. Given that the fits excluding emission from within the radius of marginal stability imply a near-maximal spin for the BH, here we pose the question “can we rule out the non-spinning case if we relax the restriction of no emission from within the radius of marginal stability?”

To answer this question we utilize the `kyrline` model, since `kerrdisk` does not yet include emission from within the ISCO. In previous fits to MCG–6-30-15 using low-spin BH models, it has been found that the fit demands an inner emission radius well within the radius of marginal stability (Dovčiak et al. 2004). Substituting two `kyrline` model

components for the `kerrdisk` component in the 2 – 10 keV fit, we freeze $a = 0.0$ and re-fit the data as in Model 2. Two `kyrline` components are used because the publicly released version of `kyrline` does not support a broken power-law emissivity index for the disk (as does `kerrdisk`), so we must divide the disk up into two effective regions: one extending outwards from r_{ms} , and one interior to r_{ms} representing the plunging region. Because the plunging region is physically distinct from the disk proper, any lack of continuity between either the emissivity indices or the fluxes of the two components is not considered problematic.

The simplest `kyrline` fit for a Schwarzschild BH is based on Model 2. Visually it does not differ perceptibly from the `kerrdisk` best fit for Model 2, and statistically it is a slightly better fit: $\Delta\chi^2/\Delta\text{dof} = -15/0$ between the two fits. Most notable about the fit, however, is that when we force $a = 0.0$, the fit demands an inner radius that is deep within the plunging region ($r_{\text{min}} = 3.43 \pm 0.19 r_{\text{g}}$ as compared with $r_{\text{ms}} = 6 r_{\text{g}}$ for a Schwarzschild BH) with an extremely high inner emissivity index $\alpha_1 = 9.08 \pm 1.36$. Within the plunging region of a Schwarzschild BH, we expect the radial component of the 4-velocity to be

$$u^r = -c \sqrt{\frac{8}{9} - \left(1 - \frac{2}{r}\right) \left(1 + \frac{12}{r^2}\right)} \quad (4.1)$$

where, here, r is measured in units of $r_{\text{g}} = GM/c^2$ (Reynolds & Begelman 1997). For $r \approx 3.43$ we have $u^r \approx -0.22c$, i.e., the material is already inflowing at mildly relativistic velocities. Hence, conservation of baryon number demands that this part of the accretion flow be extremely tenuous and, given that by assumption it is subjected to an intense X-ray irradiation, this material must be fully ionized (Reynolds & Begelman 1997; Young et al. 1998). More quantitatively, the analysis of Reynolds & Begelman shows that the ionization parameter of the accreting matter at this radius will exceed $\log \xi = 4$ for any reasonable accretion efficiency; this is essentially fully ionized and will not imprint any obvious atomic signatures on the backscattered spectrum. It is therefore extremely un-

likely that a disk with such a steep emissivity profile and an inner radius so deep within the plunging region is an accurate physical model of the real system.

We have also performed a Schwarzschild fit to the data based on the more complex best-fitting model from 0.6 – 10.0 keV (Model 5). Recall that in this case we have introduced an ionized disk reflection component to the fit, which serves the dual purpose of modeling the soft excess and the broad Fe-K α line at 6.4 keV. Whereas before in Model 5 we convolved our reflection spectrum with a `kerrconv` component, here we use a `kyconv` model instead because we are demanding that $a = 0.0$ in this case, and anticipate that a large fraction of the emission will come from within the ISCO, as was the case for our Schwarzschild fit based on Model 2 above. Following the approach outlined above, we use two `kerrconv` components to allow for a broken power-law emissivity index in the disk. Qualitatively similar results are obtained; the inner radius of the X-ray reflection in such a model is $r_{\min} = 3.02 \pm 0.31 r_g$ with an extremely steep inner emissivity index ($\alpha_1 = 15.00 \pm 3.12$). As before with the simpler case of a Schwarzschild fit to Model 2, this implies that the vast majority of the emission of this model component originates well inside the ISCO, which is not physically realistic. The ionization parameter for the reflector has also risen marginally for the Schwarzschild case from $\log \xi_{\text{refl}} = 2.03 \pm 0.03$ to 2.26 ± 1.13 . The iron abundance has remained very high at $\text{Fe}/\text{solar} = 10.0 \pm 0.23$, as was the case in Model 5. Even with these adjustments in parameters, however, the Schwarzschild fit visually fails to account for the entire breadth and shape of the 6.4 keV iron line. In this case, the formal $\chi^2/\text{dof} = 2855/1377$ (2.08), as compared with 1793/1374 (1.35) for the Model 5 fit where BH spin is a free parameter.

Based on these arguments for Model 2 and Model 5 (the best-fitting cases for 2 – 10 keV and 0.6 – 10 keV, respectively) we can make a strong case that a non-rotating BH cannot viably produce the broad iron feature in MCG–6-30-15.

4.3 Discussion

4.3.1 Summary of Results

In fitting the hard spectrum of MCG–6-30-15 with the `kerrdisk` model, we have shown that the data prefer a fit with a spin parameter that tends towards the maximum value. A non-spinning BH can produce a formally adequate fit (although still statistically worse than that achieved with a free spin parameter), but further requires a significant fraction of the X-ray reflection to originate unphysically deep within the plunging region. One might argue that for flows accreting at close to the Eddington rate, the radius of dynamical stability might be pushed to the marginally bound orbit, rather than the marginally stable orbit (Abramowicz et al. 1990; Chen et al. 1997). In principle this would mean that the optically thick part of the flow could come substantially closer to the event horizon, resulting in significantly more broad line contribution from this region. However, in the case of a Schwarzschild hole the marginally bound orbit is still at a radius of $r_{\text{mb}} = 4r_{\text{g}}$, which is well outside the minimum radius of emission we get for the Schwarzschild fit based on Model 5, where $r_{\text{min}} = 3.02 \pm 0.31 r_{\text{g}}$. The radial velocity of the infalling material at this point would be nearly $c/3$ if released from r_{mb} , so the material itself would be quite optically thin and highly ionized, and so would not be likely to contribute much to the overall iron line profile. Also, it is unlikely that MCG–6-30-15 is accreting close to the Eddington rate.

In fact, for the rapidly-spinning BH preferred by our spectral fitting, the issue of unmodeled emission from within the radius of marginal stability diminishes in importance. For such rapidly spinning BHs, the geometric area of the disk within this radius is small and the gravitational redshift of this region is extreme. Hence, we suspect that the inclusion of reasonable amounts of emission from within the radius of marginal stability will

have negligible impact on our best-fitting spectral parameters, including the spin of the BH.

The best-fitting model for the full 0.6 – 10 keV data set appears to be Model 5. The hard spectrum is best represented by a power-law continuum and two Gaussian features of iron at 6.4 (neutral) and 6.9 keV (ionized). The soft portion of the spectrum below ~ 2 keV is well fit by relativistically blurred emission reflected from the surface of an ionized disk that is modified by a two-zone WA, an iron absorption edge, and Galactic photoabsorption. This ionized emission also contributes to the breadth and morphology of the observed iron feature near 6.4 keV. As described above in §4.2.3, this model yields a formal, 90% confidence best-fit spin parameter for the BH in MCG–6-30-15 of $a = 0.989^{+0.009}_{-0.002}$. Due to the aforementioned degeneracies in the broad iron line model parameters (Chapter 3) this value should not be interpreted as exact, but the fact that near-maximal spin is approached in each of the Models 2-5 strongly indicates that the data prefer a rapidly spinning BH.

4.3.2 Conclusions

Both Dovčiak et al. and Beckwith & Done make valid points about the difficulty of accurately calculating the spin parameter of a BH based on broad line profiles from the disk alone (Beckwith & Done 2004; Dovčiak et al. 2004). Given the number of parameters governing the `kerrdisk` line profile (nine, to be exact), some degeneracy between them is certainly to be expected, and it is possible to generate statistically indistinguishable line profiles using different combinations of parameters. This does not render the use of broad lines as spin diagnostics obsolete, however: provided that one uses care in determining whether parameter values are physically reasonable, it is possible to at least constrain the spin parameter to be within a certain range of values. In the example of MCG–6-30-15 above, we have clearly shown that the data rule out a non-spinning black hole if we also

demand that the values for the disk emissivity indices are physically realistic. The plots of $\Delta\chi^2$ vs. a clearly show the improvement in fit achieved when one frees the spin parameter. In this case the fit strongly tends toward maximal spin.

The combination of such a high spin and such a high iron abundance in the disk may understandably give one pause when considering the precision of our best-fitting Model 5. Both a and Z_{Fe} push the upper limits of their respective parameter spaces in order to try to account for the extreme breadth and strength of the Fe-K α feature in the spectrum. As we have mentioned, however, in this thesis we are seeking to establish a robust method for constraining BH spin via X-ray spectroscopy and are not claiming that our best-fit parameter values should be interpreted as exact. The spin of the BH may indeed reach $a = 0.989$, but there could also be some contribution to the line from highly redshifted radiation originating from within the ISCO that we have not yet accounted for, which could reduce the need for such a high spin value. What we can say with confidence is that fits to the data with a Schwarzschild BH are not physically sound. Likewise, the disk may indeed have nearly ten times the solar value of iron, but underabundances in some of the lighter elements may also simulate an effectively iron-rich environment which could contribute to the observed width of the Fe-K α line (Reynolds et al. 1995). *Suzaku* observations of this source are already proving invaluable for untangling the parameters of the ionized reflection model (Miniutti et al. 2007). Much work remains to be done on the subjects of modeling accretion disks and isolating black hole spins, and improvements in the former will undoubtedly help us place more accurate constraints on the latter.

If MCG–6-30-15 is indeed a rapidly spinning BH, as seems likely given our spectral modeling, it is astrophysically interesting for several reasons. As mentioned in §4.1, rapidly spinning holes can, in principle, experience a magnetic torque by the fields threading the accretion disk at the radius of marginal stability. This torque can theoretically extract rotational energy from the hole itself, significantly enhancing the amount of dis-

sipation in the inner accretion disk. The steepest dissipation profiles would be obtained if the magnetic torque is applied completely at the radius of marginal stability (Agol & Krolik 2000). Therefore, only for rapidly spinning BHs would one expect to observe such a steep dissipation profile: in this scenario r_{ms} is dragged inward very close to the event horizon, so the torque is strongest here. Such an effect would manifest itself via strongly redshifted reflection features in the spectrum, since the strong dissipation very close to the event horizon would mean that most of the emission would originate from this region. Based on its own best-fit emission profile, MCG–6-30-15 may in fact be giving us a glimpse of this phenomenon at work (Wilms et al. 2001). It should be noted, however, that interpreting the detected reflection features in this way demands that little of the observed emission originate from the plunging region within r_{ms} . Taken in this context, the relatively steep emissivity index we found for the ionized disk in our best-fitting Model 5 ($a = 0.989$, $\alpha_1 = 6.06$) is not unexpected, and may be indicative of this type of magnetic torquing.

Finally, it is important to note that the 350 ks observation employed here for our spectral modeling provided us with an extraordinary number of photons to work with: well over 10^6 counts. This is due in part to the length of the exposure, but also to the intrinsic brightness of MCG–6-30-15 ($F_X \sim 6 \times 10^{-11}$ erg cm $^{-2}$ s $^{-1}$). With such a high number of counts we are able to better constrain the parameters in `kerrdisk` and `kerrconv`. Unfortunately, for many other AGN not as bright in X-rays and not as well-studied, we simply do not have enough data to constrain parameters such as BH spin as robustly as we would like. In the following Chapter we detail our analyses of several other broad iron line AGN using the techniques outlined in our studies of NGC 4593 and MCG–6-30-15.

Chapter 5

Spectral Fits to Other Broad Iron Line

AGN

We have presented detailed spectral fits for two quite different Sy-1 AGN: NGC 4593 (no evidence to support a broad iron line) and MCG–6-30-15 (evidence for the broadest iron line yet observed). These two sources represent opposite ends of the parameter space in terms of our ability to constrain BH angular momentum. Because we detect no broad Fe- $K\alpha$ feature in NGC 4593, we are unable to apply the `kerrdisk` and `kerrconv` models to fit for BH spin since we are not observing a line signature from the inner part of the disk where relativistic effects are important. It could be that the accretion disk is truncated at some large distance in this source, perhaps transitioning to an ADAF-type flow close to the event horizon. In the case of MCG–6-30-15, by contrast, we have an abundance of X-ray photons that clearly resolve a line with a broad red wing extending down to ~ 3 keV. These data have allowed us to place formal constraints on the BH spin of $a > 0.987$ (90% confidence level) although, as explained in the previous chapter, this constraint might weaken somewhat if the iron line emission region does in fact bleed inside of the ISCO.

In order to begin probing the question of BH spin distribution across the AGN pop-

ulation we clearly need to expand our sample. In this thesis we restrict our attention to several other nearby Sy-1 AGN in an effort to reduce the number of environmental variables that may be involved in spin determination (e.g., no GBHs, though we do intend to expand our source list further in the future to accommodate such objects and compare the results to those of our AGN sample). Because the `kerrdisk` and `kerrconv` models rely on the presence of broad iron lines in the X-ray spectrum in order to constrain BH spin, we have also restricted our source list to include only those Sy-1 AGN that have robustly been observed to harbor broad iron lines based on previous studies with *XMM-Newton* and/or *Chandra* (Miller 2007; Nandra et al. 2006).

The question of what BH spin distribution we should expect to see among Sy-1 AGN is not a simple one. Unlike GBHs, whose spins are thought to be chiefly natal due to the small masses and/or short lifetimes of their stellar companions, AGN are quite old and massive, and are thought to have grown from a combination of mergers and accretion over their long histories. By comparing observations of BHs in local galaxies and AGN to a model of what the BH mass function would look like for a given local population whose BHs were grown solely by accretion, Marconi et al. find that mergers are not significant in the evolution of local supermassive BHs. The authors suggest that mergers might play a more prominent role for SMBHs beyond $z = 3$ (Marconi et al. 2004). Determining the spin of such sources would therefore provide us with a new parameter to use in constraining the role and efficiency of accretion in evolving local SMBHs, and would also aid in assessing the relative contributions of accretion vs. mergers in higher redshift sources. Similarly, Volonteri et al. have used numerical simulations to predict how massive BHs should form and evolve. They find that the coalescence of comparable-mass BHs increases their BH spins, while the capture of smaller BH companions in randomly oriented orbits reduces the spin of the primary BH. Given the distribution of massive BH binary mass ratios in hierarchical models, binary mergers alone do not lead to a system-

atic spin-up or spin-down of SMBHs with time. By contrast, because of the alignment of a SMBH with the angular momentum of the outer accretion disk, gas accretion tends to increase BH spin over time. Overall in the Volonteri et al. models, accretion dominates over mergers and efficiently increases BH spin. The spin distribution is heavily skewed toward rapidly rotating holes, is already in place at early epochs, and does not change much below $z = 5$. If accretion occurs via a geometrically thin disk, about 70% of all massive BHs are maximally rotating. Even in the conservative case in which accretion is via a geometrically thick disk, about 80% of all massive BHs have $a > 0.8$ (Volonteri et al. 2005). Given these predictions and the increasing computing power of such complex numerical simulations, the time is ripe for culling observational evidence to see whether the data support such hypotheses.

In the following Section we outline the method used for the data reduction and spectral analysis of the AGN in our sample. We then discuss the modeling and results from each source in its own subsection. Finally, we compare the results from all the sources in our sample and discuss their physical implications for BH spin distribution and evolution among Sy-1 AGN.

5.1 Data Reduction and Spectral Analysis Methodology

Our source selection was based on recent work by Nandra et al. and a review by Jon Miller, both of whom consider the robustness of broad iron line detections across different source populations (Miller 2007; Nandra et al. 2006). The Miller review, in particular, collects all the recent X-ray data published on Seyfert sources and categorizes these objects by the strength and robustness of their broad iron line features. We have used these two studies as a guide for selecting the candidates for our sample.

Our data have been collected from the *XMM-Newton* Science Archive, using only

publicly available observations. *XMM-Newton* data were preferentially used as opposed to *Chandra* data because of the superior collecting area of *XMM-Newton* in the 2 – 10 keV band where the broad Fe-K α feature is the most prominent. Though *Suzaku* is producing very interesting results, there are not enough publicly available data collected by that instrument to undertake such a study at this time, though whenever possible we intend to use *Suzaku* data to supplement our *XMM-Newton* results in the future.

We focus our study exclusively on the EPIC-pn data due to cross-calibration issues mentioned previously in Chapter 2 between the pn, MOS and RGS instruments. Though the RGS spectra in particular can provide detailed insight into the 0.3 – 2.0 keV spectrum and help illuminate the nature of the soft absorption and excess seen in so many Sy-1 AGN, the cross-calibration issues unfortunately render it nearly impossible to correlate those results with the continuum and iron line spectrum observed by the EPIC-pn instrument. Because of the higher effective area of the pn, these data are more useful in our work.

For each source in question we have performed reprocessing (when necessary) and data reduction with the SAS version 7.0.0 software, including the latest CCF calibration files. Source and background spectra and light curves were extracted using the `xmmselect` task from the SAS GUI. Response matrices and ancillary response files were generated using the `rmfgen` and `arfgen` tasks. These were then grouped with the spectral files using the FTOOLS package `grppha` with a minimum of 25 counts/bin in order to use χ^2 as a meaningful goodness-of-fit statistic. Spectral analysis was carried out as before for NGC 4593 and MCG–6-30-15 with XSPEC version 11.3.2 and our local `kerrdisk` and `kerrconv` models installed.

We have made the spectral analysis method as uniform as possible for all the AGN examined. There are, however, certain intrinsic physical differences between the sources that must be taken into account in order to properly model the continuum and isolate

the iron line(s) in each case. Though all our sources are Sy-1 AGN, each system is unique in its physical properties. Some have more photons than others to work with, either because of higher flux, longer observation time or both. Some exhibit evidence for complex, multi-zone warm absorbers, whereas some show only cold absorption from neutral hydrogen along our line of sight. A soft excess is seen in some sources but not others. And of course, the strength and breadth of the Fe-K α line varies from source to source as well, though all have been chosen because they have previously shown evidence for broad iron lines.

In order to examine the iron line(s) in detail the continuum must first be accurately modeled. After excluding the energy ranges relevant to the iron line ($\sim 4.0 - 8.0$ keV) and the mirror edges ($\sim 1.5 - 2.5$ keV), we examine the rest of the $0.6 - 10.0$ keV spectrum, fitting it with a power-law continuum typical of an AGN which is then modified by cold photoabsorption from neutral hydrogen. We typically set the minimum value of N_{H} equal to the Galactic column density along our line of sight to the source¹ and allow it to vary as necessary to accommodate the cold absorption in the system. Some sources require a second, unabsorbed power-law component as well to properly model the basic continuum shape. We disregard energies below ~ 0.6 keV due to calibration uncertainties in this range for the EPIC-pn instrument.

If significant residual features remain after fitting this absorbed power-law which indicate the presence of a soft excess and/or warm absorption, we include these components one by one as long as they make a significant difference in the global goodness-of-fit according to the f -test ($\Delta\chi^2 \leq -4$ for each new parameter introduced into the fit (Bevington 1969)). The soft excess is typically parameterized by a blackbody component representing the thermal disk emission, but may also be modeled by bremsstrahlung emission or Comptonized emission from a thermal disk if either of these more complex forms gives

¹This parameter is determined from H I 21 cm surveys. See <http://heasarc.gsfc.nasa.gov/cgi-bin/Tools/w3nh/w3nh.pl> for the column density calculator and relevant references.

a significantly better reduction in χ^2 . The warm absorption is modeled using the same XSTAR-generated multiplicative table model described in Chapters 2 and 4 in the analysis of NGC 4593 and MCG–6-30-15. Solar abundances are assumed for all elements and the redshift is set at the source value. Some sources show no need for a WA model, while others statistically require up to two physically separate WA components, each exhibiting a distinct column density (N_{H}) and ionization parameter (ξ).

Once the continuum has been properly modeled, we freeze the parameter values for all components except the power-law spectral index (Γ) and normalization (flux in $\text{ph cm}^{-2} \text{s}^{-1}$) and restrict our energy range from 2.5 – 10.0 keV in order to focus on the hard X-ray spectrum and the iron line region. Including the energies from 4.0 – 8.0 keV again, we check for residual emission (or absorption) lines from 6.4 – 6.97 keV, indicating the presence of unmodeled neutral and/or partly ionized Fe-K α in the spectrum. Because these sources have been pre-determined to possess significant, broadened iron emission, such residual emission features are seen in each case. We begin by attempting to fit the 6.4 keV line of neutral iron (and any other ionized lines) with a simple Gaussian feature, with the line width frozen at $\sigma = 0$ keV (i.e., intrinsically narrow) and the redshift again set to the source value. As expected, in each case we note significant residual “wings” remaining around the Fe-K α feature after this narrow core was fit, indicating the presence of a broad component to the line.

To assess the robustness of this broad iron component and to obtain constraints on the BH spin, if possible, we then run each source through an “analysis tree” of progressively more complex modeling. Our procedure is outlined below:

1. Add in a `laor` component ($a = 0.998$) at the energy of the Fe-K α line and refit, noting the corresponding change in χ^2/dof to verify whether a broad line is statistically warranted in the model. Also note the inner radius of disk emission: a broad line with the potential to diagnose BH spin should have an inner disk radius

of $r_{\min} \lesssim 6r_g$. We relax this restriction here to allow for differences in fit that may be achieved through different models, requiring that $r_{\min} \lesssim 20r_g$.

- If the broad line is *not* statistically warranted, simply constrain the upper limit of the equivalent width of the line.
 - If the broad line is at least marginally statistically warranted, replace the `laor` component with a `kerrdisk` component ($a = 0 - 0.998$) and refit, noting again the corresponding change in χ^2/dof . The inner disk radius and BH spin as well as their statistical constraints should also be noted.
2. Rather than simply modeling the Fe-K α line in isolation, replace the broad line component with a static ionized disk reflection spectrum (Ross & Fabian 2005).
 3. To the static ionized disk reflection spectrum, add in the effects of relativistic smearing from the spacetime around a maximally rotating BH using the `kdblur` convolution model ($a = 0.998$). Again note the statistical difference in the goodness-of-fit to determine the importance of relativistic effects, as well as the inner radius of disk emission. This gives us a rigorous measure of the degree to which broadening is required even when reflection is accounted for.
 - If the inner radius of disk emission is sufficiently close to the event horizon (again using $r_{\min} \lesssim 20r_g$), the line may be sufficiently broad and relativistic effects may be sufficiently important to allow us to constrain BH spin. Replace the `kdblur` component with `kerrconv` ($a = 0 - 0.998$) in order to place statistical constraints on r_{\min} and a .

It should be noted that we force the outer radius of disk emission to be $r_{\max} = 400r_g$ (or $400r_{\text{ms}}$ in the case of `kerrdisk` and `kerrconv`, which parameterize disk emission radius in units of the radius of marginal stability) in all the broad line fits. The value

itself is somewhat arbitrary; the purpose of freezing this component at a large value is to force the inner portions of the disk to determine the line profile morphology. For the ionized disk component, we begin with the assumption of solar iron abundance and relative neutrality ($\text{Fe}/\text{solar} = 1$ and $\xi = 30$). If the fit is sufficiently robust, we then relax these assumptions and allow these two parameters to fit freely. For `kerrdisk` and `kerrconv`, we initially assume that the inner and outer portions of the disk emit under the same emissivity index: $\alpha_1 = \alpha_2$, where the disk radiates as $r^{-\alpha}$ at any given radius. Again, if the fit is sufficiently robust, these indices are "untied" and allowed to each fit freely, but due to limitations in the number of photons we have for each data set, the only source with enough counts to support a scenario where $\alpha_1 \neq \alpha_2$ is MCG–6-30-15.

5.2 Results for Our Sample of Sy-1 AGN

As mentioned in the previous Section, we have selected the AGN for our sample primarily based on the research performed by other groups on the robustness of broad iron line observations in various AGN and the likelihood of obtaining viable spin constraints from these sources using the iron line method (Miller 2007; Nandra et al. 2006). In particular, Jon Miller discusses recent results from 30 Seyfert AGN in which relativistic disk lines have been detected and published, and divides those sources up into three "tiers" based on the nature and robustness of the detections. Many of the sources overlap with those presented in Nandra et al. Though we have examined observed spectra from all of the 9 AGN listed in Tier 1 (the most robust cases), NGC 3516 and NGC 4151 were not included in our study due to their extremely complex soft spectra (Schurch et al. 2004; Turner et al. 2005). We did analyze the other 7 sources in full: 3c120, MCG–6-30-15, MCG–5-23-16, NGC 2992, NGC 4051, NGC 3783 and Mrk 766. Additionally, we have examined 3 other sources from Tier 3 that are mentioned prominently in Nandra et al.: Fairall 9, Ark 120

and 3c273.

We present the results of our spectral analysis of these sources in the following Sections.

5.2.1 MCG–5-23-16

MCG–5-23-16 is a moderately absorbed Seyfert galaxy of intermediate type (Sy-1.9). It is relatively nearby at a redshift of $z = 0.0085$, and with a typical 2 – 10 keV flux of $F_{2-10} \sim 8 \times 10^{-11} \text{ erg cm}^{-2} \text{ s}^{-1}$ it is one of the brightest known Seyfert galaxies (Reeves et al. 2006). The source has been observed previously to have a soft excess below $\sim 1 \text{ keV}$ and an absorbing column of $N_{\text{H}} \sim 10^{22} \text{ cm}^{-2}$ (Balestra et al. 2004; Dewangan et al. 2003), and *ASCA* observations have indicated the presence of a broad Fe-K α line of $EW \sim 200 \text{ eV}$ (Weaver et al. 1998, 1997). The line was successfully modeled with a narrow core at the rest-frame energy of 6.4 keV and a broad component superposed on it. This feature was modeled with similar success in the *XMM-Newton* observations of Dewangan et al. and Reeves et al. , as well as the *Suzaku* observation also published by these authors (Reeves et al. 2007).

In December 2005, MCG–5-23-16 was simultaneously observed with *XMM-Newton*, *Chandra*, *Suzaku* and *RXTE*. The *XMM-Newton* results are reported by Reeves et al. , and our data reduction followed that work (Reeves et al. 2006). The EPIC-pn instrument had a net exposure of 96 ks and returned $\sim 2.2 \times 10^6$ photons after filtering.

As suggested by Reeves et al. , a simple photoabsorbed power-law fit does not model the continuum well, especially below $\sim 1 \text{ keV}$. Adding in a source of soft thermal emission also leaves prominent residuals and does not adequately account for the shape of the soft excess, so following the lead of Reeves et al. we have employed a two-power-law model (Reeves et al. 2006): one of the power-law components is affected only by Galactic photoabsorption ($N_{\text{H}} = 8 \times 10^{20} \text{ cm}^{-2}$ as per Reeves et al.), and hence leaves

the AGN system effectively unscattered, while the other component is also subject to absorption intrinsic to the AGN, in this case with a fitted absorbing column density of $N_{\text{H}} = 1.19 \times 10^{22} \text{ cm}^{-2}$. This component also experiences scattering within the system. Both power-law indices are locked together, indicating that the two components originate from the same physical reservoir of photons with $\Gamma = 1.66$. Calculating the ratio of the flux of the scattered power-law component to the unscattered power-law component (from 0.6 – 10.0 keV, fitting only the continuum) yields an estimate of the optical depth of the scattering plasma. In this case $\tau = 7.37 \times 10^{-4} \text{ ph cm}^{-2} \text{ s}^{-1} / 1.83 \times 10^{-2} \text{ ph cm}^{-2} \text{ s}^{-1} \approx 0.04$, so the scattered fraction is low, implying that the electron plasma is optically thin.

The continuum spectrum also shows evidence for two prominent, narrow emission lines of iron $K\alpha$ and $K\beta$ (at $E_{K\alpha} = 6.4 \text{ keV}$ and $E_{K\beta} = 7.0 \text{ keV}$, with $EW_{K\alpha} = 167 \text{ eV}$ and $EW_{K\beta} = 104 \text{ eV}$, respectively), as well as three narrow absorption lines of intermediately ionized iron at $E_1 = 7.24 \text{ keV}$, $E_2 = 7.48 \text{ keV}$ and $E_3 = 7.85 \text{ keV}$ ($EW_1 = -79 \text{ eV}$, $EW_2 = -121 \text{ eV}$, and $EW_3 = -143 \text{ eV}$, respectively).

After successfully modeling the continuum and narrow line parameters for MCG–5-23-16, we restricted our attention to the hard spectrum (2.5 – 10.0 keV) and analyzed the broad line component of this source using the method outlined above in §5.1. Note that eliminating soft energies from the fit removed the statistical need for a second, soft power-law in the fit. For a full listing of best-fit model parameters and error bars for MCG–5-23-16, see Table 5.1. The residual iron line feature in the hard spectrum is shown in Fig. 5.1. Our best fit to this feature is shown in Fig. 5.2, and the relative contributions of the individual model components are shown in Fig. 5.3. The best-fitting model for MCG–5-23-16 is the ionized disk reflection spectrum (Ross & Fabian 2005) convolved with `kerrconv`. Although we were not able to constrain the BH spin in this source, we did achieve a fit constraint on the inner radius of the disk emission: $r_{\text{min}} \sim 16 r_{\text{ms}}$, which equates to $84 r_{\text{g}}$ if we convert using the fit value for BH spin ($a = 0.362$). Given that

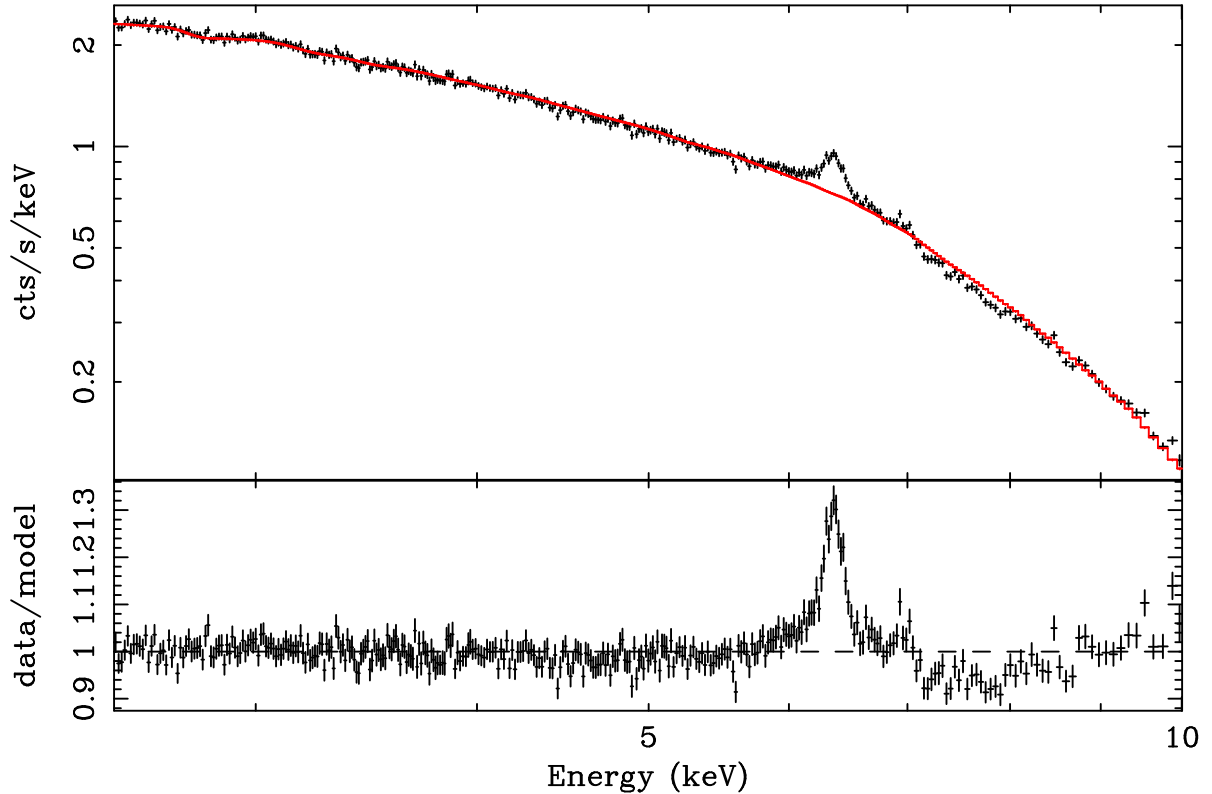


Figure 5.1: The 2.5 – 10.0 keV spectrum of MCG–5-23-16 fit with a two-power-law model modified by Galactic photoabsorption. Note the prominent residual iron feature that remains with a rest-frame energy of 6.4 keV, as well as several other emission and absorption features and a hard energy “tail” above 8 keV, indicating the possible presence of ionized disk reflection.

the effective inner edge of the disk is not within the radius of marginal stability for a Schwarzschild BH, it is not surprising that we were not able to constrain the value of the BH spin in this source.

5.2.2 NGC 3783

NGC 3783 is a bright, nearby Sy-1 galaxy at a redshift of $z = 0.0097$. It was first detected in X-rays with the *Ariel-V* all-sky survey (McHardy et al. 1981) and subsequently in the high Galactic latitude survey conducted by *HEAO-1* (Piccinotti et al. 1982). Since these early detections, there have been many observations of NGC 3783 with higher resolution instruments: A *ROSAT* observation of the source showed evidence of an ionized

Model Component	Parameter	Value
phabs	$N_{\text{H1}} (\text{cm}^{-2})$	8×10^{20}
phabs	$N_{\text{H2}} (\text{cm}^{-2})$	$1.19_{-0.01}^{+0.01} \times 10^{20}$
po	Γ_{po} flux ($\text{ph cm}^{-2} \text{s}^{-1}$)	$1.66_{-0.01}^{+0.01}$ $1.98_{-0.13}^{+0.04} \times 10^{-2}$
zgauss	E (keV) flux ($\text{ph cm}^{-2} \text{s}^{-1}$) EW (eV)	6.40 $4.00_{-0.32}^{+0.35} \times 10^{-5}$ $167.00_{-13.36}^{+14.61}$
zgauss	E (keV) flux ($\text{ph cm}^{-2} \text{s}^{-1}$) EW (eV)	7.00 $9.80_{-2.87}^{+2.98} \times 10^{-6}$ $104.00_{-30.46}^{+31.62}$
zgauss	E (keV) flux ($\text{ph cm}^{-2} \text{s}^{-1}$) EW (eV)	7.24 $-7.39_{-2.73}^{+2.84} \times 10^{-6}$ $-78.70_{-29.07}^{+30.24}$
zgauss	E (keV) flux ($\text{ph cm}^{-2} \text{s}^{-1}$) EW (eV)	7.48 $-6.93_{-2.84}^{+2.83} \times 10^{-6}$ $-121.00_{-49.59}^{+49.41}$
zgauss	E (keV) flux ($\text{ph cm}^{-2} \text{s}^{-1}$) EW (eV)	7.85 $-9.62_{-2.86}^{+2.90} \times 10^{-6}$ $-143.00_{-42.51}^{+43.11}$
kerrconv	α_1 α_2 $r_{\text{br}} (r_{\text{ms}})$ a $i (^{\circ})$ $r_{\text{min}} (r_{\text{ms}})$ $r_{\text{max}} (r_{\text{ms}})$	$2.45_{-0.61}^{+0.59}$ $2.45_{-0.61}^{+0.59}$ 6.0 — — — $45.88_{-19.42}^{+2.34}$ $15.66_{-7.33}^{+13.40}$ 400
reflion	Fe/solar ξ_{refl} Γ_{refl} flux ($\text{ph cm}^{-2} \text{s}^{-1}$)	$0.61_{-0.05}^{+0.08}$ < 31.09 $1.66_{-0.01}^{+0.01}$ $1.64_{-0.10}^{+0.10} \times 10^{-5}$
χ^2/dof		1484/1487 (1.00)

Table 5.1: Best-fitting model parameters for the 2.5 – 10.0 keV spectrum of MCG–5-23-16, including components and parameter values from 0.6 – 1.5 keV for completeness. The energies from 1.5 – 2.5 keV were not included due to the presence of absorption edges from the *XMM-Newton* mirrors. Error bars are quoted at 90% confidence. For the zgauss lines, we required each to be intrinsically narrow, i.e., $\sigma = 0.0$. Redshifts were frozen at the cosmological value for the source, in this case $z = 0.0085$. Note the absence of warm absorption and a soft excess in this object. When no error bars are quoted, the parameter in question is frozen at the given value.

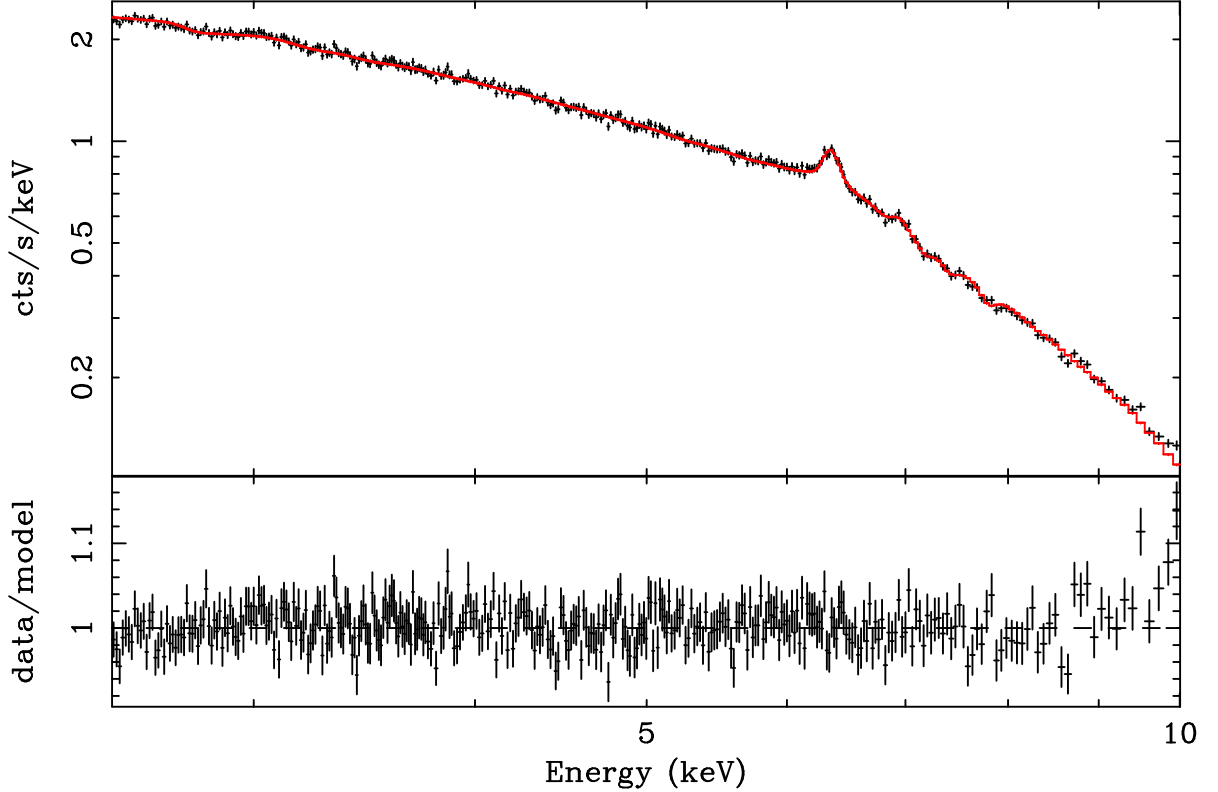


Figure 5.2: The 2.5 – 10.0 keV best-fit model for MCG–5-23-16, including our continuum model, two narrow emission lines, and five narrow absorption lines as well as an ionized disk reflection spectrum convolved with our `kerrconv` relativistic smearing kernel. The residuals have all but disappeared. For parameter values, see Table 5.1.

absorber in the soft band (Turner et al. 1993), which was confirmed during ASCA observations (George et al. 1998a, 1995). High-resolution grating observations of NGC 3783 with *Chandra* and *XMM-Newton* followed, unveiling the soft spectrum of this source in detail (Behar et al. 2003; Blustin et al. 2002; Kaspi et al. 2002, 2001, 2000). The higher signal-to-noise of *XMM-Newton*, in particular, has also enabled the iron line to be studied extensively in this source (Reeves et al. 2004). Using two observations from December 2001, Reeves et al. have obtained ~ 240 ks of data on NGC 3783. Their global fits to the merged EPIC-pn spectrum are currently second in length and depth only to the ~ 350 ks observation of MCG–6-30-15 (Fabian et al. 2002). In these observations, the source has an average 2 – 10 keV flux of $F_{2-10} = 6.8 \times 10^{-11}$ erg cm $^{-2}$ s $^{-1}$. The spectrum is noted to have iron line peaks at 6.4 keV and 7.0 keV, representing neutral Fe-K α ($EW \sim 120$ eV)

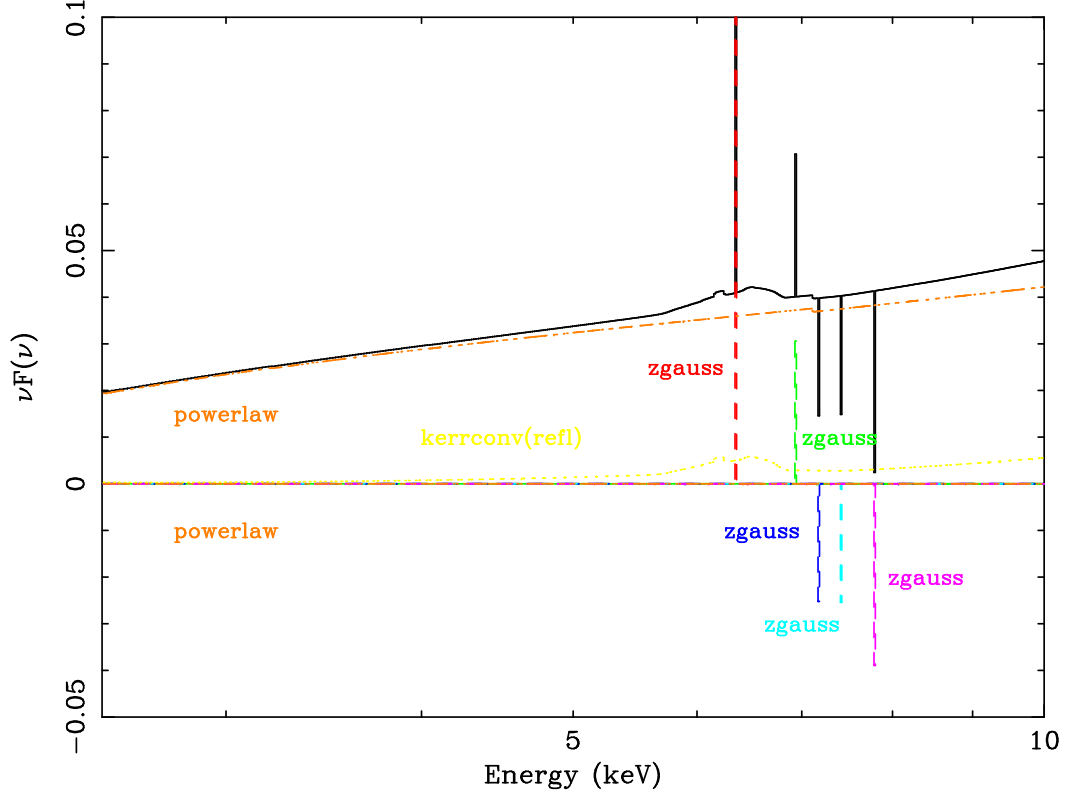


Figure 5.3: A νF_ν plot depicting the relative flux in each of the best-fit model components in the 2.5 – 10.0 keV spectrum of MCG–5-23-16.

and a blend of ionized Fe-K α and Fe-K β ($EW \sim 35$ eV), respectively. A strong absorption line of highly ionized iron is also observed at 6.67 keV that exhibits variability in direct correlation with that of the continuum flux. A weak red wing of the 6.4 keV line is noted by the authors, but once warm absorption is taken into account in the system the requirements for a broad Fe-K α component are significantly reduced (Reeves et al. 2004).

We analyzed the first of the two December 2001 *XMM-Newton* observations. We chose not to merge the event files of both data sets to avoid the uncertainties inherent in so doing, instead focusing on only one data set with an effective exposure time of ~ 120 ks and a total of $\sim 1.8 \times 10^6$ photons after filtering. This number of counts is still large enough to obtain valid statistical fits to the model parameters used. We follow the data reduction steps of Reeves et al. , excluding the last bit of the observation due to

contamination from a background flare. Our analysis follows in the same spirit as these authors, but in order to remain consistent with the method described above in §5.1 we do not make any assumptions about the soft spectrum and continuum emission based on prior RGS results (Blustin et al. 2002).

We begin our analysis of the time-averaged spectrum with a simple photoabsorbed power-law fit using the Galactic absorbing column of $N_{\text{H}} = 8.5 \times 10^{20} \text{ cm}^{-2}$, and neglecting the energy ranges associated with the mirror edges and the iron lines, as in §5.1. This fit leaves obvious residuals in all parts of the spectrum, however, and is especially poor for the soft energies below $\sim 1.5 \text{ keV}$. Continuum curvature associated with a soft excess and warm absorption are both clearly evident. As discussed by Reeves et al. , the fit is much improved with the addition of a thermal blackbody component ($kT \sim 0.07 \text{ keV}$, as compared with their value: $kT \sim 0.09 \text{ keV}$). We approach the question of the warm absorption similarly as well, using our XSTAR table model to parameterize the column density and ionization level of the absorbing medium, as do Reeves et al. As with these authors, we find statistical evidence for a two-zone warm absorption structure, though our values for the column densities and ionization parameters of these zones vary significantly from those of Reeves et al. We find $N_{\text{H1}} = 6.84 \times 10^{23}$ and $\log \xi_1 = 0.00$, with $N_{\text{H2}} = 1.58 \times 10^{23}$ and $\log \xi_2 = 1.40$, whereas Reeves et al. find $N_{\text{H1}} = 6.00 \times 10^{20}$ and $\log \xi_1 = 0.30$, with $N_{\text{H2}} = 4.60 \times 10^{22}$ and $\log \xi_2 = 2.90$. These differences are not surprising, however, because Reeves et al. base their fits on the RGS results for this source (Blustin et al. 2002). We do not use any *a priori* information to augment or guide the EPIC-pn spectral fits due to calibration uncertainties. Finally, we allowed the value of the neutral hydrogen absorbing column to vary in an effort to improve the goodness-of-fit and found that the spectrum preferred a higher value than the Galactic column: $N_{\text{H}} = 3.60 \times 10^{21} \text{ cm}^{-2}$. This was also in contrast to the Reeves et al. result, where the cold hydrogen column was held at the Galactic value and not permitted to vary.

Reeves et al. found two emission peaks in the spectrum at 6.4 keV ($EW \sim 120$ eV) and 7.0 keV ($EW \sim 35$ eV), representing cold Fe-K α and likely a blend of ionized Fe-K α and Fe-K β , respectively. The latter line, in particular, showed no appreciable variance over the observation, leading the authors to postulate a relatively distant origin for the lines away from the central parts of the accretion disk. A 6.67 keV absorption feature of highly ionized iron was also seen which did appear to vary with time and was strongest when the continuum flux was highest, suggesting an origin in the region of the warm absorber within 0.1 parsec of the nucleus. Though inclusion of the WA and this feature did lessen the statistical case for a broad iron line in NGC 3783, Reeves et al. nonetheless identified a residual broad feature which they fit using a diskline model with $\alpha \sim 3.3$, $i \sim 19^\circ$, and $EW \sim 58$ eV.

We also detected the emission and absorption features discussed by Reeves et al., though we found that the equivalent widths for the Fe-K α , Fe-K α /K β blend and ionized iron absorption lines differed from the fits performed by these authors: $EW_{K\alpha} = 79.0$ eV, $EW_{K\alpha/K\beta} = 23.9$ eV and $EW_{\text{abs}} = -25.1$ eV. We did not test the time variance of the absorption component because such an examination is beyond the scope of this work. It should also be noted that, contrary to the Reeves et al. analysis, we required the core of the 6.4 keV line to be intrinsically narrow, so it is not unusual that we obtain a smaller equivalent width than Reeves et al. When we included the broad component of the neutral K α line, the fit improved dramatically. Our best fit to the hard spectrum of NGC 3783 convolved an ionized disk reflection spectrum with `kerrconv`, as can be seen in Table 5.2 below, but due to the relative narrowness of the iron line we were not able to constrain the BH spin in this source. Not surprisingly, our constraints on the radial extent of the disk showed that $r_{\text{min}} < 390 r_{\text{ms}}$, or $< 985 r_{\text{g}}$, calculated using the nominal fit value of spin ($a = 0.869$). A line emitted from so far out in the disk would not exhibit relativistic signatures.

Model Component	Parameter	Value
phabs	$N_{\text{H}2}$ (cm ⁻²)	$3.60^{+0.01}_{-0.01} \times 10^{21}$
WA 1	$N_{\text{WA}1}$ (cm ⁻²) $\log \xi_{\text{WA}1}$	$6.84^{+0.42}_{-0.20} \times 10^{23}$ < 0.01
WA 2	$N_{\text{WA}2}$ (cm ⁻²) $\log \xi_{\text{WA}2}$	$1.58^{+0.06}_{-0.04} \times 10^{23}$ $1.40^{+0.04}_{-0.02}$
po	Γ_{po} flux (ph cm ⁻² s ⁻¹)	$2.50^{+0.02}_{-0.02}$ $4.60^{+0.09}_{-0.12} \times 10^{-4}$
bbbody	kT (keV) flux (ph cm ⁻² s ⁻¹)	$0.07^{+0.00}_{-0.00}$ $4.86^{+0.36}_{-0.31} \times 10^{-4}$
zgauss	E (keV) flux (ph cm ⁻² s ⁻¹) EW (eV)	6.40 $3.07^{+0.45}_{-0.46} \times 10^{-7}$ $79.00^{+11.58}_{-11.84}$
zgauss	E (keV) flux (ph cm ⁻² s ⁻¹) EW (eV)	7.00 $8.20^{+2.09}_{-2.05} \times 10^{-8}$ $23.90^{+6.44}_{-6.35}$
zgauss	E (keV) flux (ph cm ⁻² s ⁻¹) EW (eV)	6.67 $-1.12^{+0.21}_{-0.21} \times 10^{-7}$ $-25.10^{+4.71}_{-4.71}$
kerrconv	α_1 α_2 $r_{\text{br}} (r_{\text{ms}})$ a i (°) $r_{\text{min}} (r_{\text{ms}})$ $r_{\text{max}} (r_{\text{ms}})$	--- --- 6.0 --- 36^{+11}_{-10} < 391 400
reflion	Fe/solar ξ_{refl} Γ_{refl} flux (ph cm ⁻² s ⁻¹)	$0.19^{+0.03}_{-0.04}$ < 40.10 $2.50^{+0.02}_{-0.02}$ $2.97^{+0.74}_{-0.77} \times 10^{-6}$
χ^2/dof		1526/1486 (1.03)

Table 5.2: Best-fitting model parameters for the 2.5 – 10.0 keV spectrum of NGC 3783, including components and parameter values from 0.6 – 1.5 keV for completeness. The energies from 1.5 – 2.5 keV were not included due to the presence of absorption edges from the *XMM-Newton* mirrors. Error bars are quoted at 90% confidence. For the zgauss lines, we required each to be intrinsically narrow, i.e., $\sigma = 0.0$. Redshifts were frozen at the cosmological value for the source, in this case $z = 0.0097$. Note the two-zone warm absorber and blackbody soft excess present in this object, similar to many other Sy-1 sources.

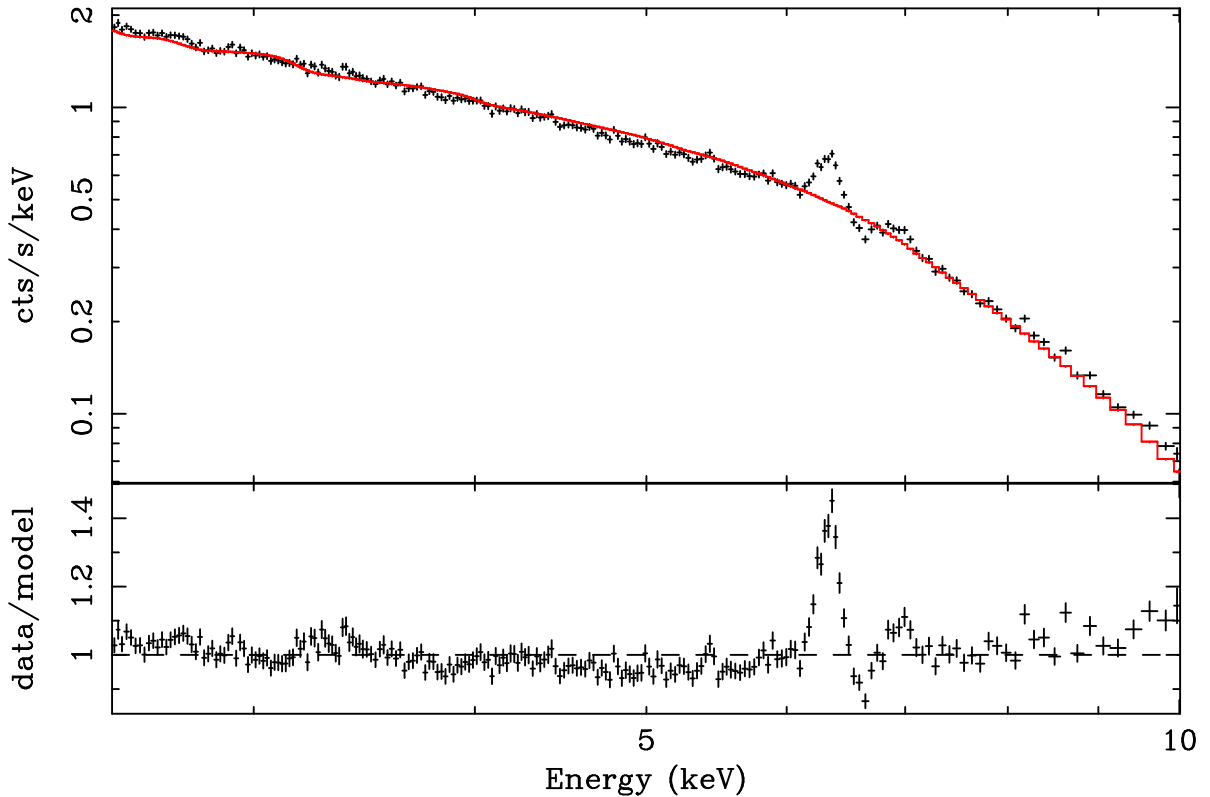


Figure 5.4: The 2.5 – 10.0 keV spectrum of NGC 3783 fit with a power-law model modified by Galactic photoabsorption, along with a two-zone warm absorber and a blackbody soft excess. Note the prominent residual iron features that remain with rest-frame energies of 6.4 keV and 7.0 keV, as well as an absorption feature of ionized iron at 6.67 keV.

5.2.3 Mrk 766

Mrk 766 is designated as a classic, bright NLS1 galaxy (Sy-1.5) with a redshift of $z = 0.0129$ and a typical 2 – 10 keV flux of $F_{2-10} \sim 2.5 \times 10^{-11} \text{ erg cm}^{-2} \text{ s}^{-1}$ (Pounds et al. 2003b). Previous X-ray observations of this source have provided contradictory evidence on the detection of a broad Fe-K α feature. Although not one of the most convincing cases, Mrk 766 was included in an *ASCA* spectral survey of bright Seyfert galaxies showing evidence of relativistic iron lines (Nandra et al. 1997). A separate analysis of simultaneous *ROSAT* and *ASCA* observations (Leighly et al. 1996), however, showed the X-ray spectrum to be described by a power-law of index increasing strongly with flux from $\Gamma \sim 1.6$, but with only a narrow Fe-K α emission line ($EW \sim 100 \text{ eV}$ at 6.4 keV). A later observa-

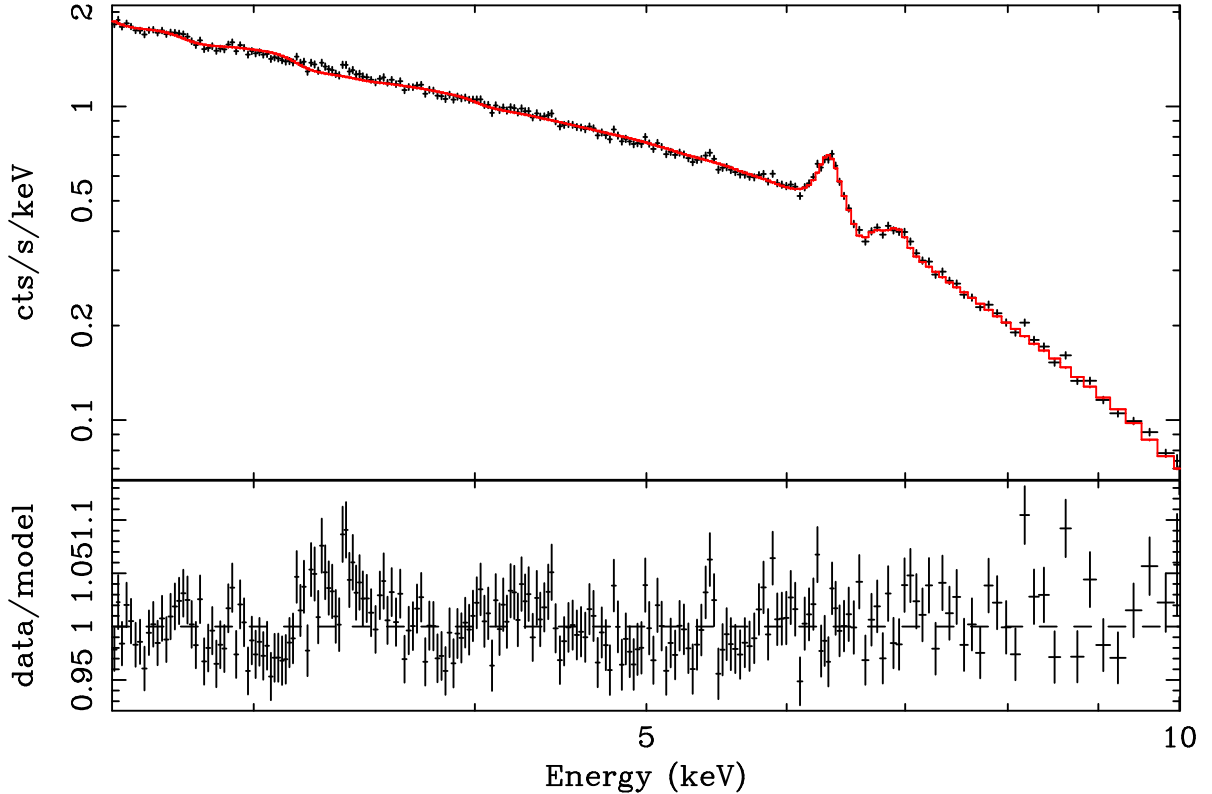


Figure 5.5: The 2.5 – 10.0 keV best-fit model for NGC 3783, including our continuum model, two narrow emission lines and a narrow absorption line as well as an ionized disk reflection spectrum convolved with our `kerrconv` relativistic smearing kernel. The residuals have all but disappeared. For parameter values, see Table 5.2.

tion with *BeppoSAX* found a steeper power-law ($\Gamma \sim 2.2$), and evidence for an absorption edge at ~ 7.4 keV (Matt et al. 2000), implying strong reflection from intermediately ionized material. Interestingly, based on *XMM-Newton* observations of the source, Turner et al. found that energy-time maps of Mrk 766 reveal a periodic energy shift in an ionized component of Fe-K α emission, with a period of ~ 165 ks. This can be interpreted as evidence for emission from orbiting gas within $\sim 100r_g$ of the central BH. A likely explanation is that this gas represents a hot spot on the disk illuminated by magnetic reconnection (Turner et al. 2006).

We examine the May 2001 *XMM-Newton* observation of Mrk 766 taken by Mason et al. , from which the RGS results were published in 2003 (Mason et al. 2003) and the EPIC spectra were explored more thoroughly by other authors (Pounds et al. 2003b; Turner et al.

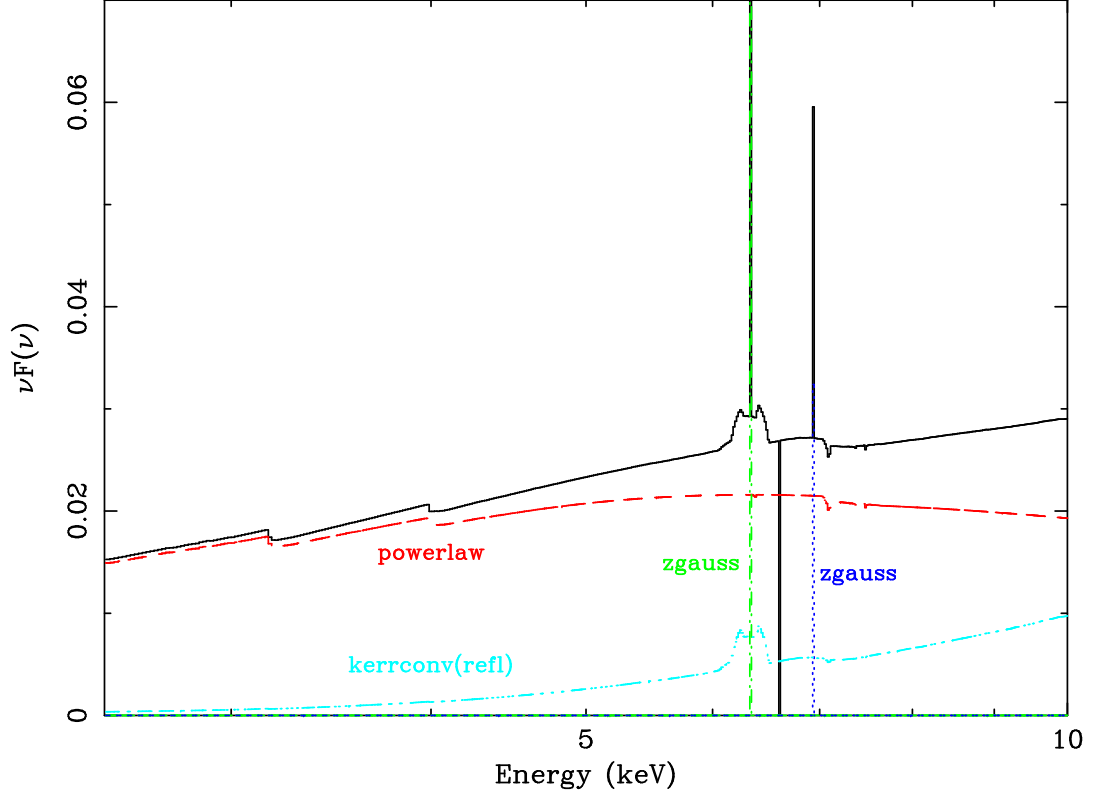


Figure 5.6: A νF_ν plot depicting the relative flux in each of the best-fit model components in the 2.5 – 10.0 keV spectrum of NGC 3783.

2006). In our re-analysis, the EPIC-pn data have an effective exposure time of 128 ks and the filtered data yield $\sim 2.92 \times 10^6$ photons.

Mrk 766 bears many spectral similarities to MCG–6-30-15, showing significant complexity beyond a simple photoabsorbed power-law fit. There is clear evidence for a thermal (bbbody: $kT = 0.08$ keV) soft excess below ~ 1 keV as well as two distinct physical zones of low ($N_{\text{H1}} = 5.26 \times 10^{22} \text{ cm}^{-2}$, $\log \xi_1 = 0.21$) to moderately ionized ($N_{\text{H2}} = 9.50 \times 10^{23} \text{ cm}^{-2}$, $\log \xi_2 = 3.04$) intrinsic absorption. These components exist in addition to cold absorption by the Milky Way ($N_{\text{H}} = 1.71 \times 10^{20} \text{ cm}^{-2}$). The power-law in this source has a spectral index of $\Gamma = 2.75$, comparable with the result published by Pounds et al. Unfortunately, these authors did not probe the spectrum below 3 keV, so we cannot compare our soft excess or warm absorption parameters to theirs. Our blackbody component has a flux that is 1% that of the power-law component.

The narrow Fe-K α core of Mrk 766 has a rest-frame energy of 6.4 keV, as expected, and an $EW = 33.7$ eV, again comparable with the findings of Pounds et al. Fitting this line with a Gaussian component leaves significant residuals strongly indicative of the presence of a broad line. This broad component is most successfully fit with a `kerrconv(refl)` model, yielding comparable results to the disk reflection model employed to model the broad iron line in Pounds et al. , though with different fit parameters. Our model also detects no absorption features above 8 keV, as discussed by Pounds et al. , possibly due to advances in modeling the reflection spectrum. The BH spin, to 90% confidence, is relatively high at $a > 0.85$ and the inner edge of the accretion disk is constrained to $r_{\min} < 2.25 r_{\text{ms}}$. The best-fit results are shown in Table 5.3. Figs. 5.7-5.9 show the iron line residual, best fit to this residual, and relative contributions of the individual model components, respectively.

5.2.4 3c273

3c273 is the most distant source in our sample at a redshift of $z = 0.1583$. Classified as a bright variable quasar, this AGN displays a strong jet and during epochs of radio-loudness it possesses the flat X-ray spectrum of a blazar, with highly beamed jet emission (Türler et al. 2006). When the jet is reduced in strength, however, this source has been observed to exhibit Sy-1-type accretion disk signatures such as a broad iron line. This minimum state occurred in March 1986 and allowed astronomers (Robson et al. 1986) to identify a new near-infrared spectral component. An even better opportunity arose in early 2004, when the sub-millimeter flux of 3c273 was observed to be almost two times lower than in 1986. This new minimum triggered a slew of simultaneous observations with instruments in all wavebands such as *INTEGRAL*, *XMM-Newton* and *RXTE*, among several other optical, radio and sub-millimeter telescopes. The 2 – 10 keV flux during this period was $F_{2-10} = 6.7 \times 10^{-11}$ erg cm $^{-2}$ s $^{-1}$. Such a low flux in 3c273 has only

Model Component	Parameter	Value
phabs	$N_{\text{H}} (\text{cm}^{-2})$	$1.71^{+0.24}_{-0.00} \times 10^{-2}$
WA 1	$N_{\text{WA1}} (\text{cm}^{-2})$	$5.26^{+0.16}_{-0.31} \times 10^{22}$
	$\log \xi_{\text{WA1}}$	$0.21^{+0.01}_{-0.03}$
WA 2	$N_{\text{WA2}} (\text{cm}^{-2})$	$9.50^{+0.05}_{-0.02} \times 10^{23}$
	$\log \xi_{\text{WA2}}$	$3.04^{+0.08}_{-0.07}$
po	Γ_{po}	$2.75^{+0.05}_{-0.06}$
	flux ($\text{ph cm}^{-2} \text{s}^{-1}$)	$2.05^{+0.08}_{-0.12} \times 10^{-4}$
bbody	kT (keV)	$0.08^{+0.00}_{-0.00}$
	flux ($\text{ph cm}^{-2} \text{s}^{-1}$)	$1.88^{+0.32}_{-0.26} \times 10^{-6}$
zgauss	E (keV)	6.40
	flux ($\text{ph cm}^{-2} \text{s}^{-1}$)	$4.71^{+1.35}_{-1.90} \times 10^{-8}$
	EW (eV)	$33.70^{+9.66}_{-13.59}$
kerrconv	α_1	$1.93^{+0.15}_{-0.13}$
	α_2	$1.93^{+0.15}_{-0.13}$
	$r_{\text{br}} (r_{\text{ms}})$	6.0
	a	$0.99^{+0.01}_{-0.14}$
	i ($^\circ$)	74^{+7}_{-1}
	$r_{\text{min}} (r_{\text{ms}})$	< 2.25
	$r_{\text{max}} (r_{\text{ms}})$	400
reflion	Fe/solar	1.0
	ξ_{refl}	579^{+274}_{-134}
	Γ_{refl}	$2.75^{+0.05}_{-0.06}$
	flux ($\text{ph cm}^{-2} \text{s}^{-1}$)	$8.29^{+1.05}_{-1.05} \times 10^{-6}$
χ^2/dof		1492/1309 (1.14)

Table 5.3: Best-fitting model parameters for the 2.5 – 10.0 keV spectrum of Mrk 766, including components and parameter values from 0.6 – 1.5 keV for completeness. The energies from 1.5 – 2.5 keV were not included due to the presence of absorption edges from the *XMM-Newton* mirrors. Error bars are quoted at 90% confidence. We required the zgauss line representing the core of the Fe-K α feature to be intrinsically narrow, i.e., $\sigma = 0.0$. Redshifts were frozen at the cosmological value for the source, in this case $z = 0.0130$. A two-zone warm absorber and blackbody soft excess are present in this object, as in MCG–6-30-15 and many other Sy-1 sources.

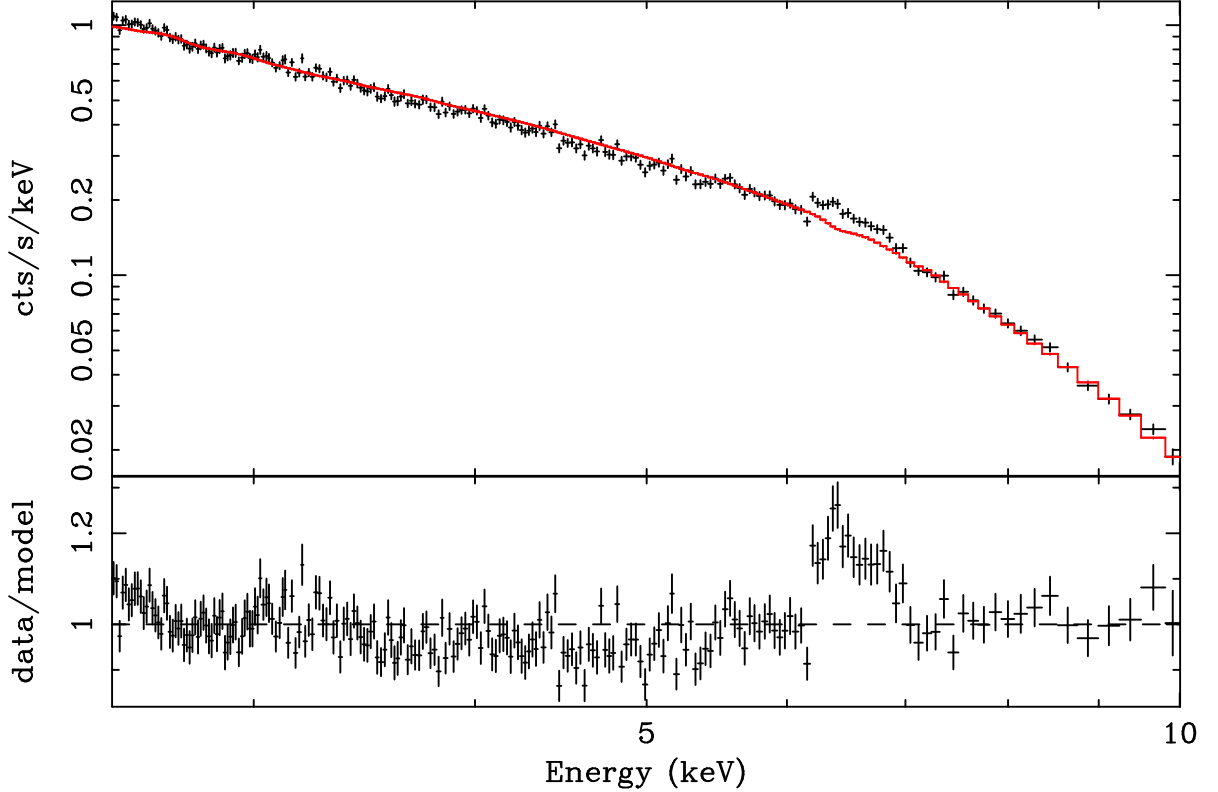


Figure 5.7: The 2.5 – 10.0 keV spectrum of Mrk 766 fit with a continuum composed of a power-law model modified by Galactic photoabsorption, a two-zone warm absorber model and a blackbody soft excess. Note the prominent residual iron feature that remains with a rest-frame energy of 6.4 keV.

been measured twice in the past, by *Ginga* in July 1987 (Turner et al. 1990) and by *BeppoSAX* on 18 July 1996 (Haardt et al. 1998), the latter of which was coincident with the low sub-mm flux mentioned above. This X-ray/sub-mm correlation strongly supports a synchrotron self-Compton origin for the X-ray jet emission in 3c273.

Türler et al. obtained a 20 ks *XMM-Newton* observation of 3c273 during this jet-minimum state in June 2004. We use their thin-filter EPIC-pn observation in the interest of collecting as many photons as possible, though due to photon pile-up it is necessary to exclude the centralmost region of the source, as detailed by the authors (Türler et al. 2006). In our filtered data set we capture $\sim 7.5 \times 10^5$ photons.

Türler et al. note the inadequacy of a simple photoabsorbed power-law fit to the data. Their best fit to the continuum is achieved using two power-law components: $\Gamma_{\text{hard}} =$

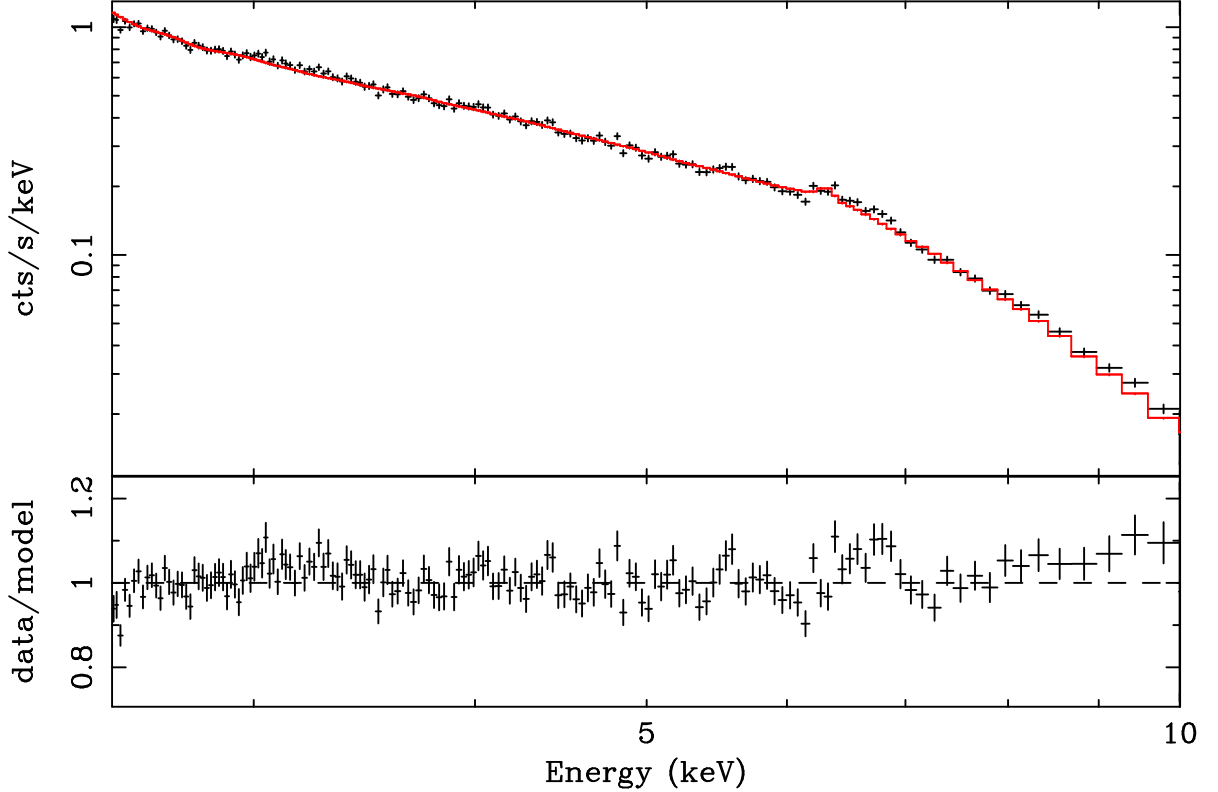


Figure 5.8: The 2.5 – 10.0 keV best-fit model for Mrk 766, including our continuum model and an ionized disk reflection spectrum convolved with our `kerrconv` relativistic smearing kernel. The residuals have mostly disappeared.

1.63 ± 0.02 and $\Gamma_{\text{soft}} = 2.69 \pm 0.06$, with the hard component flux ~ 2.3 times the soft flux. Both components were modified by Galactic photoabsorption with $N_{\text{H}} = 1.79 \times 10^{20} \text{ cm}^{-2}$. We based our initial continuum fit on theirs, with two power-law components: $\Gamma_{\text{hard}} = 1.72^{+0.11}_{-0.28}$ and $\Gamma_{\text{soft}} = 3.01^{+1.29}_{-0.71}$, both consistent with the Türlér et al. results. Our hard/soft flux ratio is 4.18, however, significantly higher than that calculated by Türlér et al. , and the error bars on the spectral indices led us to consider eliminating the soft component, in particular. Our best-fitting continuum model therefore, has only one power-law component at $\Gamma = 2.03$ and exhibits the same statistical goodness-of-fit as the two power-law model.

Evidence for excess emission from 2.5 – 7.0 keV was also found by Türlér et al. , supporting the presence of a broad Fe-K α line when 3c273 is in a jet-minimum state.

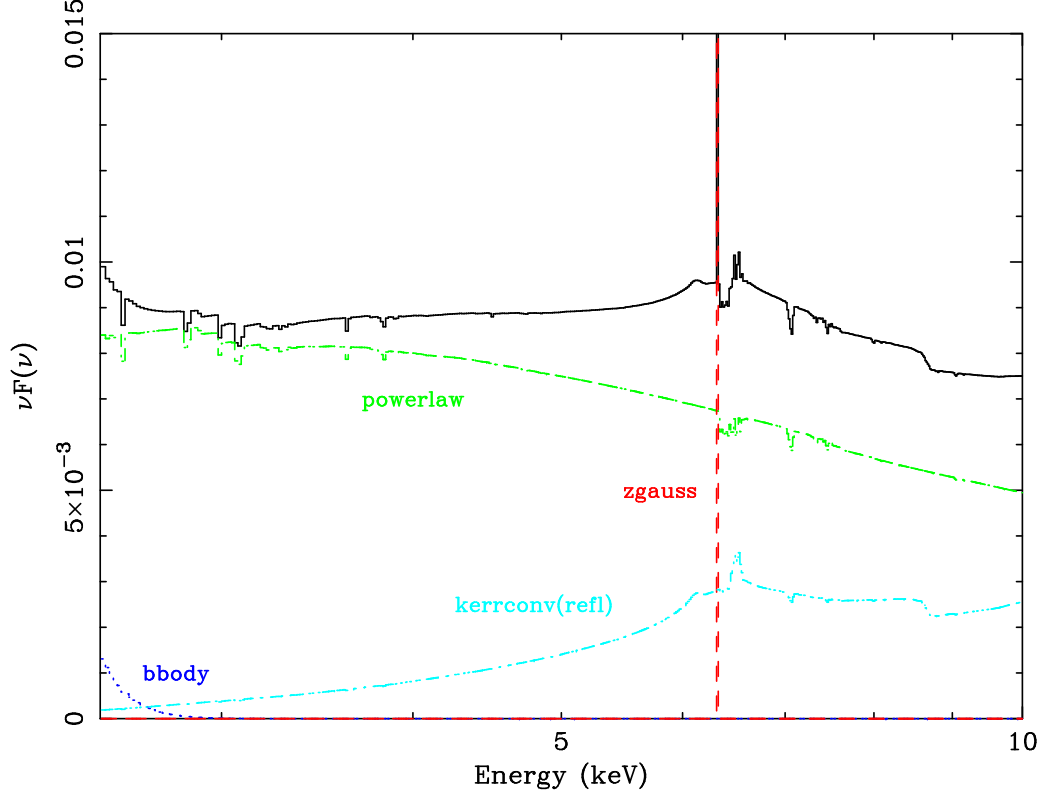


Figure 5.9: A νF_ν plot depicting the relative flux in each of the model components in the 2.5 – 10.0 keV spectrum of Mrk 766.

The authors quote this excess as significant at the 6σ level with an integrated flux of $2.6 \pm 0.4 \times 10^{-4} \text{ ph cm}^{-2} \text{ s}^{-1}$, corresponding to an $EW = 166 \pm 26 \text{ eV}$. These values are consistent with those reported from previous observations of the source in a jet-minimum state (Kataoka et al. 2002; Page et al. 2004; Yaqoob & Serlemitsos 2000). The breadth of the excess is not satisfactorily fitted by a Gaussian line or a diskline component from a non-rotating BH. If the line extent is real, the only remaining explanation, according to the authors, is that it is emitted from around a near-extreme Kerr BH. The sharp edge of the iron line at 7 keV suggests that the angle of inclination of the accretion disk is $35 - 40^\circ$ (Türler et al. 2006).

We find evidence for a similar excess around the Fe- $K\alpha$ line in our analysis. Interestingly, we do *not* see a narrow emission line at 6.4 keV, but rather the narrow line core seems to coincide with the He-like line of Fe- $K\alpha$ at 6.66 keV with an $EW = 73.3 \text{ eV}$.

This implies that the gas in this system is highly ionized, which is not surprising in such an active source. Visually, the residuals left over after fitting this narrow line suggest the presence of a broad component. Modeling this component with our analysis method only provides a marginal improvement in the global goodness-of-fit, however, so we cannot consider the presence of a broad line robust in 3c273 in spite of the suggestive appearance of the hard X-ray excess and residuals after adding in a narrow iron line. We are limited in this case by the distance of the source and the paucity of the data. With a 20 ks observation we have collected $< 3 \times 10^5$ photons from 2.5 – 10 keV. Given more observing time and a larger number of (pile-up free) photons, our line analysis would be significantly improved. Taking into account these caveats about the robustness of the broad line, our `kerrconv(refl)` model provides the best fit, as shown in Table 5.4. Figs. 5.10-5.12 show the iron line residual, best fit to this residual, and relative contributions of the individual model components in the best fit, respectively. To 90% confidence, $a > 0.72$ and $r_{\min} < 2.30 r_{\text{ms}}$.

The question of how BH spin correlates with radio-loudness still remains unanswered. Sikora et al. have examined the radio-loud/radio-quiet dichotomy in AGN and argue that BH spin is a critical factor in determining the radio-loudness of an AGN. The authors conclude that both spiral-hosted and elliptical-hosted AGN show radio-loudness increasing with decreasing Eddington ratio and that the large host-morphology-related difference between the radio-loudness reachable by AGN in disk vs. elliptical galaxies can be explained by the dual postulates that (1) the spin of a BH determines the jet outflow power, and (2) AGN BHs can reach large spins only in early type galaxies following major mergers (Sikora et al. 2007). The latter seems to conflict with the hypothesis that BHs most likely reach near-maximal spin values through steady accretion since mergers can theoretically occur with random BH spin directions (Volonteri et al. 2005). Also, the extremely high spin observed in MCG–6-30-15, in particular, serves as evidence that high BH spins

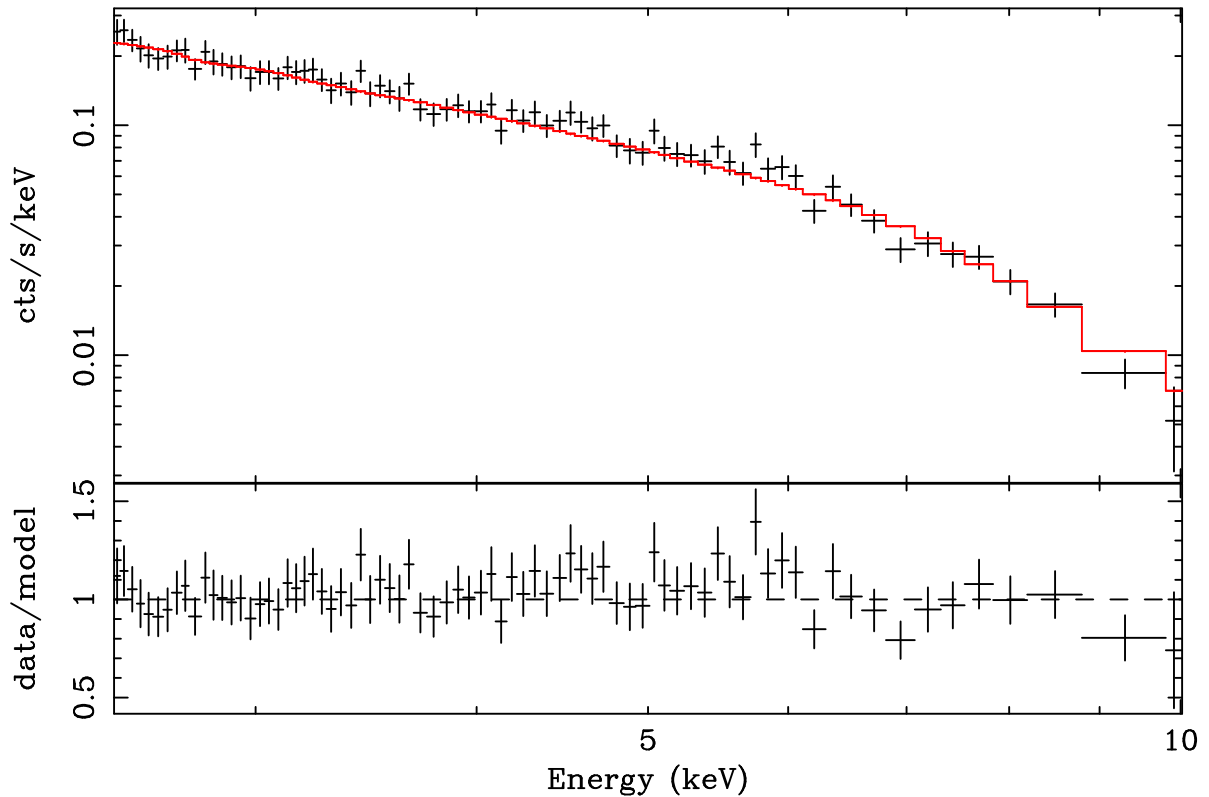


Figure 5.10: The 2.5 – 10.0 keV spectrum of 3c273 fit with a power-law model modified by Galactic photoabsorption. Note the subtle residual iron feature that remains with a rest-frame energy of 6.4 keV.

can be found in AGN hosted by disk-type galaxies. If the 3c273 result is found to be robust, we now also have an example of a radio-loud quasar with a moderately high BH spin. These conflicts between data and theory highlight the growing need for observations of BH spin in a large sample of AGN with varying physical characteristics (e.g., mass, radio-loudness, etc.).

5.2.5 3c120

Like the quasar 3c273, 3c120 is also a prominent radio source that has been seen to display broad, Sy-1-like emission lines in its optical spectrum when its jet is in a low state. Classified as a BLRG, it is the brightest such source in the sky though it is relatively distant at a redshift of $z = 0.0330$. Its 2 – 10 keV X-ray flux is quoted at $F_{2-10} =$

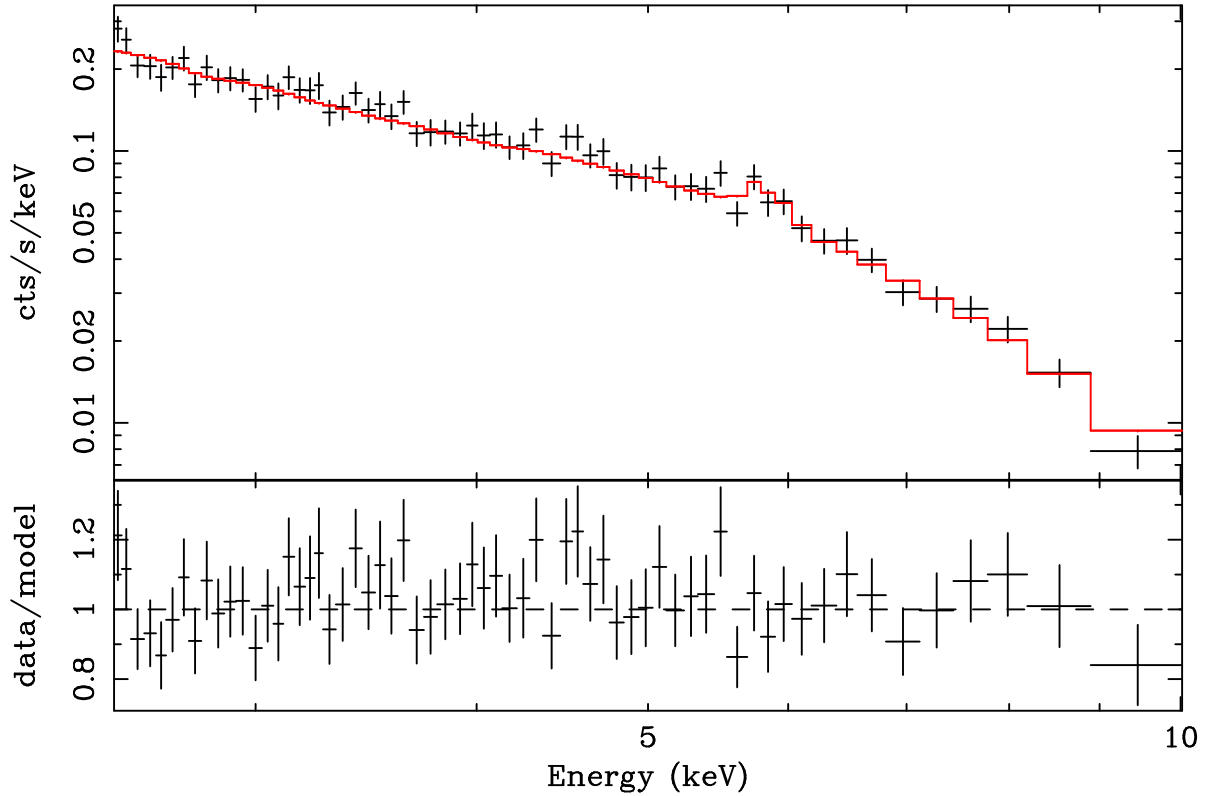


Figure 5.11: The 2.5 – 10.0 keV best-fit model for 3c273, including our continuum model and an ionized disk reflection spectrum convolved with our `kerrconv` relativistic smearing kernel. The residuals have mostly disappeared.

$4.2 \times 10^{-11} \text{ erg cm}^{-2} \text{ s}^{-1}$ (Sambruna et al. 1999). It is thought that perhaps the prodigious activity of this source could mean that it is in the late stages of a merger. This hypothesis is based on the residence of the AGN in a rather peculiar galaxy lacking much in the way of spiral structure and having a randomly oriented velocity field, in addition to showing evidence of recent starburst activity (Heckman et al. 1986). Radio observations have shown the presence of a superluminal jet ranging from sub-parsec to nearly 100-kpc scales. The upper limit on the inclination angle of the jet has been calculated to $i \leq 14^\circ$ (Eracleous & Halpern 1998), which may provide us with an independent constraint on the accretion disk inclination angle as well (Ballantyne et al. 2004). Although a very strong and broad Fe-K α line was originally detected with *ASCA* (Reynolds 1997; Sambruna et al. 1999), recent X-ray observations with *RXTE* (Eracleous et al. 2000; Gliozzi

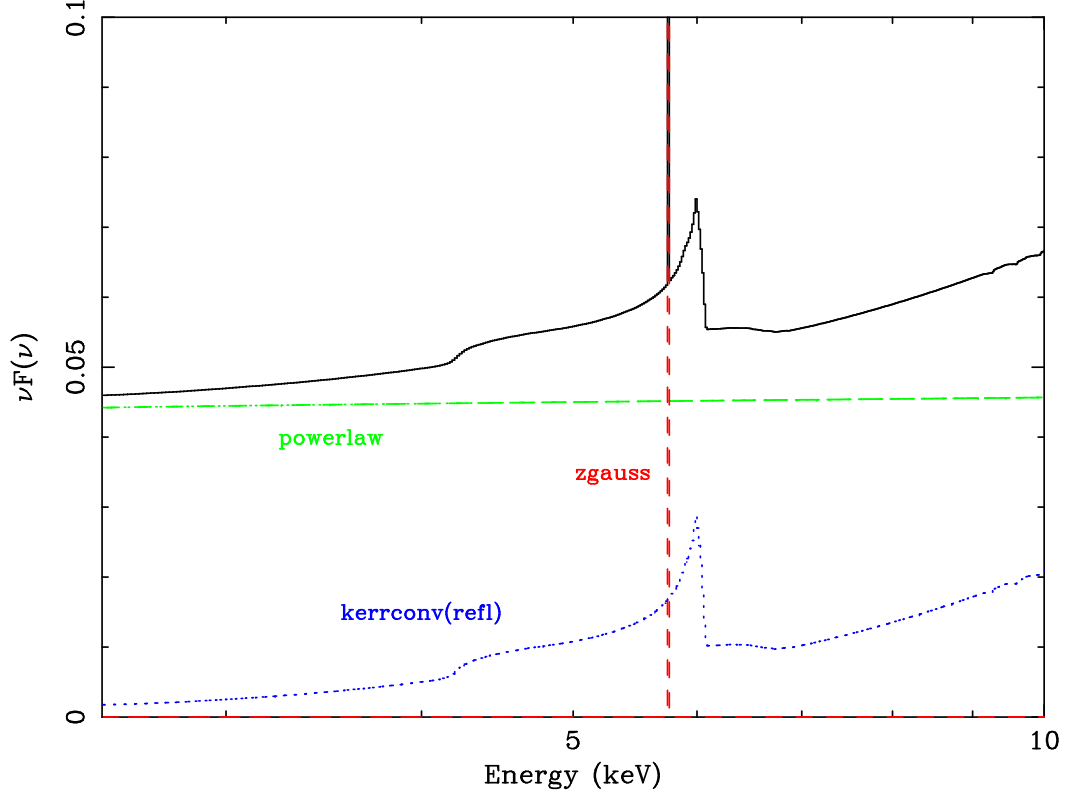


Figure 5.12: A νF_ν plot depicting the relative flux in each of the model components in the 2.5 – 10.0 keV spectrum of 3c273.

et al. 2003) and *BeppoSAX* (Zdziarski & Grandi 2001) have constrained the Fe-K α line to be only modestly strong at $EW \sim 100$ eV.

XMM-Newton observed 3c120 in August 2003 for 127 ks, yielding $\sim 2.08 \times 10^6$ photons in the filtered data set. The EPIC-pn data were analyzed fully and determined not to be affected by pile-up, and the results were published the following year along with a simultaneous *RXTE* observation (Ballantyne et al. 2004). We have re-analyzed this observation, following the data reduction of Ballantyne et al.

A soft excess is clearly seen in the data below ~ 1 keV, which is best fit with a bremsstrahlung emission model (zbremss), as suggested by Ballantyne et al. This emission, with $kT = 0.70$, is superposed on a photoabsorbed power-law continuum with $\Gamma = 1.81$ and possesses 91% of its flux. The goodness-of-fit is significantly improved with the inclusion of cold photoabsorption from neutral hydrogen within the system

Model Component	Parameter	Value
phabs	N_{H} (cm $^{-2}$)	$1.79^{+1.88}_{-0.00} \times 10^{-2}$
po	Γ_{po}	$2.03^{+0.30}_{-0.12}$
	flux (ph cm $^{-2}$ s $^{-1}$)	$3.82^{+0.47}_{-0.83} \times 10^{-2}$
zgauss	E (keV)	6.66
	flux (ph cm $^{-2}$ s $^{-1}$)	$9.30^{+0.76}_{-0.75} \times 10^{-5}$
	EW (eV)	$73.30^{+5.99}_{-5.91}$
kerrconv	α_1	$4.22^{+1.78}_{-1.48}$
	α_2	$4.22^{+1.78}_{-1.48}$
	$r_{\text{br}} (r_{\text{ms}})$	6.0
	a	> 0.72
	i ($^{\circ}$)	< 63
	$r_{\text{min}} (r_{\text{ms}})$	< 2.30
	$r_{\text{max}} (r_{\text{ms}})$	400
refl	Fe/solar	1.0
	ξ_{refl}	< 355.88
	Γ_{refl}	$2.03^{+0.30}_{-0.12}$
	flux (ph cm $^{-2}$ s $^{-1}$)	$1.70^{+10.12}_{-1.37} \times 10^{-4}$
χ^2/dof		288/265 (0.86)

Table 5.4: Best-fitting model parameters for the 2.5 – 10.0 keV spectrum of 3c273, including components and parameter values from 0.6 – 1.5 keV for completeness. The energies from 1.5 – 2.5 keV were not included due to the presence of absorption edges from the *XMM-Newton* mirrors. Error bars are quoted at 90% confidence. We required the zgauss line representing the core of the Fe-K α feature to be intrinsically narrow, i.e., $\sigma = 0.0$. Interestingly, this line was found at a moderate ionization state of iron (6.66 keV) rather than at the neutral rest-frame energy of 6.4 keV. Redshifts were frozen at the cosmological value for the source, in this case $z = 0.1583$. No warm absorption or soft excess is seen in this object.

($N_{\text{H}} = 1.35 \times 10^{21}$ cm $^{-2}$, total) on top of the absorption from our own Galaxy ($N_{\text{H}} = 1.11 \times 10^{21}$ cm $^{-2}$). Absorption from moderately ionized gas is also robustly detected with a column density of $N_{\text{WA}} = 1.51 \times 10^{22}$ cm $^{-2}$ and an ionization parameter of $\log \xi = 2.15$.

Two remaining residuals are detected around 6.4 keV and 6.9 keV, marking cold and ionized iron emission lines. The 6.9 keV line is quite weak, with an $EW = 11.9$ eV. Including another Gaussian line at 6.4 keV (with a fitted $EW = 4.5$ eV), we see that significant residuals remain around the wings of the line, strongly implying a broadened component. Running all of our broad line fits to this feature, we find that it is best mod-

eled with a `kerrconv(refl)` component, statistically, though its BH spin and the inner edge of the accretion disk are not well constrained: $a < 0.83$, $r_{\min} < 332 r_{\text{ms}}$. Even though we obtain 90% confidence constraints on the BH spin, given the uncertainty in r_{\min} we cannot claim robust evidence for a spin detection. In this case, the iron line is simply not broad enough to allow us to place meaningful constraints on BH spin. The best-fit parameter values for 3c120 are reported in Table 5.5. Figs. 5.13-5.15 show the iron line residual, best fit to this residual, and relative contributions of the individual model components in this fit. Note that we have allowed the inclination angle of the accretion disk to fit freely, not constraining its value to $i \leq 14^\circ$ as has been done in Ballantyne et al. in order to keep our results unbiased and see if we reach the same inclination angle independently. In our fit, we find that $i = 27 - 36^\circ$, with 90% confidence, and that constraining $i \leq 14^\circ$ worsens the statistical goodness-of-fit. This provides an interesting contrast to the results from radio observations.

5.2.6 NGC 2992

NGC 2992 is a Sy-1.9 galaxy that appears to show a broad iron line even though it is highly obscured. This source has been the subject of intense study due to the variability of its X-ray emission (Gilli et al. 2000). In 1997 and 1998, *BeppoSAX* caught NGC 2992 transitioning from a Compton-thick to a Compton-thin state, resulting in an order of magnitude increase in its X-ray luminosity as well as a qualitative difference in its spectral appearance, with more disk features (e.g., broad lines) being seen in several wavelengths. The source has a redshift of $z = 0.0077$. In the two *BeppoSAX* pointings, NGC 2992 displays a 2 – 10 keV X-ray fluxes of 0.63 and 7.4×10^{-11} erg cm⁻² s⁻¹ (Gilli et al. 2000).

We use the May 2003 *XMM-Newton* observation of NGC 2992, totaling 29 ks, which translates to $\sim 6.02 \times 10^5$ photons in the filtered data set. This observation appears to be unpublished, so all the fit values referenced herein are our own, compiled using the re-

Model Component	Parameter	Value
phabs	$N_{\text{H}} (\text{cm}^{-2})$	$1.35^{+0.01}_{-0.01} \times 10^{21}$
WA	$N_{\text{WA}} (\text{cm}^{-2})$	$1.51^{+0.68}_{-0.51} \times 10^{22}$
	$\log \xi_{\text{WA}}$	$2.15^{+0.33}_{-0.16}$
po	Γ_{po}	$1.81^{+0.01}_{-0.01}$
	flux ($\text{ph cm}^{-2} \text{s}^{-1}$)	$1.07^{+0.00}_{-0.02} \times 10^{-3}$
zbrems	kT (keV)	$0.70^{+0.15}_{-0.07}$
	flux ($\text{ph cm}^{-2} \text{s}^{-1}$)	$9.76^{+1.19}_{-1.73} \times 10^{-4}$
zgauss	E (keV)	6.40
	flux ($\text{ph cm}^{-2} \text{s}^{-1}$)	$1.70^{+13.16}_{-1.54} \times 10^{-7}$
	EW (eV)	$4.91^{+38.01}_{-4.45}$
zgauss	E (keV)	6.90
	flux ($\text{ph cm}^{-2} \text{s}^{-1}$)	$4.16^{+1.99}_{-1.91} \times 10^{-7}$
	EW (eV)	$11.90^{+5.69}_{-5.46}$
kerrconv	α_1	$0.24^{+1.15}_{-0.24}$
	α_2	$0.24^{+1.15}_{-0.24}$
	$r_{\text{br}} (r_{\text{ms}})$	6.0
	a	< 0.83
	i ($^\circ$)	28^{+8}_{-1}
	$r_{\text{min}} (r_{\text{ms}})$	< 332
	$r_{\text{max}} (r_{\text{ms}})$	400
reflion	Fe/solar	1.0
	ξ_{refl}	< 35.84
	Γ_{refl}	$1.81^{+0.01}_{-0.01}$
	flux ($\text{ph cm}^{-2} \text{s}^{-1}$)	$4.69^{+0.49}_{-0.36} \times 10^{-7}$
χ^2/dof		1468/1460 (1.01)

Table 5.5: Best-fitting model parameters for the 2.5 – 10.0 keV spectrum of 3c120, including components and parameter values from 0.6 – 1.5 keV for completeness. The energies from 1.5 – 2.5 keV were not included due to the presence of absorption edges from the *XMM-Newton* mirrors. Error bars are quoted at 90% confidence. We required the zgauss lines to be intrinsically narrow, i.e., $\sigma = 0.0$. Redshifts were frozen at the cosmological value for the source, in this case $z = 0.0330$. A warm absorber and bremsstrahlung soft excess are present in this object, as in many other Sy-1 sources.

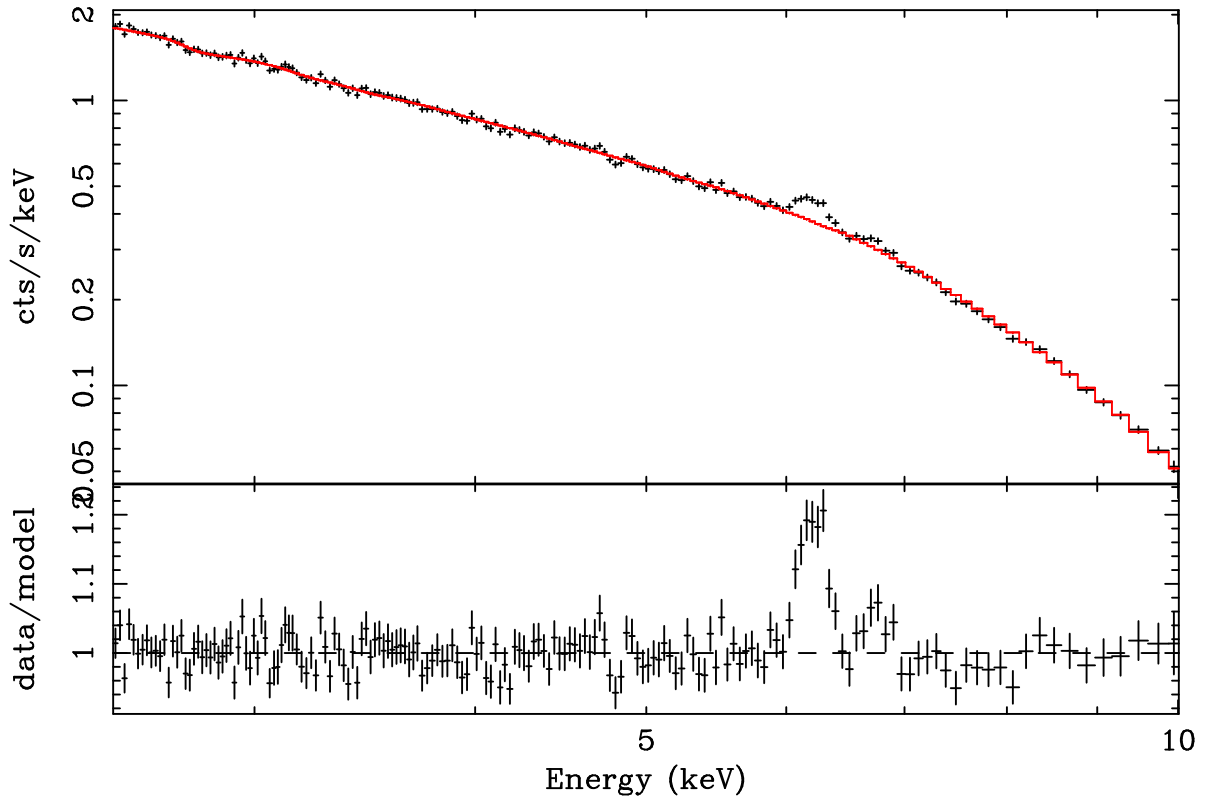


Figure 5.13: The 2.5 – 10.0 keV spectrum of 3c120 fit with a continuum composed of a power-law model modified by Galactic photoabsorption, a warm absorber model and a bremsstrahlung soft excess. Note the prominent residual iron features that remain with rest-frame energies of 6.4 keV and 6.9 keV.

duction and analysis methods detailed in the first portion of this Chapter and in particular in §5.1.

Upon first inspection, it is immediately clear that NGC 2992 is heavily absorbed below ~ 2 keV. Though statistical evidence exists for a soft excess, none of the telltale signatures of intrinsic warm absorption are present, and the flux decreases precipitously at soft energies. When a simple photoabsorbed power-law model plus blackbody emission is applied to the continuum, the remaining residuals on the soft end indicate that some absorption remains unaccounted for, but allowing the column density of hydrogen to fit freely above the Galactic value of $N_{\text{H}} = 5.26 \times 10^{20} \text{ cm}^{-2}$ neatly corrects the discrepancy. The final continuum parameters are $N_{\text{H}} = 5.11 \times 10^{21} \text{ cm}^{-2}$, $\Gamma = 1.69$ and $kT = 0.05$ keV with the power-law flux 1.4 times greater than that of the blackbody component.

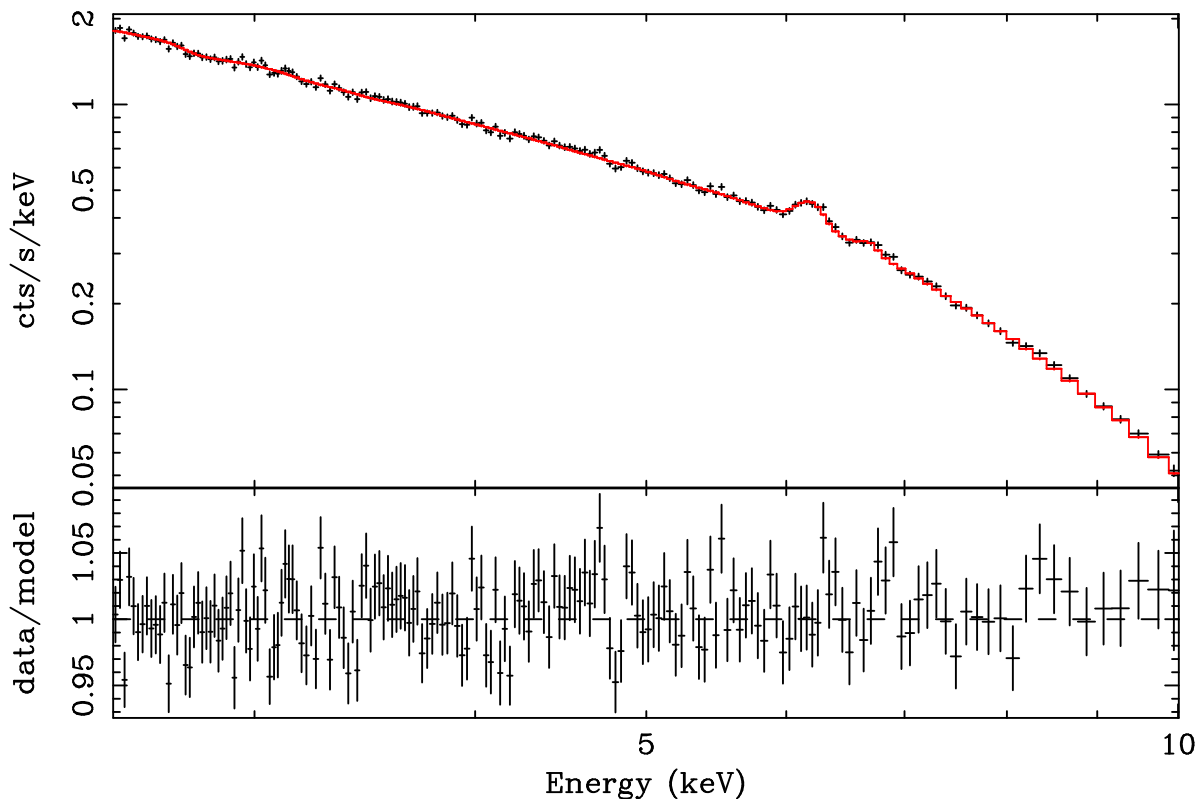


Figure 5.14: The 2.5 – 10.0 keV best-fit model for 3c120, including our continuum model and an ionized disk reflection spectrum convolved with our `kerrconv` relativistic smearing kernel. The residuals have all but disappeared.

The Fe-K α line is present with a narrow core at 6.4 keV and $EW = 38.8$ eV. Significant residuals remain surrounding the core, however, and the best statistical fit is achieved with a `kerrconv(refl)` model. See Table 5.6 for model parameters and error bars. Figs. 5.16-5.18 show the iron line residual, best fit to this residual, and relative contributions of the individual model components for the best fit. Note that the BH spin cannot be constrained. Constraints are also difficult to achieve on the disk emissivity index α , especially, though we have constrained the effective inner disk radius to $r_{\min} < 11.78 r_{\text{ms}}$. These large error bars are seen due to the paucity of photons in the hard band (2.5 – 10 keV) in this observation: with only 29 ks and a flux of $F_{2.5-10} = 8.06 \times 10^{-11}$ erg cm $^{-2}$ s $^{-1}$, we have $< 2 \times 10^5$ photons to use in spectral fitting. This is only a small fraction ($< 20\%$) of the number of counts we have at our disposal for

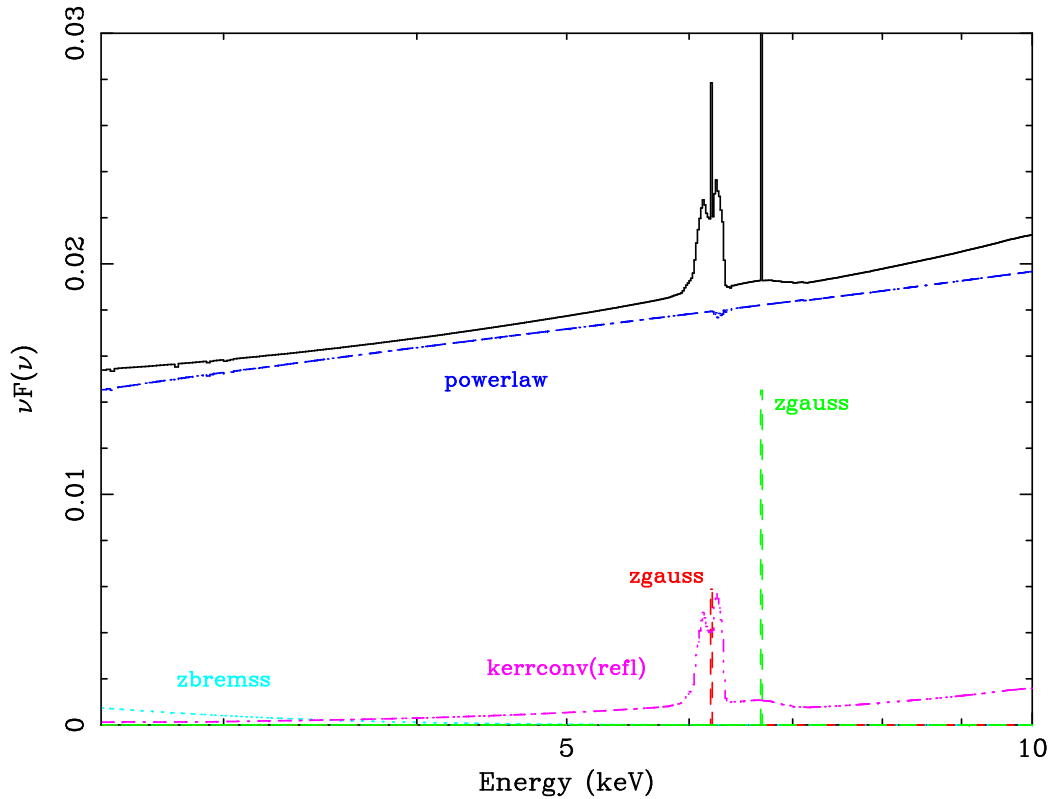


Figure 5.15: A νF_ν plot depicting the relative flux in each of the model components in the 2.5 – 10.0 keV spectrum of 3c120.

the same energy range in MCG–6-30-15, so it is not surprising that our statistics are not as sound in this case.

5.2.7 NGC 4051

NGC 4051, like NGC 2992, is a heavily absorbed Seyfert AGN (Sy-1.5; NLS1) seen to vary significantly in flux over the course of several observations (Guainazzi et al. 1996; Lamer et al. 2003). The source is at a redshift of $z = 0.0023$ and has a typical flux on the order of a few times 10^{-11} erg cm $^{-2}$ s $^{-1}$, though as stated above, this flux can vary significantly on a variety of time scales, along with the spectral characteristics of the source. Unusually low flux states in this object can last for weeks to months, during which time the X-ray spectrum shows a hard continuum power-law of spectral slope $\Gamma \sim 1$, but is dominated by a softer component at lower energies with $\Gamma \sim 3$ (Uttley et al. 2004).

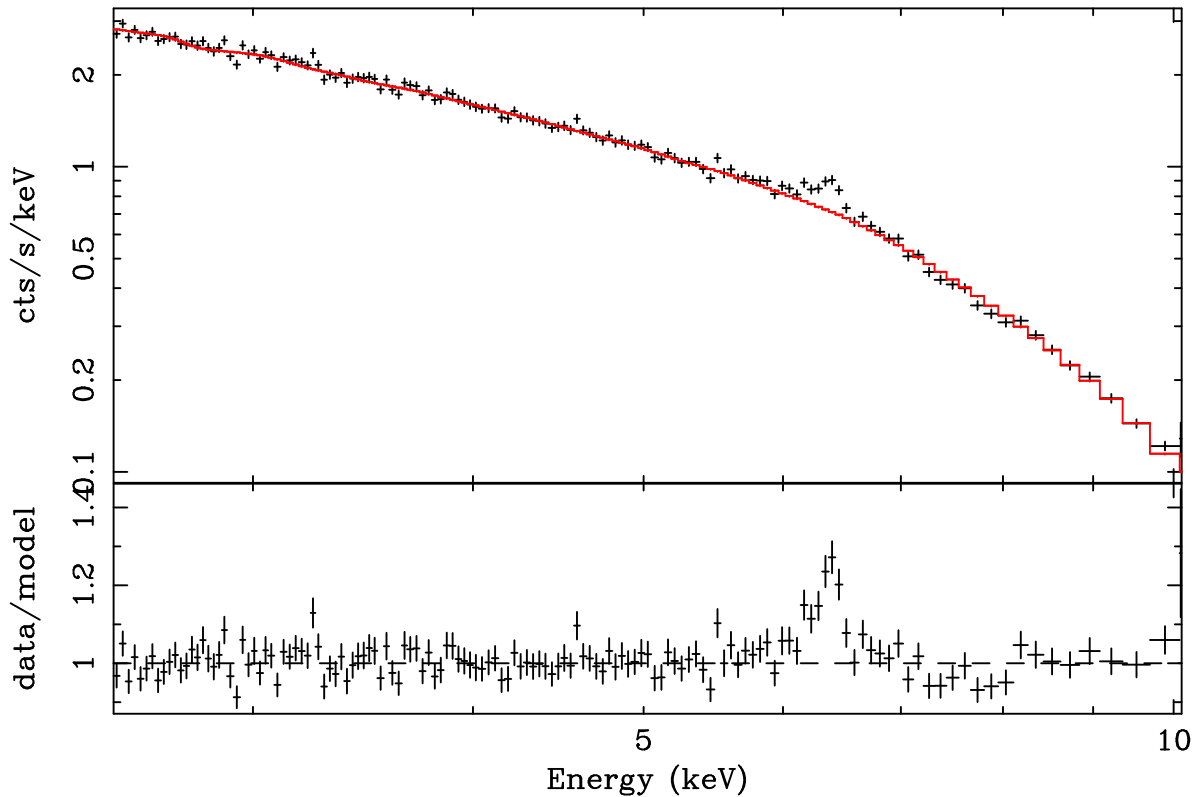


Figure 5.16: The 2.5 – 10.0 keV spectrum of NGC 2992 fit with a continuum composed of a power-law model modified by Galactic photoabsorption as well as a blackbody soft excess. Note the prominent residual iron feature that remains with a rest-frame energy of 6.4 keV.

A highly broadened and redshifted iron line has also been noted in the low flux state of NGC 4051 with *RXTE*, suggesting that reflection features from the accretion disk close to the BH may remain constant in this source in spite of the large variations in continuum properties (Uttley et al. 2003).

NGC 4051 was observed with *XMM-Newton* in May 2001 for a duration of 117 ks, yielding $\sim 3.27 \times 10^6$ photons in the filtered data set. The EPIC-pn results were first reported by Mason et al., and suggested a continuum described by a power-law “pivoting” around 100 keV, according to a simultaneous observation with *RXTE*. Ultraviolet emission from the Optical Monitor on *XMM-Newton* was found to lag the X-ray emission by ~ 0.2 days, indicating that it is likely reprocessed X-ray emission. The X-ray emission itself showed variability on time scales as small as 1 – 2 hours (Mason et al.

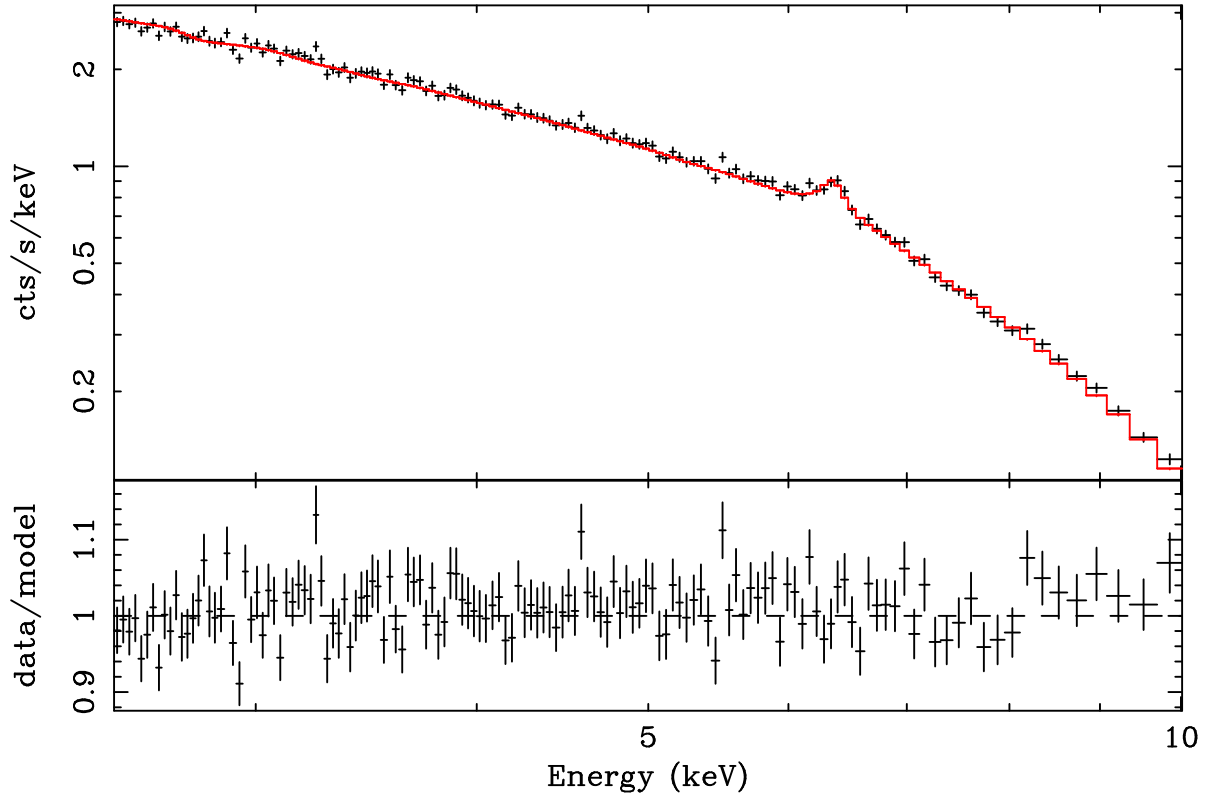


Figure 5.17: The 2.5 – 10.0 keV best-fit model for NGC 2992, including our continuum model and an ionized disk reflection spectrum convolved with our `kerrconv` relativistic smearing kernel. The residuals have all but disappeared.

2002). These results were expanded upon by Pounds et al., who noted the intermediate flux of the source at this time and validated the presence of both an iron line and a thermal soft excess during the May 2001 observation (Pounds et al. 2004). Ponti et al. recently re-analyzed this observation as well as a lower-flux pointing from November 2002 and reinforced the veracity of this model, while also considering the comparable efficacy of a model dominated by ionized reflection from radii quite close to the BH (Ponti et al. 2006).

We have also focused on the May 2001 observation of NGC 4051, following the reduction and analysis of Mason et al. and Ponti et al. but using modern calibration files. A two power-law model parameterized the continuum with much greater accuracy than either a single power-law, a broken power-law or a “pivoting” power-law of the type employed in previous X-ray spectral analyses. Hard and soft components were detected:

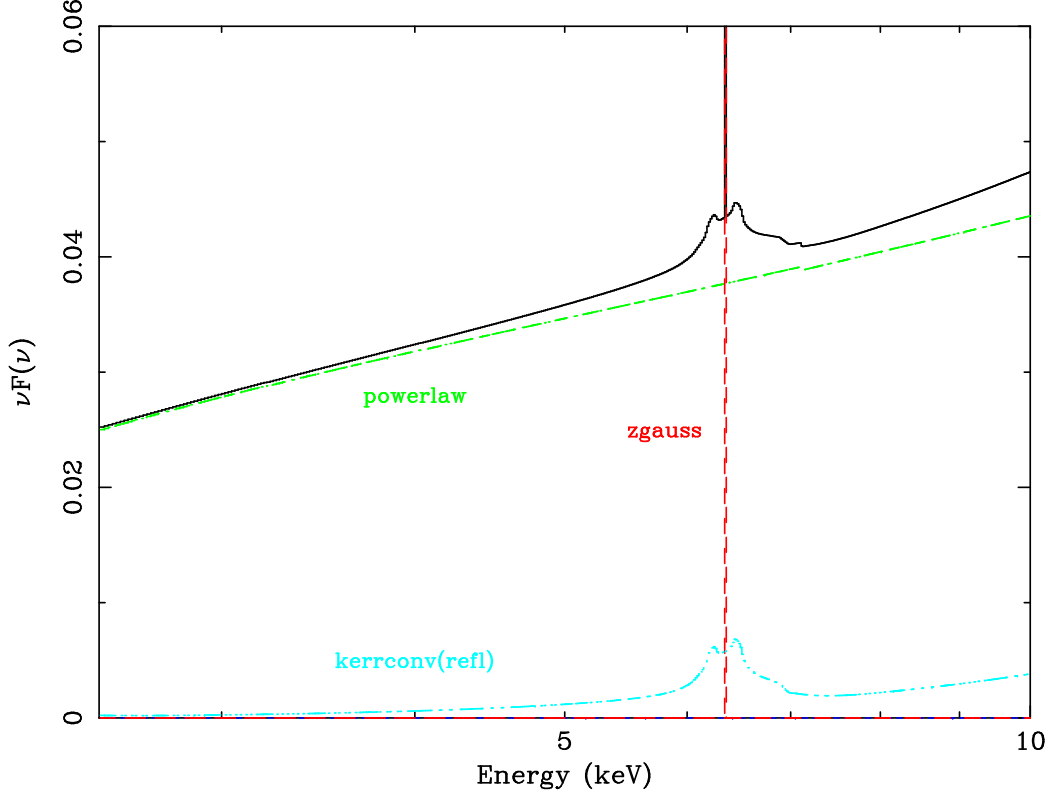


Figure 5.18: A νF_ν plot depicting the relative flux in each of the model components in the 2.5 – 10.0 keV spectrum of NGC 2992.

$\Gamma_{\text{hard}} = 2.01$ and $\Gamma_{\text{soft}} = 5.20$. The hard/soft flux ratio for these components is 1.21, and each is modified by photoabsorption from neutral hydrogen with $N_{\text{H}} = 7.63 \times 10^{20} \text{ cm}^{-2}$. This column density is greater than the Galactic value by a factor of ~ 6 , indicating the presence of cold absorption within the NGC 4051 system. Additionally, there is statistical evidence to support the presence of a warm absorber within the AGN as well: a significant improvement in the global goodness-of-fit is seen with the inclusion of one of our XSTAR multiplicative table models with a hydrogen column density of $N_{\text{WA}} = 5.08 \times 10^{22} \text{ cm}^{-2}$ and $\log \xi_{\text{WA}} = 0.06$. Note that this warm absorber is essentially neutral, implying that it does not experience significant heating from the central engine and may exist at some distance from the source of the X-ray emission in NGC 4051. Finally, a soft excess is also seen below ~ 1 keV, as in so many other Seyfert galaxies. The best fit to this feature is achieved with a thermal blackbody component, with $kT = 0.27$ and a flux ~ 120 times

Model Component	Parameter	Value
phabs	N_{H} (cm^{-2})	$5.12^{+0.09}_{-0.10} \times 10^{21}$
po	Γ_{po}	$1.69^{+0.02}_{-0.03}$
	flux ($\text{ph cm}^{-2} \text{s}^{-1}$)	$2.14^{+0.08}_{-0.07} \times 10^{-2}$
bbody	kT (keV)	$0.05^{+0.01}_{-0.01}$
	flux ($\text{ph cm}^{-2} \text{s}^{-1}$)	$1.53^{+5.01}_{-0.93} \times 10^{-2}$
zgauss	E (keV)	6.40
	flux ($\text{ph cm}^{-2} \text{s}^{-1}$)	$1.85^{+2.32}_{-1.54} \times 10^{-5}$
	EW (eV)	$38.80^{+48.66}_{-32.30}$
kerrconv	α_1	$7.36^{+2.64}_{-6.12}$
	α_2	$7.36^{+2.64}_{-6.12}$
	$r_{\text{br}} (r_{\text{ms}})$	6.0
	a	— — —
	i ($^{\circ}$)	41^{+7}_{-21}
	$r_{\text{min}} (r_{\text{ms}})$	$2.50^{+9.28}_{-1.50}$
	$r_{\text{max}} (r_{\text{ms}})$	400
reflion	Fe/solar	1.0
	ξ_{refl}	30.0
	Γ_{refl}	$1.69^{+0.02}_{-0.03}$
	flux ($\text{ph cm}^{-2} \text{s}^{-1}$)	$2.49^{+0.85}_{-0.77} \times 10^{-5}$
χ^2/dof		1402/1312 (1.07)

Table 5.6: Best-fitting model parameters for the 2.5 – 10.0 keV spectrum of NGC 2992, including components and parameter values from 0.6 – 1.5 keV for completeness. The energies from 1.5 – 2.5 keV were not included due to the presence of absorption edges from the *XMM-Newton* mirrors. Error bars are quoted at 90% confidence. We required the 6.4 keV zgauss line core to be intrinsically narrow, i.e., $\sigma = 0.0$. Redshifts were frozen at the cosmological value for the source, in this case $z = 0.0077$. No evidence for warm absorption is detected, though a soft excess is found in this object, as in many other Sy-1 sources.

smaller than the hard power-law component.

A narrow 6.4 keV Gaussian was successfully fit to the core of the Fe-K α line in this source, though by forcing the line to be narrow (i.e., freezing $\sigma = 0.0$) we note significant residuals marking the red and blue wings of the broadened line. The narrow core has an $EW = 57.8$ eV. The remaining broad line is best fit with a kerrconv(refl) model having a BH spin of $a > 0.67$ and an $r_{\text{min}} = 2.25 - 4.62 r_{\text{ms}}$. Full parameter values and 90% confidence error bars are listed in Table 5.7. Figs. 5.19-5.21 show the iron line residual,

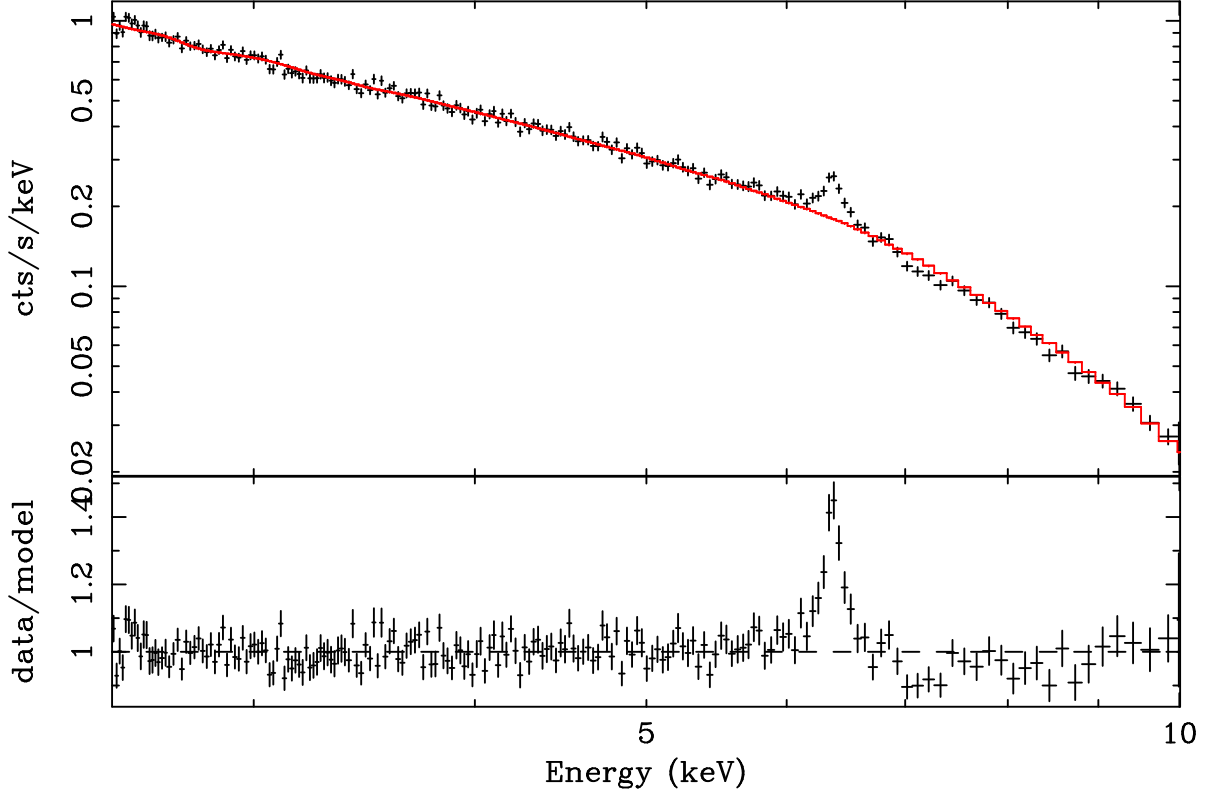


Figure 5.19: The 2.5 – 10.0 keV spectrum of NGC 4051 fit with a continuum composed of two power-law models modified by Galactic photoabsorption, a warm absorber model and a blackbody soft excess. Note the prominent residual iron feature that remains with a rest-frame energy of 6.4 keV.

best fit to this residual, and relative contributions of the individual model components, respectively.

5.2.8 Ark 120

Ark 120 is a bright Sy-1 AGN with an estimated BH mass of $\sim 2 \times 10^8 M_{\odot}$ (Wandel et al. 1999) and a bolometric luminosity of $L_{\text{bol}} \geq 10^{45} \text{ erg s}^{-1}$ (Edelson & Malkan 1986). At a redshift of $z = 0.0327$, this source has a relatively constant 2 – 10 keV X-ray flux of $F_{2-10} \sim 2.50 \times 10^{-11} \text{ erg cm}^{-2} \text{ s}^{-1}$ (Vaughan et al. 2004). The source is radio-quiet, and due to a lack of observed evidence for intrinsic absorption, Ark 120 has been labeled a “bare” Sy-1 nucleus (Ward et al. 1987). Its host galaxy is an early-type spiral of Hubble

Model Component	Parameter	Value
phabs	N_{H} (cm^{-2})	$7.63^{+1.97}_{-3.29} \times 10^{20}$
WA	N_{WA} (cm^{-2}) $\log \xi_{\text{WA}}$	$5.08^{+0.83}_{-0.72} \times 10^{22}$ < 0.06
po	Γ_{po} flux ($\text{ph cm}^{-2} \text{s}^{-1}$)	$5.20^{+0.12}_{-0.35}$ $6.13^{+0.61}_{-0.58} \times 10^{-4}$
po	Γ_{po} flux ($\text{ph cm}^{-2} \text{s}^{-1}$)	$2.01^{+0.08}_{-0.06}$ $7.43^{+0.51}_{-0.47} \times 10^{-4}$
body	kT (keV) flux ($\text{ph cm}^{-2} \text{s}^{-1}$)	$0.27^{+0.02}_{-0.01}$ $6.31^{+1.29}_{-1.14} \times 10^{-6}$
zgauss	E (keV) flux ($\text{ph cm}^{-2} \text{s}^{-1}$) EW (eV)	6.40 $1.05^{+0.33}_{-0.31} \times 10^{-6}$ $57.80^{+18.17}_{-17.06}$
kerrconv	α_1 α_2 $r_{\text{br}} (r_{\text{ms}})$ a i ($^\circ$) $r_{\text{min}} (r_{\text{ms}})$ $r_{\text{max}} (r_{\text{ms}})$	$6.78^{+3.22}_{-2.55}$ $6.78^{+3.22}_{-2.55}$ 6.0 $0.98^{+0.01}_{-0.31}$ 38^{+3}_{-3} $3.37^{+1.25}_{-1.13}$ 400
reflion	Fe/solar ξ_{refl} Γ_{refl} flux ($\text{ph cm}^{-2} \text{s}^{-1}$)	$1.89^{+3.80}_{-0.64}$ < 107.77 $2.01^{+0.08}_{-0.06}$ $7.55^{+6.28}_{-5.56} \times 10^{-7}$
χ^2/dof		1475/1394 (1.06)

Table 5.7: Best-fitting model parameters for the 2.5 – 10.0 keV spectrum of NGC 4051, including components and parameter values from 0.6 – 1.5 keV for completeness. The energies from 1.5 – 2.5 keV were not included due to the presence of absorption edges from the *XMM-Newton* mirrors. Error bars are quoted at 90% confidence. We required the 6.4 keV zgauss line to be intrinsically narrow, i.e., $\sigma = 0.0$. Redshifts were frozen at the cosmological value for the source, in this case $z = 0.0023$. A warm absorber and blackbody soft excess are present in this object, as in many other Sy-1 sources.

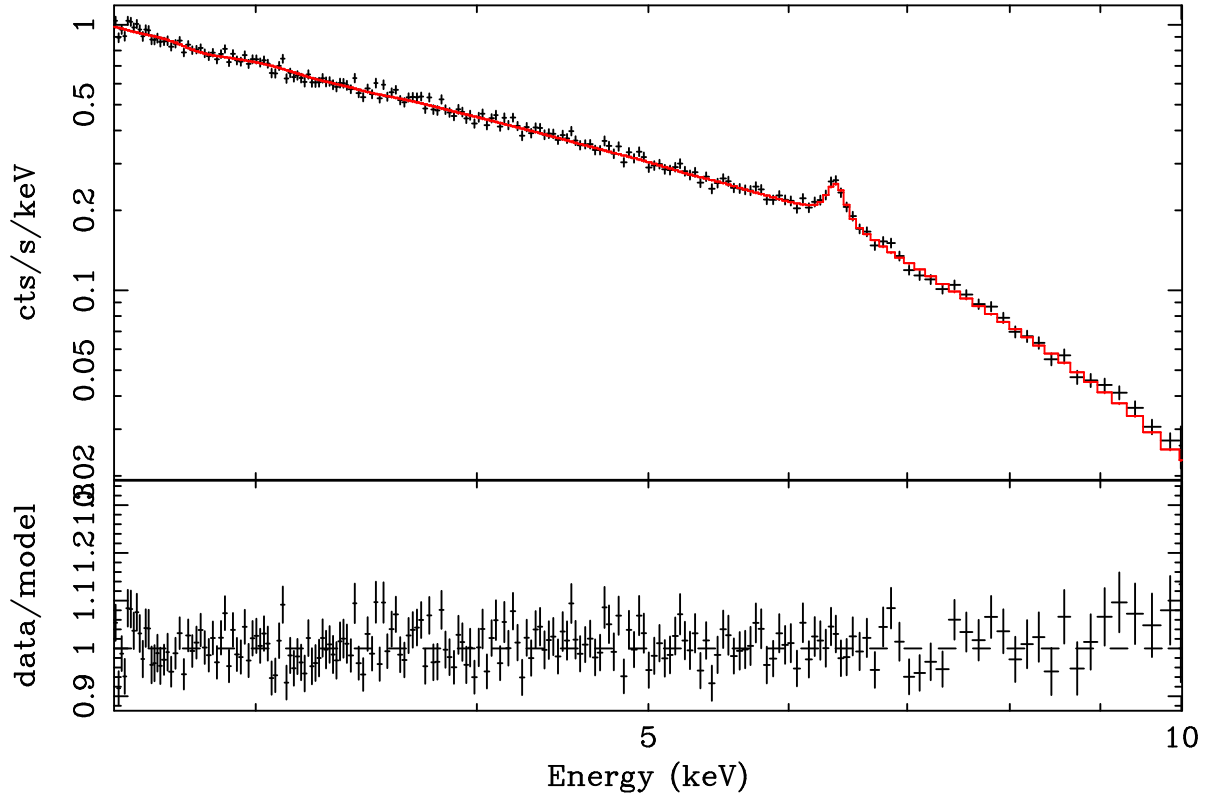


Figure 5.20: The 2.5 – 10.0 keV best-fit model for NGC 4051, including our continuum model and an ionized disk reflection spectrum convolved with our `kerrconv` relativistic smearing kernel. The residuals have all but disappeared.

type S0/a with an inclination angle of $i \approx 26^\circ$ (Nordgren et al. 1995). Ark 120 has been observed by most of the major X-ray observatories. An *EXOSAT* observation showed the source to have a steep soft X-ray spectrum (Turner & Pounds 1989), as did a subsequent *ROSAT* observation (Brandt et al. 1993). Furthermore, as mentioned above, these X-ray observations showed no indication of any warm absorption features. Similar findings were seen in ultraviolet observations (Crenshaw & Kraemer 2001; Crenshaw et al. 1999).

The source was observed by *XMM-Newton* in August 2003 for an effective duration of 100 ks ($\sim 2.74 \times 10^6$ photons) by Vaughan et al. , whose results on the EPIC-pn spectrum were reported the following year. We follow the data reduction and analysis of these authors, though we restrict our attention to the EPIC-pn camera data. Vaughan et al. find that the continuum emission is well described by a simple photoabsorbed power-law model

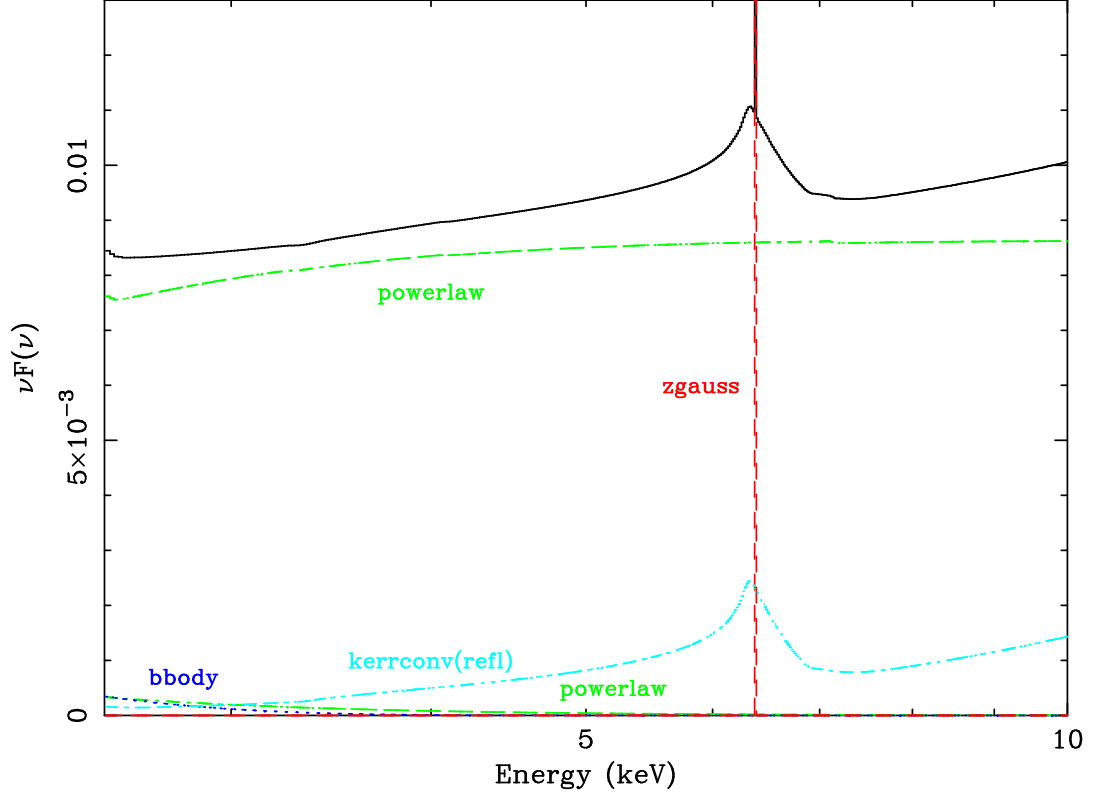


Figure 5.21: A νF_ν plot depicting the relative flux in each of the model components in the 2.5 – 10.0 keV spectrum of NGC 4051.

with no evidence for complex absorption intrinsic to the system. A multiple blackbody component for the soft excess is used to reduce residuals left over from the power-law fit below ~ 1 keV, and a slight curvature of the continuum is noted that is thought to indicate the presence of disk reflection in this source (Vaughan et al. 2004).

Our continuum fit differs from that of Vaughan et al. , most notably over whether or not a warm absorber is present. These authors relied heavily upon the RGS data to draw their conclusions about the X-ray spectrum of Ark 120 below ~ 3 keV, whereas we use only the EPIC-pn spectrum to produce our global fits to avoid dealing with the calibration problems that exist between the two instruments, as discussed in previous Chapters. We do find a similar photoabsorbed power-law, however: $\Gamma = 2.25$ and $N_{\text{H}} = 1.26 \times 10^{21} \text{ cm}^{-2}$ (the Galactic value, with no evidence for intrinsic cold absorption in the AGN). We detect the presence of a two-zone warm absorber in the system with hydrogen column den-

sities of $N_1 = 1.51 \times 10^{23} \text{ cm}^{-2}$, $N_2 = 2.90 \times 10^{22} \text{ cm}^{-2}$ and ionization parameters of $\log \xi_1 = 2.97$ and $\log \xi_2 = 1.24$. Our best fit to the soft excess required one blackbody component of $kT = 0.13 \text{ keV}$ and a flux of $F_{\text{bb}} = 1.95 \times 10^{-6} \text{ ph cm}^{-2} \text{ s}^{-1}$, a factor of 60 below the flux of the power-law component. It should be noted that adding in the first WA table resulted in a $\Delta\chi^2/\text{dof} = -838/+2$, and adding in the second table further improved the fit by $\Delta\chi^2/\text{dof} = -1163/+2$. The blackbody component resulted in $\Delta\chi^2/\text{dof} = -4416/+2$. All of these additions to the global fit are therefore statistically warranted.

Vaughan et al. detected the presence of broad and narrow components to the 6.4 keV Fe-K α line ($EW_{\text{broad}} \sim 100 \text{ eV}$, $EW_{\text{narrow}} \sim 40 \text{ eV}$). The narrow component could easily be fit with a 6.4 keV Gaussian profile, as was our Fe-K α narrow core, but Vaughan et al. found that a diskline model worked best for their broad component ($r_{\text{min}} \approx 144 r_{\text{g}}$). Interestingly, this broad component fit to a rest-frame energy of 6.56 keV rather than 6.4 keV, with the latter yielding a substantially worse global fit ($\Delta\chi^2 = +21.5$) (Vaughan et al. 2004). This energy corresponds to the line emission being dominated by mildly ionized iron (Fe XX-XXII), meaning that resonant trapping and the Auger effect should destroy the line (Ross et al. 1996).

In an effort to solve this puzzle we have fit our iron line profile with two narrow Gaussian components, one at 6.4 keV and one at 6.97 keV, representing neutral and highly ionized iron. The lines have $EW_{\text{cold}} = 54.4 \text{ eV}$ and $EW_{\text{ionized}} = 19.9 \text{ eV}$. This fit leaves a residual broad feature nicely centered at 6.4 keV, which renders this scenario physically consistent with other systems and removes the need to explain the presence of the broad line of iron in an intermediate state of ionization. We then achieve a best fit to the broad component using a `kerrconv(refl)` model, which also nicely accounts for the additional curvature noted in the spectrum by Vaughan et al. From this fit, we have constrained the spin of the BH to be $a = 0.63 - 0.68$ and $r_{\text{min}} = 1.00 - 1.09 r_{\text{ms}}$. The best-fit

parameter values and error bars are presented in Table 5.8. Figs. 5.22-5.24 show the iron line residual, best fit to this residual, and relative contributions of the individual model components for the best fit.

Though this result is intriguing for its intermediate BH spin value, one must interpret it with caution. This source, in particular, seems to have a weak emission feature present in the spectrum just below the neutral iron line in energy that sticks out as a “bump” in the spectrum. It is unclear what this feature may represent, and left unmodeled, the spectral fit seems to smooth over it rather than fit it properly. This may affect the parameter values and error bars we obtain for the `kerrconv(refl)` model. More detailed, longer observations with higher spectral resolution will be required to solve this puzzle and more reliably determine the BH spin in Ark 120.

5.2.9 Fairall 9

Fairall 9 is a radio-quiet Sy-1 type galaxy with an elliptical companion, both at a moderate redshift of $z = 0.047$. This source has not been observed to undergo very large changes in X-ray flux over the time it has been observed: the typical 2 – 10 keV flux of Fairall 9 is $F_{2-10} \sim 1.5 - 5.0 \times 10^{-11} \text{ erg cm}^{-2} \text{ s}^{-1}$ (Gondoin et al. 2001; Reynolds 1997). Previous X-ray observations with *ASCA* show that the source has a continuum well-described by a photoabsorbed power-law with a fluorescent Fe-K α line and a high-energy tail (a common signature of disk reflection, as has been discussed previously with respect to a number of other sources in this Section) (Nandra et al. 1997; Reynolds 1997). A soft excess has also been detected below ~ 2 keV (Pounds et al. 1994), though no strong evidence of warm absorption has been observed in the soft spectrum (Gondoin et al. 2001).

The source was observed with *XMM-Newton* by Jansen et al. in July 2000 for an effective duration of ~ 29 ks ($\sim 3.95 \times 10^5$ photons) (Jansen et al. 2001), and the EPIC-pn data were presented in full by Gondoin et al. the following year (Gondoin et al. 2001).

Model Component	Parameter	Value
phabs	$N_{\text{H}} (\text{cm}^{-2})$	1.26×10^{21}
WA 1	$N_{\text{WA1}} (\text{cm}^{-2})$	$1.51^{+0.37}_{-0.12} \times 10^{23}$
	$\log \xi_{\text{WA1}}$	$2.97^{+0.26}_{-0.04}$
WA 2	$N_{\text{WA2}} (\text{cm}^{-2})$	$2.90^{+0.30}_{-0.22} \times 10^{22}$
	$\log \xi_{\text{WA2}}$	$1.24^{+0.05}_{-0.02}$
po	Γ_{po}	$2.25^{+0.05}_{-0.05}$
	flux ($\text{ph cm}^{-2} \text{s}^{-1}$)	$1.27^{+0.04}_{-0.01} \times 10^{-4}$
bbody	kT (keV)	$0.14^{+0.01}_{-0.01}$
	flux ($\text{ph cm}^{-2} \text{s}^{-1}$)	$1.95^{+0.04}_{-0.06} \times 10^{-6}$
zgauss	E (keV)	6.40
	flux ($\text{ph cm}^{-2} \text{s}^{-1}$)	$1.15^{+0.23}_{-0.14} \times 10^{-7}$
	EW (eV)	$54.40^{+10.88}_{-6.62}$
zgauss	E (keV)	6.97
	flux ($\text{ph cm}^{-2} \text{s}^{-1}$)	$5.40^{+1.69}_{-1.64} \times 10^{-8}$
	EW (eV)	$19.90^{+6.23}_{-6.04}$
kerrconv	α_1	$2.34^{+0.11}_{-0.05}$
	α_2	$2.34^{+0.11}_{-0.05}$
	$r_{\text{br}} (r_{\text{ms}})$	6.0
	a	$0.65^{+0.03}_{-0.02}$
	i ($^\circ$)	79^{+1}_{-0}
	$r_{\text{min}} (r_{\text{ms}})$	< 1.09
	$r_{\text{max}} (r_{\text{ms}})$	400
reflion	Fe/solar	1.0
	ξ_{refl}	30.0
	Γ_{refl}	$2.25^{+0.05}_{-0.05}$
	flux ($\text{ph cm}^{-2} \text{s}^{-1}$)	$4.03^{+1.96}_{-0.10} \times 10^{-7}$
χ^2/dof		1543/1421 (1.09)

Table 5.8: Best-fitting model parameters for the 2.5 – 10.0 keV spectrum of Ark 120, including components and parameter values from 0.6 – 1.5 keV for completeness. The energies from 1.5 – 2.5 keV were not included due to the presence of absorption edges from the *XMM-Newton* mirrors. Error bars are quoted at 90% confidence. We required the zgauss lines to be intrinsically narrow, i.e., $\sigma = 0.0$. Redshifts were frozen at the cosmological value for the source, in this case $z = 0.0327$. A two-zone warm absorber and blackbody soft excess are present in this object, as in many other Sy-1 sources.

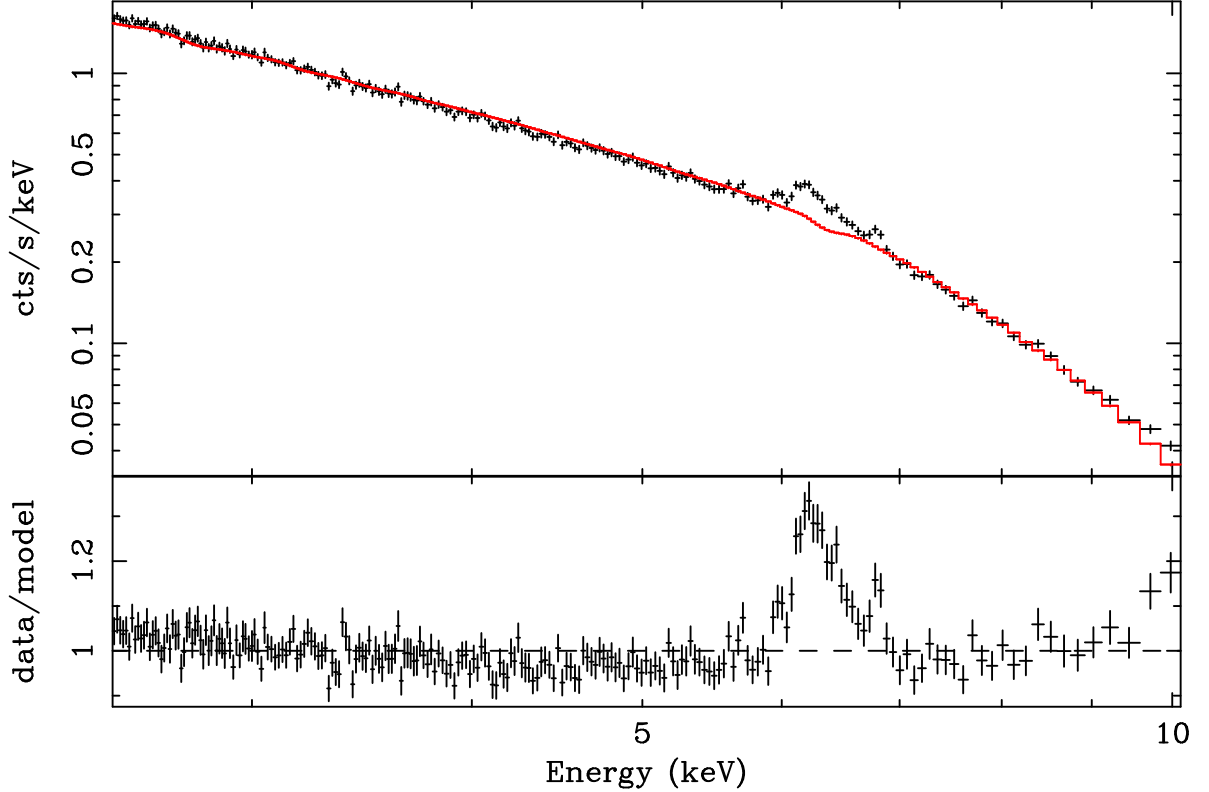


Figure 5.22: The 2.5 – 10.0 keV spectrum of Ark 120 fit with a continuum composed of a power-law model modified by Galactic photoabsorption, a two-zone warm absorber model and a blackbody soft excess. Note the prominent residual iron features that remain with rest-frame energies of 6.4 keV and 6.97 keV.

We have followed the general procedures for data reduction and analysis discussed by Gondoin et al. , using the most up-to-date calibration files and software as we have for all other sources analyzed in this work.

Gondoin et al. find that continuum of Fairall 9 is best modeled with a photoabsorbed power-law ($N_{\text{H}} = 3 \times 10^{20} \text{ cm}^{-2}$, $\Gamma = 1.80$), in which the absorbing column density of neutral hydrogen gas is approximately equal to its Galactic value along the line of sight to this source ($N_{\text{H}} = 3.19 \times 10^{20} \text{ cm}^{-2}$). A soft excess is noted below $\sim 2 \text{ keV}$, and an RGS analysis yielded a best-fitting blackbody model for this component: $kT = 0.17 \text{ keV}$. Incorporating reflection from an ionized disk with solar abundances and a reflection fraction of $f_{\text{refl}} = 1.0$, the authors find that the high-energy tail is quite well modeled by a disk at an inclination angle of $i = 26^\circ$ (Gondoin et al. 2001). We have performed a similar fit

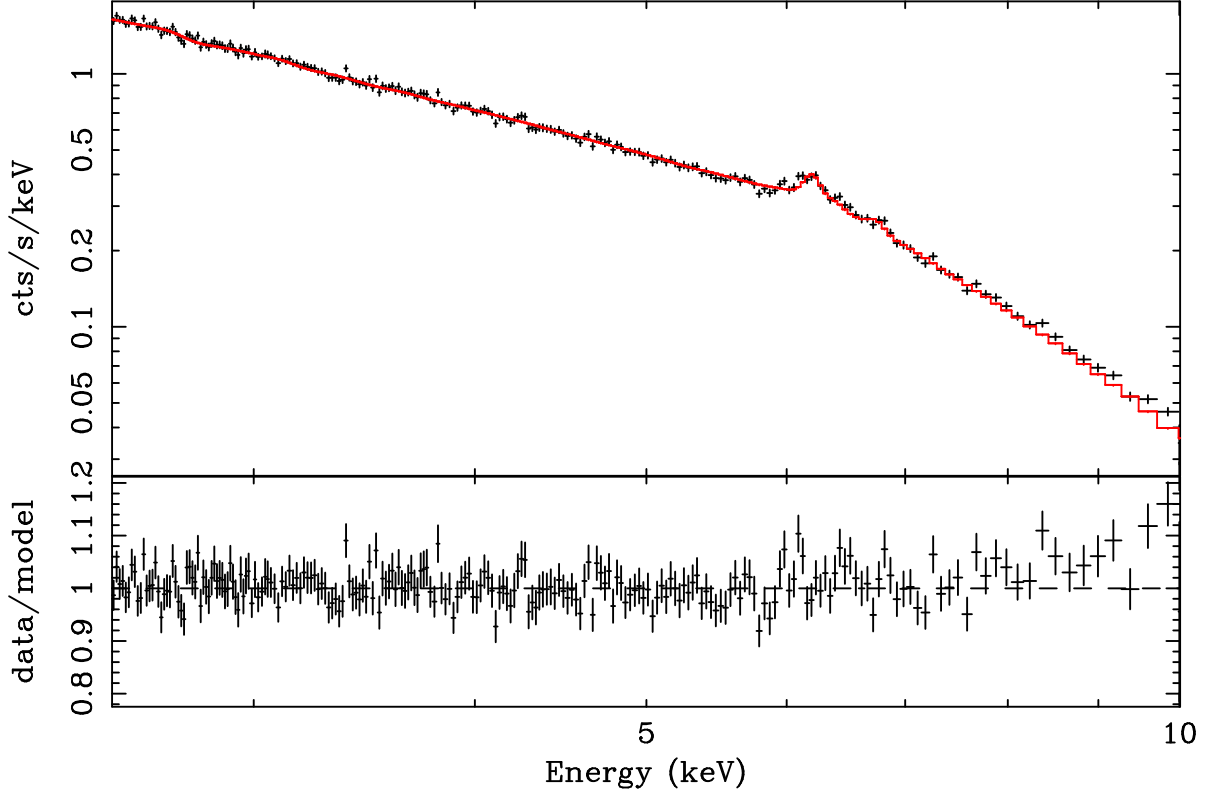


Figure 5.23: The 2.5 – 10.0 keV best-fit model for Ark 120, including our continuum model and an ionized disk reflection spectrum convolved with our `kerrconv` relativistic smearing kernel. The residuals have all but disappeared.

using only the EPIC-pn data, and find some similar parameters describing the power-law, blackbody soft excess and reflection components (the column density of neutral hydrogen absorption was frozen at the Galactic value): $\Gamma = 2.04$, $kT = 0.20$ keV with a flux $\sim 0.5\%$ that of the power-law component, and the disk inclination angle is $i = 57^\circ$ for solar abundance and assumed near-neutrality. Unfortunately, due to the relatively small number of photons, the disk ionization and metallicity were not able to be adequately constrained, hence the assumptions of solar metallicity and near-neutrality. In contrast to the Gondoin et al. analysis, we do detect evidence for a warm absorber within the system with $N_{\text{WA}} = 1.21 \times 10^{23} \text{ cm}^{-2}$ and $\log \xi_{\text{WA}} = 2.85$. Inclusion of this component improves the global goodness-of-fit by $\Delta\chi^2/\text{dof} = -13/+2$, making it statistically significant according to the f -test. The presence of the warm absorber also eliminates some of the residual

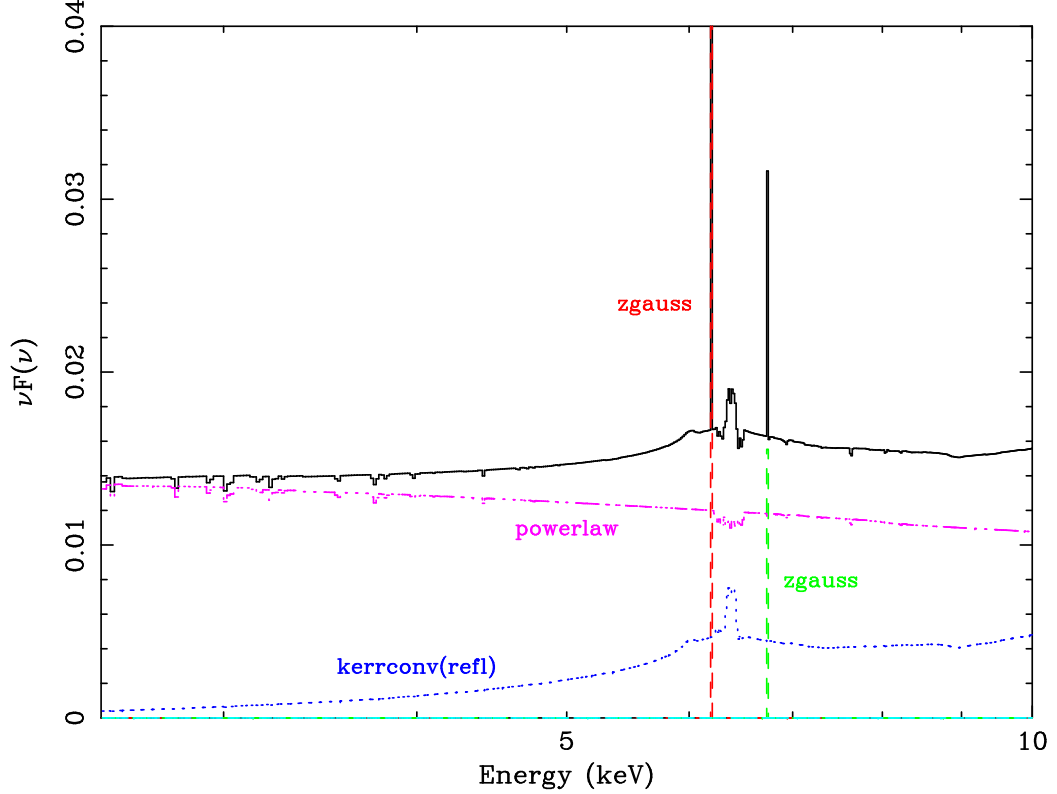


Figure 5.24: A νF_{ν} plot depicting the relative flux in each of the model components in the 2.5 – 10.0 keV spectrum of Ark 120.

continuum curvature in the soft spectrum.

Gondoin et al. also note the presence of a 6.4 keV Fe-K α line in the spectrum with $EW \sim 120$ eV, which they modeled with a Gaussian component. Due to its relatively narrow profile, the line is suggested to originate from low-ionization material orbiting relatively far out in the disk. Additionally, an Fe-K absorption edge is also noted at 7.64 keV with $\tau = 0.18$, consistent with reflection from cold, optically thick material. We find that the inclusion of such an edge is not statistically robust in our model once reflection is included, but we do find the 6.4 keV line in emission and model it first with a narrow Gaussian feature representing the core of the Fe-K α line. This feature has an $EW = 133$ eV, but even after its inclusion residual features remain indicating the presence of a broader iron line component. The best fit for this line, which is physically consistent with our disk reflection model, is achieved using a `kerrconv(refl)` component with an

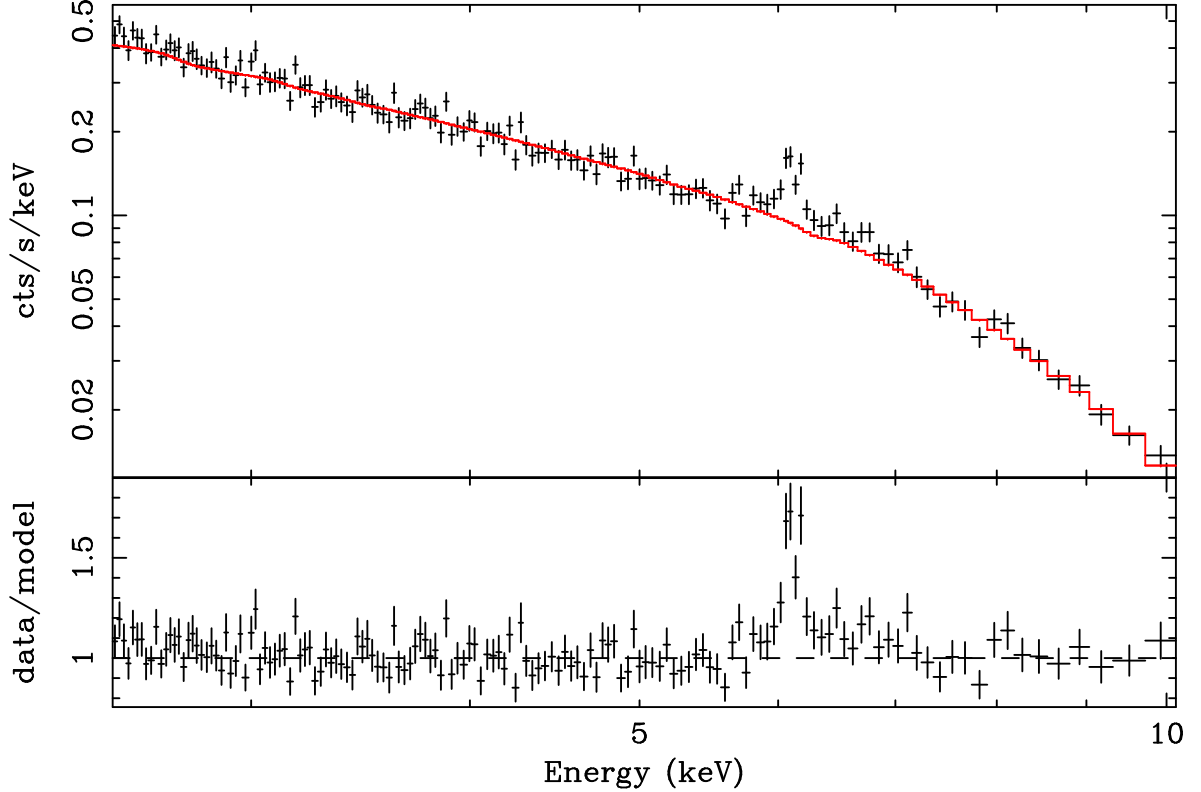


Figure 5.25: The 2.5 – 10.0 keV spectrum of Fairall 9 fit with a continuum composed of a power-law model modified by Galactic photoabsorption, a warm absorber model and a blackbody soft excess. Note the prominent residual iron feature that remains with a rest-frame energy of 6.4 keV.

inner radius of emission of $r_{\min} < 6.27 r_{\text{ms}}$, or $< 10.75 r_{\text{g}}$, calculated using the fit value of BH spin ($a = 0.972$). The BH spin itself, however, was unable to be constrained. Best-fit values and error bars for all the parameters in our model are listed in Table 5.9. Figs. 5.25–5.27 show the iron line residual, best fit to this residual, and relative contributions of the individual model components, respectively.

5.3 Comparison of Sample Results

We have compiled the relevant parameter constraints from all of our spectral fits to ten Sy-1 sources: MCG–6-30-15, MCG–5-23-16, Mrk 766, NGC 3783, NGC 4051, Ark 120, Fairall 9, NGC 2992, 3c273 and 3c120. The constraints on the relativistic disk parameters

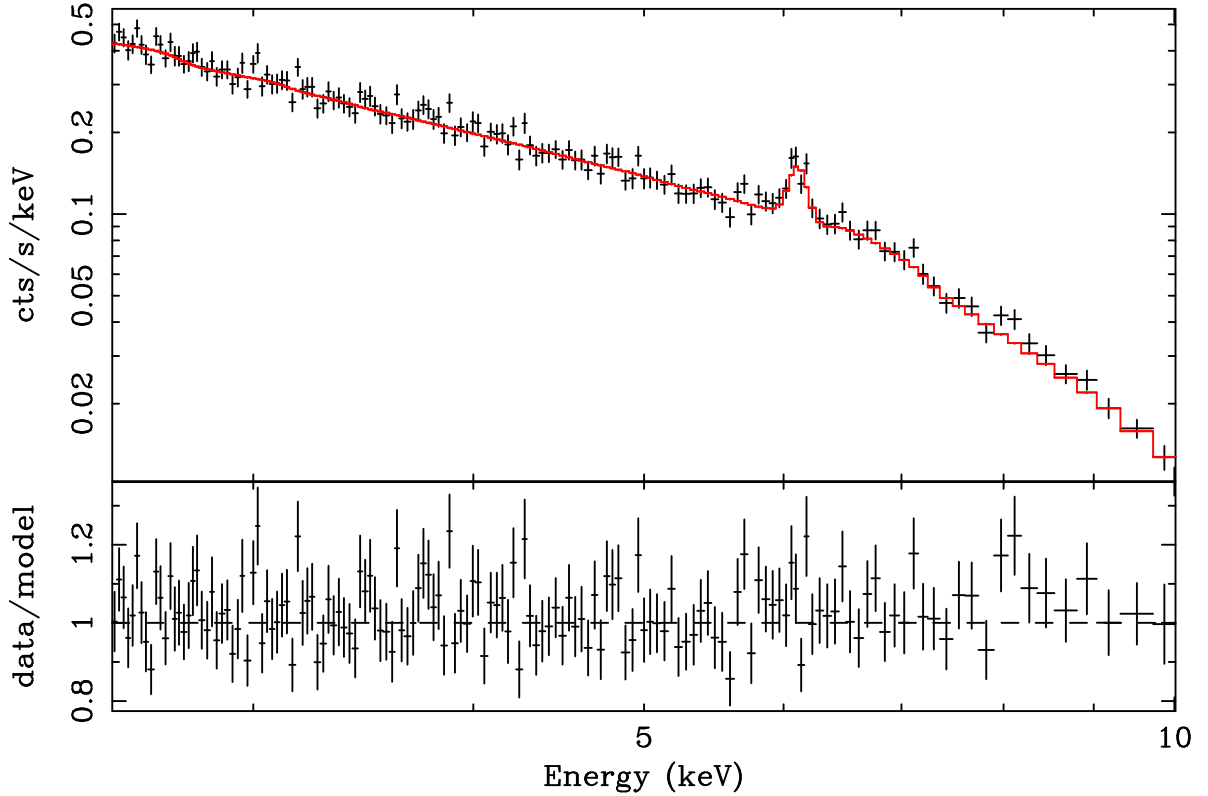


Figure 5.26: The 2.5 – 10.0 keV best-fit model for Fairall 9, including our continuum model and an ionized disk reflection spectrum convolved with our `kerrconv` relativistic smearing kernel. The residuals have all but disappeared.

for each object are presented in Tables 5.10-5.12. Note that in each case a model including reflection from an ionized disk convolved with a relativistic smearing kernel provides the best statistical fit, and that in almost every case the `kerrconv` model (with arbitrary spin) provides a better fit than the `kdblur` model (spin fixed at $a = 0.998$).

To assess whether evidence exists for a relativistically broadened iron line, we first considered the `laor` fits in which BH spin is fixed at $a = 0.998$. While each source demonstrated a significant improvement in its global fit as compared to a model fitting only a narrow iron line core with a Gaussian component, the important parameter to evaluate in this case is the inner radius of disk emission. Roughly speaking, as stated in §5.1, if $r_{\min} \lesssim 20r_g$ we can say with some confidence that there is substantial emission from the inner part of the accretion disk where relativistic effects (such as BH spin) become impor-

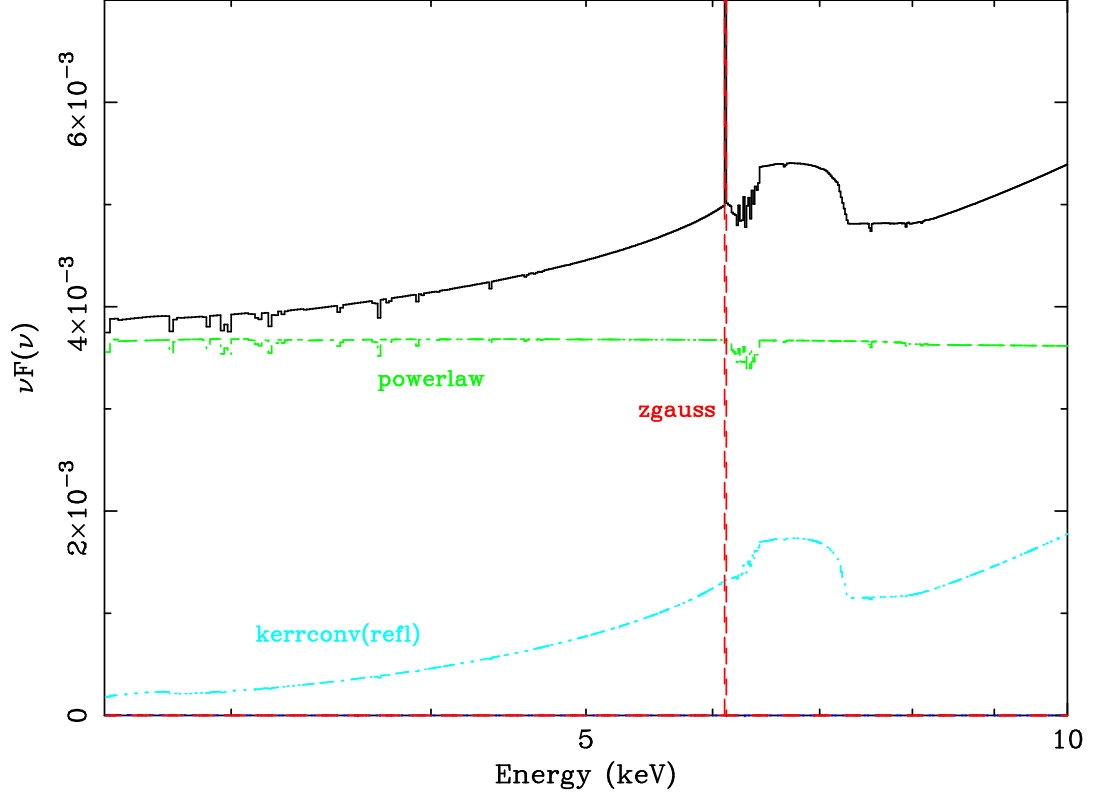


Figure 5.27: A νF_ν plot depicting the relative flux in each of the model components in the 2.5 – 10.0 keV spectrum of Fairall 9.

tant in shaping the overall iron line profile. Out of our ten sources, five did *not* meet this criterion outright (MCG–5-23-16, NGC 3783, Ark 120, Fairall 9 and 3c120) while one source spectrum possesses so few photons that it is difficult to quote parameter values and error bars with confidence (3c273). Allowing for arbitrary BH spin via `kerrdisk` instead of `laor` does help the situation somewhat: only 3c120 and NGC 3783 did not meet the r_{\min} criterion in this fit, though for none of the sources is the global fit greatly improved over its `laor` value. Fairall 9 and 3c273 have spins that cannot be constrained with the `kerrdisk` model.

We have also examined the question of how robust the presence of a broad line is in the spectrum when reflection is included. Beginning with a base continuum model including an ionized disk reflection spectrum (Ross & Fabian 2005), we noted the overall goodness-of-fit and the residual features remaining, especially around the iron line region.

Model Component	Parameter	Value
phabs	N_{H} (cm ⁻²)	$3.19^{+0.42}_{-0.00} \times 10^{20}$
WA	N_{WA} (cm ⁻²)	$1.21^{+1.60}_{-0.97} \times 10^{23}$
	$\log \xi_{\text{WA}}$	$2.85^{+0.89}_{-0.79}$
po	Γ_{po}	$2.04^{+0.14}_{-0.10}$
	flux (ph cm ⁻² s ⁻¹)	$3.28^{+0.47}_{-0.30} \times 10^{-4}$
bbody	kT (keV)	$0.20^{+0.01}_{-0.02}$
	flux (ph cm ⁻² s ⁻¹)	$1.57^{+0.40}_{-0.35} \times 10^{-6}$
zgauss	E (keV)	6.40
	flux (ph cm ⁻² s ⁻¹)	$1.16^{+0.42}_{-0.27} \times 10^{-6}$
	EW (eV)	133^{+48}_{-31}
kerrconv	α_1	$5.17^{+4.83}_{-3.31}$
	α_2	$5.17^{+4.83}_{-3.31}$
	$r_{\text{br}} (r_{\text{ms}})$	6.0
	a	---
	i (°)	57^{+7}_{-5}
	$r_{\text{min}} (r_{\text{ms}})$	< 6.27
	$r_{\text{max}} (r_{\text{ms}})$	400
reflion	Fe/solar	1.0
	ξ_{refl}	30.0
	Γ_{refl}	$2.04^{+0.14}_{-0.10}$
	flux (ph cm ⁻² s ⁻¹)	$8.10^{+4.21}_{-2.66} \times 10^{-7}$
χ^2/dof		665/691 (0.96)

Table 5.9: Best-fitting model parameters for the 2.5 – 10.0 keV spectrum of Fairall 9, including components and parameter values from 0.6 – 1.5 keV for completeness. The energies from 1.5 – 2.5 keV were not included due to the presence of absorption edges from the *XMM-Newton* mirrors. Error bars are quoted at 90% confidence. We required the 6.4 keV zgauss line to be intrinsically narrow, i.e., $\sigma = 0.0$. Redshifts were frozen at the cosmological value for the source, in this case $z = 0.0470$. A warm absorber and blackbody soft excess are present in this object, as in many other Sy-1 sources.

We then convolved this model with relativistic effects, first using the `kdblur` smearing kernel, then substituting in `kerrconv`. A significant improvement in the global fit with `kdblur` indicates that relativistic smearing is important in the system, and further significant improvement with `kerrconv` instead of `kdblur` indicates that although relativity is important, in the best fit scenario the BH spin deviates from its maximal value. Whenever possible we allowed the iron abundance and ionization parameter to fit freely in the

ionized disk model, though in some cases these additional degrees of freedom prevented us from obtaining a reliable fit. For these sources it was necessary to assume a neutral disk ($\xi = 30$) and solar iron abundance ($\text{Fe}/\text{solar}=1$): Ark 120, Fairall 9 and 3c273. The `kdblur` and `kerrconv` fits returned similar results in terms of parameter constraints and overall fit to the iron line profile in each source, and in nearly all cases also produced a statistically significant improvement in the overall goodness-of-fit, with the exception being NGC 3783, in which only a marginal improvement in the goodness-of-fit was seen. The `kerrconv` model fit was clearly superior to the `kdblur` fit in two cases: MCG–6-30-15 and Ark 120.

We have obtained formal constraints on BH spin in four of the ten cases: MCG–6-30-15 ($a > 0.96$ from 2.5 – 10.0 keV, $a > 0.987$ based on our 0.6 – 10.0 keV fit discussed in Chapter 4); Ark 120 ($a = 0.63 - 0.68$), Mrk 766 ($a > 0.85$) and NGC 4051 ($a > 0.67$). We fit a BH spin of $a > 0.72$ to 3c273, but as mentioned previously, this result must be considered questionable due to the paucity of photons in our data set. Interestingly, we also were able to constrain the BH spin of 3c120 with `kerrconv` to $a < 0.83$, but given the poor constraints on many of the other parameters of this source (e.g., $r_{\text{min}} < 332 r_{\text{ms}}$), this value lacks credibility. We were unable to constrain BH spin in MCG–5-23-16, NGC 3783, Fairall 9 and NGC 2992 in the `kerrconv` fits.

There are several potential reasons why one might not be able to obtain a good spin constraint for a given source. Firstly, a lack of sufficient photons in the data set is a severe limitation for obvious reasons. This is certainly the case in 3c273, for example, and also plays a role in the spectra of NGC 2992 and Fairall 9. Generally speaking, the more photons one has to work with, the better the fit constraints will be.

Secondly, if the iron line is not sufficiently broad, then the fit will be more likely to have difficulty picking out the role of relativistic contributors like BH spin to the overall line shape. A narrow iron line could originate from far out in the disk, away from

the spacetime where relativistic effects become important. This scenario would make it impossible to know the spin of the BH. Even iron lines from the inner regions of non-spinning BHs show the spectral signatures of relativity, as shown in Chapter 3, so even if the line originates from fairly close range in the disk around a non-spinning BH, we should be able to constrain its spin. Therefore, we should not be surprised that the sources for which we are unable to get spin constraints all share a common characteristic: constraints on r_{\min} that fall outside the inner portion of the disk, i.e., well outside of $6r_g$.

AGN	α	a	i ($^\circ$)	r_{\min} (r_g)	χ^2/dof
MCG-6-30-15	2.84 – 2.95	0.998	30 – 32	1.71 – 2.11	940/1002 (0.94)
	5.93 – 6.37, 2.27 – 2.46, 10.28 – 13.99	0.97 – 0.98	30 – 31	1.68 – 2.67	907/999 (0.91)
MCG-5-23-16	1.98 – 4.30	0.998	21 – 37	18 – 44	1509/1490 (1.01)
	2.27 – 2.82	< 0.71	38 – 39	32 – 65	1514/1489 (1.03)
Mrk 766	1.78 – 2.05	0.998	85 – 86	1.24 – 1.82	1542/1311 (1.18)
	2.14 – 2.33	0.39 – 0.62	77 – 78	4.41 – 4.67	1539/1310 (1.17)
NGC 3783	9.23 – 10.00	0.998	< 18	1.24 – 1.80	1741/1489 (1.17)
	– – –	> 0.89	17 – 18	315 – 388	1732/1488 (1.16)
NGC 4051	2.45 – 3.63	0.998	30 – 39	3.96 – 6.98	1480/1397 (1.06)
	4.24 – 10.00	< 0.87	32 – 41	3.63 – 5.67	1479/1396 (1.06)
Fairall 9	1.40 – 2.70	0.998	> 50	1.24 – 25	672/692 (0.97)
	1.79 – 3.50	– – –	52 – 69	3.86 – 59	671/691 (0.97)
Ark 120	– – –	0.998	52 – 69	> 150.00	1639/1422 (1.15)
	1.65 – 1.98	< 0.69	67 – 69	3.94 – 6.43	1620/1421 (1.14)
NGC 2992	1.31 – 3.15	0.998	37 – 55	3.07 – 4.27	1399/1310 (1.07)
	3.90 – 10.00	> 0.97	38 – 49	1.67 – 6.22	1399/1309 (1.07)
3c273	2.83 – 6.37	0.998	< 67	1.24 – 3.18	228/267 (0.854)
	– – –	– – –	< 35	1.64 – 3.99	229/266 (0.86)
3c120	– – –	0.998	> 72	> 253	1474/1462 (1.01)
	1.74 – 10.00	– – –	13 – 14	44 – 47	1482/1461 (1.01)

Table 5.10: Comparison of the spectral fitting results for the 2.5 – 10.0 keV spectra using the laor and kerrdisk models. All AGN in our sample that are thought to possess broad iron lines are presented. For each source the top row represents the laor range in parameter value while the bottom row represents the kerrdisk range in parameter value. Ranges are given at 90% confidence. Note that MCG-6-30-15 is able to be fit with a broken power-law emissivity index, which is listed under α as α_1 , α_2 , r_{br} (r_g). For all other sources, $\alpha_1 = \alpha_2$ and $r_{\text{br}} = 6.0r_g$.

AGN	Fe/solar	ξ	α	i ($^\circ$)	r_{\min} (r_g)	χ^2/dof
MCG-6-30-15	9.57 – 10.00	249 – 273	8.89 – 10.00	39 – 40	4.47 – 4.94	1296/1003 (1.29)
	5.97 – 10.00	< 39				887/1000 (0.87)
MCG-5-23-16	0.53 – 0.83	< 34	1.05 – 4.40	22 – 37	1.24 – 64	1555/1492 (1.04)
	0.48 – 0.72	< 31				1485/1488 (1.00)
Mrk 766	1.00	1742 – 3886	1.71 – 2.04	73 – 81	1.24 – 2.96	1534/1313 (1.17)
	1.00	413 – 672				1495/1310 (1.14)
NGC 3783	0.18 – 0.34	< 53				1534/1490 (1.03)
	0.14 – 0.23	< 46	– – –	< 35	> 102	1525/1487 (1.03)
NGC 4051	1.21 – 4.27	< 57	3.08 – 4.29	32 – 38	1.24 – 7.36	1506/1398 (1.08)
	1.29 – 10.00	< 122				1476/1395 (1.06)
Fairall 9	1.00	30.00	2.47 – 10.00	50 – 87	1.24 – 8.25	680/695 (0.98)
	1.00	30.00				665/692 (0.96)
Ark 120	1.00	30.00	1.59 – 1.83	82 – 86	1.24 – 2.02	1717/1425 (1.20)
	1.00	30.00				1576/1422 (1.11)
NGC 2992	1.00	30.00	1.50 – 4.17	17 – 42	– – –	1414/1313 (1.08)
	1.00	30.00				1405/1310 (1.07)
3c273	1.00	30.00	2.45 – 10.00	< 60	1.24 – 11	235/269 (0.87)
	1.00	30.00				228/266 (0.86)
3c120	1.44 – 10.00	47 – 186	– – –	17 – 39	> 71	1485/1463 (1.02)
	0.92 – 10.00	< 160				1471/1460 (1.01)

Table 5.11: Comparison of the spectral fitting results for the 2.5 – 10.0 keV spectra using the ionized reflection model `reflion` and `kdblur` (`refl`), which convolves the reflection spectrum with a smearing kernel from a maximally-spinning BH. All AGN in our sample that are thought to possess broad iron lines are presented. For each column of data, the top row represents the `reflion` range in parameter values while the bottom row represents the `kdblur` (`refl`) range in parameter values. For the `reflion` component, the value of the incident power-law spectral index is set equal to that of the continuum. Ranges are given at 90% confidence.

AGN	Fe/solar	ξ	α	a	i ($^\circ$)	r_{\min} (r_g)	χ^2/dof
MCG-6-30-15	4.75 – 10.00	< 83	5.46 – 6.95, 2.34 – 2.66, 7 – 11	> 0.96	30 – 32	1.43 – 2.22	834/997 (0.84)
MCG-5-23-16	0.55 – 0.69	< 31	1.84 – 3.04	– – –	26 – 48	44 – 152	1483/1487 (1.00)
Mrk 766	1.00	444 – 852	1.80 – 2.08	> 0.85	73 – 81	< 2.78	1492/1309 (1.14)
NGC 3783	0.15 – 0.22	< 40	– – –	– – –	26 – 46	< 983	1526/1486 (1.03)
NGC 4051	1.25 – 5.69	< 108	4.23 – 10.00	> 0.67	36 – 40	3.50 – 7.19	1475/1394 (1.06)
Fairall 9	1.00	30.00	1.86 – 10.00	– – –	52 – 64	– – –	665/691 (0.96)
Ark 120	1.00	30.00	2.29 – 2.44	0.63 – 0.68	79 – 80	3.62 – 3.95	1543/1421 (1.09)
NGC 2992	1.00	30.00	1.24 – 10.00	– – –	20 – 48	5.57 – 12.00	1402/1312 (1.07)
3c273	1.00	< 356	2.74 – 10.00	> 0.72	< 63	1.24 – 2.84	228/265 (0.86)
3c120	1.00	< 36	< 1.39	< 0.83	27 – 36	2.76 – 915.00	1468/1460 (1.01)

Table 5.12: Comparison of the spectral fitting results for the 2.5 – 10.0 keV spectra using the ionized reflection model `reflion` convolved with a smearing kernel from a BH of arbitrary spin `kerrconv`. All AGN in our sample are presented, based on the fits shown above in Tables 5.10-5.11. For the `reflion` component, the value of the incident power-law spectral index is set equal to that of the continuum. Parameter value ranges are given at 90% confidence. Note that MCG-6-30-15 is able to be fit with a broken power-law emissivity index, which is listed under α as α_1 , α_2 , r_{br} (r_g). For all other sources, $\alpha_1 = \alpha_2$ and $r_{\text{br}} = 6.0 r_g$.

Chapter 6

Conclusions

This thesis explores the use of broad iron emission lines to constrain black hole spin, and makes the first steps toward estimating the spins in a small and relatively homogeneous sample of AGN. Our study of ten prominent Sy-1 AGN observed to have prominent iron lines has provided us with some intriguing data on this subject and has also put us in an excellent position to apply our spectral fitting techniques to many other sources in the future.

6.1 Summary of Results

We began this work by discussing the importance of BH spin, both as a fundamental property of the BH itself as well as a means of extending the physical influence of the BH to its surroundings, both near (gravitationally and magnetically on the accretion disk) and far (AGN jets can extend up to kpc or even Mpc scales, providing feedback in galaxy clusters and perhaps solving the so-called “cooling flow” problem). We then presented the strengths of the iron line spectral fitting method we use to constrain BH spin in Chapter 1, and stressed the importance of X-ray observations of AGN in this vein. We reviewed the history of X-ray astronomy in order to place our current work in context, and to emphasize

the unprecedented spectral resolution and throughput of modern detectors such as *XMM-Newton*, *Chandra* and *Suzaku*.

Chapter 1 provides an overview of the complex interaction between a BH and its accretion disk, as well as its other surroundings, and discusses the use and efficacy of the iron line spectral fitting method as a BH spin diagnostic. In Chapter 2 we expand upon the caveats one must take into account when using spectral modeling to assess spin, most notably the complication of absorption. In order to isolate the effects of spin on the shape of the iron line profile it is imperative to first model the continuum accurately, including any absorption features present. These lines and edges, whether Galactic in origin or intrinsic to the AGN system as either cold or ionized “warm” absorption, can alter the curvature of the continuum and, if not properly accounted for, can give the misleading impression of a broad red wing to an iron line profile. To illustrate the complexities inherent in properly modeling the spectral continuum we present an analysis of the Sy-1 AGN NGC 4593. While this source does *not* appear to harbor a broad iron line or show any other features indicative of reflection from the inner portions of an ionized accretion disk, it is an excellent example of a spectrum complicated by absorption and a soft excess, and provided an important test case for us to use in developing our systematic approach to modeling the continuum in an AGN.

With the aforementioned new detectors currently in orbit and sending back spectra of unprecedented quality, we are now in a position to start extracting meaningful constraints on BH spin for the first time. To do so, however, requires a fully relativistic iron line model that allows the BH spin to be a free parameter in the spectral fit. Chapter 3 presents our version of this model, called `kerrdisk`, as well as its incorporation into a convolution model that can be applied to a full ionized disk reflection spectrum, `kerrconv`. We discuss the construction of this model in detail and compare its results to those of the publicly available models within the XSPEC X-ray spectral modeling package, as well as

similar models with free BH spin that are currently being developed by other groups. We find that our model outperforms both the public `diskline` ($a = 0$) and `laor` ($a = 0.998$) models in terms of accuracy and noise reduction. Though we do not yet include emission from within the marginally stable orbit of the accretion disk, our results from outside the plunging region mimic the precision and accuracy of the other groups with free-spin models. Whereas these other groups rely on large, heavily sampled pre-computed tables of the photon transfer function, however, we sample the transfer function more sparsely and linearly interpolate between tabulated points. This works because the transfer function is a slowly-varying function over radius, relative redshift, spin and inclination angle. While this method is more computationally intensive, it produces the same spectral line profile and the table takes up only ~ 40 MB of disk space as opposed to the multi-GB required for the tables of similar codes being developed. This makes our code much more portable without sacrificing quality.

Chapter 4 discusses our application of these new models to the spectrum of MCG–6-30-15, a Sy-1 AGN with the broadest iron line yet observed. Using a 350 ks *XMM-Newton* EPIC-pn observation with over 4×10^6 photons, we were able to accurately model the continuum with a power-law modified by both Galactic and intrinsic warm absorption and a thermal soft excess below 2 keV. Above 3 keV the red wing of the iron line becomes evident, and though this feature is well fit by a narrow Gaussian core at 6.4 keV and a broad `kerrdisk` component at the same energy (as well as an ionized line of iron at 6.9 keV), the best fit is achieved by convolving an ionized disk reflection spectrum with the `kerrconv` model. This model has the physical appeal of simultaneously accounting for the soft excess (thought to be thermal emission from the disk) and the broad iron line, as well as the so-called “hard tail” of excess emission seen above 8 keV. The model fit yields a formal 90% confidence constraint on the BH spin of $a > 0.987$, with $r_{\min} = 1.62 r_g$, and statistically rules out the possibility of a Schwarzschild BH in this source.

More detailed observations may statistically constrain the BH spin in MCG–6-30-15 at a slightly lower value, but the goodness-of-fit of our model to the data strongly indicates that this is a rapidly spinning BH. Additionally, due to an enhancement of emission seen in the innermost portion of the disk ($\alpha_1 \sim 6$ within $r = 5.56 r_g$), we may be witnessing the extraction of rotational energy from the BH by the accretion disk via magnetic torquing at the ISCO in MCG–6-30-15. Though this excess inner emission could also be explained by gravitational light bending acting on a centrally-concentrated X-ray continuum source located just above the BH/disk, we are undoubtedly seeing strong relativistic effects in this source, which will continue to remain an object of intense study in the future as we pursue answers to these questions, among others.

We extend the application of our new models to other Sy-1 AGN thought to harbor broad iron lines in Chapter 5. All data were obtained from the *XMM-Newton* public archive, and only the EPIC-pn spectra were examined. Using our work on NGC 4593 and MCG–6-30-15 as templates for establishing our spectral fitting method, we first model the continuum of each source, taking the effects of absorption into account as well as any soft excess that might be present. We then restrict our attention to the hard spectrum from 2.5 – 10.0 keV and focus on fitting the iron line in each source using a systematic approach designed to assess the presence of a broad component, determine if disk reflection is a factor, and parameterize the line as accurately as possible in order to extract the best statistical constraints we can on the BH spin for each object. The hard spectrum of MCG–6-30-15 is revisited, as well as nine other AGN identified through the prominence of their iron lines. Of these nine, we were able to get reliable spin constraints for three: Ark 120 ($a = 0.63 - 0.68$), Mrk 766 ($a = 0.59 - 0.84$), and NGC 4051 ($a > 0.67$). In each of the nine cases the best fit was given by a *kerrconv* model including reflection, and the three cases with reliable spin constraints each showed a significant improvement in their overall goodness-of-fit using a *kerrconv* component as opposed to a *kdblur*

component, where the spin is hardwired at $a = 0.998$. A fourth source, 3c273, was able to have its spin constrained in our fits to $a > 0.72$, but due to the paucity of photons in the observation this constraint cannot be considered robust. If future observations support this spin constraint, however, it will be an interesting result because 3c273 is ordinarily radio-loud and was observed by *XMM-Newton* in a rare quiescent state when the broad line could be detected. The other radio-loud source in our sample, 3c120, was not able to have its spin constrained.

6.2 Discussion

The demographics of BH spin are unknown, and, until recently, unknowable. The advent of high-resolution X-ray spectroscopy and the promising development of gravitational wave detectors are now making this field of research accessible. For the first time in the history of astronomy we are now in a position of being able to calculate a BH's mass and spin, thus completely defining it in a mathematical sense.

This thesis represents the first-ever survey to quantify the angular momenta of BHs in AGN using relativistically broadened iron lines as spin diagnostics. Because this method is mass-independent and because the Fe-K α line is prevalent in BH/accretion disk systems, we anticipate that this work will serve as a stepping stone for guiding future spin surveys across a wide range of environments, including AGN of varying host galaxy morphology, and supermassive BHs vs. stellar-mass BHs, to name two interesting population comparisons.

Though our sample of ten Sy-1 AGN is far too small to allow us to draw any robust conclusions about the distribution of BH spins in this group of objects as a whole, this work has allowed us to design a viable method for evaluating the presence of a broad iron line in the data and using it to place constraints on the BH spin with our new models,

kerrdisk and kerrconv. Based on our data analysis we have arrived at several important conclusions that we hope will inform subsequent BH spin surveys:

1. It is necessary to have a certain minimum number of photons in order to have a spectrum of the quality needed to extract spin information. Based on our results, this number is $\gtrsim 10^6$ photons. This makes sense, given that spectral line fitting of any kind is a statistical process and without enough data points one cannot expect to model a line with any statistical certainty.
2. A broad iron line is needed in order to constrain spin. Simply put, a narrow line cannot represent emission from the inner part of the disk because it would show signatures of Doppler shifting and relativistic effects that combine to give good diagnostic disk lines their characteristic shapes. If a line does not originate in the inner disk, then relativity is not important to its morphology, and it cannot be used as a spin diagnostic because spin is a relativistic effect.
3. We are seeing broad lines in many Sy-1 sources, robustly. Five out of ten sources showed a significant improvement in their global goodness-of-fit when relativistic smearing was added to a static ionized disk reflection spectrum. Granted, these sources were selected based on prior observations of a broadened iron line in their spectra, but it is thought that broad iron lines may inhabit the spectra of a significant portion of AGN.
4. Across our sample of radio-quiet Sy-1 sources, we see a mix of spin constraints from moderate to very high, though interestingly we do *not* see any non-spinning sources. This shows that radio-loudness is not dependent on spin alone: it must be determined by at least one other parameter. Magnetic fields and/or thick disks are likely candidates: the Blandford-Znajek process is thought to be critical in jet formation, and most sources with radio jets are hypothesized to emanate from systems

with truncated thin disks (perhaps ADAFs).

5. Unfortunately, nature may be working against us in terms of measuring BH spin in radio-loud sources using the iron line method. Jet activity tends to overwhelm the spectrum along lines of sight to the broad line region, effectively burying the broad line and other disk signatures. For such radio-loud sources it may be necessary to rely on other methods of diagnosing spin such as thermal continuum fitting and polarimetry.

6.3 Future Work

Because we know so little about the spin distributions of black holes, much work remains to be done in this field. While the development of free-spin models such as `kerrdisk` and `kerrconv` has allowed us to begin attacking this question quantitatively and robustly for the first time among AGN sources, our survey represents only a first step in a much larger picture. Clearly, we need more sources with broad iron lines to form a larger statistical sample. We need better quality data with more photons and higher spectral resolution in order to better constrain the BH/disk parameters in broad iron line sources. We can get this through longer observations with active observatories such as *XMM-Newton*, *Chandra* and *Suzaku*, as well as coordinated observations in other wavebands (e.g., radio and optical) which can help us form a more complete picture of the physics at work in these systems. The upcoming *GLAST* mission (2008) will give us a tool with which to better investigate the nature of jets and other relativistic outflows from these systems which may depend in part on BH spin. In the coming decade X-ray astronomers will hopefully have an even more powerful instrument if *Constellation-X* receives the funding it needs. The calorimeters on board this mission promise unprecedented spectral resolution that will be invaluable to iron line studies.

We also need to expand our search radius to include stellar-mass BHs. These objects are thought to have their natal spins intact, so it will be interesting to see how the spin distribution in this population compares to that of AGN, especially given the physical similarities between AGN and GBHs in so many other areas. The advantage of the iron line method is its lack of dependence on BH mass, so this is an ideal technique to employ for such a comparison. Given the presence of other methods to diagnose BH spin, it will also be important to see how our results compare to those obtained using thermal continuum fitting, polarimetry and QPOs. Ideally, the spin constraints calculated using each different method should be consistent.

Finally, we can improve the accuracy of the `kerrdisk` and `kerrconv` models by including the effects of relativity on emission produced from within the ISCO of the disk. In so doing, however, it is crucial to properly account for the ionization level and optical depth of the material in the plunging region. Because this gas is subject to greater tidal forces and incident blueshifted radiation than the gas outside the ISCO, it is likely to be quite rarefied, optically thin and highly ionized. Proper modeling of the gas physics in this region is necessary in order to evaluate the overall contribution of emission from this region to the broad iron line.

The pace of discovery in this field is ever-increasing. With access to new X-ray data each day and detectors such as *Constellation-X* and *LISA* on the horizon, it is an exciting time to explore the nature of black holes and what they can tell us about the accuracy of General Relativity in the strong-field limit. We are poised to answer some of science's most fundamental questions in the new millennium.

Appendix A

Computing `kerrdisk` Line Profiles

We include here the FORTRAN driver program for computing line profiles with `kerrdisk`. This program is called as a subroutine in the XSPEC spectral modeling package. The basic principles of the code are expanded upon in detail in Chapter 3. This program creates a simulated emission line profile from matter orbiting an accretion disk around a black hole. It uses photon ray-tracing and fully relativistic calculations to compute the energies and trajectories of each photon leaving the system (Cunningham 1975; Speith et al. 1995), storing this information in a table that is accessed by the driver code each time it is run. Several parameters are input by the user, among them BH spin (a) and disk inclination angle (i). Because the photon transfer function varies slowly over these two parameters, we use linear interpolation to calculate the value of the transfer function between tabulated points. This technique produces a very accurate line profile without having to reference a table that is hundreds of GB in size, as must be done in many similar line emission codes that allow BH spin to be a free parameter in the model fit.

Parameters that must be input by the user are given below:

1. Rest-frame line energy (E) in keV.
2. The emissivity index of the inner disk (α_1); the disk radiates as $r^{-\alpha}$ at a given

radius. Parameter range is $\alpha = 0 - 10$.

3. The emissivity index of the outer disk (α_2). Same parameter range as above.
4. The break radius (r_{br}) at which the disk switches from the inner to outer emissivity index, in units of the radius of marginal stability (r_{ms}). Possible values range from $1 - 400 r_{ms}$.
5. The dimensionless spin of the BH (a), which can range from $a = 0 - 0.998$.
6. The inclination angle of the accretion disk to our line of sight (i), ranging from $0 - 90^\circ$.
7. The inner emitting radius of the accretion disk (r_{min}) in units of r_{ms} . We do not include emission from within r_{ms} at this time, so the possible values range from $1 - 400 r_{ms}$.
8. The outer emitting radius of the accretion disk (r_{max}) in units of r_{ms} . The maximum possible value is $400 r_{ms}$.

The code is presented in full below:

```
subroutine spin(EAR,NE,PARAM,IFL,PHOTAR,PHOTER)
c
c XSPECv11 subroutine to produce an emission line profile from a thin
c Keplerian disk around a Kerr black hole with arbitrary spin
c parameter. Method relies on the transfer function approach
c of Cunningham (1975); the line profile can be computed via a
c simple integral with an analytic integrand apart from the
c effects of gravitational light bending/lensing. These are
c incorporated into a slowly varying transfer function computed
c via the code of Speith et al. (1995) and sparsely tabulated in the
c accompanying table "kerrtable.dat". High quality results are
c obtained despite the sparse sampling of the TF through
c linear interpolation of this slowly varying function.
c
```

```

c      This code also generates the basic relativistic disk kernel
c      used for the convolution model kerrconv.
c
c      Two features have been hardwired into this code but are simple
c      to change.  First, we assume that the line emissivity is described
c      with a broken powerlaw (see comment starting "EMISSIVITY PROFILE").
c      It is trivial to include any functional form.  Second, we have
c      used the same limb-darkening rule as used in Laor (1991; see
c      comment starting "LIMB DARKENING").  This is readily changed to any
c      functional form.
c
c      For other details of this code see Brenneman & Reynolds (2006).
c      Please reference this paper if you publish results derived from this
c      model.
c
c      Developed by Laura Brenneman and Chris Reynolds
c      Dept. of Astronomy, University of Maryland, College Park.
c
c
c      IMPLICIT NONE
c      INTEGER IFL, NE
c      REAL*4 EAR(0:NE), PARAM(9), PHOTAR(NE), PHOTER(NE)
c
c-----Initialization-----
c
c      real*8 rplus,sumspec
c      integer nradii,ng,readflag,ia,imu0,abins,mu0bins
c      parameter(nradii=50,ng=20,abins=20,mu0bins=20)
c      real*8 a,theta0,mu0,gstar(ng),g(nradii,ng),cosneh(2)
c      real*8 a_tab(abins),mu0_tab(mu0bins),temp
c      real*8 aintfac,mu0intfac
c      real*8 trff_tab(nradii,ng,2,abins,mu0bins)
c      real*8 cosne_tab(nradii,ng,2,abins,mu0bins)
c      real*8 gmin_tab(nradii,abins,mu0bins)
c      real*8 gmax_tab(nradii,abins,mu0bins)
c      real*8 trffh(2),re(nradii),gmin(nradii)
c      real*8 gmax(nradii),trff(nradii,ng,2),cosne(nradii,ng,2)
c      real*8 ispec,lspec(ne),normspec(ne),eoo(0:ne)
c      real*8 lspecfine(4*ne),eeofine(4*ne)
c      real*8 intgmin,intgmax,inttf(ng,2),intmu(ng,2),rad,lgrad,intfac
c      real*8 intgs
c      real*8 rms,marginal,gee,gstar2,trf,mu,eem1,eem2
c      real*8 rmin,rmax,alp1,alp2,rbreak,lineE,z

```

```

real*8 rmin_grid,rmax_grid
real*8 pi,r1,r2,r(nradii),wr(nradii),g1,g2,wg(ng)
integer energy(10000)
integer i,j,k,ii,jj,ii1,ii2,igstar2,irad
external gauleg
save a_tab,trff_tab,cosne_tab,gmin_tab,gmax_tab,mu0_tab
c
c Get parameters of model from xspec.
c
lineE=param(1)
alp1=param(2)
alp2=param(3)
rbreak=param(4)
a=param(5)
theta0=param(6)
rmin=param(7)
rmax=param(8)
z=param(9)

rms=marginal(a)

rmin=rmin*rms
rmax=rmax*rms
c
c Set pi and convert angle variables.
c
pi = 4.d0*atan(1.d0)
theta0=theta0*pi/180.d0
mu0=cos(theta0)
c
c Read in transfer function from the kerrtable.dat file. We use
c the value of a_tab(1) to determine whether this is the first call
c to the code in a given xspec session. On subsequent calls, we
c do not need to read the file.
c
if ( dabs(a_tab(1) - 1.0e-2) .gt. 1.0e-3) then
c
c USER MUST SPECIFY FULL PATH TO KERRTABLE.DAT HERE
c
open (8,file=
&' /n/artemis/lwb/software/xspec_local_models/kerrtableb.dat'
& ,status='unknown')
read(8,*) ,ii,jj
read(8,*) ,a_tab

```

```

read(8,*) ,mu0_tab
do i=1,abins
  do j=1,mu0bins
    read(8,*) ,gmin
    read(8,*) ,gmax
    read(8,*) ,trff
    read(8,*) ,cosne
    do ii=1,nradii
      gmin_tab(ii,i,j)=gmin(ii)
      gmax_tab(ii,i,j)=gmax(ii)
      do jj=1,ng
        do k=1,2
          trff_tab(ii,jj,k,i,j)=trff(ii,jj,k)
          cosne_tab(ii,jj,k,i,j)=cosne(ii,jj,k)
        enddo
      enddo
    enddo
  enddo
enddo
close(8)
endif

c
c Work out interpolation factors in spin and mu0 directions.
c
  ia=1
  do i=1,abins
    if (a_tab(i) .lt. a) ia=i
  enddo
  aintfac=(a-a_tab(ia))/(a_tab(ia+1)-a_tab(ia))
  imu0=1
  do i=1,mu0bins
    if (mu0_tab(i) .lt. mu0) imu0=i
  enddo
  mu0intfac=(mu0-mu0_tab(imu0))/(mu0_tab(imu0+1)-mu0_tab(imu0))

c
c Attempt to fix low-inclination problem
c
  if (mu0_tab(mu0bins) .lt. mu0) then
    imu0=mu0bins-1
    mu0intfac=1
  endif

c
c Interpolate transfer function in a and mu0 plane.
c

```

```

do i=1,nradii
  gmin(i)=(1.0-aintfac)*(1.0-mu0intfac) *
$     gmin_tab(i,ia,imu0)
$     +aintfac*(1.0-mu0intfac)*
$     gmin_tab(i,ia+1,imu0)
$     +(1.0-aintfac)*mu0intfac*
$     gmin_tab(i,ia,imu0+1)
$     +aintfac*mu0intfac*
$     gmin_tab(i,ia+1,imu0+1)
  gmax(i)=(1.0-aintfac)*(1.0-mu0intfac) *
$     gmax_tab(i,ia,imu0)
$     +aintfac*(1.0-mu0intfac)*
$     gmax_tab(i,ia+1,imu0)
$     +(1.0-aintfac)*mu0intfac*
$     gmax_tab(i,ia,imu0+1)
$     +aintfac*mu0intfac*
$     gmax_tab(i,ia+1,imu0+1)
  do j=1,ng
    do k=1,2
      trff(i,j,k)=(1.0-aintfac)*(1.0-mu0intfac) *
$         trff_tab(i,j,k,ia,imu0)
$         +aintfac*(1.0-mu0intfac)*
$         trff_tab(i,j,k,ia+1,imu0)
$         +(1.0-aintfac)*mu0intfac*
$         trff_tab(i,j,k,ia,imu0+1)
$         +aintfac*mu0intfac*
$         trff_tab(i,j,k,ia+1,imu0+1)
      cosne(i,j,k)=(1.0-aintfac)*(1.0-mu0intfac) *
$         cosne_tab(i,j,k,ia,imu0)
$         +aintfac*(1.0-mu0intfac)*
$         cosne_tab(i,j,k,ia+1,imu0)
$         +(1.0-aintfac)*mu0intfac*
$         cosne_tab(i,j,k,ia,imu0+1)
$         +aintfac*mu0intfac*
$         cosne_tab(i,j,k,ia+1,imu0+1)
    enddo
  enddo
enddo
c
c   Set up a radial grid: inversely spaced, and define integration values
c   for g* via gauleg as in radial case.
c
  rmin_grid=rms
  rmax_grid=2500*rms

```

```

r1=1.d0/sqrt(rmax_grid)
r2=1.d0/sqrt(rmin_grid)
call gauleg(r1,r2,r,wr,nradii)
do i=1,nradii
    re(i)=1.d0/(r(i)**2.0)
enddo
g1=0.d0
g2=1.d0
call gauleg(g1,g2,gstar,wg,ng)
c
c-----Integrate the line profile-----
c
c
c
c   Generate energy grid and finer grid within it (4 x finer)
c   to effectively get greater resolution than before without
c   smoothing. We will linearly interpolate between grid point
c   values later.
c
do ii=0,ne
    lspec(ii)=0.d0
    eeo(ii)=dble(ear(ii))
enddo
do ii=1,ne
    do j=1,4
        lspecfine((ii-1)*4+j)=0.d0
        intfac=float(j)/4.0
        eeofine((ii-1)*4+j) =
&            intfac*eeo(ii)+(1.0-intfac)*eeo(ii-1)
    enddo
enddo
c
c   Latest generation of line integration. Integrates over a
c   large number of radii, using linear radial interpolation
c   of the TF as well as gmin and gmax.
c
irad=nradii-1
do ii=1,nradii
    if (rmin .lt. re(ii)) irad=ii
enddo
do lgrad=dlog10(re(nradii)),dlog10(re(1)),0.2/float(ne)
    rad=10.0**(lgrad)
    if ((rad .gt. rmin) .and. (rad .lt. rmax)) then
        if (rad .gt. re(irad)) irad=irad-1
    end if
enddo

```

```

intfac=(rad-re(irad+1))/(re(irad)-re(irad+1))
do j=1,ng
  do k=1,2
    inttf(j,k)=intfac*trff(irad,j,k) +
&      (1.0-intfac)*trff(irad+1,j,k)
    intmu(j,k)=intfac*cosne(irad,j,k) +
&      (1.0-intfac)*cosne(irad+1,j,k)
  enddo
enddo
intgmin=intfac*gmin(irad)+(1.0-intfac)*gmin(irad+1)
intgmax=intfac*gmax(irad)+(1.0-intfac)*gmax(irad+1)
c
c Emissivity profile is hardwired in here. Currently a broken
c powerlaw.
c
  if (rad .lt. rbreak) then
    ispec=(rad/rbreak)**(-alp1)
  else
    ispec=(rad/rbreak)**(-alp2)
  endif
c
eem1=lineE*intgmin/(1.0d0+z)
eem2=lineE*intgmax/(1.0d0+z)
ii1=1
ii2=1

do ii=1,4*ne
  if (eofine(ii) .lt. eem1) ii1=ii
enddo
do ii=ii1-1,4*ne
  if (eofine(ii) .lt. eem2) ii2=ii
enddo

if ((ii1 .gt. 1) .and. (ii2 .gt. 1)) then
2005  do ii=ii1+1,ii2
      gee=eofine(ii)/(lineE/(1.0d0+z))
      gstar2=(gee-intgmin)/(intgmax-intgmin)
      do k=1,2
        if (gstar2 .le. gstar(1)) then
          trf=inttf(1,k)
          mu=intmu(1,k)
        endif
      if (gstar2 .ge. gstar(ng)) then
        trf=inttf(ng,k)

```

```

        mu=intmu(ng,k)
    endif
    if ((gstar2 .lt. gstar(ng)) .and.
&      (gstar2 .gt. gstar(1))) then
        do j=1,ng-1
            if (gstar(j) .lt. gstar2) igstar2=j
        enddo
        intgs=(gstar2-gstar(igstar2))/
&          (gstar(igstar2+1)-gstar(igstar2))
        trf=intgs*inttf(igstar2,k) +
&          (1.0-intgs)*inttf(igstar2+1,k)
        mu=intgs*intmu(igstar2,k) +
&          (1.0-intgs)*intmu(igstar2+1,k)
    endif
c
c    Next line actually is the guts of the integral. The
c    LIMB DARKENING is hardwired in here. It is currently set to
c    mu*(1+2.06*mu), as per Laor (1991).
c
        lspecfine(ii)=lspecfine(ii) +
&          rad*gee*(2.0*pi*gee)**2.0
&          *trf*ispec*(1.0+2.06*mu)*rad/
&          (sqrt(gstar2-gstar2**2.0)*(intgmax-intgmin))
    enddo
    enddo
    endif
    endif
    enddo
c
c    Bin up lspecfine to give to lspec.
c
    do i=1,ne
        do j=1,4
            lspec(i)=lspec(i)+lspecfine((i-1)*4+j)
        enddo
    enddo
c
c-----Output of spectral luminosity-----
c
c    Divide each lspec(ii) by the observed energy of that
c    gridpoint --> ph/cm^2/s units.
c
    do ii=1,ne

```

```

        lspec(ii)=lspec(ii)/eeo(ii)
    enddo
    sumspec=0.d0
    do ii=1,ne
        if (lspec(ii) .gt. 0.d0) then
c
c      Sumspec weighted by the energy bin size.
c
            sumspec=sumspec+lspec(ii)*(eeo(ii)-eeo(ii-1))
        endif
    enddo
c    open(7,file='lspec.dat',status='unknown')
    do ii=1,ne
        if (lspec(ii) .gt. 0.d0) then
c
c      Normspec weighted by the energy bin size.
c
            normspec(ii)=lspec(ii)*(eeo(ii)-eeo(ii-1))/sumspec
        else
            normspec(ii)=0.d0
        endif
        photar(ii)=normspec(ii)
c    write(7,*) eeo(ii),normspec(ii)
    enddo
c    close(unit=7)

    end

c
c-----Subroutines-----
c
c
c
c  Subroutine to calculate rms for a given spin (a).  Assumes only prograde BHs.
c
    function marginal(a)
    implicit none
    real*8 marginal,a,Z1,Z2
    Z1=1.0+(1.0-a**2.0)**0.33*((1.0+a)**0.33+(1.0-a)**0.33)
    Z2=((3.0*a**2.0)+(Z1**2.0))**0.5
    marginal=3.0+Z2-((3.0-Z1)*(3.0+Z1+(2*Z2)))*0.5
    return

    end

```

```

C=====
C Subroutine to calculate the abscissas and weights for the Gauss-Legendre-
C Quadrature. The routine is based on the NUMERICAL RECIPES and uses an
C algorithem of G.B. Rybicki.
C Input: x1 ,x2: range of integration.
C        n: order of the orthogonal polynomials and the quadrature formula.
C Output: x = x(n): array of the abscissas.
C        w = w(n): array of the weights.

```

```

SUBROUTINE GAULEG(X1,X2,X,W,N)

```

```

INTEGER N,M,I,J
REAL*8 X1,X2,X(N),W(N)
REAL*8 PI, XM, XL, Z, P1, P2, P3, Z1, PP, EPS
PARAMETER (PI = 3.14159265358979323846D0)
PARAMETER (EPS=3.D-14)

```

```

M=(N+1)/2
XM=0.5D0*(X2+X1)
XL=0.5D0*(X2-X1)
DO 12 I=1,M
    Z=COS(PI*(I-.25D0)/(N+.5D0))
1    CONTINUE
    P1=1.D0
    P2=0.D0
    DO 11 J=1,N
        P3=P2
        P2=P1
        P1=((2.D0*J-1.D0)*Z*P2-(J-1.D0)*P3)/J
11   CONTINUE
    PP=N*(Z*P1-P2)/(Z*Z-1.D0)
    Z1=Z
    Z=Z1-P1/PP
    IF(ABS(Z-Z1).GT.EPS) GOTO 1
    X(I)=XM-XL*Z
    X(N+1-I)=XM+XL*Z
    W(I)=2.D0*XL/((1.D0-Z*Z)*PP*PP)
    W(N+1-I)=W(I)
12  CONTINUE
RETURN
END

```

Bibliography

- Abramowicz, M. A., Livio, M., Soker, N., & Szuszkiewicz, E. 1990, *Astr. Astrophys.*, 239, 399
- Agol, E. & Krolik, J. H. 2000, *Astrophys. J.*, 528, 161, arXiv:arXiv:astro-ph/9908049
- Anders, E. & Grevesse, N. 1989, *Geo. Cosm. Acta*, 53, 197
- Arnaud, K. A. in , Astronomical Society of the Pacific Conference Series, Vol. 101, Astronomical Data Analysis Software and Systems V, ed. G. H. JacobyJ. Barnes, 17–+
- Awaki, H., Koyama, K., Kunieda, H., & Tawara, Y. 1990, *Nature*, 346, 544
- Balbus, S. A. & Hawley, J. F. 1991, *Astrophys. J.*, 376, 214
- Balestra, I., Bianchi, S., & Matt, G. 2004, *Astr. Astrophys.*, 415, 437, arXiv:arXiv:astro-ph/0311316
- Ballantyne, D. R., Fabian, A. C., & Iwasawa, K. 2004, *Mon. Not. R. astr. Soc.*, 354, 839, arXiv:arXiv:astro-ph/0407453
- Ballantyne, D. R., Vaughan, S., & Fabian, A. C. 2003, *Mon. Not. R. astr. Soc.*, 342, 239, arXiv:arXiv:astro-ph/0302288
- Balucinska-Church, M. & McCammon, D. 1992, *Astrophys. J.*, 400, 699
- Basko, M. M. 1978, *Astrophys. J.*, 223, 268
- Bechtold, J., Czerny, B., Elvis, M., Fabbiano, G., & Green, R. F. 1987, *Astrophys. J.*, 314, 699
- Beckwith, K. & Done, C. 2004, *Mon. Not. R. astr. Soc.*, 352, 353

- Behar, E., Rasmussen, A. P., Blustin, A. J., Sako, M., Kahn, S. M., Kaastra, J. S., Branduardi-Raymont, G., & Steenbrugge, K. C. 2003, *Astrophys. J.*, 598, 232, arXiv:arXiv:astro-ph/0307467
- Bevington, P. R. 1969, *Data reduction and error analysis for the physical sciences* (New York: McGraw-Hill, 1969)
- Blandford, R. D. & Begelman, M. C. 1999, *Mon. Not. R. astr. Soc.*, 303, L1
- Blandford, R. D. & Payne, D. G. 1982, *Mon. Not. R. astr. Soc.*, 199, 883
- Blandford, R. D. & Znajek, R. L. 1977, *Mon. Not. R. astr. Soc.*, 179, 433
- Blustin, A. J., Branduardi-Raymont, G., Behar, E., Kaastra, J. S., Kahn, S. M., Page, M. J., Sako, M., & Steenbrugge, K. C. 2002, *Astr. Astrophys.*, 392, 453, arXiv:arXiv:astro-ph/0206316
- Blustin, A. J., Page, M. J., Fuerst, S. V., Branduardi-Raymont, G., & Ashton, C. E. 2005, *Astr. Astrophys.*, 431, 111
- Boller, T., Brandt, W. N., Fabian, A. C., & Fink, H. H. 1997, *Mon. Not. R. astr. Soc.*, 289, 393
- Bondi, H. & Hoyle, F. 1944, *Mon. Not. R. astr. Soc.*, 104, 273
- Bradt, H. V. D., Ohashi, T., & Pounds, K. A. 1992, *Ann. Rev. Astr. Astrophys.*, 30, 391
- Brandt, W. N., Fabian, A. C., Nandra, K., & Tsuruta, S. 1993, *Mon. Not. R. astr. Soc.*, 265, 996
- Brenneman, L. W. & Reynolds, C. S. 2006, *Astrophys. J.*, 652, 1028
- Čadež, A. & Calvani, M. 2005, *Mon. Not. R. astr. Soc.*, 363, 177
- Chen, X., Taam, R. E., Abramowicz, M. A., & Igumenshchev, I. V. 1997, *Mon. Not. R. astr. Soc.*, 285, 439, arXiv:arXiv:astro-ph/9612123
- Chiang, J., Reynolds, C. S., Blaes, O. M., Nowak, M. A., Murray, N., Madejski, G., Marshall, H. L., & Magdziarz, P. 2000, *Astrophys. J.*, 528, 292, arXiv:astro-ph/9907114
- Crenshaw, D. M. & Kraemer, S. B. 2001, *Astrophys. J. Lett.*, 562, L29, arXiv:arXiv:astro-

ph/0110304

- Crenshaw, D. M., Kraemer, S. B., Boggess, A., Maran, S. P., Mushotzky, R. F., & Wu, C.-C. 1999, *Astrophys. J.*, 516, 750, arXiv:arXiv:astro-ph/9812265
- Cunningham, C. T. 1975, *Astrophys. J.*, 202, 788
- Dabrowski, Y., Fabian, A. C., Iwasawa, K., Lasenby, A. N., & Reynolds, C. S. 1997, *Mon. Not. R. astr. Soc.*, 288, L11
- Day, C. S. R., Fabian, A. C., George, I. M., & Kunieda, H. 1990, *Mon. Not. R. astr. Soc.*, 247, 15P
- Dewangan, G. C., Griffiths, R. E., & Schurch, N. J. 2003, *Astrophys. J.*, 592, 52
- Dovčiak, M., Karas, V., & Yaqoob, T. 2004, *Astrophys. J. Suppl.*, 153, 205
- Edelson, R. A. & Krolik, J. H. 1988, *Astrophys. J.*, 333, 646
- Edelson, R. A. & Malkan, M. A. 1986, *Astrophys. J.*, 308, 59
- Elvis, M., Wilkes, B. J., & Lockman, F. J. 1989, *Astr. J.*, 97, 777
- Eracleous, M. & Halpern, J. P. 1998, *Astrophys. J.*, 505, 577, arXiv:arXiv:astro-ph/9804253
- Eracleous, M., Sambruna, R., & Mushotzky, R. F. 2000, *Astrophys. J.*, 537, 654, arXiv:arXiv:astro-ph/0002265
- Fabian, A. C., Nandra, K., Reynolds, C. S., Brandt, W. N., Otani, C., Tanaka, Y., Inoue, H., & Iwasawa, K. 1995, *Mon. Not. R. astr. Soc.*, 277, L11
- Fabian, A. C., Rees, M. J., Stella, L., & White, N. 1989, *Mon. Not. R. astr. Soc.*, 238, 729
- Fabian, A. C., Vaughan, S., Nandra, K., Iwasawa, K., Ballantyne, D. R., Lee, J. C., de Rosa, A., Turner, A., & Young, A. J. 2002, *Mon. Not. R. astr. Soc.*, 335, L1
- Forman, W., Jones, C., Cominsky, L., Julien, P., Murray, S., Peters, G., Tannanbaum, H., & Giacconi, R. 1978, *Astrophys. J. Suppl.*, 38, 357
- Friedman, H., Lichtman, S. W., & Byrum, E. T. 1951, *Phys. Rev.*, 83, 1025
- Garofalo, D. & Reynolds, C. S. 2005, *Astrophys. J.*, 624, 94, arXiv:arXiv:astro-

ph/0501455

- Gebhardt, K., Kormendy, J., Ho, L. C., Bender, R., Bower, G., Dressler, A., Faber, S. M., Filippenko, A. V., Green, R., Grillmair, C., Lauer, T. R., Magorrian, J., Pinkney, J., Richstone, D., & Tremaine, S. 2000, *Astrophys. J. Lett.*, 543, L5, arXiv:astro-ph/0007123
- George, I. M. & Fabian, A. C. 1991, *Mon. Not. R. astr. Soc.*, 249, 352
- George, I. M., Turner, T. J., Mushotzky, R., Nandra, K., & Netzer, H. 1998a, *Astrophys. J.*, 503, 174, arXiv:arXiv:astro-ph/9803051
- George, I. M., Turner, T. J., & Netzer, H. 1995, *Astrophys. J. Lett.*, 438, L67
- George, I. M., Turner, T. J., Netzer, H., Nandra, K., Mushotzky, R. F., & Yaqoob, T. 1998b, *Astrophys. J. Suppl.*, 114, 73, arXiv:arXiv:astro-ph/9708046
- Giacconi, R., Gursky, H., Paolini, F. R., & Rossi, B. B. 1962, *Phys. Rev. Lett.*, 9, 439
- Gilli, R., Comastri, A., & Hasinger, G. 2007, *Astr. Astrophys.*, 463, 79
- Gilli, R., Maiolino, R., Marconi, A., Risaliti, G., Dadina, M., Weaver, K. A., & Colbert, E. J. M. 2000, *Astr. Astrophys.*, 355, 485, arXiv:arXiv:astro-ph/0001107
- Gliozzi, M., Sambruna, R. M., & Eracleous, M. 2003, *Astrophys. J.*, 584, 176, arXiv:arXiv:astro-ph/0210300
- Gondoin, P., Lumb, D., Siddiqui, H., Guainazzi, M., & Scharrel, N. 2001, *Astr. Astrophys.*, 373, 805
- Gondoin, P., Orr, A., Lumb, D., & Santos-Lleo, M. 2002, *Astr. Astrophys.*, 388, 74
- Grupe, D., Wills, B. J., Leighly, K. M., & Meusinger, H. 2004, *Astr. J.*, 127, 156, arXiv:arXiv:astro-ph/0310027
- Guainazzi, M., Matt, G., Molendi, S., Orr, A., Fiore, F., Grandi, P., Matteuzzi, A., Mineo, T., Perola, G. C., Parmar, A. N., & Piro, L. 1999, *Astr. Astrophys.*, 341, L27
- Guainazzi, M., Mihara, T., Otani, C., & Matsuoka, M. 1996, *Publ. astr. Soc. Japan*, 48, 781, arXiv:arXiv:astro-ph/9610180
- Guilbert, P. W. & Rees, M. J. 1988, *Mon. Not. R. astr. Soc.*, 233, 475

- Haardt, F., Fossati, G., Grandi, P., Celotti, A., Pian, E., Ghisellini, G., Malizia, A., Maraschi, L., Paciesas, W., Raiteri, C. M., Tagliaferri, G., Treves, A., Urry, C. M., Villata, M., & Wagner, S. 1998, *Astr. Astrophys.*, 340, 35, arXiv:arXiv:astro-ph/9806229
- Halpern, J. P. 1984, *Astrophys. J.*, 281, 90
- Heckman, T. M., Smith, E. P., Baum, S. A., van Breugel, W. J. M., Miley, G. K., Illingworth, G. D., Bothun, G. D., & Balick, B. 1986, *Astrophys. J.*, 311, 526
- Houck, J. C. 2002, in High Resolution X-ray Spectroscopy with XMM-Newton and Chandra, ed. G. Branduardi-Raymont
- Ichimaru, S. 1977, *Astrophys. J.*, 214, 840
- Iwasawa, K., Fabian, A. C., Reynolds, C. S., Nandra, K., Otani, C., Inoue, H., Hayashida, K., Brandt, W. N., Dotani, T., Kunieda, H., Matsuoka, K., & Tanaka, K. 1996, *Mon. Not. R. astr. Soc.*, 282, 1038
- Jansen, F., Lumb, D., Altieri, B., Clavel, J., Ehle, M., Erd, C., Gabriel, C., Guainazzi, M., Gondoin, P., Much, R., Munoz, R., Santos, M., Schartel, N., Texier, D., & Vacanti, G. 2001, *Astr. Astrophys.*, 365, L1
- Juett, A. M., Galloway, D. K., & Chakrabarty, D. 2003, *Astrophys. J.*, 587, 754
- Kaastra, J. S. & Steenbrugge, K. C. in , X-ray Emission from Accretion onto Black Holes, ed. T. Yaqoob J. H. Krolik
- Kaspi, S., Brandt, W. N., George, I. M., Netzer, H., Crenshaw, D. M., Gabel, J. R., Hamann, F. W., Kaiser, M. E., Koratkar, A., Kraemer, S. B., Kriss, G. A., Mathur, S., Mushotzky, R. F., Nandra, K., Peterson, B. M., Shields, J. C., Turner, T. J., & Zheng, W. 2002, *Astrophys. J.*, 574, 643, arXiv:arXiv:astro-ph/0203263
- Kaspi, S., Brandt, W. N., Netzer, H., George, I. M., Chartas, G., Behar, E., Sambruna, R. M., Garmire, G. P., & Nousek, J. A. 2001, *Astrophys. J.*, 554, 216, arXiv:arXiv:astro-ph/0101540
- Kaspi, S., Brandt, W. N., Netzer, H., Sambruna, R., Chartas, G., Garmire, G. P., &

- Nousek, J. A. 2000, *Astrophys. J. Lett.*, 535, L17
- Kataoka, J., Tanihata, C., Kawai, N., Takahara, F., Takahashi, T., Edwards, P. G., & Makino, F. 2002, *Mon. Not. R. astr. Soc.*, 336, 932, arXiv:arXiv:astro-ph/0207003
- Kirsch, M. G., Abbey, A., Altieri, B., Baskill, D., Dennerl, K., van Dooren, J., Fauste, J., Freyberg, M. J., Gabriel, C., Haberl, F., Hartmann, H., Hartner, G., Meidinger, N., Metcalfe, L., Olabarri, B., Pollock, A. M., Read, A. M., Rives, S., Sembay, S., Smith, M. J., Stuhlinger, M., & Talavera, A. 2005, in Presented at the Society of Photo-Optical Instrumentation Engineers (SPIE) Conference, Vol. 5898, UV, X-Ray, and Gamma-Ray Space Instrumentation for Astronomy XIV. Edited by Siegmund, Oswald H. W. Proceedings of the SPIE, Volume 5898, pp. 224-235 (2005)., ed. O. H. W. Siegmund, 224–235
- Krolik, J. H., Hawley, J. F., & Hirose, S. 2005, *Astrophys. J.*, 622, 1008, arXiv:astro-ph/0409231
- Krolik, J. H. & Kriss, G. A. 2001, *Astrophys. J.*, 561, 684
- Kruper, J. S., Canizares, C. R., & Urry, C. M. 1990, *Astrophys. J. Suppl.*, 74, 347
- Lamer, G., McHardy, I. M., Uttley, P., & Jahoda, K. 2003, *Mon. Not. R. astr. Soc.*, 338, 323, arXiv:arXiv:astro-ph/0209155
- Lamer, G., Uttley, P., & McHardy, I. M. 2001, *Amer. Inst. Phys. Conf.*, 599, 710
- Laor, A. 1991, *Astrophys. J.*, 376, 90
- Lee, J. C., Fabian, A. C., Brandt, W. N., Reynolds, C. S., & Iwasawa, K. 1999, *Mon. Not. R. astr. Soc.*, 310, 973
- Lee, J. C., Fabian, A. C., Reynolds, C. S., Brandt, W. N., & Iwasawa, K. 2000, *Mon. Not. R. astr. Soc.*, 318, 857
- Lee, J. C., Iwasawa, K., Houck, J. C., Fabian, A. C., Marshall, H. L., & Canizares, C. R. 2002, *Astrophys. J.*, 570, L47
- Lee, J. C., Ogle, P. M., Canizares, C. R., Marshall, H. L., Schulz, N. S., Morales, R., Fabian, A. C., & Iwasawa, K. 2001, *Astrophys. J.*, 554, L13

- Leighly, K. M., Mushotzky, R. F., Yaqoob, T., Kunieda, H., & Edelson, R. 1996, *Astrophys. J.*, 469, 147, arXiv:arXiv:astro-ph/9603091
- Lewis, D. W., MacAlpine, G. M., & Koski, A. T. 1978, in Bulletin of the American Astronomical Society, Vol. 10, Bulletin of the American Astronomical Society, 388–+
- Liedahl, D. A., Osterheld, A. L., & Goldstein, W. H. 1995, *Astrophys. J. Lett.*, 438, L115
- Lightman, A. P. & White, T. R. 1988, *Astrophys. J.*, 335, 57
- Marconi, A., Risaliti, G., Gilli, R., Hunt, L. K., Maiolino, R., & Salvati, M. 2004, *Mon. Not. R. astr. Soc.*, 351, 169, arXiv:arXiv:astro-ph/0311619
- Markowitz, A. 2005, *Astrophys. J.*, 635, 180, arXiv:astro-ph/0508521
- Martocchia, A. & Matt, G. 1996, *Mon. Not. R. astr. Soc.*, 282, L53
- Mason, K. O., Branduardi-Raymont, G., Ogle, P. M., Page, M. J., Puchnarewicz, E. M., Behar, E., Córdova, F. A., Davis, S., Maraschi, L., McHardy, I. M., O’Brien, P. T., Priedhorsky, W. C., & Sasseen, T. P. 2003, *Astrophys. J.*, 582, 95, arXiv:arXiv:astro-ph/0209145
- Mason, K. O., McHardy, I. M., Page, M. J., Uttley, P., Córdova, F. A., Maraschi, L., Priedhorsky, W. C., Puchnarewicz, E. M., & Sasseen, T. 2002, *Astrophys. J. Lett.*, 580, L117
- Matsuoka, M., Piro, L., Yamauchi, M., & Murakami, T. 1990, *Astrophys. J.*, 361, 440
- Matt, G., Fabian, A. C., & Reynolds, C. S. 1997, *Mon. Not. R. astr. Soc.*, 289, 175
- Matt, G., Fabian, A. C., & Ross, R. R. 1993, *Mon. Not. R. astr. Soc.*, 262, 179
- Matt, G., Perola, G. C., Fiore, F., Guainazzi, M., Nicastro, F., & Piro, L. 2000, *Astr. Astrophys.*, 363, 863, arXiv:arXiv:astro-ph/0009322
- Matt, G., Perola, G. C., & Piro, L. 1991, *Astr. Astrophys.*, 247, 25
- McHardy, I. M., Gunn, K. F., Uttley, P., & Goad, M. R. 2005, *Mon. Not. R. astr. Soc.*, 359, 1469, arXiv:arXiv:astro-ph/0503100
- McHardy, I. M., Lawrence, A., Pye, J. P., & Pounds, K. A. 1981, *Mon. Not. R. astr. Soc.*, 197, 893

- McHardy, I. M., Papadakis, I. E., Uttley, P., Page, M. J., & Mason, K. O. 2004, *Mon. Not. R. astr. Soc.*, 348, 783, arXiv:astro-ph/0311220
- McKernan, B., Yaqoob, T., George, I. M., & Turner, T. J. 2003, *Astrophys. J.*, 593, 142, arXiv:astro-ph/0304403
- Merloni, A. & Fabian, A. C. 2002, *Mon. Not. R. astr. Soc.*, 332, 165
- Mewe, R., Gronenschild, E. H. B. M., & van den Oord, G. H. J. 1985, *Astr. Astrophys.*, 62, 197
- Mewe, R., Lemen, J. R., & van den Oord, G. H. J. 1986, *Astr. Astrophys.*, 65, 511
- Miller, J. M. 2007, ArXiv e-prints, 705, arXiv:0705.0540
- Miller, J. M., Fabian, A. C., Reynolds, C. S., Nowak, M. A., Homan, J., Freyberg, M. J., Ehle, M., Belloni, T., Wijnands, R., van der Klis, M., Charles, P. A., & Lewin, W. H. G. 2004, *Astrophys. J.*, 606, L131
- Miller, J. M., Raymond, J., Fabian, A., Steeghs, D., Homan, J., Reynolds, C., van der Klis, M., & Wijnands, R. 2006a, *Nature*, 441, 953
- Miller, J. M., Raymond, J., Homan, J., Fabian, A. C., Steeghs, D., Wijnands, R., Rupen, M., Charles, P., van der Klis, M., & Lewin, W. H. G. 2006b, *Astrophys. J.*, 646, 394
- Miller, J. S. & Antonucci, R. R. J. 1983, *Astrophys. J. Lett.*, 271, L7
- Miller, M. C. & Colbert, E. J. M. 2004, *Intern. J. Mod. Phys. D.*, 13, 1
- Miniutti, G. & Fabian, A. C. 2004, *Mon. Not. R. astr. Soc.*, 349, 1435, arXiv:arXiv:astro-ph/0309064
- Miniutti, G., Fabian, A. C., Anabuki, N., Crummy, J., Fukazawa, Y., Gallo, L., Haba, Y., Hayashida, K., Holt, S., Kunieda, H., Larsson, J., Markowitz, A., Matsumoto, C., Ohno, M., Reeves, J. N., Takahashi, T., Tanaka, Y., Terashima, Y., Torii, K., Ueda, Y., Ushio, M., Watanabe, S., Yamauchi, M., & Yaqoob, T. 2007, *Publ. astr. Soc. Japan*, 59, 315
- Miyamoto, S., Kitamoto, S., Mitsuda, K., & Dotani, T. 1988, *Nature*, 336, 450
- Mushotzky, R. F., Fabian, A. C., Iwasawa, K., Kunieda, H., Matsuoka, M., Nandra, K., &

- Tanaka, Y. 1995, *Mon. Not. R. astr. Soc.*, 272, L9
- Nandra, K., George, I. M., Mushotzky, R. F., Turner, T. J., & Yaqoob, T. 1997, *Astrophys. J.*, 476, 70
- Nandra, K., O'Neill, P. M., George, I. M., Reeves, J. N., & Turner, T. J. 2006, *Astron. Nachr.*, 327, 1039
- Nandra, K., Pounds, K. A., & Stewart, G. C. 1990, *Mon. Not. R. astr. Soc.*, 242, 660
- Nandra, K., Pounds, K. A., Stewart, G. C., Fabian, A. C., & Rees, M. J. 1989, *Mon. Not. R. astr. Soc.*, 236, 39P
- Narayan, R. & Yi, I. 1994, *Astrophys. J.*, 428, L13
- Nelson, C. H. & Whittle, M. 1995, *Astrophys. J. Suppl.*, 99, 67
- Nordgren, T. E., Helou, G., Chengalur, J. N., Terzian, Y., & Khachikian, E. 1995, *Astrophys. J. Suppl.*, 99, 461
- Novikov, I. D. & Thorne, K. S. 1974, *Black Holes* (New York, Gordon & Breach, 1974, p. 343)
- Nowak, M. A. & Chiang, J. 2000, *Astrophys. J. Lett.*, 531, L13, arXiv:arXiv:astro-ph/9906371
- Nowak, M. A., Wilms, J., & Dove, J. B. 2002, *Mon. Not. R. astr. Soc.*, 332, 856, arXiv:astro-ph/0201383
- Nowak, M. A., Wilms, J., Vaughan, B. A., Dove, J. B., & Begelman, M. C. 1999, *Astrophys. J.*, 515, 726
- Otani, C., Kii, T., Reynolds, C. S., Fabian, A. C., Iwasawa, K., Hayashida, K., Inoue, H., Kunieda, H., Makino, F., Matsuoka, M., & Tanaka, Y. 1996, *Publ. astr. Soc. Japan*, 48, 211, arXiv:arXiv:astro-ph/9511063
- Paczynski, B. 1978, *Acta Astron.*, 28, 241
- Page, D. N. & Thorne, K. S. 1974, *Astrophys. J.*, 191, 499
- Page, K. L., Turner, M. J. L., Done, C., O'Brien, P. T., Reeves, J. N., Sembay, S., & Stuhlinger, M. 2004, *Mon. Not. R. astr. Soc.*, 349, 57, arXiv:arXiv:astro-ph/0312148

- Papadakis, I. E., Kazanas, D., & Akylas, A. 2005, *Astrophys. J.*, 631, 727, arXiv:astro-ph/0506299
- Piccinotti, G., Mushotzky, R. F., Boldt, E. A., Holt, S. S., Marshall, F. E., Serlemitsos, P. J., & Shafer, R. A. 1982, *Astrophys. J.*, 253, 485
- Ponti, G., Miniutti, G., Cappi, M., Maraschi, L., Fabian, A. C., & Iwasawa, K. 2006, *Mon. Not. R. astr. Soc.*, 368, 903, arXiv:arXiv:astro-ph/0602191
- Pottschmidt, K., Wilms, J., Nowak, M. A., Pooley, G. G., Gleissner, T., Heindl, W. A., Smith, D. M., Remillard, R., & Staubert, R. 2003, *Astr. Astrophys.*, 407, 1039, arXiv:astro-ph/0202258
- Pounds, K. A., Nandra, K., Fink, H. H., & Makino, F. 1994, *Mon. Not. R. astr. Soc.*, 267, 193
- Pounds, K. A., Nandra, K., Stewart, G. C., George, I. M., & Fabian, A. C. 1990, *Nature*, 344, 132
- Pounds, K. A., Nandra, K., Stewart, G. C., & Leighly, K. 1989, *Mon. Not. R. astr. Soc.*, 240, 769
- Pounds, K. A., Reeves, J. N., King, A. R., & Page, K. L. 2004, *Mon. Not. R. astr. Soc.*, 350, 10, arXiv:arXiv:astro-ph/0310257
- Pounds, K. A., Reeves, J. N., King, A. R., Page, K. L., O'Brien, P. T., & Turner, M. J. L. 2003a, *Mon. Not. R. astr. Soc.*, 345, 705, arXiv:arXiv:astro-ph/0303603
- Pounds, K. A., Reeves, J. N., Page, K. L., Wynn, G. A., & O'Brien, P. T. 2003b, *Mon. Not. R. astr. Soc.*, 342, 1147
- Pounds, K. A. & Turner, T. J. 1988, *Soc. Astr. Ital. Mem.*, 59, 261
- Priedhorsky, W., Hasinger, G., Lewin, W. H. G., Middleditch, J., Parmar, A., Stella, L., & White, N. 1986, *Astrophys. J.*, 306, L91
- Rees, M. J. in , American Institute of Physics Conference Series, Vol. 83, The Galactic Center, ed. G. R. Riegler R. D. Blandford, 166–176
- Reeves, J. N., Awaki, H., Dewangan, G. C., Fabian, A. C., Fukazawa, Y., Gallo, L., Grif-

- fiths, R., Inoue, H., Kunieda, H., Markowitz, A., Miniutti, G., Mizuno, T., Mushotzky, R., Okajima, T., Ptak, A., Takahashi, T., Terashima, Y., Ushio, M., Watanabe, S., Yamasaki, T., Yamauchi, M., & Yaqoob, T. 2007, *Publ. astr. Soc. Japan*, 59, 301
- Reeves, J. N., Fabian, A. C., Kataoka, J., Kunieda, H., Markowitz, A., Miniutti, G., Okajima, T., Serlemitsos, P., Takahashi, T., Terashima, Y., & Yaqoob, T. 2006, *Astronomische Nachrichten*, 327, 1079, arXiv:arXiv:astro-ph/0610436
- Reeves, J. N., Nandra, K., George, I. M., Pounds, K. A., Turner, T. J., & Yaqoob, T. 2004, *Astrophys. J.*, 602, 648, arXiv:arXiv:astro-ph/0310820
- Reeves, J. N., O'Brien, P. T., & Ward, M. J. 2003, *ApJ*, 593, L65, arXiv:arXiv:astro-ph/0307127
- Reynolds, C. S. 1997, *Mon. Not. R. astr. Soc.*, 236, 513
- . 2000, *Astrophys. J.*, 533, 811, arXiv:arXiv:astro-ph/9912001
- Reynolds, C. S. & Begelman, M. C. 1997, *Astrophys. J.*, 488, 109
- Reynolds, C. S., Brenneman, L. W., & Stocke, J. T. 2005, *Mon. Not. R. astr. Soc.*, 357, 381
- Reynolds, C. S., Brenneman, L. W., Wilms, J., & Kaiser, M. E. 2004a, *Mon. Not. R. astr. Soc.*, 352, 205, arXiv:arXiv:astro-ph/0404187
- Reynolds, C. S. & Fabian, A. C. 1995, *Mon. Not. R. astr. Soc.*, 273, 1167
- Reynolds, C. S., Fabian, A. C., & Inoue, H. 1995, *Mon. Not. R. astr. Soc.*, 276, 1311, arXiv:arXiv:astro-ph/9504095
- Reynolds, C. S. & Nowak, M. A. 2003, *Phys. Reports*, 377, 389
- Reynolds, C. S., Ward, M. J., Fabian, A. C., & Celotti, A. 1997, *Mon. Not. R. astr. Soc.*, 291, 403, arXiv:arXiv:astro-ph/9707160
- Reynolds, C. S. & Wilms, J. 2000, *Astrophys. J.*, 533, 821
- Reynolds, C. S., Wilms, J., Begelman, M. C., Staubert, R., & Kendziorra, E. 2004b, *Mon. Not. R. astr. Soc.*, 349, 1153, arXiv:arXiv:astro-ph/0401305
- Robson, E. I., Gear, W. K., Brown, L. M. J., Courvoisier, T. J.-L., & Smith, M. G. 1986,

Nature, 323, 134

Ross, R. R. & Fabian, A. C. 2005, *Mon. Not. R. astr. Soc.*, 358, 211

Ross, R. R., Fabian, A. C., & Brandt, W. N. 1996, *Mon. Not. R. astr. Soc.*, 278, 1082,
arXiv:arXiv:astro-ph/9510022

Rybicki, G. B. & Lightman, A. P. 1979, *Radiative Processes in Astrophysics* (New York, Wiley-Interscience, 1979. 393 p.)

Sako, M., Kahn, S. M., Branduardi-Raymont, G., Kaastra, J. S., Brinkman, A. C., Page, M. J., Behar, E., Paerels, F., Kinkhabwala, A., Liedahl, D. A., & den Herder, J. W. 2003, *Astrophys. J.*, 596, 114, arXiv:arXiv:astro-ph/0112436

Sambruna, R. M., Eracleous, M., & Mushotzky, R. F. 1999, *Astrophys. J.*, 526, 60, arXiv:arXiv:astro-ph/9905365

Schurch, N. J., Warwick, R. S., Griffiths, R. E., & Kahn, S. M. 2004, *Mon. Not. R. astr. Soc.*, 350, 1, arXiv:arXiv:astro-ph/0401550

Shakura, N. I. & Sunyaev, R. A. 1973, *Astr. Astrophys.*, 24, 337

Sikora, M., Stawarz, Ł., & Lasota, J.-P. 2007, *Astrophys. J.*, 658, 815, arXiv:arXiv:astro-ph/0604095

Speith, R., Riffert, H., & Ruder, H. 1995, *Comp. Phys. Communic.*, 88, 109

Stella, L. & Angelini, L. *Astronomical Society of the Pacific Conference Series*, Vol. 25, ,
Astronomical Data Analysis Software and Systems I, ed. D. M. Worrall, C. Biemesderfer & J. Barnes, 103–+

Tanaka, Y., Nandra, K., Fabian, A. C., Inoue, H., Otani, C., Dotani, T., Hayashida, K., Iwasawa, K., Kii, T., Kunieda, H., Makino, F., & Matsuoka, K. 1995, *Nature*, 375, 659

Thorne, K. S. 1974, *Astrophys. J.*, 191, 507

Titarchuk, L. 1994, *Astrophys. J.*, 434, 570

Türler, M., Chernyakova, M., Courvoisier, T. J.-L., Foellmi, C., Aller, M. F., Aller, H. D., Kraus, A., Krichbaum, T. P., Lähteenmäki, A., Marscher, A., McHardy, I. M., O'Brien,

- P. T., Page, K. L., Popescu, L., Robson, E. I., Tornikoski, M., & Ungerechts, H. 2006, *Astr. Astrophys.*, 451, L1, [arXiv:arXiv:astro-ph/0603579](#)
- Turner, A. K., Fabian, A. C., Vaughan, S., & Lee, J. C. 2003, *Mon. Not. R. astr. Soc.*, 346, 833, [arXiv:arXiv:astro-ph/0303418](#)
- Turner, A. K., Lee, J. C., Fabian, A. C., & Vaughan, S. 2004, *Mon. Not. R. astr. Soc.*, 353, 319
- Turner, M. J. L., Williams, O. R., Courvoisier, T. J. L., Stewart, G. C., Nandra, K., Pounds, K. A., Ohashi, T., Makishima, K., Inoue, H., Kii, T., Makino, F., Hayashida, K., Tanaka, Y., Takano, S., & Koyama, K. 1990, *Mon. Not. R. astr. Soc.*, 244, 310
- Turner, T. J., Kraemer, S. B., George, I. M., Reeves, J. N., & Bottorff, M. C. 2005, *Astrophys. J.*, 618, 155, [arXiv:arXiv:astro-ph/0409091](#)
- Turner, T. J., Miller, L., George, I. M., & Reeves, J. N. 2006, *Astr. Astrophys.*, 445, 59, [arXiv:arXiv:astro-ph/0506223](#)
- Turner, T. J., Mushotzky, R. F., Yaqoob, T., George, I. M., Snowden, S. L., Netzer, H., Kraemer, S. B., Nandra, K., & Chelouche, D. 2002, *Astrophys. J.*, 574, L123
- Turner, T. J., Nandra, K., George, I. M., Fabian, A. C., & Pounds, K. A. 1993, *Astrophys. J.*, 419, 127
- Turner, T. J. & Pounds, K. A. 1989, *Mon. Not. R. astr. Soc.*, 240, 833
- Uttley, P., Fruscione, A., McHardy, I., & Lamer, G. 2003, *Astrophys. J.*, 595, 656, [arXiv:arXiv:astro-ph/0306234](#)
- Uttley, P., Taylor, R. D., McHardy, I. M., Page, M. J., Mason, K. O., Lamer, G., & Fruscione, A. 2004, *Mon. Not. R. astr. Soc.*, 347, 1345, [arXiv:arXiv:astro-ph/0310701](#)
- van der Klis, M. 1989, *Ann. Rev. Astr. Astrophys.*, 27, 517
- Vaughan, S. & Fabian, A. C. 2004, *Mon. Not. R. astr. Soc.*, 348, 1415
- Vaughan, S., Fabian, A. C., Ballantyne, D. R., De Rosa, A., Piro, L., & Matt, G. 2004, *Mon. Not. R. astr. Soc.*, 351, 193, [arXiv:arXiv:astro-ph/0402660](#)
- Vaughan, S., Fabian, A. C., & Nandra, K. 2003, *Mon. Not. R. astr. Soc.*, 339, 1237,

- arXiv:astro-ph/0211421
- Volonteri, M., Madau, P., Quataert, E., & Rees, M. J. 2005, *Astrophys. J.*, 620, 69, arXiv:arXiv:astro-ph/0410342
- Wagner, R. M., Starrfield, S. G., Hjellming, R. M., Howell, S. B., & Kreidl, T. J. 1994, *Astrophys. J.*, 429, L25
- Wandel, A., Peterson, B. M., & Malkan, M. A. 1999, *Astrophys. J.*, 526, 579, arXiv:arXiv:astro-ph/9905224
- Ward, M., Elvis, M., Fabbiano, G., Carleton, N. P., Willner, S. P., & Lawrence, A. 1987, *Astrophys. J.*, 315, 74
- Weaver, K. A., Gelbord, J., & Yaqoob, T. 2001, *Astrophys. J.*, 550, 261, arXiv:astro-ph/0008522
- Weaver, K. A., Krolik, J. H., & Pier, E. A. 1998, *Astrophys. J.*, 498, 213, arXiv:arXiv:astro-ph/9712035
- Weaver, K. A., Yaqoob, T., Mushotzky, R. F., Nousek, J., Hayashi, I., & Koyama, K. 1997, *Astrophys. J.*, 474, 675
- White, N. E., Peacock, A., & Taylor, B. G. 1985, *Astrophys. J.*, 296, 475
- Wilkes, B. J. & Elvis, M. 1987, *Astrophys. J.*, 323, 243
- Wilms, J., Nowak, M. A., Dove, J. B., Fender, R. P., & di Matteo, T. 1999, *Astrophys. J.*, 522, 460
- Wilms, J., Reynolds, C. S., Begelman, M. C., Reeves, J., Molendi, S., Staubert, R., & Kendziorra, E. 2001, *Mon. Not. R. astr. Soc.*, 328, L27
- Worrall, D. M., Boldt, E. A., Holt, S. S., Mushotzky, R. F., & Serlemitsos, P. J. 1981, *Astrophys. J.*, 243, 53
- Yaqoob, T. & Serlemitsos, P. 2000, *Astrophys. J. Lett.*, 544, L95, arXiv:arXiv:astro-ph/0009435
- Ye, Y.-C., Wang, D.-X., & Ma, R.-Y. 2007, ArXiv Astrophysics e-prints, arXiv:astro-ph/0701802

- Young, A. J., Lee, J. C., Fabian, A. C., Reynolds, C. S., Gibson, R. R., & Canizares, C. R. 2005, *Astrophys. J.*, 631, 733
- Young, A. J., Ross, R. R., & Fabian, A. C. 1998, *Mon. Not. R. astr. Soc.*, 300, L11
- Zdziarski, A. A. & Grandi, P. 2001, *Astrophys. J.*, 551, 186, arXiv:arXiv:astro-ph/0011543